

**CHARACTERISING THE FORCE BALANCE
BETWEEN ACTIVE PHARMACEUTICAL
INGREDIENTS FOR INHALATION AND ITS
IMPACT ON DEPOSITION**

MATTHEW JOHN PIGGOTT

MRPharmS

**Thesis submitted to The University of
Nottingham for the degree of Doctor of
Philosophy**

DECEMBER 2013



IMAGING SERVICES NORTH

Boston Spa, Wetherby
West Yorkshire, LS23 7BQ
www.bl.uk

TEXT BOUND CLOSE TO THE SPINE IN THE ORIGINAL THESIS

IMAGING SERVICES NORTH

Boston Spa, Wetherby

West Yorkshire, LS23 7BQ

www.bl.uk

BEST COPY AVAILABLE.

VARIABLE PRINT QUALITY

Dedicated to Bette, Les, Nancy and John

**“Thank you Mario! But our princess is
in *another* castle...!”**

-Super Mario Bros-

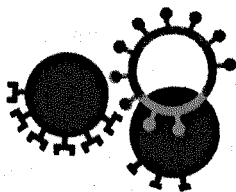




The University of
Nottingham

UNITED KINGDOM • CHINA • MALAYSIA

3M



BBSRC
bioscience for the future

Abstract

Interparticulate interactions play a significant role in determining the down stream behaviours of all pharmaceutical formulations and are therefore essential considerations when approaching formulation design. Inhalation product formulation in particular is inherently bound to an understanding of these forces. Delivery of drugs to the lower airways to treat conditions like asthma and COPD requires a particle size of below $5\mu\text{m}$. This implicitly demands micronization of the active pharmaceutical ingredients (APIs) and this process renders many particles of large surface area with high surface energies and an auto-adhesive tendency. There is therefore a concurrent reduction in the flowability and dispersion properties of these systems. The interactive character predisposes agglomeration, flocculation or device retention and will compromise manufacture, stability, device function, and the aerosolization behavior of a formulation. Ultimately the ability of any aerosolized API to reach the deep airways is dependent upon adhesion force dynamics. As such, an appreciation of the forces of attraction and scale of particulate interactions within inhaler technology is critical if a successful drug delivery device is to be realized.

The advancement of the atomic force microscope (AFM) as a force probing apparatus, has meant that it is now possible to measure the force of adhesion between two particles of interest. However these measurements could not easily be compared, because there is no simple means to account for differences in the contact regime (geometrics) between measurements. However, the development of the cohesive adhesive balance (CAB) approach by Begat, Morton, Stainforth and Price in 2004 has offered a means to negate this limitation. Using a colloidal probe microscopy (CPM) derived technique a particle of a selected material of interest (API, carrier molecule etc.) is attached to an AFM cantilever and ramped onto and off the surface of another material of interest (adhesion measurement), and to a surface of the same material as the tip (cohesion measurement). By graphically plotting the adhesive force values of a series of tips, as a function of the cohesive force values of the same tips, a representation of the relative particle interaction can be obtained. Quantitative information regarding the adhesive/cohesive nature of the interaction can then be extracted from the graph and a description of the interaction formulated that can be compared to other material combinations.

The CAB work carried out to date has used recrystallized model substrates. These molecularly flat surfaces ensured there would be no difference between the contact geometry of a functionalised AFM probe and the adhesive and cohesive surfaces of the study respectively. In this fashion the only variable between the two measurements would be the chemical interactivity, and not the interactive surface area. However while using such methodology guarantees the validity of the approach, it is not necessarily a true representation of the materials '*in-situ*' and requires more complex sample preparation and complex experimental design. For a variety of reasons this can be misleading in its own right.

This thesis details the investigation into the application of an adapted CAB approach in characterizing the force balance between APIs for inhalation in their real state. In so doing, the aim was to see whether such a CAB would offer a quicker and simpler, yet relevant and informative assessment of a drug system force balance. It was hoped that said force balance could in turn be associated with a measurable impact upon the formulation performance of the characterised ingredients as measured '*in-vitro*'. This interest was particularly directed at the lesser characterized pressurized metered dose inhaler (pMDI) systems. While these formulations are solvent based, it was of interest to identify whether a simple API to API challenge could infer a descriptive balance that could link to '*in-vitro*' performance. Furthermore there was interest in evaluating the use of a range of surface specific imaging techniques to analyse the deposition dynamics of the combination formulations. It was hoped that by doing so, the localisation of the individual components within the binary deposits could again be associated back to the force balance of that system, and that an appreciation of the capability of the techniques involved would be gained.

The work that follows therefore commences with the evaluation and description of the capacity for the CAB approach to be adapted to measure force relationships between real beclomethasone dipropionate (BDP) particles and pMDI component surfaces. From this assessment it was found that even with relatively smooth substrates, the combination of bulky functional particles and the inherent substrate roughness caused a critical failure in the CAB model. The parity between cohesive and adhesive geometries of contact was excessively stretched, leading to a loss of force normalisation which was reflected in uncorrelated CAB plots. As a consequence little could be confidently gleaned from the force data acquired,

although there was the suggestion that the use of a fluorinated ethylene propylene (FEP) coating reduced the adhesive interaction between the APIs and the pMDI canister wall.

This was then followed by an attempt to find a compromise between the model crystal substrates of a pure CAB process and the real particle morphologies that had caused the CAB model to fail. Using a compression process to form API powder compacts, in conjunction with small and discreet functional particles, a confident CAB was achieved for two combinations of APIs selected on the basis of surface energy and physical stability analysis. Salbutamol sulphate was characterised with beclomethasone dipropionate, and salmeterol xinafoate with fluticasone propionate. Both combinations showed CAB plots with a sufficiently strong linear regression analysis to suggest a broad accuracy of force balance assessment. Both β_2 -agonists showed cohesively dominated relationships with respect to the paired glucocorticoids, while in reverse both glucocorticoids showed adhesively dominated relationships with the β_2 -agonists. There was concern raised over the compression process of the powder discs, and its impact on the physicochemical state of the APIs, with some thermodynamic evidence of polymorphic changes that required further work.

The next chapter looks at the '*in-vitro*' deposition performance of the two API combinations from a HFA134a pMDI system by analysis in an Andersen Cascade Impactor (ACI). The co-formulation of salmeterol with fluticasone induced an improvement in the fine particle performance of fluticasone, with a concurrent decrease in the fine particle performance of salmeterol. This impact was hypothesised to be related to alterations in the structure and strength of particle-particle agglomerates. The impact on deposition performance of co-formulating beclomethasone and salbutamol was unclear, as a critical unexplained loss of beclomethasone by total recovered mass was seen from all beclomethasone containing formulations. This instability of beclomethasone within the HFA134a system, precluded an accurate assessment of a direct impact on salbutamol deposition.

The final chapter, compared a range of surface specific imaging techniques, including scanning electron microscopy (SEM), desorption electrospray ionization mass spectrometry (DESI), Raman spectrometry and time-of-flight secondary ion mass spectrometry (ToF-SIMS) in assessing the extent and nature of '*in-vitro*' co-deposition from the salmeterol and fluticasone pMDI formulations. It was apparent that the deposition of the two APIs on ACI plates was not likely to be directly comparable assessment of the incidence of particle co-deposition '*in-vivo*' due to the

forced nature of nozzle directed impaction. However the combination of techniques employed produced a wealth of physical and chemical data that did suggest that the two APIs showed extensive co-ordination '*in-vitro*'. Raman spectroscopy was able to identify individual particle character and showed frequent salmeterol and fluticasone particle combinations, but suffered from exceptionally long run times and anomalies from photoreactive surface elements. The use of a multivariate approach to ToF-SIMS analysis defined the strong co-association of the two APIs, although could not differentiate particle to particle deposition. Multivariate curve resolution (MCR) was used and produced distinct components that segregated ions from both APIs from the background plate but not from each other. SEM imaging was able to define the morphologies of the deposited particles, but was unable to differentiate the two. DESI imaging showed the presence of the two APIs together within several drug spots, but could not be used to investigate individual drug spots, and the distribution within, due to inadequate spatial resolution and differences in desorption efficacy. While the co-association of the two APIs was observed, the lack of a comparator in another combination of APIs made the link between deposition performance and force balance purely descriptive. It was unclear as to whether the force balance of the system lends itself to a particular increase in co-deposition behaviour. However it was apparent that the analytical techniques employed all had respective strengths and weaknesses as mapping tools, and with further work with other formulations could be used to provide a tailored formulation screening process, if subsequent links to force balances could be made.

To conclude, the work in this thesis details the successful process of adapting an AFM technique in characterising the broad force balance of combinations of APIs. In so doing a force balance has been linked to the alteration in deposition behaviour of two APIs when co-formulated in a HFA134 formulation. The subsequent co-deposition of the two APIs was then analysed by a series of surface analytical techniques. This highlighted a general co-deposition trend, but the collective results were unable to definitively link to the force balance of the system. The information obtained forms the beginnings of what could be utilised as a fast and facile broad predictor of pMDI formulation performance, and an indication of appropriate analytical techniques for investigating particle association '*in-vitro*'.

Acknowledgments

My sincerest thanks go first to my supervisors Professors Clive Roberts, Martyn Davies and Morgan Alexander for all their support, assistance and guidance throughout my experimentation and analysis. Not all work ends in triumph, or is quick and simple to perform and I particularly wish to thank them for their vision and redirection following the many fruitless days sat at an AFM that enabled me to compile a body of work worth writing about.

Special gratitude goes to my external supervisor Phil Jinks at 3M Drug Delivery whose expertise and technical resources made large parts of this work possible. I also extend the warmest thanks and praise to Xinyong Chen, whose teachings in AFM technique and theory were invaluable and whose enthusiasm no matter the diabolical nature of my errors was boundless. I am also very grateful to the BBSRC and 3M Healthcare Ltd for providing the funding that enabled my studies.

I would also like to acknowledge the technical experts that helped me through my experimentation. David Scurr for his operational and analytical assistance with ToF-SIMS imaging and multivariate analysis, Wei Rao for his skills with DESI operation and Christine Grainger-Boulton for her assistance with SEM imaging.

In addition special thanks go to my friend and colleague Abdennour Bouhroum, whose assistance at the beginning of my study was invaluable. I thank all my colleagues in the LBSA for having made it an enjoyable three years and been of great assistance to me when I needed it.

Finally, I owe the largest gratitude to my family. Without the care, compassion and support of my parents in particular I would never have achieved a fraction of what I am so proud of today. The example they set will forever be a standard to which I aspire, and my hard work is only a reflection of their own.

Abbreviations

A	-	Hamaker Constant
ACI	-	Andersen Cascade Impactor
API	-	Active Pharmaceutical Ingredient
AFM	-	Atomic Force Microscopy
BDP	-	Beclomethasone Dipropionate
BUD	-	Budesonide
CAB	-	Cohesive Adhesive Balance
CFC	-	Chlorofluorocarbon
CFC 11	-	Trichlorofluoromethane
CFC 12	-	Dichlorodifluoromethane
COPD	-	Chronic Obstructive Pulmonary Disease
CPM	-	Colloidal Probe Microscopy
CRT	-	Cathode Ray Tube
DESI	-	Desorption Electrospray Ionization Mass Spectrometry
DMF	-	N,N- Dimethyl-formamide
DMT	-	Derjaguin-Muller-Toporov
DPI	-	Dry Powder Inhaler
EP	-	European Pharmacopoeia
F_{adh}	-	Force of Adhesion
F_c	-	Capillary Forces
$F_{centrifugal}$	-	Centrifugal Force
F_{coh}	-	Force of Cohesion (Autoadhesion)
F_{es}	-	Electrostatic Forces
F_{vdw}	-	van der Waals Forces

Abbreviations

FEG	-	Field Emission Gun
FEP	-	Fluorinated Ethylene Propylene
FP	-	Fluticasone Propionate
FPD	-	Fine Particle Dose
FPF	-	Fine Particle Fraction
FT-IR	-	Fourier Transform Infrared Spectroscopy
HFA	-	Hydrofluoroalkane
HFA134a	-	1,1,1,2-tetrafluoromethane
HFA227ea	-	1,1,1,2,3,3,3-heptafluoropropane
HFPE	-	2H, 3H perfluoropentane
HPLC	-	High Performance Liquid Chromatography
ICS	-	Inhaled Corticosteroid
IPA	-	Isopropylalcohol
IR	-	Infrared
JKR	-	Johnson-Kendall-Roberts
LABA	-	Long Acting Beta Agonist
LD	-	Laser Diffractometry
MCR	-	Multivariate Curve Resolution
MS	-	Mass Spectrometer
MSLI	-	Multi-Stage Liquid Impinger
MVA	-	Multivariate Analysis
m/z	-	Mass to Charge Ratio
NGI	-	Next Generation Impactor
PCA	-	Principal Component Analysis
PDA	-	Phase-Doppler Particle Size Analysis

Abbreviations

PTFE	-	Polytetrafluoroethylene
pMDI	-	Pressurized Metered Dose Inhaler
R^2	-	Coefficient of Determination
R_q	-	Root Mean Square Roughness
R_a	-	Arithmetic Mean Average Roughness
R_{max}	-	Maximum Asperity Height
RH	-	Relative Humidity
SEM	-	Scanning Electron Microscopy
SFA	-	Surface Forces Apparatus
SPM	-	Scanning Probe Microscopy
SS	-	Salbutamol Sulphate
SX	-	Salmeterol Xinafoate
TEM	-	Transmission Electron Microscopy
TFA	-	Trifluoroacetic Acid
TIRM	-	Total Internal Reflection Microscopy
TOF	-	Particle Time-of-Flight
ToF-SIMS	-	Time-of-Flight Secondary Ion Mass Spectrometry
UK	-	United Kingdom
USA	-	United States of America
USP	-	United States Pharmacopoeia
W_A	-	Work of Adhesion
XRPD	-	X-Ray Powder Diffraction

Contents

Abstract	I
Acknowledgements	V
Abbreviations	VI
Contents	IX
List of Figures	XVII
List of Tables	XXXV
Thesis Aims and Objectives	XXXVII
Chapter 1: Introduction	1
1.1 Drug Delivery via Inhalation	1
1.2 The Human Respiratory Tract	2
1.2.1 Physiology of the Respiratory Tract	2
1.3 Active Pharmaceutical Agents for Respiratory Diseases	4
1.3.1 Common Classes of Active Pharmaceutical Agent	4
1.3.2 Beta ₂ -Adrenoceptor Agonists	5
1.3.3 Glucocorticoids	7
1.4 Delivering Active Pharmaceutical Agents to the Respiratory System	10
1.4.1 Nebulisers	10
1.4.2 Dry Powder Inhalers	11
1.4.3 Pressurized Metered Dose Inhalers	12
1.4.4 Hydrofluoroalkane (HFA) Propellants	13
1.5 The Deposition of Drugs Delivered to the Respiratory Tract	17
1.5.1 Inertial Impaction	17
1.5.2 Gravitational Sedimentation	18
1.5.3 Diffusion (Brownian Motion)	19
1.5.4 Assessing Formulation Deposition ' <i>in-vitro</i> '	19

1.6	Interparticulate Interactions within Inhalation Formulations	20
1.6.1	Interparticulate Interaction	21
1.6.2	The Forces of Adhesion and Cohesion	22
1.7	Interfacial Surface Forces	23
1.7.1	Capillary forces	23
1.7.2	Electrostatic forces	24
1.7.3	Van der Waals forces	25
1.8	Adhesion Theory	29
1.8.1	The Hertz Approximation	29
1.8.2	The Johnson-Kendall-Roberts Model	31
1.8.3	The Derjaguin-Muller-Toporov Model	32
1.8.4	The Tabor Number	33
1.9	Other Factors Affecting Adhesion	34
1.9.1	Surface Roughness	34
1.9.2	Young's Modulus	34
1.9.3	Surface Free Energy	34
1.10	Experimental Methods of Surface Forces Determination	35
1.10.1	Centrifugation	35
1.10.2	Tensile Stress Methods	38
1.10.3	Surface Forces Apparatus	40
1.10.4	Total Internal Reflection Microscopy	41
1.10.5	Osmotic Stress Method	42
1.10.6	Impaction Methods	43
1.10.7	The Limitations of Bulk Adhesion Measurement	43
1.11	Atomic Force Microscopy	44
1.12	Colloidal Probe Microscopy	47

1.13	The Cohesive-Adhesive Balance Approach	50
	1.13.1 The CAB Method	50
	1.13.2 CAB Studies	54
	1.13.3 The Cohesive Adhesive Balance: A Summation	57
1.14	References	59
 Chapter 2: Materials and Methods		66
2.1	General Introduction	66
2.2	Materials	66
	2.2.1 Active Pharmaceutical Ingredients (APIs), Propellants and Excipients	66
	2.2.2 Pressurised Metered Dose Inhaler Components	70
2.3	Methods	72
	2.3.1 Atomic Force Microscopy	72
	2.3.2 Time of Flight Secondary Ion Mass Spectrometry and Multivariate Analysis	72
	2.3.3 Raman Spectroscopy	79
	2.3.4 Scanning Electron Microscopy	82
	2.3.5 Andersen Cascade Impaction	85
	2.3.6 High Performance Liquid Chromatography	90
	2.3.7 Desorption Electrospray Ionization Mass Spectrometry	92
	2.3.8 Differential Scanning Calorimetry	94
	2.3.9 X-Ray Powder Diffractometry	96
2.4	References	97
 Chapter 3: Application of the CAB Approach to Inhalation Materials with 'Non-Ideal' Surfaces		100
3.1	General Introduction	100
	3.1.1 Limitations of the Cohesive Adhesive Balance	100

3.1.2	pMDI Formulation Topographies	100
3.1.3	Interpreting data from Recrystallized Substrates	102
3.1.4	Clathrates	103
3.2	Chapter Aims and Objectives	104
3.2.1	Chapter Aim	104
3.2.2	Chapter Objectives	104
3.3	Materials and Methods	105
3.3.1	Materials	105
3.3.2	Methods	105
3.4	Results	109
3.4.1	Characterization of Beclomethasone and the Beclomethasone Clathrates	109
3.4.2	Characterization of the pressurized metered dose inhaler components	120
3.4.3	Cohesive Adhesive Balance of Beclomethasone APIs and the pMDI Components	124
3.5	Discussion	135
3.5.1	Characterization of Beclomethasone and the Beclomethasone Clathrates	135
3.5.2	Characterization of the pMDI Components	138
3.5.3	The Cohesive Adhesive Balance of the BDP APIs and pMDI Components	140
3.6	Conclusion	147
3.7	References	149

Chapter 4: Application of the CAB approach to, and Characterization of Semi-Model Inhalation Substrates	152
--	------------

4.1	General Introduction	152
	4.1.1 Semi-model Substrates for CAB studies	152
	4.1.2 Modification of CAB materials	152
4.2	Chapter Aims and Objectives	154
	4.2.1 Chapter Aim	154
	4.2.2 Chapter Objectives	154
4.3	Materials and Methods	155
	4.3.1 Materials	155
	4.3.2 Methods	155
4.4	Results	160
	4.4.1 AFM Derived Surface Free Energy Determination of Compressed APIs	160
	4.4.2 Differential Scanning Calorimetry Analysis on the Effects of API Compression	163
	4.4.3 The Cohesive Adhesive Balance of Salbutamol Sulphate and Beclomethasone Dipropionate using Compressed Powder Substrates	166
	4.4.4 The Cohesive Adhesive Balance of Salmeterol Xinafolate and Fluticasone Propionate using Compressed Powder Substrates	182
4.5	Discussion	193
	4.5.1 Characterizing the API Power Compresses	193
	4.5.2 The Cohesive Adhesive Balance of Salbutamol Sulphate and Beclomethasone Dipropionate using Semi-Model Substrates	199
	4.5.3 The Cohesive Adhesive Balance of Salmeterol Xinafolate and Fluticasone Propionate using Semi-Model Substrates	202
4.6	Conclusions	207
4.7	References	209

Chapter 5: The Cohesive Adhesive Balance of Inhalation Formulations and their 'in-vitro' Deposition Performance	210
5.1 General Introduction	210
5.1.1 Associating Force Balances to 'in-vitro' Deposition Performance	210
5.2 Chapter Aims and Objectives	211
5.2.1 Chapter Aim	211
5.2.2 Chapter Objectives	211
5.3 Materials and Methods	212
5.3.1 Materials	212
5.3.2 Methods	213
5.4 Results and Discussion	224
5.4.1 Deposition of the Solo and Co-Formulated Salbutamol Sulphate and Beclomethasone Dipropionate	224
5.4.2 Deposition of the Solo and Co-Formulated Salmeterol Xinafoate and Fluticasone Propionate	234
5.5 Conclusions	245
5.6 References	247
Chapter 6: Investigating the Co-Deposition of Active Pharmaceutical Ingredients from HFA134a pMDI systems	248
6.1 General Introduction	248
6.1.1 Combination Inhalers for the Treatment of Airways Disease	248
6.1.2 The Co-Deposition of Salmeterol Xinafoate and Fluticasone Propionate	249
6.1.3 Assessing 'in-vitro' Co-Deposition	250

Contents

6.2	Aims and Objectives	251
6.2.1	Chapter Aim	251
6.2.2	Chapter Objectives	251
6.3	Materials and Methods	252
6.3.1	Materials	252
6.3.2	Methods	252
6.4	Results and Discussion	258
6.4.1	The Deposition of Salbutamol Sulphate and Beclomethasone Dipropionate	258
6.4.2	Investigating the Co-Deposition of Salmeterol and Fluticasone	264
6.5	Conclusions	297
6.6	References	300
Chapter 7: Final Conclusions		302
7.1	General Introduction	302
7.2	Application of the CAB Approach to Inhalation Materials with 'Non-Ideal' Surfaces	302
7.3	Application of the CAB approach to, and Characterization of Semi-Model Inhalation Substrates	303
7.4	The Cohesive Adhesive Balance of Inhalation Formulations and their 'in-vitro' Deposition Performance	304

7.5	Investigating the Co-Deposition of Salmeterol Xinafolate and Fluticasone Propionate from a HFA134a Pressurized Metered Dose Inhaler System	304
7.6	Future Research Suggestions	305

List of Figures

Chapter 1

Figure 1.1	Diagram of the respiratory system	3
Figure 1.2	Salbutamol Sulphate Monograph	5
Figure 1.3	Salmeterol Xinafoate Monograph	6
Figure 1.4	Beclomethasone Dipropionate Monograph	8
Figure 1.5	Budesonide Monograph	9
Figure 1.6	Fluticasone Propionate Monograph	9
Figure 1.7	Schematic of a pMDI device	13
Figure 1.8	The chemical structures of CFC and HFA propellants	14
Figure 1.9	The Hertz Model of contact	29
Figure 1.10	The JKR model of contact	31
Figure 1.11	The DMT contact model	32
Figure 1.12	Basic design of a centrifuge cell	36

Figure 1.13	A modified tensiometer designed for F_{adh} measurements	39
Figure 1.14	Schematic of a Surface Forces Apparatus	41
Figure 1.15	Basic concept of evanescent wave generation	42
Figure 1.16	A schematic of an atomic force microscope	45
Figure 1.17	Force deflection (displacement) plot of an atomic force microscope	47
Figure 1.18	Theoretical CAB graph for a binary system	52

Chapter 2

Figure 2.1	Salbutamol Sulphate Monograph	66
Figure 2.2	Beclomethasone Dipropionate Monograph	67
Figure 2.3	Salmeterol Xinafoate Monograph	68
Figure 2.4	Fluticasone Propionate Monograph	68
Figure 2.5	Budesonide Monograph	69
Figure 2.6	Structure of HFA134a	69

List of Figures and Tables

Figure 2.7	Schematic representation of ion mass separation in the ToF field-free drift tube	73
Figure 2.8	Schematic of a TOF-SIMS analysis	74
Figure 2.9	2D representation of a principal component analysis (PCA)	77
Figure 2.10	2D representation of multivariate curve resolution	78
Figure 2.11	Possible energy state changes of the different scattering processes	80
Figure 2.12	Schematic of a scanning electron microscope	83
Figure 2.13	Schematic of an Andersen Cascade Impactor	86
Figure 2.14	Aerodynamic particle separation in an ACI	87
Figure 2.15	A) Schematic of HPLC apparatus and B) an example chromatogram	91
Figure 2.16	A) Schematic of DESI in operation and B) an example point mass spectrum	93
Figure 2.17	A DSC thermogram of Beclomethasone Monohydrate	95

Chapter 3

Figure 3.1	SEM images of the Anhydrous Beclomethasone Dipropionate powder particles at various magnifications	110
Figure 3.2	SEM Images of the synthesized BDP CFC-11 Clathrate powder particles at various magnifications	111
Figure 3.3	SEM images of the synthesized BDP IPA Clathrate powder particles at various magnifications	112
Figure 3.4	X-Ray Powder Diffractograms for the observed synthesized BDP CFC-11 Clathrate and the calculated Cambridge Structural Database reference	113
Figure 3.5	X-Ray Powder Diffractogram for the synthesized BDP IPA Clathrate	113
Figure 3.6	DSC heating thermograms of (A) anhydrous BDP, (B) BDP CFC-11 Clathrates and (C) BDP IPA Clathrates.	115
Figure 3.7	DSC heating thermograms of (A) BDP CFC-11 Clathrate and (B) BDP IPA Clathrate	116

Figure 3.8	5μm x 5μm Tapping mode AFM height (left) and phase (right) images of (A) Anhydrous BDP powder bed, (B) BDP CFC-11 Clathrate particle main face, (C) BDP CFC-11 Clathrate particle lateral face and (D) BDP IPA Clathrate particle face	118
Figure 3.9	SEM images of A) FEP coated pMDI canister B) Uncoated pMDI canister and C) pMDI stainless steel metering chamber	121
Figure 3.10	AFM height and 3D interpretation of (A) FEP Coated Canister, (B) Un-coated Canister and (C) Metering Chamber	123
Figure 3.11	Mean Cohesive and Adhesive Force Values of Anhydrous BDP tips against CAB substrates	125
Figure 3.12	Mean Cohesive and Adhesive Force Values of BDP CFC-11 tips against CAB substrates	125
Figure 3.13	Mean Cohesive and Adhesive Force Values of BDP IPA tips against CAB substrates	126
Figure 3.14	Example box plots showing force data from A) Anhydrous BDP tips on anhydrous BDP (post adhesion measurements), B) BDP CFC-11 tips on BDP CFC-11 (post adhesion measurements) and C) BDP IPA tips on FEP coated canister	127

Figure 3.15	Example cohesive force curves from functionalized anhydrous BDP tips, BDP-IPA tips and BDP CFC-11 tips A) Accepted force curves and B) Rejected force curves	129
Figure 3.16	CAB plot for anhydrous BDP tips against pMDI components	131
Figure 3.17	CAB plot for BDP CFC-11 tips against pMDI components	131
Figure 3.18	CAB plot for BDP IPA tips against pMDI components	132
Figure 3.19	Low Vacuum SEM images of functionalized tips of A) Anhydrous BDP, B) BDP CFC-11 Clathrate and C) BDP IPA Clathrate both prior to (1) and after (2) AFM force curve acquisition	133
Figure 3.20	Hypothetical Spherical Particle Contact on A) Smooth and B) Rough Surfaces	142

Chapter 4

Figure 4.1	Average surface energies of compressed Beclomethasone Dipropionate (BDP), Salmeterol Xinafoate (SX), Salbutamol Sulphate (SS), Fluticasone Propionate (FP) and Budesonide (BUD) determined by AFM	161
-------------------	--	------------

Figure 4.2	Differential scanning calorimetry thermograms of the pre-compressed powders of Beclomethasone Dipropionate (BDP), Salbutamol Sulphate (SS), Fluticasone Propionate (FP) and Salmeterol Xinafoate (SX)	163
Figure 4.3	Differential scanning calorimetry thermograms of the compressed powders of Beclomethasone Dipropionate (BDP), Salbutamol Sulphate (SS), Fluticasone Propionate (FP) and Salmeterol Xinafoate (SX)	164
Figure 4.4	Comparison of the differential scanning calorimetry thermograms of the pre-compressed and post compressed powders of Beclomethasone Dipropionate (BDP), Salbutamol Sulphate (SS), Fluticasone Propionate (FP) and Salmeterol Xinafoate (SX)	165
Figure 4.4A	SEM images of Salbutamol Sulphate (SS) and Beclomethasone Dipropionate (BDP) micronized powders before compression at A) 550x magnification and B) 8,000x magnification	167
Figure 4.5	SEM images of Salbutamol Sulphate (SS) and Beclomethasone Dipropionate (BDP) powders after compression at A) 250x magnification and B) 2,000x magnification	168
Figure 4.6	Example tapping mode AFM images of Beclomethasone Dipropionate (BDP) and Salbutamol Sulphate (SS) pre compression at (A) 5μm x 5μm and (B) 10μm x 10μm scan sizes	169

Figure 4.7	Representative tapping mode AFM images of Beclomethasone Dipropionate (BDP) and Salbutamol Sulphate (SS) after compression at (A) 5µm x 5µm and (B) 10µm x 10µm scan sizes	170
Figure 4.8	Comparison of the average root mean square roughness of Beclomethasone Dipropionate (BDP) and Salbutamol Sulphate (SS) powders pre- and post- compression as derived from 5µmx5µm and 10µmx10µm tapping mode AFM images	174
Figure 4.9	Example SEM images of functionalised AFM tips with Beclomethasone Dipropionate (BDP), and Salbutamol Sulphate (SS) particulates	175
Figure 4.10	CAB plot for Beclomethasone Dipropionate (BDP) tips with Salbutamol Sulphate (SS)	177
Figure 4.11	CAB plot for Salbutamol Sulphate (SS) tips with Beclomethasone Dipropionate (BDP)	177
Figure 4.12	Example A) cohesive and B) adhesive force curves using the same Beclomethasone Dipropionate (BDP) and (SS) functionalised tips respectively	179
Figure 4.13	Box plots of the force of adhesion measurements of Salbutamol Sulphate tips on a A) Salbutamol Sulphate substrate and B) Beclomethasone Dipropionate substrate	180

Figure 4.14	Box plots of the force of adhesion measurements of Beclomethasone Dipropionate tips on a A) Beclomethasone Dipropionate substrate and B) Salbutamol Sulphate substrate	181
Figure 4.15	SEM images of Salmeterol Xinafoate (SX) and Fluticasone Propionate (FP) micronized powders before compression at A) 500x magnification and B) 3,500x magnification	182
Figure 4.16	SEM images of Salmeterol Xinafoate (SX) and Fluticasone Propionate (FP) micronized powders after compression at A) 500x magnification and B) 4000-5000x magnification	183
Figure 4.17	Representative tapping mode AFM images of Salmeterol Xinafoate (SX) and Fluticasone Propionate (FP) after compression at 5μm x 5μm 8(A) and 10μm x 10μm (B) scan sizes	185
Figure 4.18	Average Root Mean Square Roughness Analysis of Fluticasone Propionate and Salmeterol Xinafoate Powder Compacts at 5μm x 5μm and 10μm x 10μm scan sizes.	186
Figure 4.19	Example SEM images of functionalised AFM tips with Salmeterol Xinafoate (SX A B), and Fluticasone Propionate (FP A B) particulates at various magnifications	187

Figure 4.20	Example A) cohesive and B) adhesive force curves using the same Fluticasone Propionate (FP) and Salmeterol Xinafoate (SX) functionalized tips respectively	189
Figure 4.21	CAB plot for Fluticasone Propionate (FP) tips with Salmeterol Xinafoate (SX)	190
Figure 4.22	CAB plot for Salmeterol Xinafoate (SX) tips with Fluticasone Propionate (FP)	190
Figure 4.23	Box plots of the force of adhesion measurements of Salmeterol Xinafoate tips on a A) Salmeterol Xinafoate substrate and B) Fluticasone Propionate substrate	191
Figure 4.24	Box plots of the force of adhesion measurements of Fluticasone Propionate tips on a A) Fluticasone Propionate substrate and B) Salmeterol Xinafoate substrate	192
 Chapter 5		
Figure 5.1	Schematic of an Andersen Cascade Impactor and associated particle size separation	215
Figure 5.1A	Example chromatogram of salmeterol xinafoate and fluticasone propionate sample solution (3M Healthcare Ltd)	221

Figure 5.2	Percentage deposition profile across an Andersen Cascade Impactor of total collected dose of salbutamol sulphate from a Ventolin® pMDI formulation	225
Figure 5.3	Percentage deposition profile across an Andersen Cascade Impactor of total collected dose of salbutamol sulphate from a salbutamol sulphate 100µg / actuation pMDI formulation	225
Figure 5.4	Percentage deposition profile from an Andersen Cascade Impactor of total collected salbutamol sulphate from a salbutamol sulphate and beclomethasone dipropionate 50µg / actuation pMDI formulation	226
Figure 5.5	Percentage ACI deposition profile of total collected salbutamol sulphate from a salbutamol sulphate and beclomethasone dipropionate 100µg / actuation pMDI formulation	226
Figure 5.6	Percentage ACI deposition profiles of total collected dose of salbutamol sulphate from all formulations	227
Figure 5.7	Percentage ACI deposition profile of total collected beclomethasone dipropionate from a beclomethasone 100µg / actuation pMDI formulation	230

Figure 5.8	Percentage ACI deposition profile of total collected beclomethasone dipropionate from a salbutamol sulphate and beclomethasone 50µg / actuation pMDI formulation	230
Figure 5.9	Percentage ACI deposition profile of total collected beclomethasone dipropionate from a salbutamol sulphate and beclomethasone 100µg / actuation pMDI formulation.	231
Figure 5.10	Percentage ACI deposition profiles of total collected dose of beclomethasone dipropionate from all formulations	231
Figure 5.11	Percentage deposition profile across an Andersen Cascade Impactor of total collected salmeterol xinafoate from a salmeterol 100µg / actuation pMDI formulation	236
Figure 5.12	Percentage deposition profile across an Andersen Cascade Impactor of total collected salmeterol xinafoate from a salmeterol and fluticasone propionate 50µg / actuation pMDI formulation	236
Figure 5.13	Percentage deposition profile across an Andersen Cascade Impactor of total collected salmeterol xinafoate from a salmeterol and fluticasone propionate 100µg / actuation pMDI formulation	237
Figure 5.14	Percentage deposition profile across an Andersen Cascade Impactor of total collected salmeterol xinafoate from all pMDI formulations	237

Figure 5.15	Percentage deposition profile across an Andersen Cascade Impactor of total collected fluticasone propionate from a fluticasone 100µg / actuation pMDI formulation	240
Figure 5.16	Percentage deposition profile across an Andersen Cascade Impactor of total collected fluticasone propionate from a fluticasone and salmeterol xinafoate 50µg / actuation pMDI formulation	240
Figure 5.17	Percentage deposition profile across an Andersen Cascade Impactor of total collected fluticasone propionate from a fluticasone and salmeterol xinafoate 100µg / actuation pMDI formulation	241
Figure 5.18	Percentage deposition profile across an Andersen Cascade Impactor of total collected fluticasone propionate from all pMDI formulations	241

Chapter 6

Figure 6.1	1cm x 1cm DESI chemical maps of deposited beclomethasone dipropionate (543 m/z) and salbutamol sulphate (240 m/z) from an SS BDP 100 HFA134a pMDI formulation on plates 4, 5 and 6 of Andersen Cascade Impactor	259
Figure 6.2	Representative DESI spectra of the parent BDP (543 m/z) and SS (240 m/z) molecular ions from within a single drug spot from a SS BDP 100 formulation on plate 4 of an Andersen Cascade Impactor	259

Figure 6.3	Reference Raman Spectra of BDP and SS at 532nm (Green Laser)	261
Figure 6.4	Raman Spectroscopy derived scores map of a 250µm diameter circular area of plate 3 and plate 4 deposition of SS and BDP from a SS BDP 100 formulation	261
Figure 6.5	Representative differential scanning calorimetry thermograms of anhydrous BDP (green) and the BDP extracted from the BDP 100 formulation (red) after propellant evaporation	263
Figure 6.6	SEM images of an API deposit from a SS FP 100 formulation in an Andersen Cascade Impactor. A) x100 image of entire deposit and surrounding scatter, B) x500 image of deposit periphery, C) x750 image of deposit centre and D) x500 image with 45° sample tilt of entire API deposit	264
Figure 6.7	1cm x 1cm DESI chemical maps of deposited salmeterol xinafoate (417 m/z) from an SX FP 100 HFA134a pMDI formulation on plates 1-7 of an Anderson Cascade Impactor	267
Figure 6.8	1cm x 1cm DESI chemical maps of deposited fluticasone propionate (523 m/z) from an SX FP 100 HFA134a pMDI formulation on plates 1-7 of an Anderson Cascade Impactor	267
Figure 6.9	Reference NIR Raman spectra (785nm) of salmeterol xinafoate, fluticasone propionate and the stainless steel ACI plate	269

List of Figures and Tables

Figure 6.10	100μm x 100μm hyperspectral Raman spectroscopy derived scores Modeled overlay to salmeterol xinafoate deposition from a SS 100 formulation on plate 4 of an Andersen Cascade Impactor	270
Figure 6.11	100μm x 100μm hyperspectral Raman spectroscopy derived scores modelled overlay to fluticasone propionate deposition from a FP 100 formulation on plate 4 of an Andersen Cascade Impactor	272
Figure 6.12	100μm x 100μm hyperspectral Raman spectroscopy derived scores model of salmeterol xinafoate and fluticasone propionate deposition from a SS 100 formulation on plate 4 of an Andersen Cascade Impactor In two separate deposits A and B	272
Figure 6.13	120μm x 200μm Raman spectroscopy derived scores model of salmeterol xinafoate and fluticasone propionate deposition from a SS 50 formulation on plate 4 of an Andersen Cascade Impactor and associated point spectra of A) SX B) FP C) transparent anomaly and D) yellow anomaly	273
Figure 6.14	600μm x 800μm optical microscope image of a deposited API spot from a SS FP 50 HFA134a formulation on plate 4 of an Anderson Cascade Impactor	275
Figure 6.15	600μm x 800μm Raman spectroscopy derived scores model of salmeterol xinafoate and fluticasone propionate deposition from a SS 50 formulation on plate 4 of an Andersen Cascade Impactor	275

Figure 6.16	600μm x 800μm optical microscope image of a deposited API spot from a SS FP 100 HFA134a formulation on plate 4 of an Anderson Cascade Impactor	276
Figure 6.17	600μm x 800μm Raman spectroscopy derived scores model of salmeterol Xinafoate and fluticasone propionate deposition from a SS 100 formulation on plate 4 of an Andersen Cascade Impactor	276
Figure 6.18	Positive Spectrum Eigenvalue plot and PCA score images on principal components 1 – 12 from a 500μm x 500μm area around a single API spot from a SX FP 100 formulation on plate 4 of an Andersen Cascade Impactor	279
Figure 6.19	Negative Spectrum Eigenvalue plot and PCA score images on principal components 1 – 12 from a 500μm x 500μm area around a single API spot from a SX FP 100 formulation on plate 5 of an Andersen Cascade Impactor	280
Figure 6.20	Positive Spectrum Eigenvalue plot and PCA score Images on principal components 1 – 12 from a 500μm x 500μm area around a single API spot from a SX FP 100 formulation on plate 6 of an Andersen Cascade Impactor	281

Figure 6.21	Negative Spectrum Eigenvalue plot and PCA score images on principal components 1 – 12 from a 500µm x 500µm area around a single API spot from a SX FP 100 formulation on plate 7 of an Andersen Cascade Impactor	282
Figure 6.22	500µm x 500µm images of the positive spectrum MCR scores on four components for plates 0 – 7 of a SX FP 100 pMDI deposit	285
Figure 6.23	500µm x 500µm images of the negative spectrum MCR scores on four components for plates 0 – 7 of a SX FP 100 pMDI deposit	286
Figure 6.24	Positive Spectrum loadings and ion mass assignments on MCR component 1 of plate 5 of a SX FP 100 formulation deposit	287
Figure 6.25	Positive Spectrum loadings and ion mass assignments on MCR component 2 of plate 5 of a SX FP 100 formulation deposit	287
Figure 6.26	Positive Spectrum loadings and ion mass assignments on MCR component 3 of plate 5 of a SX FP 100 formulation deposit	288
Figure 6.27	Positive Spectrum loadings and ion mass assignments on MCR component 4 of plate 5 of a SX FP 100 formulation deposit	288
Figure 6.28	Negative Spectrum loadings and ion mass assignments on MCR component 1 of plate 5 of a SX FP 100 formulation deposit	289

Figure 6.29	Negative Spectrum loadings and ion mass assignments on MCR component 2 of plate 5 of a SX FP 100 formulation deposit	289
Figure 6.30	Negative Spectrum loadings and ion mass assignments on MCR component 3 of plate 5 of a SX FP 100 formulation deposit	290
Figure 6.31	Negative Spectrum loadings and ion mass assignments on MCR component 4 of plate 5 of a SX FP 100 formulation deposit	290
Figure 6.32	Positive Spectrum loadings and ion mass assignments on MCR components showing halo effect	293
Figure 6.33	Negative Spectrum loadings and ion mass assignments on MCR components showing halo effect	294
Figure 6.34	Negative spectrum single ion images of an Andersen Cascade Impactor plate 7 SS FX 100 deposit with the relative intensities of each ion found in the sample references	295

List of Tables

Chapter 2

Table 2.1	Standardized ACI stage definitions	88
-----------	------------------------------------	----

Chapter 3

Table 3.1	Arithmetic mean roughness and root mean square roughness values for Anhydrous BDP, BDP CFC-11 Clathrates and BDP IPA Clathrates over a $5\mu\text{m} \times 5\mu\text{m}$ area	119
-----------	--	-----

Table 3.2	Average mean roughness (R_a) and root mean square roughness (R_q) values for pMDI components over a $5\mu\text{m}^2$ area	122
-----------	---	-----

Chapter 4

Table 4.1	The force of adhesion, work of adhesion and surface energy of Inhalation APIs as determined by AFM	162
-----------	--	-----

Table 4.2	$5\mu\text{m} \times 5\mu\text{m}$ tapping mode image R_q , R_a and R_{max} Roughness analysis of Beclomethasone Dipropionate (BDP) and Salbutamol Sulphate (SS) powders before and after compression	172
-----------	--	-----

Table 4.3	$10\mu\text{m} \times 10\mu\text{m}$ tapping mode Image R_q , R_a and R_{max} roughness analysis of Beclomethasone Dipropionate (BDP) and Salbutamol Sulphate (SS) powders before and after compression	173
-----------	--	-----

Chapter 5

Table 5.1	Salbutamol sulphate ACI stage diluent rinse volumes	218
Table 5.2	Salmeterol xinafoate and fluticasone propionate ACI stage diluent rinse volumes	221
Table 5.3	Salbutamol sulphate recovery breakdown from ACI / HPLC data across all formulations	227
Table 5.4	Beclomethasone dipropionate deposition indicators from ACI / HPLC data across all formulations	232
Table 5.5	Salmeterol xinafoate deposition indicators from ACI / HPLC data across all formulations	238
Table 5.6	Salmeterol xinafoate deposition indicators from ACI / HPLC data across all formulations	242

Thesis Aims and Objectives

The aim of this thesis was to investigate the application of the atomic force microscopy derived cohesive adhesive balance approach to inhalation based (pMDI) API particles with 'non-ideal' surfaces (i.e. those with real particle character). In so doing it was hoped that the tolerance for substrate roughness of the model could be described, and that broad force balances could be achieved between combinations of APIs and pMDI device components more representative of '*in-situ*' states. If these force balances could then be linked to '*in-vitro*' measures of formulation performance, such as aerodynamic particle size profiling, it would open up the potential for predicting deposition performance success or failure from simple AFM based methodologies. It was further expected that a range of complementary surface specific analytical techniques could be employed in conjunction; so as to better understand API particle characterisation and the link between a force balance and aerosol deposition mechanics.

The primary objectives of this work were therefore as follows:

- **Investigate the use of a CAB approach to real particulate materials.**
- **Define the limits of the CAB approach with regards substrate roughness.**
- **Describe the force balance of a combination of APIs.**
- **Describe the force balance of APIs with pMDI device components.**
- **Link the force balances measured to changes in '*in-vitro*' deposition performance.**
- **Use multiple surface specific techniques to analyse the deposition character of API combinations and link this with the force balances achieved.**

1.0 Introduction

1.1 Drug Delivery via Inhalation

The delivery of therapeutic agents via inhalation to treat respiratory disorders can be traced back over 4000 years (Grossman et al, 1994). Early documented examples included the use of volatile aromatics such as menthol, thymol and eucalyptus to aid breathing, or the fumes from burning leaves such as *Atropa belladonna* and *Datura stramonium* as hallucinogens (Zeng et al, 2001). The invention of the glass bulb nebuliser during the industrial revolution of the nineteenth century heralded a significant proliferation in physiological, formulation and device understanding in relation to what we now consider modern inhalation therapy (Grossman et al, 1994). Indeed, such has the field developed that prevalent respiratory disorders such as asthma and chronic obstructive pulmonary disorder (COPD) have become synonymous with the use of sophisticated inhaler devices and a range of associated respirable active pharmaceutical agents (APIs).

The attraction of treating such conditions via this particular route is in essence linked to the simple facility of being able to target the site of disease directly. The predominant sites of disease in the above conditions are within the tracheobronchial tree and the lungs themselves. Therefore with the use of inhalation therapy it is possible to deliver APIs directly to these sites, allowing for a rapid and predictable onset of pharmacodynamic action with negation of the adverse pharmacokinetic issues of systemic treatments (Virchow et al, 2008). These principally include degradation within the digestive tract, system wide biodistribution and first pass metabolism (Timsina et al, 1994). As a consequence smaller doses than would otherwise have to be delivered can be used, and the rest of the body is much less likely to see any of the API by distribution, thereby significantly decreasing the likelihood of adverse side effects. In addition inhalation therapy is generally considered patient friendly, being a non invasive route of delivery, and with the high solute permeability of the airways, large surface area (70 – 140 m² (Groneberg et al, 2003)) and limited proteolytic activity (Sung et al, 2007) it can be considered an attractive target for a broad range of APIs in local disease treatment. Furthermore because the lungs possess a very large vascular supply for gaseous exchange, separated from the air space by only a thin layer of epithelial cells, there has been significant interest in using inhalation therapy as a means to deliver agents for systemic treatments (Zeng et al, 2001). Of

particular interest is the inhalation of biopharmaceutics (DNA, RNA, genes, polypeptides etc). Such materials have little or no oral bioavailability and attempts to deliver APIs such as insulin to treat conditions like diabetes would avoid invasive administration (subcutaneous injections) and potentially offer better bioavailability and pharmacodynamics. However this area of research is still in its infancy in comparison to the established delivery of topical agents.

1.2 The Human Respiratory Tract

1.2.1 Physiology of the Respiratory Tract

The respiratory system is a complex region of the human body responsible for the gaseous exchange between the atmosphere and the systemic circulation of oxygen and carbon dioxide necessary for cellular respiration. By association it is also critical in the blood pH homeostasis mechanism and the provision of vocal expression (Zeng et al, 2001).

The respiratory tract can be divided into three main regions (Finlay, 2001):

- **The Extrathoracic Region** – The upper airways proximal to the trachea consisting of the nose, mouth and throat (nasopharynx and oropharynx) and the larynx.
- **The Tracheo-Bronchial Region** - The branching conducting airways that include the trachea, bronchi and bronchioles.
- **The Alveolar Region** – All parts of the lung containing alveoli starting at the respiratory bronchioles and progressing to the alveolar ducts, and alveolar sacs.

Each of these regions has particular roles within the system as a whole. The upper extrathoracic airway is responsible primarily for inspiratory air intake, conditioning and filtration, as well as playing a role in olfactory sensation and vocal expression. The tracheo-bronchial region serves to conduct air from the larynx to the alveolar region where gas exchange takes place. Taken together the extrathoracic and tracheo-bronchial airways can be termed the conducting airways, in respect to the above functions. However they also provide structural support and are

responsible for the removal of particulate matter that has passed the extrathoracic region by constant epithelial mucociliary clearance.

The alveolar region is directly responsible for the gaseous exchange essential for blood oxygenation. The anatomical arrangement of these regions often gives rise to the term of the 'pulmonary tree'. This is because the system may be viewed as a series of irregularly dichotomous branching passageways, from below the trachea down to the alveoli (figure 1.1). These branches are dichotomous because each 'mother' passage leads to two 'daughter' passages, but irregular because the 'daughter' branches are not necessarily of the same size. (Davies et al, 2003). There are approximately 23 generations before the respiratory bronchioles give way to the alveoli where gaseous exchange ultimately takes place (Hindle, 2010).

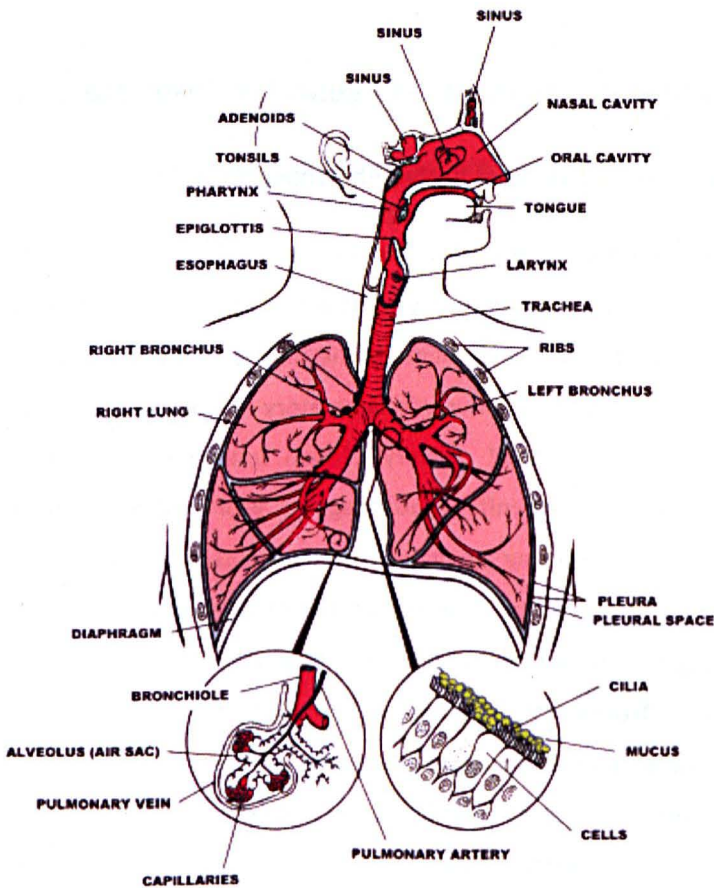


Figure 1.1 Diagram of the respiratory system. Adapted from lung.ca Accessed on the 1/11/11

As the respiratory system moves down from the mouth, through the trachea to the alveolar sac, there develops a significant airflow dynamic due to this dichotomous branching. Whilst the conducting airways decrease in diameter with each branching generation, there is a massive increase in cross sectional area, (particularly between the terminal bronchiole and alveolar sac) as a consequence of the propagation of new branches. The velocity of air as it progresses through the tract is therefore rapidly reduced and within the alveolar region, flow velocity falls below that of diffusing oxygen molecules, allowing the maximum diffusive capability to be established (Hickey, Thompson, 1992). This sequential decreasing airways calibre is also essential in developing a controlled penetration of air to the deep lung on tidal breathing that allows lung (and therefore chest) expansion (Hickey, Thompson, 1992). There is also established a maximum alveolar surface area in conjunction with the minimum volume possible (Davies et al, 2003).

1.3 Active Pharmaceutical Agents for Respiratory Diseases

1.3.1 Common Classes of Active Pharmaceutical Agent

The most prominent respiratory conditions experienced are asthma and COPD. It is therefore the case that the most commonly used active pharmaceutical agents, are those designed to treat these conditions. Fundamentally the hallmark of both conditions is a reduction in local airway calibre and marked airway inflammatory responses. Consequently the crux of treatment is based around the local delivery of two fundamental categories of therapeutic agent; bronchodilators and anti-inflammatory agents. Bronchodilators are responsible for maintaining airway calibre or reversing airway constriction. Anti-inflammatory agents are used to inhibit or prevent the inflammatory response of the local airway environment that may compromise airway calibre. In broad terms both agent types are often used in combination to bring patients long term control over their condition. Bronchodilators predominantly include β_2 adrenoceptor agonists and muscarinic-receptor antagonists, while anti-inflammatory agents are confined to a group of glucocorticoids. Further bronchodilatory (such as the xanthine theophylline), and anti-inflammatory agents (such as the leukotriene receptor antagonists, montelukast and zafirlukast) are used at more advanced stages of disease, but are administered systemically via the oral route and much less prominent.

1.3.2 Beta₂-Adrenoceptor Agonists

The primary responsibility of the β_2 -agonists is to illicit direct action of the β_2 -adrenoceptors on the smooth muscle in the bronchi. The β_2 -adrenoceptors are physiological antagonists, responsible for smooth muscle relaxation that is initiated via a G-protein coupled response and an adenylate cyclase based secondary messenger system. Their effect occurs even in the presence of spasmogens. They also have a secondary effect in working to inhibit inflammatory mediator release from mast cells (such as histamine) and monocytes (such as TNF α). It is also believed they may directly increase mucus clearance by effects on the cilia (Rang et al, 2003). There are two distinct categories of β_2 -agonist; short acting and long acting (LABAs). This distinction is straightforwardly based upon the time taken to reach maximal effect. Short acting β_2 -agonists include salbutamol sulphate and terbutaline sulphate, and these reach maximum effect within 30 minutes of administration, with a duration of action of 4-6 hours. LABAs include salmeterol xinafoate and formoterol fumerate, and have an extended duration of effect of around 12 hours (Rang et al, 2003). Consequentially, short acting β_2 -agonists are used as rescue, or 'as required' reliever therapy for episodes of breathlessness while LABAs are used in regular dosing regimes as a 'preventer' to maintain airway calibre over longer periods of time. Two of the most common β_2 -agonists that were used in this body of work are discussed in more detail below:

1.3.2.1 Salbutamol Sulphate

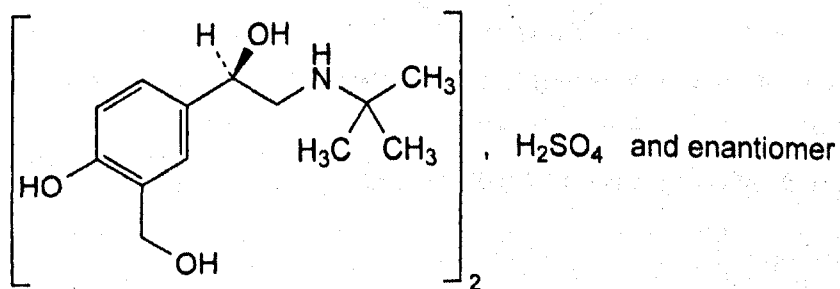


Figure 1.2: Salbutamol Sulphate Monograph (British Pharmacopoeia, 2012)

Salbutamol sulphate (figure 1.2) is a short acting β_2 -agonist which is typically delivered via the inhalation route for local and immediate bronchial smooth muscle relaxation. Chemically the *meta* phenol group of the catecholamine skeleton is substituted with a hydroxymethylene group that hides the molecule from rapid metabolism by the enzyme catechol-o-methyl-transferase (Patrick, 2005). It is typically dosed at 200-400 μ g as required for asthma sufferers but may be used regularly in COPD patients, or increased in dose and frequency in severe episodes of airways challenge (BNF, 2012). It is available as a solution for nebulisation, dry powder inhalation (DPI) and pressurised metered dose inhalation (pMDI). It can be delivered systemically, via either the oral or parenteral routes, but these modes of administration are reserved for refractory airways disease, emergency management in critical care or uterine smooth muscle relaxation to delay pregnancy. Typically it may induce side effects such as a fine tremor, nervous tension, headaches, tachycardia or palpitations due to some residual β_1 -adrenoceptor agonism (BNF, 2012). It is metabolised hepatically and renally excreted, with a half-life of 1.6 hours (European Pharmacopoeia, 2012).

1.3.2.2 Salmeterol Xinafoate

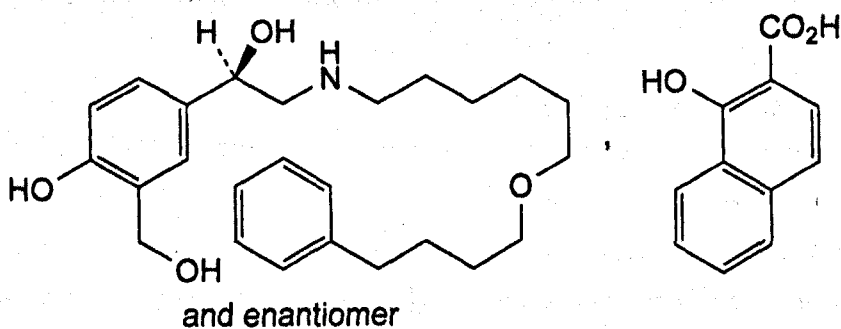


Figure 1.3 Salmeterol Xinafoate Monograph (British Pharmacopoeia, 2012).

Salmeterol xinafoate (figure 1.3) is a LABA, delivered exclusively by inhalation for prolonged airways smooth muscle relaxation. It is added to asthma therapy when short acting β_2 -agonists alone and in combination with low dose glucocorticoids have been insufficient to control

symptoms (BTS, SIGN, 2011). As such, it is most commonly prescribed as a combination formulation with a concurrent glucocorticoid (e.g. with fluticasone propionate in Seretide®) and is available as both pMDI and DPI formulations. It's additional lipophilicity, by virtue of a lengthened N-substituent with a further hydrocarbon chain and aromatic ring, allows stronger binding to the tissues surrounding the β_2 -adrenoceptors. This results in double the potency of salmeterol as compared to salbutamol and an extended duration of action of 12 hours (Patrick, 2005). Hence, given its long time of action it is unsuitable for 'as required' relief, and therefore commonly used at doses of 50-100 μ g twice a day as a regular prophylactic. It can induce side effects in the same fashion as salbutamol, and is metabolized and excreted in the same manner with a half-life of 5.5 hours (European Pharmacopeia, 2012).

1.3.3 Glucocorticoids

These agents are not used in the immediate phase of an asthma attack, but are employed to suppress the immune response capability of the bronchial region. This has a twofold impact, preventing attacks occurring in the first instance and also suppressing the inflammatory 'late' phase reaction of an asthma attack. Their mode of action is based in glucocorticoid receptor mediated alterations to genetic transcription that result in a cascade response with a reduction in a vast array of inflammatory cytokines. In particular, with respect to asthma and COPD this includes the Th₂ cytokines responsible for eosinophil recruitment and activation, IgE production and IgE receptor expression. The inhibition of the arachidonic acid pathway enzyme cyclooxygenase-2 also results in reduced production of the vasodilating prostaglandins PGE₂ and PGI₂. And by the induction of lipocortin there is a reduction in the production of the spasmogens LTC₄ and LTD₄ as well as the leukocyte chemotaxins LTB₄ and platelet activating factor. Glucocorticoids will also upregulate the expression of the β_2 -adrenoceptors, increasing the facility for smooth muscle relaxation, as well as decreasing microvascular permeability and reducing eosinophil mediator release (Rang et al, 2003). Because these effects are related to genetic repression or induction, the effects take several days to take effect, therefore further establishing these APIs as regular dosed prophylactics. The commonly employed inhaled glucocorticoids include beclomethasone dipropionate, budesonide and fluticasone propionate. All three of these corticosteroids were used in this thesis, and are discussed briefly below.

1.3.3.1 Beclomethasone Dipropionate

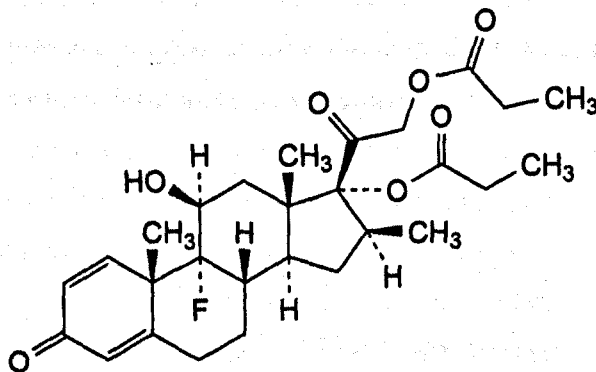


Figure 1.4 Beclomethasone Dipropionate Monograph (British Pharmacopoeia 2012)

Beclomethasone dipropionate (figure 1.4) is a potent glucocorticoid that is utilised for the regular symptom maintenance of asthmatics (or some COPD sufferers). It is considered the reference standard for corticosteroid dosing in airways disease and is prescribed when short acting β_2 -agonists alone are not enough to control a patients symptoms (BTS SIGN, 2011). It is commonly dosed at between 200-800 μ g daily, usually split into a twice daily regimen. More refractory disease can see doses of up to 2000 μ g a day. It is available currently as both pMDI (Clenil Modulite[®], Qvar[®]) and DPI formulations (Asmabec[®], Becodisk[®]). It can also be formulated in combination with LABAs (with formoterol fumerate in Fostair[®]) to increase compliance where appropriate. It has uses topically for the treatment of inflammatory skin disorders, or as a nasal formulation for allergic and vasomotor rhinitis (BNF, 2012). Side effects of beclomethasone are typical of all corticosteroids. Large doses can be associated with systemic effects such as adrenal suppression, bone mineral density depression or glaucoma. More commonly, due to significant local impaction from inhaled formulations, oropharyngeal candidiasis may occur (BNF, 2012). It is metabolised hepatically and has a half-life of 2.8 hours. It's mode of excretion is not yet fully characterised (European Pharmacopeia, 2012).

1.3.3.2 Budesonide

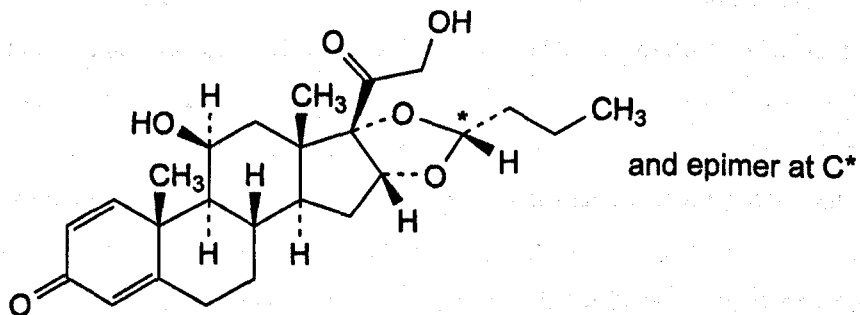


Figure 1.5 Budesonide Monograph (British Pharmacopoeia, 2012).

Budesonide (figure 1.5) is a glucocorticoid used for the regular management of inflammatory airways disease. It is only available in DPI formulations in the UK (Pulmicort[®]) and is usually dosed at 100-800 μ g twice a day. Given enterally it treats inflammatory bowel disorders such as Crohn's disease and ulcerative colitis or as a nasal treatment for rhinitis or nasal polyps (BNF, 2012). It is more often co-formulated with the LABA formoterol fumerate (Symbicort[®]), which due to formoterol's abridged character between a short acting β_2 -agonist and LABA may be used both as a regular prophylactic and as a when required reliever. It is metabolised hepatically, excreted renally and has a half-life of 2-3.6 hours (European Pharmacopoeia, 2012).

1.3.3.3 Fluticasone Propionate

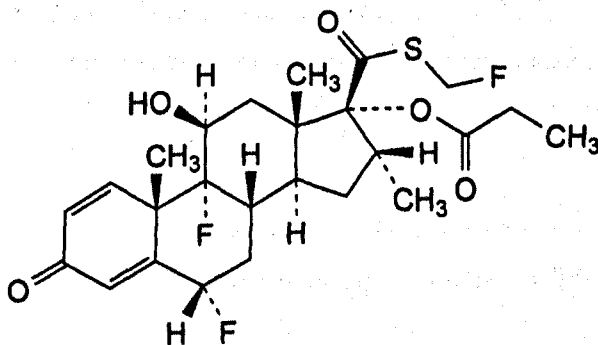


Figure 1.6 Fluticasone Propionate Monograph (British Pharmacopoeia, 2012).

Fluticasone propionate (figure 1.6) is another glucocorticoid used via inhalation for the management of inflammatory airways disease. It is available as a nebulised solution, pMDI and DPI formulation on its own (Flixotide®). It is also widely prescribed in combination with the LABA salmeterol xinafoate (Seretide®) as both a pMDI and DPI formulation for regular prophylaxis only. It is twice as potent as beclomethasone and budesonide and is therefore commonly dosed at 100-500µg twice a day. It is absorbed to a very small extent from the digestive tract and undergoes almost complete first-pass metabolism, therefore being less associated with systemic side effects (Rang et al, 2003). Fluticasone can also be used as a nasal treatment for rhinitis or polyps, and is occasionally used as a potent treatment for refractory inflammatory skin conditions such as eczema or dermatitis. It has the longest half-life of the inhaled corticosteroids at 7.8 hours, but remains hepatically metabolised and renally excreted.

1.4 Delivering Active Pharmaceutical Agents to the Respiratory System

The APIs described above can only elicit the desired physiological effect if delivered successfully to the tracheo-bronchial region of the respiratory tract where the problem occurs. One of the principal difficulties in doing this is how to break up the bulk amounts of compound in the formulation into micron sized particles suitably sized to reach this region of the respiratory tract. To do so requires energy to overcome the attractive forces between the molecules (as discussed below). The number of bonds broken is proportional to the amount of a new surface being created. Therefore the amount of energy required to break up a bulk compound into respirable droplets or particles is proportional to the increase in surface area (Finlay, 2001). Currently there are three methods utilised to achieve aerosolization. These are via nebulisation, dry powder inhalation or pressurized metered dose inhalation. These delivery systems are discussed briefly below:

1.4.1 Nebulisers

Nebulisers are one of the oldest and simplest means to aerosolize an API. If an API can be suspended or dissolved into a liquid media such as water, then by blowing air at high speed over the surface of the suspension or solution, sufficient energy to break up the bulk liquid into

droplets will be provided (Finlay, 2001). Devices working on such a principle are termed jet nebulisers, and there are several different models. In basic terms, each utilises a pressurized air supply with subsequent baffle induced particle size reduction to obtain a suitable respirable particle stream that a user inhales with normal tidal breathing for a given period of time. These devices are large and bulky by nature and therefore not easily transported. They are also functionally noisy in operation, and require several minutes operation for a given dose to be taken. For this reason they are often the choice for patients with end stage, or advanced disease states that are hospitalised or house bound. Their principal benefit is that by the use of a facemask delivery system, they are a passive means of delivering the API, that requires little patient co-ordination or inspiratory effort.

While jet nebulisers are the most predominant nebuliser in use, there is also a subsequent nebuliser technique. Ultrasonic nebulisers use piezoelectric crystals vibrating at a high frequency (1-3 MHz) to provide the energy to aerosolize droplets. This mechanism is based on a fixed crystal causing sufficiently strong vibrations through the media to illicit a fountain of liquid at the surface from which droplets will escape as a respirable 'mist' (Hindle, 2010). These devices will then either use a fan based system, or simply the inspiratory flow from the user to draw these droplets out of the device for inhalation. While these devices are much quieter than jet nebulisers, they often suffer from large dose wastage as much of the droplet cloud will coalesce and return to the reservoir. Even when the device is run to 'dry', much of the particulate dose can be left behind in the nebuliser. Most recently a type of ultrasonic nebuliser called a 'vibrating mesh nebuliser' has adapted this technique to use an ultrasonic horn to force the reservoir suspension through a simultaneously vibrating mesh with a controlled pore size. This has resulted in improved particle sizing and subsequently better dosing efficiencies.

1.4.2 Dry Powder Inhalers

Dry powder inhalers are unique among respiratory API delivery systems, as they do not use a dissolved or suspended API reservoir. Rather they depend on the direct formulation of blended API and excipient powders into capsules or blisters that are pierced by the device immediately prior to inhalation. A patient's inspiratory flow is used to aerosolize the powder bed. Because of the intrinsic adhesive character of micronized particles, using the API powder alone results in

excessive agglomeration, poor flowability and aerodynamic particle sizing. This problem is usually addressed by using a large coarse carrier molecule of an inert excipient such as α -lactose monohydrate ($>60\mu\text{m}$) (Hooton et al, 2006). In this scenario the carrier and drug are blended with the intention that the API particles adhere to the surface of the larger carrier rather than themselves. The lack of small particle cohesion results in a marked improvement in powder flow and homogeneity, enabling successful manufacture, dosing and fluidization of the API (Jones et al, 2008a). Upon fluidization the two particulate species disassociate in the air stream and while the API ideally reaches its respiratory target, the larger carrier harmlessly impacts on the throat and is swallowed. However the application of a carrier molecule will only be useful in terms of powder behavior if the forces of adhesion between the carrier and API are greater than the forces of cohesion between the API molecules (i.e. adhesion $>$ autoadhesion) (Podczec et al, 1994). As a clinical device DPIs require less co-ordination than other types of inhalation device. However they also require greater levels of cleaning, and a large inspiratory effort to aerosolize the powder bed, which may not be possible for those who are infirm. Furthermore, some people can't tolerate the excessive impaction sensation in the oropharynx. Nether less DPI formulations often offer the most stable API combinations, where suspension or dissolution of an ingredient has proved challenging.

1.4.3 Pressurized Metered Dose Inhalers

Pressurized metered dose inhalers (pMDIs) are the most commonly used device for delivering APIs to the airways. The concept is based upon the API being dissolved or suspended within a volatile propellant (with other excipients for lubrication, stabilization etc) which is then metered and expelled from a canister upon actuation via a mouthpiece (actuator). The propellant which is liquefied under pressure in the canister vaporizes rapidly on a release and carries with it the suspended or solubilised pharmaceutical agent (figure 1.7). The first pMDI devices (3M Riker's Medihaler Epi®) were developed by Riker Laboratories and marketed in 1956 as a replacement for the inexact squeeze-bulb nebulizer (Newman, 2005). The device technology has now become the most commonly used for delivering APIs to the airways. A great proportion of their success has been founded in their cheap cost to manufacture and that the propellant driven system does not require as great an inspiratory effort for effective aerosolization as with DPIs. A pMDI

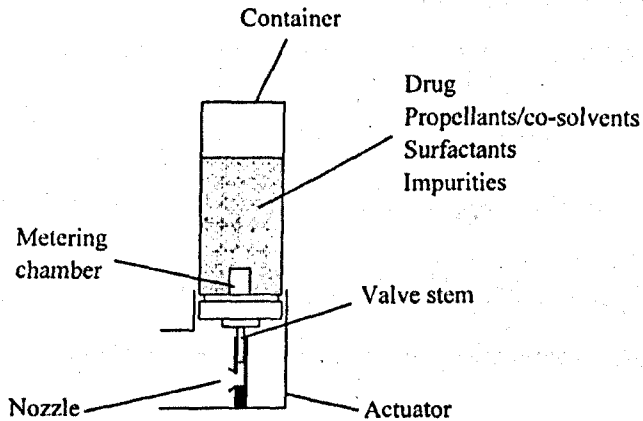


Figure 1.7: Schematic of a pMDI device (Vervaet, Byron, 1999)

device consists of a canister containing the API solution or suspension, the metering valve and the actuator. To overcome problems of API adhesive character (inappropriate flocculation behavior, sedimentation and irreversible caking (Vervaet, Byron, 1999)) as well as the interaction between the APIs and the physical inhaler components themselves (device entrainment, nucleation and crystallization) pMDI formulations are often stabilized by the use of surfactants and co-solvents. Surfactants use steric means to prevent interparticulate contact and agglomeration (Bower et al, 1996), while co-solvents ensure the API remains solvated within the propellant. Traditionally these were non-ionic surfactants such as oleic acid, lecithin, and sorbitan tri- or mono-oleate. However the recent re-formulation of suspension pMDIs to function without chlorine based propellants has demanded a rethink.

1.4.4 Hydrofluoroalkane (HFA) Propellants

1.4.4.1 CFC to HFA Transition

The original pMDI formulations were based on chlorofluorocarbon (CFC) propellants (figure 1.8). These were considered ideal due to their chemical inertness, non-toxicity, high vapour pressure (constant under storage), compatibility with common APIs, appropriate boiling points and

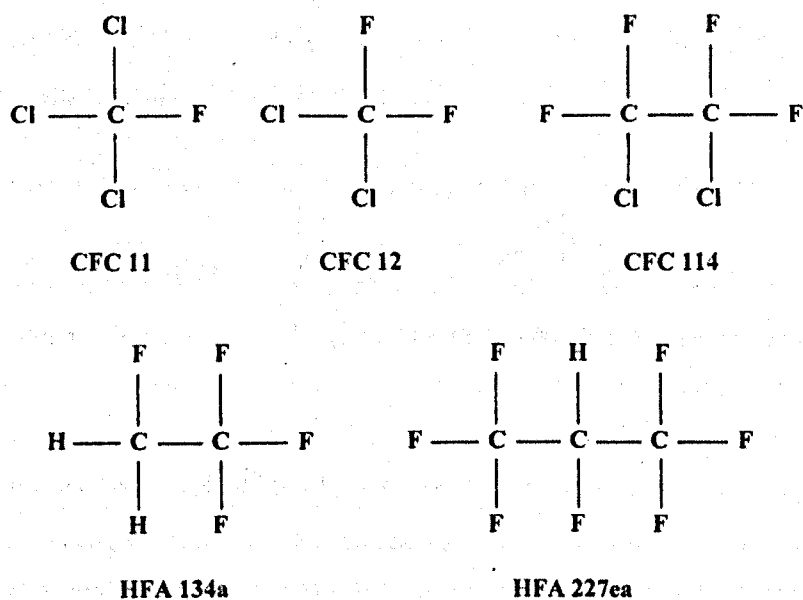


Figure 1.8: The chemical structures of CFC and HFA propellants (Veravet, Byron, 1999).

densities (Newman, 2005). Yet despite an excellent functional performance, it was subsequently proven that the release of chlorine in the degradation of the CFCs was contributing significantly to ozone depletion in the stratosphere (Molina, Rowland, 1974). As per the subsequent Montreal Protocol (1989) the use of CFCs was therefore phased out. pMDI inhalers were given a temporary exemption, to prevent the unavailability of essential medicines to patients, but it was still necessary for the manufacturers of CFC based pMDI devices to consider reformulation. Emphasis was put on either finding an alternative propellant or using alternative technologies (such as DPIs). Such an exemption for pMDI formulation CFC use has now passed, and it has been the emergence of Hydrofluoroalkanes (HFAs) as alternative propellants that has dominated the new pMDI markets. The HFAs (figure 1.8) contain hydrogen, fluorine and carbon but no chlorine. Hence they are readily metabolized by the environment and will not cause ozone depletion (Manzer, 1990). 1,1,1,2-tetrafluoroethane (HFA134a) and 1,1,1,2,3,3,3-heptafluoropropane (HFA227ea) have generally been accepted as the next generation CFC replacements. However as a consequence of not being fully halogenated and having one or two

hydrogen atoms in their structure, they confer a degree of polarity which has had consequences for the propellant interactions observed, namely an insolubility of non-polar surfactants (Veravet, Byron, 1999). A desire to formulate suspensions or solutions with acceptable stability coupled with the changes in physicochemical nature of the propellant (demanding the use of additional co-solvents or novel surfactants) places even more emphasis on an understanding of particle-particle adhesion. The use of a propellant means that the pMDI formulations exist as colloidal suspensions. As such pMDI formulations are subject to solvent based forces and these are highly important in determining physicochemical behavior and stability, as well as describing the contribution of the propellant itself, to a broader interparticulate force model.

1.4.4.2 Solvent Forces

Derjaguin, Landau, Verwey and Overbeek (DVLO) (Derjaguin, Landau, 1941) theory describes the stability of colloidal suspensions and dictates that such formulations will see particulate surfaces in a liquid medium (HFA) developing an interfacial relationship depending on the relative genesis of attractive and repulsive forces. The model describes the contributions from the attractive dispersive (London) van der Waals forces (discussed in more detail below) and the repulsive electrostatic interaction. (Traini et al, 2005). The essential difference to the adhesion forces between the constituent particles in air comes principally from the nature and extent of surface charging and the electrostatics involved at the solid-liquid interface. Charging can occur as a result of one of several processes. For example solvent ions can adsorb to a surface, or charged ions on the solid surface can dissociate into the medium (Florence, Attwood 2012). Resultant surface charges can cause an electric field, which in turn can lead to the attraction of counter ions from the medium, and in so doing develop an 'electrostatic double layer' (Butt, 2010). For example a particle surface that possesses or generates a negative charge will attract positive ions to the surface. This develops what is known as the 'Stern' layer (Florence, Attwood, 2012). Thermal motion within this layer leads to a perpetual movement of these counter ions away and back to the surface that in turn creates a 'diffuse' layer, extending further into the liquid media containing both positive and negative ions. It is the interaction of these double layers between particulates that can affect and govern adhesive character, with like surface charges leading to repulsion and opposite charges leading to attraction (Israelachvili, 1991). The modification of interparticulate forces between particles in liquids is therefore driven by the

chemical character of the solvent in relation to that of the solutes. Polar media have the capacity, through their potential for polarization to either facilitate or suppress the attraction between two surfaces (Stone, 2013).

HFAs are however low dielectric solvents, despite being significantly more polar than traditional CFCs (HFA 134a has a dielectric constant of 9.5, where CFC-11 is 2.3). The potential for significant double layer induced repulsion is therefore significantly lower than in aqueous media (Veravet, Byron, 1999). Assuming uncharged API particles (essential for respiratory delivery), low polar contributions and interparticle distances well in excess of electronic van der Waals radii, the dominant pre-disposition (assuming no moisture ingress) of a suspended API in a HFA will usually remain the attractive London van der Waals forces. This lends the suspended API towards agglomeration, flocculation or caking without the introduction of additional stabilizing excipients. Steric stabilization is therefore common place using a range of surfactants, which in turn, given the increased polarity of the HFAs, are often co-formulated with co-solvents. The resultant formulation is therefore a complex relationship between API surface chemistry, solvent chemistry, the steric repulsion of surfactants and the degree of solubility of all the solutes.

This thesis will move on to examine the fundamental force balance between the APIs in a binary HFA134a formulation. It is obvious that the adhesion forces at work between APIs in suspension will undoubtedly be influenced by the contribution of the HFA media and it's manipulation of surface forces. However this body of work was designed to try and quantify a basal dispersive interaction between co-formulated APIs and in turn see if this could be related this to '*in-vitro*' performance outcomes. As such the force balances carried out were done so outside of a model propellant to characterize dispersive forces, the impact of co-formulation upon them and any discernible relationship to deposition studies. The contribution of the HFA solvent should not be ignored however and further work beyond this thesis to accommodate the impact of the liquid and gaseous media upon a force balance will be of interest and essential to expand upon the relationships observed.

1.5 The Deposition of Drugs Delivered to the Respiratory Tract

The passage of aerosolized API from an inhalation device to the respiratory tract or lung is governed by a complicated relationship of factors. These can broadly be grouped into the physical factors that determine the deposition of the drug from the mouth and onto the surface of the airway lumen, and the pharmacokinetic factors that determine the amount of the deposited API that passes from the airway lumen into the smooth muscle cells (Hickey, 1992). The adsorption, distribution, metabolism and excretion (pharmacokinetics) of the APIs delivered for inhaled use are not in the scope of this thesis and will therefore not be considered here. However it is worth pointing out that the pharmacokinetics of APIs in the airways differ according to the site of deposition, and this places an emphasis on the correct physical characteristics of an aerosol in reaching the targeted location of deposition. Particles deposit on the airways by three main mechanisms. These are inertial impaction, gravitational sedimentation and diffusion (Hindle, 2010).

1.5.1 Inertial Impaction

Inertial impaction is the deposition of particles onto a surface as a consequence of their own inertia. As inspired air moves down the respiratory tract, it will change direction due to the physiological structure of the airways. Every time this occurs, particles or particle agglomerates will travel a given distance in the original direction of the airflow due their momentum. This is dependent upon the particle velocity and mass. If a particle has sufficient inertia, it may not be able to relax back into the air stream before travelling a distance that results in impaction on a structural surface in front of them (Gonda, 1990). If a particle with mass m is moving with an initial velocity v_0 through still air then it can be shown that as a result of frictional forces it will stop after travelling distance S :

$$S = B \times m \times V_0 \quad (1.1)$$

Where B is the mechanical mobility of the particle as velocity per unit force (Hickey, 1992). As such the greater the particle mobility, mass and initial velocity the further it will travel in its original trajectory. As such, aerosolized particles with an aerodynamic particle size in excess of $10\mu\text{m}$ will inertially impact at the oropharynx and be swallowed. Those with an aerodynamic particle size of less than this will generally be able to pass down towards the central airways. Further impaction occurs at the higher physiological structures, such as the branching of the trachea and left and right bronchus. This accounts for smaller and smaller particles.

1.5.2 Gravitational Sedimentation

As the airways progress, and airstream velocity decreases, inertial impaction becomes less important and it is gravitational sedimentation that becomes more critical for smaller particles of $2\text{-}5\mu\text{m}$. These will often deposit on the bronchioles or alveoli, where they can elicit the desired physiological effects for appropriate treatment of such ailments as asthma (Hindle, 2010). These smaller particulates will settle under gravity, after acceleration to a terminal velocity when the gravitational force is balanced by the resistance of the air through which it is travelling. A sphere of diameter D , and density d under the influence of gravitational force F_g will have a terminal settling velocity v_{ts} in the laminar region governed by Stokes law:

$$v_{ts} = (d \times D^2 \times g) / (18 \times \eta) = B \times F_g \quad (1.2)$$

Where g is the gravitational acceleration and η is the viscosity of air (Hickey, 1992). Therefore this process is shown to be more likely with increasing particle mobility. It is also time dependent and therefore aided by breath holding (Hindle, 2010).

1.5.3 Diffusion (Brownian Motion)

Particles with even smaller aerodynamic particle sizes ($< 0.5\mu\text{m}$) may be subject to diffusive processes. Here it is gas molecule bombardment that initiates random movements, which in turn leads to deposition. In contrast to impaction and sedimentation diffusional deposition is indirectly proportional to the particle diameter (Finlay, 2001). That is to say that with decreasing particle size we see increasing diffusional deposition.

1.5.4 Assessing Formulation Deposition '*in-vitro*'

Characterizing the particle size and distribution of discharged aerosols has become one of the key tests applied to inhaled products. This is because, as shown above, these variables are explicitly linked to the deposition efficiency and location within the respiratory tract of the formulation '*in-vivo*'. A variety of methods exist to do so. Such methods can be broadly split into two groups; inertial impaction and optical scattering. Optical methods such as particle time of flight (TOF), laser diffractometry (LD), and Phase-Doppler particle size analysis (PDA) provide a rapid collection of particle size distribution over a small number of actuations. However, they are unable to distinguish API particles from excipient, or indeed a combination API. Furthermore they determine volume-equivalent particle size, rather than the more important aerodynamic particle size. This is a significant drawback, as it means that particle sizing is non-specific and can generate a biased impression of the true particle size (Copley, 2008).

Inertial impactors are the most predominantly used means of characterizing aerosol particle sizes. They function on the basis of separating particles according to their inertia, which is in turn intrinsically linked to the particle mass (size) and velocity. Therefore in a controlled airflow, and with a given size exclusion mechanism it is possible to infer the particle size distribution of a formulation. Such devices allow the collection of entire actuations of API, and importantly give the operator the ability to independently assess the particle size distribution of several APIs from within the same formulation. The most commonly used inertial impactor is the Anderson cascade impactor (ACI), originally developed for the analysis of environmental pollutants (Munroe, 2007). The ACI consists of stack of sequential nozzle sets with precisely controlled reducing nozzle sizes, calibrated to define given aerodynamic particle sizes. These are fitted with

metal plates below each stage. Airflow is drawn through the stack, and a formulation is actuated into the stack via a throat piece. On entering the impactor, the aerosol is passed through successive nozzles and over impaction plates. Air velocity increases as the particles pass further down the stack due to a reduction in nozzle size and number. Eventually this generates sufficient particle inertia to prevent the aerosolized particle relaxing back into the airstream before travelling in its normal direction and impacting onto the relevant plate. Other impactor types such as the next generation impactor (NGI), or the multi stage liquid impinger (MSLI) do exist and offer specific stack attributes that compliment certain experimental designs. However in essence all the impaction techniques work by broadly the same mechanism, and both the ACI and NGI are included within the United States and European Pharmacopeia as standard tests for aerosol assessment.

1.6 Interparticulate Interactions within Inhalation Formulations

From the above it is explicitly evident that the predominant factors that determine API particle deposition location and efficiency will be the aerosol particle size and polydispersity. While there are other significant variables that come into play, such as patient manoeuvres and airway disease state etc., in terms of formulation design we are aware that only particles sized below 5µm will be able to reach the tracheobronchial region and initiate the requisite physiological effect. Therefore control over the aerodynamic particle size of an aerosol is critical and will determine to a significant degree the effectiveness of that formulation. Aerodynamic particle size is however not simply a reflection of the parent API particle size. Fundamentally, it is an interplay that represents the particle size and the interactivity of that particle with its surroundings. These may be other particles of API or excipient, the propellant, the device components or even contaminants. Indeed it is the size, scale and frequency of interparticulate interaction that ultimately dictates the final aerodynamic sizing and aerosol structure of an inhalation API.

1.6.1 Interparticulate Interaction

Understanding the nature and scale of interparticulate interaction within pharmaceutical compounds and formulations is a matter of huge importance for all current industrial practice. This has its genesis in the realization of the imperative contribution of particle-particle and particle-surface interactions to critical formulation downstream process specific behaviors. In real terms, such interactions are represented by the forces of adhesion (F_{adh}) between the micro-scale particulates (and associated surfaces) in pharmaceutical systems. Therefore characterizing the F_{adh} between formulation components is a potentially crucial tool in defining the character, extent and significance of fine particle-particle interaction and the impact these can have (Roberts, 2005). The scope of impact of particle F_{adh} is very broad ranging, and can be a means to exploit and refine a successful drug delivery system, or an unintentional driver for failure at multiple levels of production and utilization. For example the success of powder mixing and powder flow behavior in the production of dosage forms is highly dependent upon the strength of interaction (or lack thereof) between the material components involved (George, Goddard, 2006). Equally, further downstream, formulation stability and performance is inherently linked to particle F_{adh} .

API flocculation from suspensions or creaming and sedimentation from solutions, product-device retention, API release profiles etc. are just a small number of examples where behaviors can be linked to the management of intrinsic adhesive forces between the particulate components and their associated delivery devices (Hooton et al, 2004). Therefore it is obvious that managing F_{adh} is an essential consideration when approaching pharmaceutical system design, formulation and therapeutic efficacy. As a result there is increasing demand for characterization processes which accurately map the adhesive character of particle interactions. These can serve as a hugely significant research and pre-formulation indicator, with specific regard to potential new pharmaceutical systems (Roberts, 2005).

1.6.2 The Forces of Adhesion and Cohesion

Before considering further the implications of particle-particle interaction and associated adhesive forces it is important to exactly define the fundamental terms involved. Adhesion is well accepted to be the attractive interaction of two dissimilar molecules or particles. It should be differentiated from the concept of cohesion. The force of cohesion (F_{coh}) in its purest sense refers to the attractive interaction of two like-molecules within a single solid body (Zimon, 1982). However within recent research, particularly into interparticulate interaction of powders, the term has very often been used to describe the attractive interaction between two like-molecules or particles in two separate bodies i.e. between two particles of the same API. This is technically better described as a force of auto-adhesion (Podczeczek et al, 1994). Given the frequent use of 'cohesion' instead of 'auto-adhesion' within key literature and techniques associated with this thesis, the terms will be used interchangeably but fundamentally reflect the interactive force between two particles, or particle agglomerates of the same material.

The F_{adh} (or F_{coh}) between pharmaceutical particles is dependent on a hugely complex combination of physical and chemical forces. When two particles contact each other the F_{adh} that results between the bodies can be most basically be described as the result of the deformation of those bodies in contact and the surface forces that develop between them at this interface (Kappl, Butt, 2002). As such the two fundamental drivers of adhesion force upon interparticle contact are particle contact geometry and the physicochemical environment of that contact process. These two factors are intrinsically related through a complicated interdependence i.e. surface forces will develop according to changes in particle geometry upon contact (deformation) and contact geometry will often develop in response to the surface forces (Derjaguin et al, 1975). Significant work has been done into modeling such relationships, and this is discussed in more detail below. However due to the array of contributing factors to both these attributes in their own right, it is overtly apparent that this relationship is not necessarily a universal one and theoretical particle-particle adhesion forces are difficult to predict accurately. However the importance of the fundamental principles involved still remains paramount and understanding them gives crucial insight to adhesion force development and the potential consequences for a pharmaceutical system.

1.7 Interfacial Surface Forces

The three primary components of interfacial particle adhesion (in air) are universally recognized as van der Waals forces (F_{vdw}), electrostatic forces (F_{es}) and capillary forces (F_c):

$$F_{adh} = F_{vdw} + F_c + F_{es} \quad (1.3)$$

The relative contributions of each of these components to the total F_{adh} are dependent in turn on the environmental and physicochemical properties of the contacting bodies. These include surface chemistry and surface free energy, particle size and morphology, the viscoelastic / plastic behavior of the contacting bodies, surface roughness, effective contact area and contact geometry as well as environmental conditions (temperature and humidity) (Davies et al, 2005, Podczek et al, 1994). Because of the breadth of these influential factors, it is a highly complex procedure to predict interparticulate forces accurately. These interactive forces are discussed in more detail below but fundamentally van der Waals forces are considered the dominant interaction that define the F_{adh} , as they occur between all surfaces and in all conditions (Morris et al, 1999). Capillary forces will be prominent only above a threshold concentration of moisture at the interacting interface, and electrostatic forces may often be negligible in pharmaceuticals due to low dielectric constants, low ionic strengths and the absence of an electric field (Salazar-Banda et al, 2007).

1.7.1 Capillary forces

Capillary forces are the result of dynamic condensation of water molecules onto particle surfaces. On approach of one particle to another, if such condensation to the gap between the two surfaces is sufficient, a meniscus is created. As liquid is drawn around the contact points by capillary action, this forms an attractive force via surface tension effects on a relatively large scale (Begat et al, 2004a, Coelho and Harnby, 1978) . The exact size of such capillary forces are dependent upon numerous factors, including the surface free energy, the geometry of the

contact area and the resultant gap geometry, surface chemistry, surface hydrophilicity and the meniscus curvature (Hooton et al, 2004). Fisher and Israelachvili proposed the following equation to determine the capillary interaction between two spherical particles (Fisher, Israelachvili, 1981):

$$F_c = 4\pi R^* \gamma_L \cos\theta + 4\pi R^* \gamma_{SL} \quad (1.4)$$

Where R^* is the harmonic mean of the particle radius (or contact radius), γ_L is the water surface tension, γ_{SL} is the solid-liquid interfacial free energy and θ is the contact angle of the liquid with the particle surface. Whilst the contact radius is evidently of particular significance in F_c generation it is also obvious that the most significant influence on the generation of capillary forces will be the availability of water molecules to form capillary bridges and the meniscus curvature (Young et al, 2006). In this regard the relative humidity (RH) of the environment is therefore crucial, as this dictates the amount of moisture available. It is therefore reasonable to suggest that depending upon the physicochemical nature of a particle surface, increasing the relative humidity will have a direct influence on the interparticulate interaction (Hooton et al, 2004) so that in a completely dry environment (RH 0%) capillary forces will be non-existent, but in a very humid atmosphere capillary forces may dominate adhesive character. It is also important to realize that the presence of water at a contact interface may lead to structural changes in the contacting particulates. Dissolution of water soluble material is possible, or indeed the water may act as a plasticizing agent that affects the deformation of the contacting bodies and in this fashion adhesive character will be affected by changes to surface chemistry or contact geometry (Buckton, 1995).

1.7.2 Electrostatic Forces

Electrostatic forces (Coulombic) are formed between surfaces that acquire a charge. This is usually by either frictional force or artificially by the existence of an electric field around a surface. They are by far the strongest of the physical forces, stronger indeed than most chemical

binding forces and have a very long range (Israelachvili, 1991). Should a charged particle contact an uncharged surface then an equal but opposite charge will be generated on the surface, leading to adhesion. Such a force can be determined by (Butt et al, 2005):

$$F_{adh} = \frac{Q^2}{l^2} \quad (1.5)$$

Where Q is the charge on the particle and l is the distance between the centers of charge. It is rare in pharmaceutical formulations that any particles are adept at maintaining charge as this would often be counterproductive. Therefore electrostatic charges are usually negligible due to low dielectric constants, and rapid charge dissipation (Salazar-Banda et al, 2007). The presence of moisture will rapidly eliminate any electrostatic charge that does exist, as the interface at the surfaces becomes conductive and charge will be lost by dissipation (Coelho, Harnby, 1978). Thus in humid environments electrostatic charges will be negated.

1.7.3 Van der Waals Forces

Van der Waals forces are usually the most important contributor to F_{adh} in pharmaceutical materials and systems. They are somewhat ambiguous as a single term, indicating the summation of attractive (or repulsive) forces between molecules, and are better described themselves as three types of distinct interaction force that all show an inverse sixth power relationship with respect to the separation distance of the bodies involved.

1.7.3.1 Keesom Forces

Permanent dipole to permanent dipole interactions. These are based on the electrostatic attraction that exists between molecules with a permanent dipole moment. Here two atoms constituting a bond within a molecule have significantly different electronegativities, making the bond permanently polar in nature and capable of attracting other molecules with permanently

polar domains if correctly charge orientated. By this virtue these interactions tend to result in molecular alignment (reduction in potential energy) with a net attraction and are sometimes termed orientational forces.

1.7.3.2 Debye Forces

Permanent dipole to induced dipole interactions. A permanently polar bond in one molecule can induce a dipole in a neighboring molecule (of polar or non-polar nature). The permanent dipole generates an electric field which will disrupt neighboring molecules electron charges. Charge separation occurs and this results in an induced dipole which is attracted to the permanent dipole. As a consequence these interactions are sometimes termed induction forces.

1.7.3.3 London Forces

These are considered the most important of the three Van der Waals constituents, as they occur on all surfaces at all times (Israelachvili, 1991). They are instantaneous dipole to instantaneous dipole interactions, more commonly known as dispersion forces because the natural frequencies of resonance that result in dipole formation and interaction have the same physical foundation as that of the absorption spectrum i.e. the wavelength-dependent manipulation of light that leads white light to disperse into the spectrum of the rainbow (Parsegian, 2006). They are interaction outcomes of transient dipole moments of molecules without permanent multipole moments. Whilst still dependent upon the attraction of opposite charges on the contacting surfaces, these derive from electron fluctuations that render transiently electron dense and electron deficient areas of the molecular surface. Such instantaneous dipoles generate an electric field that polarizes other neutral atoms or molecules, inducing a dipole moment in them. The resulting interaction gives rise to an instantaneous attractive force that is time limited. The main characteristics of dispersion forces can be described as thus (Israelachvili, 1991):

- They are effective from relatively large distances (>10nm) down to interatomic separations (~0.2nm).

- They may be repulsive or attractive, and often cannot be described by simple power laws.
- They usually incur a weak alignment of molecules in addition to their attraction.
- The presence of other bodies nearby influences the dispersion interaction between two set bodies, and therefore these forces are not additive.

Fritz London (for whom the forces are named) proposed that the dispersion energy of interaction between two molecules V can be given as (Finlay 2001):

$$V = -\frac{3}{4} h\nu_0 \frac{\alpha^2}{d^6} \quad (1.6)$$

Where α is the polarisability, h is Planck's constant, ν_0 the characteristic frequency and d the separation distance between the two molecules. Hamaker (Hamaker, 1937) developed this work to describe those interactions occurring between macroscale bodies based on their component molecular interactions. By pair-wise integration of the dispersion energies over the volumes of the bodies involved he calculated the interaction energy between two solid objects as:

$$E = - \int_{V_1} \int_{V_2} \frac{q_1 q_2 d\nu_1 d\nu_2 \lambda_{1,2}^d}{r^6} \quad (1.7)$$

Where E is the total energy of interaction, $\nu_1 \nu_2$ are the total volumes of the particles bodies in contact, $q_1 q_2$ the number of atoms per unit volume of those particle bodies, r the separation distance and $\lambda_{1,2}^d$ is the London dispersion constant born from eq. 1.8:

$$\lambda_{1,2}^d = \frac{3}{2} h f a^2 \quad (1.8)$$

Where f is the vibration frequency of the interacting electronic oscillators. Using this approach, van der Waals forces could then be described between bodies of differing but distinct geometries (sphere, cylinder, planar surface etc.) as follows:

$$\text{Sphere - Sphere} \quad F = \frac{A}{12r^2} \left(\frac{d_1 d_2}{d_1 + d_2} \right) \quad (1.9)$$

$$\text{Sphere - Planar Surface} \quad F = \frac{A_{11} d_1}{6r^2} \quad (1.10)$$

Where $d_1 d_2$ are the sphere diameters, r is the separation distance between the contacting bodies (in a vacuum) and A is the Hamaker constant, a material property representing the strength of the consequent van der Waals interaction (Hamaker, 1937):

$$A = \pi^2 q_1 q_2 \lambda_{1,2}^d \quad (1.11)$$

Whilst adaptations of these equations were devised to describe the Van der Waals force of interaction between macroscale bodies of varying geometries there remained several limitations. Firstly, the Hamaker equation (eq. 1.7) assumed simple pairwise addition between contacting bodies. As already stated however, dispersive forces are non-additive. Secondly there is no consideration of pre-existing differences in electronegativities or polarizabilities between the atoms concerned, which would lead to increased contributions from Keesom and Debye forces. In response to these weaknesses the Lifshitz theory (Lifshitz, 1956) derived the forces between large bodies from bulk properties rather than atomic properties, by treating the solids as continuous materials. In effect this was defined by a different calculation of the Hamaker constant. While the detail behind such macroscopic theory is beyond the scope of this introduction, such an approach results in the following equation:

$$F = A^* \frac{d}{12D^2} \quad (1.12)$$

Where A^* is the modified Hamaker constant (Lifshitz-van der Waals constant adapted) d is the diameter of a spherical particle, and D is the distance between this sphere and a planar wall.

1.8 Adhesion Theory

1.8.1 The Hertz Approximation

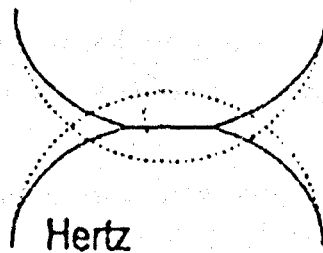


Figure 1.9: The Hertz Model of contact

Lifshitz theory remains too basic to model accurately real pharmaceutical contacts, as it assumes uniform physical properties and does not account for separation distances of molecular dimensions (Butt et al, 2003). Furthermore, such equations can account for the genesis of adhesive forces, but neglect the fact that real contacting bodies do not remain rigid on contact. In reality all solids have a finite elasticity, and will deform on contact, thereby altering the geometry of that contact regime (Butt et al, 2003). This deformation process has itself been modeled. Most models are derived from the Hertz approximation which described the spherical contact of elastic bodies. He proposed a relationship between the contact radius and the applied load (force) as follows (Hertz, 1881):

$$\alpha^3 = \frac{3R^*}{4E^*} \cdot F \quad (1.13)$$

Where α is the contact radius, F is the load, R^* is the effective particle radius, and E^* the reduced Young's Modulus as defined by (Butt et al., 2003):

$$R^* = \frac{R_1 \times R_2}{R_1 + R_2} \quad (1.14)$$

$$\frac{1}{E^*} = \frac{1-\nu_1^2}{E_1} + \frac{1-\nu_2^2}{E_2} \quad (1.15)$$

Where R_1 is the radius of sphere 1 and R_2 is the radius of sphere 2 and, E_1, E_2, ν_1 and ν_2 are the Young's modulus and Poisson ratio of sphere 1 and 2 respectively. The contact radius at the same time determines the indentation:

$$\delta = \frac{\alpha^2}{R^*} \quad (1.16)$$

However the Hertz model does not account for the surface forces described above, that often attract two surfaces with no load. It also assumes small contact radii with a normal loading direction without any frictional forces. This thereby prevents its application to complex particle contacts (Davies, 2005).

1.8.2 The Johnson-Kendall-Roberts Model

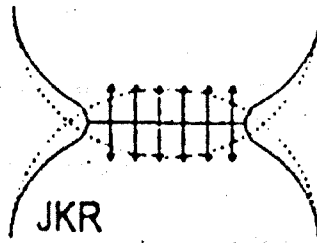


Figure 1.10: The JKR model of contact

Johnson, Kendall and Roberts (Johnson et al., 1971) adapted the Hertz model to account for surface forces between the contacting bodies. The JKR model assumes that two elastic spheres, with smooth surfaces experience surface forces inside the contact region, causing a non-Hertzian deformation. This deformation is conceptualized as a 'neck', due to the contact stress being compressive only in the centre of the contact spot, but tensile around the outside. This gives rise to bulging, instead of simple Hertzian flattening (Podczec, 1998). The model predicts that the two surfaces will separate from a given contact area only when a defined pull-off force is reached to overcome the adhesion of the two solids. This force can be calculated as follows:

$$F_{adh} = 3/2\pi WR^* \quad (1.17)$$

Where F_{adh} is the force of adhesion and W is the work of adhesion. The work of adhesion can in turn be expressed in terms of the surface energies of the contacting solids γ_1 and γ_2 by:

$$W = 2\gamma_1\gamma_2 \quad (1.18)$$

This can therefore be related to the F_{adh} by inserting eq. 1.18 into 1.17 as follows:

$$F_{adh} = 3/2\pi\gamma_1\gamma_2R^* \quad (1.19)$$

This model has therefore been widely used in both calculating the force of interaction between solids, and therefore on the calculation of effective surface free energy. The model is particularly applicable in systems with high surface energies, low elastic moduli, and low loading forces (Podczec, 1998).

1.8.3 The Derjaguin-Muller-Toporov Model

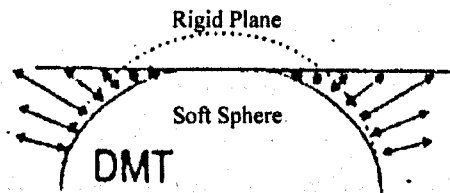


Figure 1.11: The DMT contact model

The JKR model is often used but assumes there is no surface interaction outside of the contact 'neck'. In reality surface forces are active outside of the direct contact between solids. Derjaguin, Muller and Toporov took this into account and developed the DMT theory (Derjaguin et al, 1975) where the shape of the deformed surface of the sphere in the contact zone follows the Hertz theory, but surface forces outside of the contact region are predicted. The theory predicts the force needed to pull a sphere and surface apart, considering a point contact only. This can be calculated as follows:

$$F_{adh} = 2\pi R^*W \quad (1.20)$$

The DMT model is more suitable for less rigid materials of a low surface energy (Podczec, 1998)

1.8.4 The Tabor Number

In effect the DMT and JKR models represent opposite ends of the same scale, and the choice of model is vastly important, as for the same interaction both may offer very different results. The discrepancy between the models was clarified by the advent of the dimensionless parameter the Tabor number, which describes the ratio of the elastic deformation resulting from adhesion to the effective range of surface forces (Zheng, Zu, 2007). The two models correspond to the opposite extremes of the Tabor number, and therefore it can be used to aid the selection of an appropriate model (Tabor, 1976):

$$\phi = \left(\frac{W^2 R}{E^* Z_0^3} \right)^{\frac{1}{3}} \quad (1.21)$$

Where ϕ is the Tabor number, W is the work of adhesion, R is the particle radius, E^* is the reduced Young's modulus and Z_0 is the distance of closest approach. If $\phi > 0.3$ then the JKR is more suitable, while if $\phi < 0.3$ the DMT would be better suited (Bunker, 2005). Further work has also suggested other models and parameters that refine the base assumptions of both these models. For example the Maugis-Dugdale model was designed to describe behavior between the extremes of the JKR and DMT models, and is regarded by some to better characterize interactive forces in many circumstances (Bunker, 2005).

1.9 Other Factors Affecting Adhesion

1.9.1 Surface Roughness

Surface and particle roughness is of great importance in determining interparticulate interaction (Bunker, 2005). This is simply because if two particle surfaces make contact, the contact regime is dependent upon the topography of both surfaces at the contact point. Real particles are not perfectly spherical, and asperities on their surfaces can serve to either increase or decrease the effective contact area on interparticulate contact. If a particle is smaller than the distance between asperities on an infinite surface, the particle may enter a trough, thus leading to an effective increase in contact area. Furthermore such asperities may prevent lateral forces facilitating the separation of that particle (Podczeczek, 1998). Yet if the particle is larger than the distance between asperities it will be unable to contact the dominant surface structure, thereby reducing the effective contact area and the prospective force generation between particle and surface. Surface roughness can therefore give rise to significant variability between the predicted of and experimentally measured force of adhesion.

1.9.2 Young's Modulus

The Young's modulus of a material represents its resistance to elastic deformation. It is the ratio of a materials stress to strain (Podczeczek, 1998). Materials with large Young's moduli are particularly stiff, i.e. showing low strain under high stress, and therefore resistant to deformation. Materials with low Young's moduli are less stiff and more susceptible to elastic deformation i.e. showing large strain under low stress. The Young's moduli of contacting particles will therefore play a role in determining the extent of deformation on contact, and this in turn will define to some degree the scale of interactive force that develops between the two surfaces.

1.9.3 Surface Free Energy

The surface free energy reflects the potential interactivity of a surface, which arises from the difference in net force acting upon molecules at the surface of a material from the bulk material

below and the phase state above it. In air, as the strength of interaction with the vapor phase is usually less than the surrounding molecules there will be an inward attraction of the molecule. As this force is effectively contracting the surface it is said to have generated a tension. If the surrounding medium is liquid, this net force becomes a surface tension. If the surrounding medium is solid however it becomes a surface free energy as it is describing the force stretching the surface. Consequently the surface free energy of a material can be defined as the energy required to increase the surface energy of a substance by one unit area in a vacuum (Podczek, 1998). This measure is very important as it describes the 'desire' of the surface to aggregate together or interact with another material so as to reduce the surface free energy. If we consider the goal to generate aerosols with well dispersed particles, it is obvious that high surface free energies will contradict an ideal suspension, or aerosol, and as such knowledge of this attribute is key in predicting formulation efficacy and behavior

1.10 Experimental Methods of Surface Forces Determination

With an appreciation of how important the forces of adhesion are in pharmaceutical applications it is appreciable that methods of experimentally quantifying these forces have long been sought. Estimations of the F_{adh} have been carried out by a number of contrasting experimental techniques for some years now. Some of the traditional methods include impaction, centrifugation, tensiometry and other various direct and indirect manipulation techniques (Lohrmann et al, 2007). The most significant of these are overviewed briefly below.

1.10.1 Centrifugation

The centrifuge technique is perhaps the most popular of the older techniques, and involves the particles of an interactive mixture being adhered to a disc in a special device rotating in a centrifuge. An example of such a setup is given in figure 1.12:

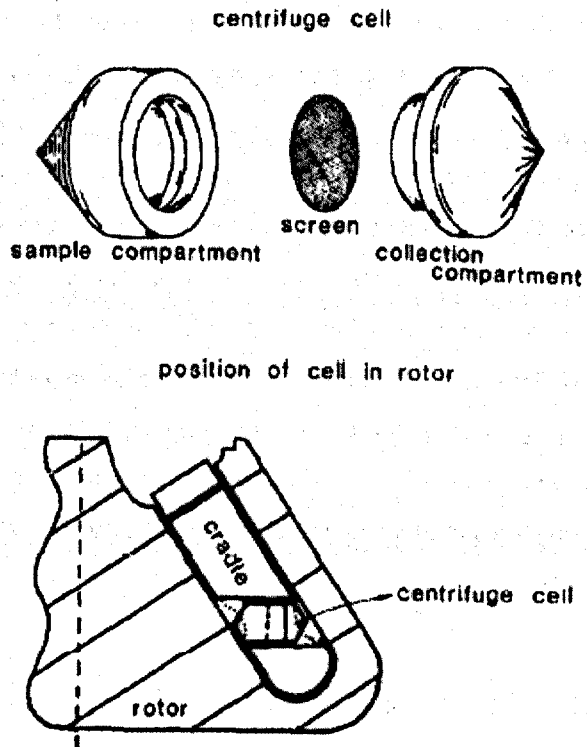


Figure 1.12: Basic design of a centrifuge cell. (Kulvanich, Stewart, 1987)

The principle is that above a critical centrifugal speed, the resulting force from the angular speed rotation of a particle with a defined mass, in a known distance to the rotation centre, will exceed the adhesion force between the particle and the surface (Salazar-Banda et al, 2007). Particles will therefore detach from the disc or substrate at a given centrifugal force, from which the F_{adh} can be calculated. In essence the technique is based upon the assumption that the F_{adh} is of the same magnitude, but opposite signal to the centrifugal detachment force i.e. (Felicetti et al, 2008):

$$F_{adh} = -F_{centrifugal} \quad (1.22)$$

The centrifugal detachment force ($F_{\text{centrifugal}}$) applied is directed outwards from the center of rotation through the center of gravity of the particle and is governed by Newton's second Law (Kulvanich, Stewart, 1987):

$$F_{\text{centrifugal}} = M(a + g) \quad (1.23)$$

Where M is the mass of the particle, a is the centrifugal acceleration and g is the acceleration due to gravity. Centrifugal acceleration is dependent upon angular velocity (ω_d) and the distance between the particle and axis of rotation (d_c):

$$a = \omega_d^2 d_c \quad (1.24)$$

Angular velocity is derived from the particle geometry and the centrifugal speed (S):

$$\omega_d = 2\pi S \quad (1.25)$$

Hence when $\omega_d^2 d_c \gg g$ our original equation can be rewritten as:

$$F_{\text{centrifugal}} = M\omega_d^2 d_c \quad (1.26)$$

Therefore the F_{adh} can be calculated accordingly. It is essential to analyze the amount of particles adhering to the surface at each incremental level of centrifugal speed, and this is usually done by some form of optical imagery and data analysis software. This technique was considered an

easily accessible method for adhesion force measurement with a good deal of credibility. Indeed it does offer the advantage of allowing measurements between real particles with both regular and irregular shape and size on smooth or rough surfaces, which is one of the primary limitations of atomic force microscopy (see below) (Felicetti et al, 2008). Furthermore it is capable of determining the F_{adh} based on the distribution of the adhesion force within a very large group of particles on a substrate. This is very useful in bulk characterization (Salazar-Banda et al, 2007). However there are several problems with the centrifugation technique. Perhaps most significantly, the very nature of the physics involved, as simplistically indicated above, means that particles are not necessarily separated from the substrate as a function of their F_{adh} . Indeed if two particles with the same F_{adh} , but different masses are conceptualized, it is obvious that they will not separate simultaneously. The particle with the larger mass will be subject to an increased centrifugal force at a lower centrifugal speed than the smaller massed particle, and hence will separate sooner. Furthermore, it is almost realistically impossible to characterize a polydisperse system by mass so that the centrifugal force can be calculated. This would require a determination of particle size distribution of the particles detached at each speed of centrifugation, which is incredibly complex (Kulvanich, Stewart, 1987). As such only homogeneous particle matter is an ideal candidate for such a technique. Yet even in this case because the arbitrary form of centrifugal force (in the form of rotor speed squared) is often used due to the difficulty in assessing particle size in a simple system, it may be impossible to calculate true adhesion force values (Kulvanich, Stewart, 1987). Furthermore some experimental work has indicated that the detachment force for particles of the same size, mass, and F_{adh} will not be the same depending upon their position on the carrier due to changes in the angle between the direction of the applied force and the plane of the surface (St. John, Montgomery, 1971).

1.10.2 Tensile Stress Methods

The tensile strength method is one that has perhaps had a narrower application to pharmaceuticals and has only been applied to a small range of materials. It has traditionally been used to measure the F_{coh} acting between two powder layers. In this situation a measuring device based on a suspended plate with a flat sticky surface attached to a micro-balance is dipped into

a loose powder bed. After a determined contact time the device is removed and the force required for separation of the two powder layers (i.e. that of the powder bed and that coating the device surface) is measured (Lohrmann et al, 2007). However adhesive measurements can be performed by adapting the technique. Figure 1.13 below describes a modified tensiometer designed for such work. Here, the two powder surfaces are prepared before measurement by fixing one to a measuring device of known weight, suspended from a micro-balance and the other on another disc parallel to the surface upon a moveable table. The layers are brought into contact by raising the table, and contact causes a decrease of load on the balance. User definition determines to what extent this decrease is continued, before the surfaces are left in motionless contact for a set contact time and then separated again on table lowering. The adhesive force upon withdrawal is registered by the micro-balance as a hyper-extension of the force beyond its free level (Lohrmann et al, 2007).

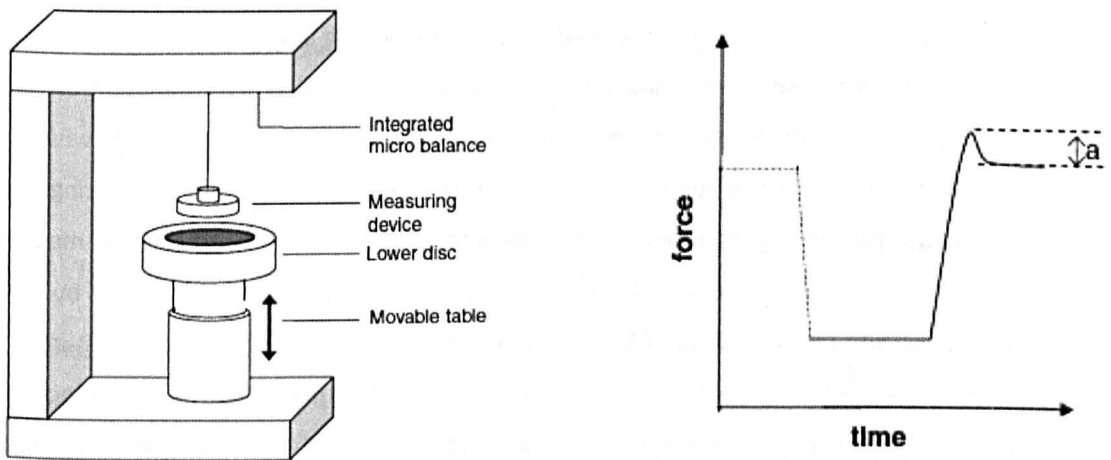


Figure 1.13: A modified tensiometer designed for F_{adh} measurements. (Lohrmann et al, 2007)

This technique is quick and simple to perform and has the benefit of being able to vary the conditions in which it is employed so that the effect of important factors such as humidity can be observed. However, it does have several limitations. The first is that the system only provides an appreciation of bulk behavior, and there is no capability to map the interaction on a particle

by particle basis or investigate the effects of changing contact geometry, surface roughness etc. Secondly the technique relies upon a perfectly parallel contact, or rather detachment, of the two surfaces to ensure all the contact points between the materials separate simultaneously. If this is not the case there will be an inaccurate reading of the F_{adh} from the microbalance (Lohrmann et al, 2007). There is also a degree of reliance of the F_{adh} recorded on the speed of detachment. This is suggested to be due to air pressure effects, where too rapid detachment causes a low pressure gap between plates that 'sucks' the plates back together again (Lohrmann et al, 2007).

1.10.3 Surface Forces Apparatus

The surface forces apparatus (SFA) device (Tabor, Winterton, 1969) allows a direct measurement of the F_{adh} in air, or liquids and vapors at Angstrom resolution level (Forces ~ 10 nN, distances $\sim 1\text{\AA}$). It consists of two crossed atomically smooth mica cylinders of about 1cm radii between which forces are measured. Prior to positioning in the apparatus the mica surfaces are coated with a semi-reflecting layer of silver to allow optical determination of the separation distance. One mica cylinder is mounted to a piezoelectric translator through which the distance between cylinders is adjusted while the other cylinder is mounted to a spring of known and adjustable spring constant. The separation between the surfaces is measured by an interferometric technique (multiple beam superposition analysis) and by knowing this separation the deflection of the spring and the force can be calculated (Butt et al, 2005). The surfaces can then be coated with various materials to investigate their interaction force with excellent force resolution. In a solvent environment, SFA can even measure the oscillatory solvation and structural forces arising from the packing of individual layers of solvent molecules and can be employed to measure the electrostatic 'double layer' forces between charged surfaces in an aqueous medium with an electrolyte. However the drawback of the approach is that it requires materials with very good lateral homogeneity (i.e. no rough surfaces) and a well-controlled thickness that can be applied to the mica (Leckband, 1995). It is also a highly complex piece of apparatus to utilize that requires a great degree of operational competence, and while being surface specific, does not allow an individual particle-particle adhesion force assessment.

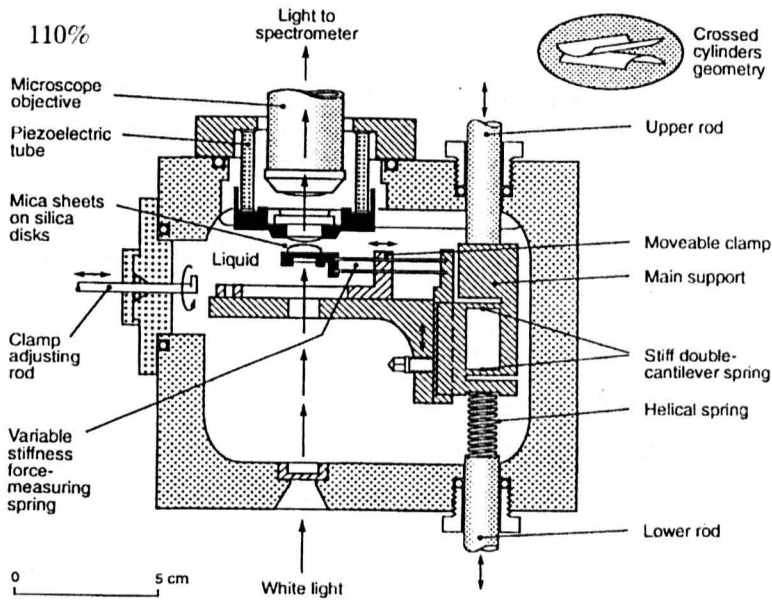


Figure 1.14: Schematic of a Surface Forces Apparatus device. (Leckband, 1995)

1.10.4 Total Internal Reflection Microscopy

Total Internal Reflection Microscopy (TIRM) allows the instantaneous changes in distance between a single microscopic sphere immersed in a liquid, and a transparent plate to be determined. This can be achieved to nanometre resolution by using an evanescent wave produced through the plate to illuminate the sphere, and by calculating the resulting intensity of light scatter (Axelrod et al, 1984). The principle is that when a sphere with a refractive index different from that of the liquid medium is in proximity to a surface where total internal reflection occurs, some of the evanescent wave is scattered as a result of what is termed 'frustrated' total internal reflection. The amount of light scattered is sensitive to the proximity of the sphere to the surface and thus can be used to map the interaction of the two bodies (Axelrod et al, 1984).

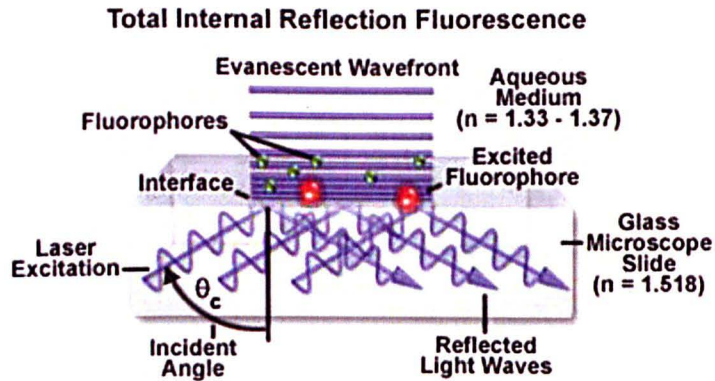


Figure 1.15: Basic concept of evanescent wave generation. Adapted from www.microscopyu.com accessed 25/11/2008

The primary disadvantage of using this technique is the incredibly complicated nature of the process and precision required to carry it out, particularly in orientating the incident light source to produce an effective evanescent wave. It is also constrained by the requirement of a liquid media with particular optical properties, reducing its application to solid-state based investigations.

1.10.5 Osmotic Stress Method

The osmotic stress method employs an indirect measurement of F_{adh} between macromolecules. A dispersion of selected macromolecules or biological lipids is first equilibrated to a reservoir solution containing water and other small solutes which are capable of free exchange into the dispersion phase. The reservoir then has a polymer incapable of diffusion added, the concentration of which determines the osmotic stress acting upon the dispersion. The proximity of the macromolecules is measured (using x-ray diffraction) as a function of increasing osmotic pressure to generate pressure-distance curves that can be analyzed in a similar fashion to force distance curves in atomic force microscopy (LeNeveu et al, 1977). This method is predominantly useful when studying vesicle or macromolecular interactions in organic systems and is almost

inapplicable to inorganic solid phase systems. Those systems under study all require liquid stability and need to be immune to interaction with the other elements of the dispersion phase.

1.10.6 Impaction Methods

There are several less technically specific techniques that rely on applying various means of an impaction force (e.g. hammer fall) to the opposite side of a substrate with particles adhered, and quantifying the amount of particulate loss as a function of the increasing impaction force. This type of set up is very easy to arrange, but relatively non-specific in force determination and in reality only has relevance if interest lies in the state of the particles that have been lost from the substrate (e.g. examining the electric charge present) (Derjaguin, 1968).

1.10.7 The Limitations of Bulk Adhesion Measurement

As indicated by the brief overview of the techniques mentioned above, they are all based on experimentation citing bulk systems and/or multiple particulate surfaces. They also suffer from very specific material property requirements. This poses several key problems. Firstly any F_{adh} experiment technique where there is a very precise prerequisite for given material tolerances or physical states can in turn only have a very limited scope for use. While coherent and relevant data may be generated for very specific materials there is little room for more complicated multi-particulate formulations. When considering the realm of inhaled drug delivery this is very appreciable, and obviously many of the techniques outlined would struggle to be adapted for use. DPI formulations will not tolerate liquid based analysis, but equally pMDI systems may require measurement in a liquid state under pressure for a true force appreciation. Furthermore whilst bulk material adhesion data is useful in describing the general effects of adhesion and cohesion on formulation, manufacture and performance there is little characterization of the nature of the component attractive forces involved. (Davies et al, 2005). Being able to assess the individual particle to particle adhesion in addition to bulk behavior would allow much more depth in understanding of the complex interplay of the forces and factors involved in dictating particle interactions, and potentially a view to beneficial modifications or critical constraints (Roberts, 2005). Critically many of the methods above lack any delicate control over the critical

parameters cited in adhesion force theory (i.e. environment, surface roughness, contact geometry etc.) to allow a more precise assessment of the fundamental forces of interaction. In an ideal situation, the ability to subtly alter these individual variables and characterize the changes to the result would be employed. Some drug systems are much more sensitive to micro- and even nano-scale interaction than others. For example in some inhaler systems very small amounts of material or drug are used (e.g. formoterol fumerate) , and interactions on an individual particle basis become more significant, as problems such as dose reproducibility and the use of bulking agents complicate issues (James et al, 2008). In such instances an appreciation of bulk behavior can only be of a limited degree of assistance in evaluating the system dynamics. The ability to study single particle interactions, the forces involved, and to do so within a system with scope for control over important variables is therefore very desirable. Realizing this desire has however become possible with the advent of the atomic force microscope (AFM) (Binnig et al, 1986).

1.11 Atomic Force Microscopy

The atomic force microscope (AFM) is an example of a scanning probe microscope, which allows the imaging and analysis of molecular surfaces with sub-nanometre resolution (Allen et al, 1997). In AFM a sample is scanned by a very sharp micron-sized tip mounted on a cantilever spring. When scanning, the force between the tip and the sample can be measured by monitoring the deflection of the cantilever. This is quantified by a laser signal focused on the cantilever tip and reflected onto a position sensitive photodiode. By plotting the deflection of the cantilever against its position on the sample, it is possible to map the samples topography. Alternatively the height of the translation stage can be mapped in maintaining a constant force against the surface, where a feedback loop is initiated using piezoelectric input (Butt et al, 2005). In this way images of nano-scale can be generated. Figure 1.16 shows a simplified AFM setup:

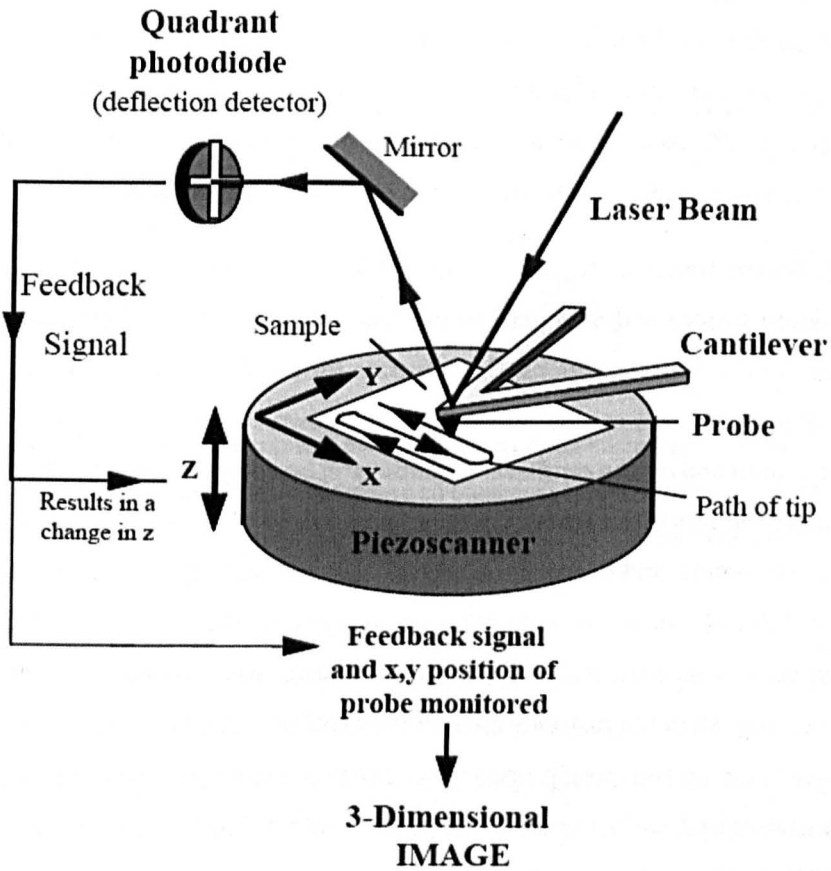


Figure 1.16: A schematic of an atomic force microscope (Allen et al 1997).

AFM imaging can traditionally be done using two separate techniques; contact mode or tapping mode. In contact mode the AFM tip is raster scanned across the surface of the interest whilst in constant contact. Whilst this method ensures the highest resolution of imaging, as the tip responds to the changes in surface topography directly, it is also the most likely to cause damage to a fragile surface or even the tip itself. The applied force of the tip on the surface can be exaggerated extensively due to the very small surface area involved (Butt et al, 2003). Tapping mode can to some extent avoid this problem. Here the cantilever is oscillated at its resonant frequency. As the tip approaches a surface, there will be a dampening of the vibration amplitude because the tip either starts to hit the surface or is affected by attractive or repulsive surface forces. Therefore if the surface is scanned by a constant reduction in tip vibration

amplitude the laser signal will plot the effective topography of the surface. This therefore reduces the direct contact between tip and surface and can better preserve fragile substrates. The downside to this technique is a loss in resolution, but significantly by monitoring the surface effects on the wave mechanics of the tip oscillation, additional information about the local mechanical properties of the surface can be generated (Butt et al, 2003).

Significantly however the AFM not only has a role as an imaging tool, but can also be used to measure surface and interfacial forces (Ducker, Cook, 1990). If the cantilever and sample are kept in fixed lateral positions, the substrate (or cantilever depending upon the particular AFM arrangement used) can be rastered up and down by the piezo translation stage it is carried upon, onto and off the cantilever (or substrate) by applying a voltage. When nearing contact the sample will very often attract the tip prior to a fixed level contact, causing a 'jump in' deflection (i.e. tip bends under attractive forces into contact). The piezo input then continues the sample/cantilever movement until a pre-set value for the stage height (z-coordinate) is reached. The stage then reverses, and the sample and tip will separate. However this separation will occur only when the restoring force of the cantilever (spring constant) surpasses the interaction force of the tip and sample, and as such the negative deflection of the cantilever below the non-contact output can be used to quantify the interaction force described (Sindel, Zimmermann, 2001). By applying Hooke's law:

$$F = -kz \quad (1.27)$$

where k is the spring constant of the cantilever and z is the cantilever deflection at the moment of separation, the force of interaction F can be calculated. This method of operation is called 'force' mode and figure 1.17 shows a representation of the generation and interpretation of a single force curve and the relative deflection signals involved:

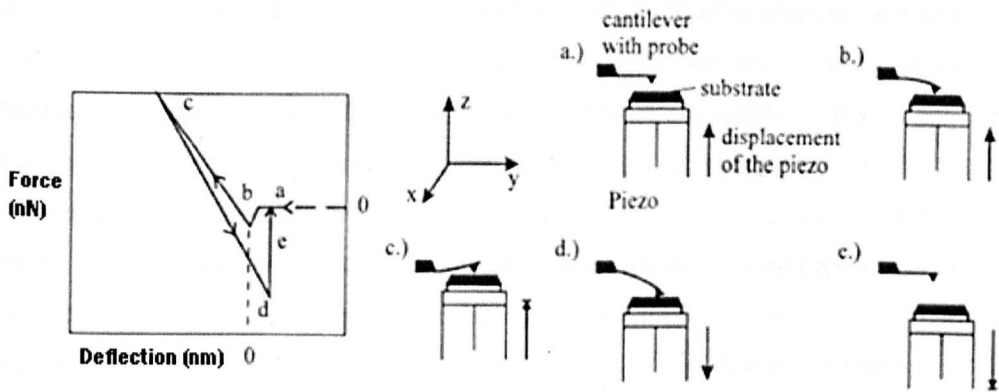


Figure 1.17: Force deflection (displacement) plot of an atomic force microscope – a.) Non-contact area b.) 'Jump in' of tip under attraction of substrate c.) Maximum height of substrate d.) Maximum interaction force e.) Separation of tip and sample. (Sindel, Zimmermann, 2001)

Hence running AFM in force mode allows characteristic work to be done on the interaction between a surface and tip. However this is only of limited use when considering the aspects of pharmaceutical interaction that concern inhaler technology. While some material properties can be gleaned from such a procedure, such as the surface free energy or Young's modulus of that material, the interaction between a cantilever and tip (usually silicon nitride) and a material of interest will not provide characterization of the multi-particulate forces involved in API-exipient mix or those of an API with a device component.

1.12 Colloidal Probe Microscopy

It was with the advent of colloidal probe microscopy (CPM) that the capacity to adapt AFM to measuring the interaction between two materials of interest was borne. CPM involves the attachment of a well-defined colloidal particle to the tip of the AFM cantilever, and performing force measurements between that particle and a given surface (Ducker et al, 1991). Such materials as silica gave special spherical probes that allowed fine geometric definition and extensive work to be done on colloidal contact mechanics and force measurement (Bunker et al, 2005). Whilst undoubtedly of great value for theoretical advancement such work was not capable of characterizing broader systems. Critically the CPM method was the precursor to a

more recent 'real particle' technique, where individual particles of interest e.g. drug molecules, cells, polymers etc. are attached to a cantilever and used to produce force measurements (Ibrahim et al, 2000). The distinction between colloidal particle probes and real particle probes has been somewhat blurred so as that the use of real particles is still often referred to as 'colloid probe microscopy'. Therefore for the purpose of this thesis the term will be used to refer to the use of drug particle probes. Such a technique allows direct measurement of the F_{adh} / F_{coh} between two particles. This has the facility to be inherently applicable to pharmaceutical formulations, especially inhalation therapy, and has therefore been utilized in many studies to analyze interparticulate adhesion within DPI and pMDI formulations.

Essentially this technique affords a method of experimentally determining the F_{adh} on a single particle level, and a means to explore the very nature of the interfacial forces involved. The AFM therefore fulfills many of the ideal properties that former adhesion force techniques failed to. Primarily it has the advantage of allowing a large number of essential parameters to be adjusted or maintained on an experimental basis. For example environmental chambers allow control of temperature, humidity etc., and therefore allow a direct assessment of the effect of these individual factors, or the removal of force critical components (e.g. preventing capillary interaction by removing residual moisture). More critically, the technique analyzes micro-scale contact, and prospectively individual particle-particle contact. This offers a unique chance to manipulate substrate size, shape, geometry etc. and characterize resulting changes to adhesion force trends. While other techniques may offer certain controls on individual variables, AFM offers the chance to manipulate several. One of the most basic advantages with AFM is that force measurements can be taken in liquid or air, without compromising any other element of the technique. This is of particular importance to inhalation pharmaceuticals as it offers a means to evaluate adhesion forces in both pMDI formulations with the use of model propellants (i.e. chemically and physically similar but non-volatile) and DPI formulations. Additionally AFM software is fairly well advanced following several seminal years of work in many areas of adapted use. Hence it is capable of running force measurements at a multitude of points over a defined area of the substrate surface very quickly so that many measurements with a tip on a surface may be taken with consummate ease (concept of force volume mode).

However the use of real particles to probe surfaces still has obvious problems associated with it. Firstly by using a 'real' particle, there is an almost complete loss of control of the morphology of

your tip. Considering the importance of contact geometry upon such fine scale interaction, as described above, this has rendered adhesion measurements made by this technique specific on a probe by probe basis. Hence, even adhesion measurements on the same substrate made with two different tips of the same material, may often exhibit huge differences in the forces calculated, and therefore it is very difficult to compare experimental data (Farschchi-Tabrizi et al, 2006). To allow any relative conclusions to be drawn between two sample materials, the same tip therefore needs to be employed for force measurement. This can be problematic in itself, as continued tip use pre-disposes to tip-wear, which in turn alters the geometry of the scanning particle and hence the surface contact mechanics (Butt et al, 2005). This has a significant effect upon the validity of the force values observed.

Secondly there is a fundamental change to the cantilever's physical characteristics with the attachment of a particle. The spring constant quoted or calculated for the unmodified cantilever may no longer be applicable, as the added mass of the particle can have an impact. As such the spring constant of the modified cantilever may require re-calculation. A method based on the intensity of thermal noise (Hutter, Bechhofer, 1993) has become particularly popular due to its non-invasive character. Other methods such as a technique using the resonant frequency and quality factor of the cantilever (Sader et al, 1999), an added mass method (Cleveland et al, 1993) or various others based on alternate force applications e.g. gravitational force, hydrodynamic force, acoustic radiation (Butt et al, 2005), are less attractive due to the complexities involved in maintaining the integrity of particulate tip.

There is also an issue with the actual fixation of a particle to a cantilever. This is usually performed by a micromanipulation technique, where a tiny amount of glue ($\sim 10^{-18}$ m³ epoxy based resin) is placed on the end of the cantilever and then the probe particle is brought into contact with this spot. This requires using fine wires to either move the glue and particle around the cantilever or the cantilever to the glue and particle (Kappl, Butt, 2002). Such manipulation usually occurs under control of a light microscope and therefore there is a limit to the size of particle that can be attached to around 1 μ m or above. Where bare AFM tips are a matter of nanometres in size this potentially massive increase in tip size incurs much greater forces of adhesion (increased radius, contact area etc.) By virtue of the limited range of the piezo-movement and dynamic range of the split photodiode detector, stiffer cantilevers than normal

are therefore required to ensure that the particle detaches from the surface on withdrawal (Kappl, Butt, 2002). This is to the detriment of force resolution.

Furthermore it is crucial that no excessive resin is left accessible to the tip's substrate or coats the attached particle surface, otherwise the adhesion measurement could be compromised. It is also essential to ensure successful attachment of the particle, and therefore tip characterization by further imaging is usually undertaken (e.g. SEM, TEM) after fixation. Indeed this is repeated after each set of adhesion results to verify the continued presence of the tip and any potential changes to it (Jones et al, 2008b). All in all therefore the process is very time consuming and labour intensive, which will often limit the number of probes that will be produced on an experiment by experiment basis (Roberts, 2005).

These problems all occur in addition to those that generally impair AFM force measurements. Such issues as hysteresis and creep are persistently a problem and affect the accuracy of distance determination (Davies et al, 2005). There can be difficulties in making measurements on very 'sticky' substrates (although unlikely in inhalation therapy to be significant) where the tip becomes trapped on the surface, or operation in liquids can induce hydrodynamic interference, with the tip approach and retraction inducing liquid perturbation and liquid dumping that impedes measurements (Butt et al, 2005). Lack of sensitivity of the photo-diode itself is possible, especially as this is dependent upon the size and shape of the laser beam. Hence distortion of the beam for any reason can lead to a poor sensitivity and reduced accuracy of force measurement.

1.13 The Cohesive-Adhesive Balance Approach

1.13.1 The CAB Method

With an inability to directly compare results from CPM based work it seemed that AFM, despite all its positives, remained fundamentally quite a relative process with a limited application in force determination. However an approach developed by Begat, Morton, Stainforth and Price in 2004 (Begat et al, 2004a) offered an extension to real particle probing that would potentially allow data from different probes and different experiments to be compared (Roberts, 2005).

The cohesive-adhesive balance approach (CAB) is a CPM adaptation based in a change of analysis rather than an extensive change to practical process. Instead of trying to compare probe to probe results in F_{adh} directly, the technique compares the ratio of a probe's cohesive character to its adhesive character with a given substrate. As already highlighted, experimental and theoretical adhesion force measurements are often several orders of magnitude different, and this is assumed to be due to the differences in the predicted and actual contact area of the two interacting surfaces. However with the application of the CAB approach the severe difficulty in determining or accounting for the probe-substrate contact area is precluded by treating the adhesion forces as a function of the cohesive forces of the same probe (Jones et al, 2008). From the equations cited when we considered the contributions to interparticulate interactions, the cohesive-adhesive balance can be expressed as a ratio of the summation of capillary and van der Waals forces (3,5) (Begat et al, 2004a):

$$\frac{F_{coh}}{F_{adh}} = \frac{R_{A-A}^*[\eta\pi W_{A-A} + (4\pi\gamma_{water} \cos \theta_{A-A} + 4\pi\gamma_{A-water})]}{R_{A-B}^*[\eta\pi W_{A-B} + (4\pi\gamma_{water} \cos \theta_{A-B} + 4\pi\gamma_{A-water})]} \quad (1.28)$$

Where F_{coh} and F_{adh} are the cohesive and adhesive forces respectively, R_{A-A}^* and R_{A-B}^* are the contact radii, η is the contact model specific constant (JKR, DMT etc), W_{A-A} and W_{A-B} are the cohesive and adhesive thermodynamic work of adhesion values, θ_{A-A} and θ_{A-B} are the measured contact angles of the liquid with the relative particle surfaces, γ_{water} is the surface tension of water and $\gamma_{A-water}$ is the particle liquid interfacial free energy.

From this equation it can be concluded that in a constant environment (temperature, humidity etc.) the W_A and θ will only be dependent upon the material's physical characteristics. Hence in such a set up the only parameters liable to vary will be the contact radii R_{A-A}^* and R_{A-B}^* . Therefore as long as there is a gross similarity between the surface geometrics of the two substrates used and assuming the same probe is used on both with no alteration to its morphology, the cohesion-adhesion ratio should theoretically remain constant between a number of probes (Traini et al, 2005a). Therefore by plotting the F_{coh} as a function of the F_{adh} for several probes on a substrate, the force balance within a system of interest can be quantified through the regression of these values (Begat et al, 2004a).

In essence therefore, force measurements are performed between a series of functional probes (of a given material of interest) and molecularly smooth crystal faces of the other material of interest. Quantitative AFM measurements of the cohesive forces versus the adhesive forces for that series of probes are then plotted graphically (Hooton et al, 2006). In such a fashion a CAB plot is compiled from which, with some basic statistical analysis a quantitative measurement of the specific cohesive/adhesive ratio can be calculated. An example of a CAB plot is given below in fig 1.18:

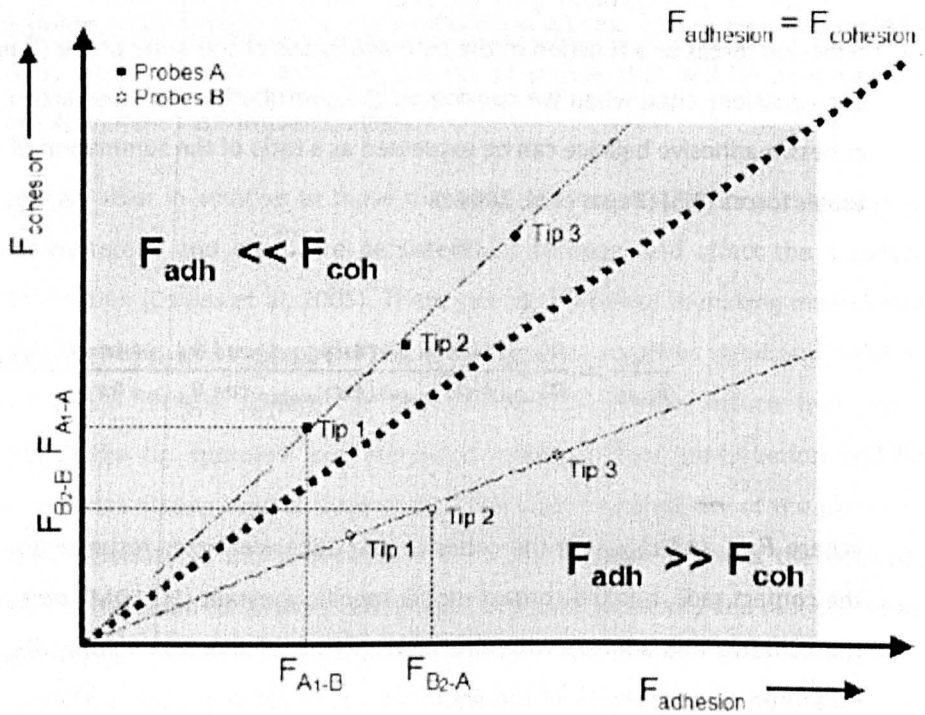


Figure 1.18: Theoretical CAB graph for a binary system. (P.Begat et al, 2004a)

Here the adhesive force measurements for a number of probes of interacting materials F_{A1-B} and F_{B2-A} are plotted on the x-axis against the relative cohesive force measurements of the same probe materials F_{A1-A} and F_{B2-B} . Assuming the contact geometries are the same, the force data of several probes (i.e. tip 1, tip 2 and tip 3) should follow a linear fit because of a consistency in the cohesive-adhesive ratio (F_{A1-B}/F_{A1-A} and F_{B2-A}/F_{B2-B}). The bisecting line therefore represents equilibrium between F_{adh} and F_{coh} , and serves to divide the plots into two distinct regions. That above the line is the cohesive domain where $F_{\text{coh}} > F_{\text{adh}}$, and that below the

line is the adhesive domain where $F_{adh} > F_{coh}$. Hence the relative position of a series of aligned plots to this bisection represents either an affinity (as a larger force of adhesion) of a probe material for itself or for the substrate respectively (Traini et al, 2005a).

By linear regression analysis of the respective slopes of the plot values from a tip series, the relative strength of the adhesive/cohesive interactions can be measured (Begat et al, 2004a). The difference in the gradients between tip series of different probe-substrate measurements can be used to directly compare the cohesive and adhesive tendencies (Hooton et al, 2006). It is also possible to use the coefficient of determination (R^2) to assess the uniformity of contact between the surfaces and the tips in evaluating the legitimacy of the mathematical outcomes (Begat et al, 2004a).

The most obvious benefit of this technique is that it allows quantification of the relationship between the theoretical work of adhesion and cohesion and corresponding AFM measurements (Traini et al, 2005a). As critiqued, the principle hindrance to AFM based real particle force data was the lack of control over the tip geometry leading to an unknown contact area. This meant massive variations in F_{adh} that couldn't be calibrated for to allow fair comparison with other substrates, and subsequently limited the conclusions possible. The CAB technique manages to solve this redundancy by using the cohesive force of the probe as a means of normalization for the adhesion force. In so doing the predominant adhesive-cohesive character of a system (e.g. API and carrier molecule) can be qualified and quantified by a CAB value. Potentially therefore this technique offers a means to answer some of the critical pre-formulation questions that thus far no other method has accurately provided: How does the drug-drug cohesion compare to the drug-carrier/excipient/device adhesion? Will this system therefore have adequate stability, reproducibility and in vivo performance? How does the force balance of one combination of API and carrier, or of two APIs compare and how does this influence the formulation performance.

1.13.2 CAB Studies

Thus far the CAB approach has been used by several authors to critique the potential of and '*in-vitro*' performance of various inhaler APIs and excipients in answering these questions. The examples given below highlight some of the key applications the approach has been put to use in, and the potential it has for furthering our understanding of the influence of interparticulate interaction. Begat et al, in defining the technique, used it to characterize the interaction of DPI ingredients salbutamol and budesonide with the carrier molecule α -lactose monohydrate (Begat et al, 2004a). The study suggested that the salbutamol-lactose system was adhesive in nature (16.88 times greater interaction of salbutamol tip with lactose than salbutamol tip on salbutamol) and therefore that the two would exhibit good powder properties as a homogeneous blend. However the budesonide-lactose system was cohesive in nature (budesonide probes exhibiting 3.84 fold greater affinity for budesonide surfaces than lactose) and this suggested that such a binary system would exhibit poor blend homogeneity without the introduction of large shear stresses to overcome the cohesive bonds (Begat et al, 2004a).

This simple but useful summation led the same group to then attempt to define the implied impact of such a cohesive-adhesive balance on DPI formulation aerosolization and delivery. By using the same APIs and carrier molecule and formulating inhalation powder blends that were subject to morphological, particle size, chemical, content uniformity and '*in-vitro*' deposition characterization (Begat et al, 2004b). These tests verified the initial work of the group, in that the budesonide-lactose system exhibited less homogeneity than the salbutamol-lactose blend (SD dose content uniformity 28.1% and 4.2% respectively). They also identified expected trends based on the cohesive-adhesive balance of the formulations upon emitted dose and fine particle fraction when in comparison to API only delivery. However more interestingly in the course of the '*in-vitro*' impaction studies they discovered a paradoxical relationship, whereby budesonide alone and with lactose, evidenced a lower total emission efficacy, but produced a greater fine particle fraction (FPF) than salbutamol alone or with lactose. This was explained by factoring in the effect of air stream dynamics, whereby a more cohesive formulation leads to larger drug aggregates on inspiration that were subject to increased drag forces which in turn effectively gave rise to improved de-agglomeration and dispersion in the airstream. Hence the CAB approach was ratified in predicting the behavioral differences between separate formulations.

However this study also identified the complicated nature of its application to inhalation therapy as a whole and a need for more work.

Traini, Rogueda, Young and Price adapted the CAB approach as a means to experimentally compare the derivation of particle cohesion and adhesion forces with other techniques, providing a theoretical measurement of the interfacial free energy of particulate interactions in multi-drug pMDIs (Traini et al, 2005a). The work found the CAB approach to concur with the broad theoretical predictions in considering the cohesive/adhesive character of three APIs with one another (Salbutamol, Formoterol, Budesonide) in the model propellant 2H, 3H perfluoropentane (HPFP). There was however not a consistent compliance with the actual values calculated. This discrepancy was put down to a slight polarity of HPFP that was not factored into the theoretical calculation (will effect liquid-liquid surface tension prediction) or the use of a single dominant crystal face in the AFM force measurements. Here there may be a discrepancy to the contact angle data derived from molecular compacts where surface free energy values may be higher. Despite this the study went some way to validating the CAB approach as an accurate means to characterize interparticulate interaction, and more specifically within a pMDI set up.

The same authors later tried to determine a relationship between adhesive and cohesive character of the same API based pMDI systems and '*in-vitro*' deposition testing using an Anderson Cascade Impactor (ACI) and flocculation studies. The CAB analysis suggested that salbutamol had a largely cohesive character with respect to other APIs, while the budesonide and formoterol were more adhesive. This was supported with vast changes in single agent delivery to multi-agent delivery and these were associated with the nature of interaction involved. Salbutamol delivered alone exhibited strong relative cohesive character, seen as compact flocculation to a small sedimentation volume. But when combined with APIs to which it demonstrated relatively lower adhesive character (budesonide, formoterol), there was aggregation to more loosely bound and easily re-dispersible flocs, capable of higher performance delivery (3 times greater as total emitted dose). Conversely budesonide and formoterol showed higher sedimentation volumes with loose flocs when examined alone, but when combined with salbutamol, flocculation was more compact and the emitted dose decreased. This interesting study highlighted the potential for CAB analysis to assess potential multi-drug pMDI formulations for expected delivery behaviors, and associated this to

flocculation behavior. However crucially it did not examine the effect of the CAB on the fine particle fraction (FPF) of the formulation which as it has been suggested previously, may tend to oppose the trend for total emitted dose.

A CAB study by Hooton, Jones and Price attempted to predict the behavior of sugar carriers in DPI formulations (Hooton et al, 2006). Using micronized salbutamol probes they performed a CAB analysis on 5 sugar molecules with potential for use as carrier molecules. They then compared the CAB graphs generated with '*in-vitro*' performance data using an ACI. They discovered that the rank order of FPF performance of the β_2 -agonist and sugar carriers corresponded to the reverse trend in adhesive character. This association was found to be linearly correlated and was deemed to confirm that in adhesive systems the stronger the adhesive nature of an interaction the better the interactive mixture, but the less successful the detachment upon air stream entrainment. Therefore with decreasing adhesive character the balance of interactive forces may allow better disaggregation and dispersion efficacy. Importantly however this shift may induce instability in the system which may lead to segregation of the API within the formulation, giving higher device retention and potentially reduced dose reproducibility. The performance of cohesive systems remained unclear, although it was again hypothesized that agglomeration and segregation of the API in such a system is countered by drag force effects leading to higher eventual dispersion levels.

Following on from this work, Jones, Hooton, Dawson, Ferrie and Price used the CAB approach to investigate the dispersion of DPI ternary formulations '*in-vitro*' (Jones et al, 2007). CAB ratios were produced for drug-'fine' and 'fine'-carrier probes and the results highlighted the importance of such carrier 'fines'. The work suggested that stronger API-fine adhesion led to larger combination agglomerates attached to carrier particles. These were then subject to greater deagglomeration forces during aerosolization than smaller API only agglomerates and were better dispersed. Furthermore the data suggested that ternary cohesive systems were associated with an increase in performance independent of a drug-fines interaction. This was hypothesized to be due to increased deagglomeration forces as a consequence of increased particle-particle collisions. Here a more than 400% increase in individual particles over binary formulations may result in many more interparticulate collisions, which are very effective in causing drug particle detachment from a carrier.

Another study from Hooton, Jones, Harris, Shur and Price then expanded upon a question raised in the previous study; whether the particular crystal habit of a given API had an influence on the cohesive/adhesive character recorded? (Hooton et al, 2008). In the DPI system studied the authors used the CAB approach to characterize two different crystal habits of budesonide formed by differing solvent and anti-solvent combinations with 5 different sugar carrier molecules. The results suggested that the CAB was very different for the two crystal habits with cohesive nature of the {102} faces being approximately twice that of the {002} faces. Although this did not directly affect the rank order of adhesive character with the sugars, there was a significant effect on FPF as recorded by an ACI. The loss of adhesive character with the {102} face led to an increase in FPF up to a plateau. The differences in CAB were attributed to the molecularly modeled surface chemistry differences of the two habits giving rise to increased contributions of the {102} face to van der Waals interactions.

1.13.3 The Cohesive Adhesive Balance: A Summation

As can be seen above, the CAB approach has been well adapted to suit some fundamental investigations into interactions on a micro-scale and would seem to offer the potential to drastically further our understanding of the area as a whole. It has proven a viable tool in assessing a number of concepts surrounding adhesion forces and their implications of inhalation formulation. Indeed the technique has to some extent already been validated in its accurate assessment of the adhesive/cohesive nature of compound formulations. However this is not to say that the technique is without limitations. It cannot be forgotten that the CAB approach is based in AFM methodology and therefore suffers the same inadequacies as those cited earlier which will serve to distort the results achieved. What is more of a specific problem with the approach is the necessity for crystalline smooth surfaces to perform measurements upon. As indicated, the principle of the CAB approach is that the surfaces of cohesion and adhesion are morphologically identical, and therefore the only way to ensure this has been to use crystalline material with validated surface homogeneity. This is of course not an accurate representation of actual particle morphology in formulation, and therefore it would be expected that AFM measurements on the lowest energy faces of crystalline substrates may either underestimate the forces of cohesion and adhesion, or through a deliberate ignorance of actual roughness,

indeed overestimate them (Jones et al, 2008a). This has wider implications in that, as has been alluded to in several studies, the very handling of the tip material and substrate will in itself lead to changes in the force measurements made. This may be through providing different crystal habits (Hooton et al, 2008) or any other chemical or physical difference (Jones et al, 2008b).

Furthermore, the necessity to recrystallize a substrate for use in a force balance experiment reduces its application to some materials, as well as reducing the capacity for use in a quick a simple assessment of an API mix. Such a facility would be invaluable if the capacity to measure a force balance was combined with real particle states and simple technical operation. If force balances between APIs and inhaler components, APIs and excipients or even multiple APIs could be linked to the performance of an inhaled formulation this would then allow a simple CPM technique to offer a potentially rapid and accessible pre-formulation screen that would infer the potential of a blend of formulation components.

1.14 References

S.Allen, M.C.Davies, C.J.Roberts, S.J.B.Tendler, P.M.Williams. (1997) Atomic force microscopy in analytical biotechnology. *Tibtech*; 15:101-105

D.Axelrod, T.P.Burghardt, N.L.Thompson. (1984) Total Internal Reflection Fluorescence. *Annual Review of Biophysics and Bioengineering*; 13:247-268

P.Begat, D.A.V.Morton, J.N.Staniforth, R.Price. (2004a) The Cohesive-Adhesive Balances in Dry Powder Inhaler Formulations I: Direct Quantification by Atomic Force Microscopy. *Pharmaceutical Research*; 21:9:1591-1597

P.Begat, D.A.V.Morton, J.N.Staniforth, R.Price. (2004b) The Cohesive-Adhesive Balances in Dry Powder Inhaler Formulations II: Influence on Fine Particle Delivery Characteristics. *Pharmaceutical Research*; 21:10:1826-1833

G.Binnig, C.F.Quate, C.Geber. (1986) Atomic force microscope. *Physical Review Letters*; 56:9:930-933

BNF (2012). British National Formulary no 63. *BMJ Group Pharmaceutical Press, London, UK*

British Pharmacopoeia (2012) British Pharmacopoeia Commission, London, England

British Thoracic Society, Scottish Intercollegiate Guidelines Network. (2011) British Guideline on the Management of Asthma Quick Reference Guide. www.brit-thoracic.org.uk; accessed November 2011

G.Buckton, P.Darcy, D.McCarthy. (1995) The extent or errors associated with contact angles. 3 – The influence of surface-roughness effects on angles measured using a wilhelmy plate technique for powders. *Colloids and Surfaces A – Physicochemical and Engineering Aspects*; 95:27-35

M.Bunker, M.Davies, C.Roberts. (2005) Towards screening of inhalation formulations: measuring interactions with atomic force microscopy. *Expert Opinion on Drug Delivery*; 2:4:613-624

H-J.Butt, G.Karlheinz, M.Kappl. (2003) Physics and chemistry of interfaces. *Wiley-VCH Verlag GmbH & Co. KGaA, Weinheim, Germany*

H-J.Butt, B.Cappella, M.Kappl. (2005) Force Measurements with the atomic force microscope: Technique, interpretation and applications. *Surface Science Reports; 59:1-152*

J. P.Cleveland, S.Manne, D.Bocek, P.K.Hansma. (1993) A nondestructive method for determining the spring constant of cantilevers for scanning force microscopy. *Review Scientific Instruments; 64:403-405*

M.C.Coelho, N.Harnby. (1978) Moisture bonding in powders. *Powder Technology; 20:201-205*

M.Copley. (2008) Cascade Impactors: Theory, design and practical design for optimal testing. *Inhalation Magazine; 1-5*

A.Davies, C.Moores, R.Britton. (2003) The Respiratory System. Elsevier Science Ltd, London, UK,

B.V.Derjaguin, I.N.Aleinikova, Y.P.Toporov. (1968) On the role of electrostatic forces in the adhesion of polymer particles to solid surfaces. *Powder Technology; 2:154-158*

B.V.Derjaguin, V.M.Muller, YU.P.Toporov. (1975) Effect of contact deformations on the adhesion of particles. *Journal of Colloid and Interface Science; 53:2:314-326*

B.V.Derjaguin, L.D.Landau (1941). Theory of the stability of strongly charged lyophobic solutions and of the adhesion of strongly charged particles in solutions of electrolytes. *Acta Physicochimica; 14:663*

W.A.Ducker. R.F.Cook. (1990) Rapid measurement of static and dynamic surface forces. *Applied Physics Letters; 56:24:2408-2410*

European Pharmacopeia (2012) [viewed May 2012] European Directorate for the Quality of Medicines and Healthcare. Available from <http://www.edqm.eu>

M.Farshchi-Tabrizi, M.Kappl, Y.Cheng, J.Gutmann, H-J.Butt. (2006) On the Adhesion between Fine Particles and Nanocontacts: An Atomic Force Microscope Study. *Langmuir; 22:2171-2184*

M.A.Felicetti, F.Piantino, J.R.Coury, M.L.Aguiar. (2008) Influence of removal time and particle size on the particle substrate adhesion force. *Brazilian Journal of Chemical Engineering*; 25:1:71-82

W.H.Finlay. (2001) The Mechanics of Inhaled Pharmaceutical Aerosols: An Introduction. *Academic Press, London, UK*

L.R.Fisher, J.N.Israelachvili. (1981) Direct measurements of the effect of meniscus forces on adhesion: a study of the applicability of macroscopic thermodynamics to microscopic surfaces. *Colloids and Surfaces*; 3:303-319

A.T.Florence, D.Attwood. (1998) Physicochemical Properties of Pharmacy. 3rd Edition. *Pharmaceutical Press, London, UK*

M.George, D.T.Goddard. (2006) The characterization of rough particle contacts by atomic force microscopy. *Journal of Colloid and Interface Science*; 299:665-672

I.Gonda. (1990) Aerosols for delivery of therapeutic and diagnostic agents to the respiratory tract. *Critical Reviews in Therapeutic Drug Carrier Systems*; 6:273-313

D.A.Groneberg, C.Witt, U.Wagner, K.F.Chung, A.Fischer (2003). Fundamentals of pulmonary drug delivery. *Respiratory Medicine*; 97:382-387

J.Grossman. (1994) The Evolution of Inhaler Technology. *Journal of Asthma*; 31:55-64

H.C.Hamaker. (1937) The London-Van der Waals attraction between spherical particles. *Physica*; 4:10:1058-1072

H.Hertz. (1881) Study on the contact of elastic solid bodies (SLA translations, SLA-57-1164). *Zeitschr.F.Reine Angewandte Mathehmatik*; 29:156-171

A.J.Hickey, D.C.Thompson. (1992) Physiology of the Airways. In: A.J.Hickey. *Pharmaceutical Inhalation Aerosol Technology*; 1-27. Marcel Dekker INC, New York, USA.

M.Hindle. (2010) Aerosol Drug Delivery. Pharmaceutical Sciences Encyclopedia: Drug Discovery, Development, and Manufacturing. *John Wiley & Sons Ltd, Virginia, USA*

J.C.Hooton, C.S.German, S.Allen, M.C.Davies, C.J.Roberts, S.J.B.Tendler, P.M.Williams. (2004) An Atomic Force Microscopy Study of the Effect of Nanoscale Contact Geometry and Surface Chemistry on the Adhesion of Pharmaceutical Particles. *Pharmaceutical Research*; 21:6:953-961

J.C.Hooton, M.D.Jones, R.Price. (2006) Predicting the Behaviour of Novel Sugar Carriers for Dry Powder Inhaler Formulations via the Use of a Cohesive-Adhesive Force Balance Approach. *Journal of Pharmaceutical Science*; 95:6:1288-1297

J.C.Hooton, M.D.Jones, H.Harris, J.Shur, R.Price. (2008) The Influence of Crystal Habit on the Prediction of Dry Powder Inhalation Formulation Performance Using the Cohesive-Adhesive Force Balance Approach. *Drug Development and Industrial Pharmacy*; 34:974-983

J.L.Hutter, J.Bechhoefer. (1993) Calibration of atomic-force microscope tips. *Review of Scientific Instruments*; 64:1868-1873

T.H.Ibrahim, T.R.Burk, F.M.Etzler, R.D.Neuman. (2000) Direct adhesion measurements of pharmaceutical particles to gelatine capsule surfaces. *Journal of Adhesive Science Technology*; 14:1225-1242

J.Israelachvili. (1991) Intermolecular and Surface Forces. 2nd Edition. *Academic Press Ltd, London, UK*

J.James, B.Crean, M.Davies, R.Toon, P.Jinks, C.J.Roberts. (2008) The surface characterization and comparison of two potential sub-micron sugar bulking excipients for use in low-dose, suspension formulations in metered dose inhalers. *International Journal of Pharmaceutics*; 361:209-221

M.D.Jones, H.Harris, J.C.Hooton, J.Shur, G.S.King, C.A.Mathoulin, K.Nichol, T.L.Smith, M.L.Dawson, A.R.Ferrie, R.Price. (2008a) An investigation into the relationship between carrier-based dry powder inhalation performance and formulation cohesive-adhesive force balances. *European Journal of Pharmaceutics and Biopharmaceutics*; 69:496-507

M.D.Jones, J.C.Hooton, M.L.Dawson, A.R.Ferrie, R.Price. (2008b) An Investigation into the Dispersion Mechanisms of Ternary Dry Powder Inhaler Formulations by the Quantification of Interparticulate Forces. *Pharmaceutical Research*; 25:2:337-348

M.Kappl, H-J.Butt. (2002) The Colloidal Probe Technique and its Application to Adhesion Force Measurements. *Particle & Particle Systems Characterization*; 19:129-143

P.Kulvanich, P.J.Stewart. (1987) Fundamental considerations in the measurement of adhesional force between particles using the centrifuge method. *International Journal of Pharmaceutics*; 35:111-120

D.Leckband. (1995) The surface force apparatus – a tool for probing molecular protein interactions. *Nature*; 376:617-618

D.M.LeNeveu, R.P.Rand, V.A.Parsegian, D.Gingell. (1977) Measurement and modification of forces between lecithin bilayers. *Biophysical Journal*; 18:209-230

E.M.Lifshitz. (1956) The Theory of Molecular Attractive Forces Between Solids. *Soviet Physics JETP-USSR*; 2:73-83

M.Lohrmann, M.Kappl, H-J.Butt, N.A.Urbanetz, B.C.Lippold. (2007) Adhesion forces in interactive mixtures for dry powder inhalers – Evaluation of a new measuring method. *European Journal of Pharmaceutics and Biopharmaceutics*; 67:579-586

L.E.Manzer. (1990) The CFC-ozone issue: progress on the development of alternatives to CFCs. *Science*; 249:31-5

M.J.Molina, F.S.Rowland. (1974) Stratospheric sink for chlorofluoromethanes – chlorine atomic-catalyzed destruction of ozone. *Nature*; 249:810-812

V.J.Morris, A.R.Kirby, A.P.Gunning. (1999) AFM for Biologists. Imperial College Press, London, UK

S.J.M.Munroe, A.L.Cripps. (2007) Metered Dose Inhalers. In: J.Swarbrick (2007) Encyclopedia of Pharmaceutical Technology. *Informa Healthcare, New York, USA.*

S.P.Newman. (2005). Principles of Metered-Dose Inhaler Design. *Respiratory Care*; 50(9):1177-1190

V.A.Parsegian. (2006) Van Der Waals Forces: A Handbook for Biologists, Chemists, Engineers, and Physicists. *Cambridge University Press, New York, USA*

G.L.Patrick. (2005) An Introduction to Medicinal Chemistry. 3rd Edition. *Oxford University Press, USA*

F.Podczek, J.M.Newton, M.B.James. (1994) Assessment of adhesion and autoadhesion forces between particles and surfaces: I. The investigation of autoadhesion phenomena of salmeterol xinafoate and lactose monohydrate particles using compacted powder surfaces. *Journal of Adhesion Science Technology*; 8:12: 1459-1472

F.Podczek. (1998) Particle-particle Adhesion in Pharmaceutical Powder Handling. *Imperial College Press, London, UK*

H.P.Rang, M.M.Dale, J.M.Dale. (2003) Pharmacology 5th Edition. *Churchill Livingstone, Edinburgh, UK*

C.J.Roberts. (2005) What can we learn from atomic force microscopy adhesion measurements with single drug particles? *European Journal of Pharmaceutical Sciences*; 24:153-157

G.R.Salazar-Banda, M.A.Felicetti, J.A.S.Goncalves, J.R.Coury, M.L.Aguiar. (2007) Determination of the adhesion force between particles and a flat surface, using the centrifuge technique. *Powder Technology*; 173:107-117

U.Sindel, I.Zimmermann. (2001) Measurement of interaction forces between individual powder particles using an atomic force microscope. *Powder Technology*; 117:247-254

A.J.Stone. (2013) The Theory of Intermolecular Forces 2nd Edition. *Oxford University Press, Oxford, UK*

J.C.Sung, B.L.Pulliam, D.A.Edwards. (2007) Nanoparticles for drug delivery to the lungs. *TRENDS in biotechnology*; 25(12):563-570

D.Tabor, R.H.S.Winterton. (1969) The direct measurement of normal and retarded van der Waals forces. *Proceedings of the Royal Society of London*; A312:435-450

D.Tabor. (1976) Surface forces and surface interactions. *Journal of Colloid Interface Science*; 58:1:2-13

M.P.Timsina, G.P.Martin, C.Marriott, D.Gander-ton, M.Yianneskis. (1994) Drug Delivery to the Respiratory Tract using Dry Powder Inhalers. *International Journal of Pharmaceutics*; 101:1-13

D.Traini, P.Rogueda, P.Young, R.Price. (2005a) Surface Energy and Interparticulate Forces Correlations in Model pMDI Formulations. *Pharmaceutical Research*; 22:5:816-825

C.Vervaet, P.R.Byron. (1999) Drug-surfactant-propellant interactions in HFA-formulations. *International Journal of Pharmaceutics*; 186:13-30

J.C.Virchow, G.K.Crompton, R.Dal Negro, S.Pedersen, A.Magnan, J.Seidenberg, P.J.Barnes. (2008) Importance of Inhaler Devices In The Management of Airways Diseases. *Respiratory Medicine*; 102:10-19

L.Wu, R.P.S.Robson, S.R.P.da Rocha. (2007) Understanding Solvation in Hydrofluoroalkanes: Ab Initio Calculations and Chemical Force Microscopy. *Journal of Physical Chemistry*; 11:8096-8104

P.M.Young, M.J.Tobyn, R.Price, M.Buttrum, F.Dey. (2006) The Use of Colloid Probe Microscopy to Predict Aerosolization Performance in Dry Powder Inhalers: AFM and In Vitro Correlation. *Journal of Pharmaceutical Sciences*; 95:8:1800-1809

Z.Zheng, J.Yu. (2007) Using the Dugdale approximation to match a specific interaction in the adhesive contact of elastic objects. *Journal of Colloid and Interface Science*; 310:27-34

A.D.Zimon. (1982) Adhesion of Dust and Powders .2nd edition. Consultants Bureau, New York, United States (1982).

2.0 Materials and Methods

2.1 General Introduction

This chapter will introduce and explain the background to the materials and primary methods used within the experimental chapters and relevant to the area of research to follow. This will include the basic active pharmaceutical ingredients utilised, the pMDI components and formulation materials and the experimental and analytical techniques used in the subsequent chapters. Each of the following chapters will cover in more detail the precise methodologies and individual techniques employed but this chapter is designed to afford a basic description and understanding of the principals involved in the key analytical procedures as well as the general materials investigated. The techniques covered will principally include atomic force microscopy (AFM) and its variants, scanning electron microscopy (SEM), time-of flight secondary ion mass spectrometry (ToF-SIMS), Raman spectrometry, desorption electrospray ionization mass spectrometry (DESI) and Andersen cascade impaction (ACI).

2.2 Materials

2.2.1 Active Pharmaceutical Ingredients (APIs), Propellants and Excipients

The principal APIs used throughout the course of these studies are described below:

2.2.1.1 Salbutamol Sulphate

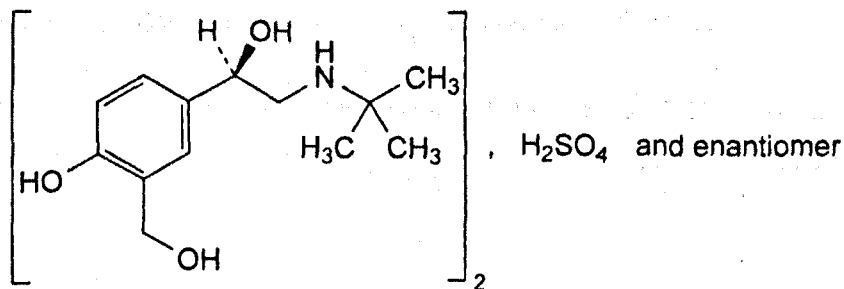


Figure 2.1 Salbutamol Sulphate Monograph (British Pharmacopoeia, 2012)

Salbutamol sulphate is a beta₂-adrenoceptor agonist, used as a rapid and short acting bronchodilator that exists as a white or almost white crystalline powder, freely soluble in water and virtually insoluble in ethanol. It has a chemical formula of $(C_{13}H_{21}NO_3)_2H_2SO_4$ and molecular weight of 576.7 (British Pharmacopeia, 2012). Salbutamol sulphate was supplied by 3M Healthcare (Loughborough, UK).

2.2.1.2 Beclomethasone Dipropionate

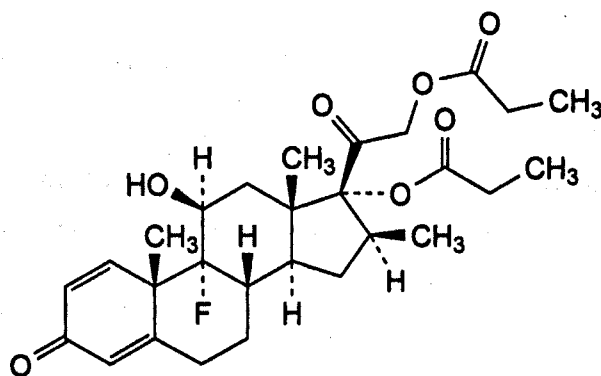


Figure 2.2 Beclomethasone Dipropionate Monograph (British Pharmacopeia 2012)

Beclomethasone dipropionate is a glucocorticoid, used in prophylaxis against inflammatory airways conditions. It is a white or near white crystalline powder practically insoluble in water but freely soluble in acetone and methylene chloride while sparingly soluble in ethanol. It has the chemical formula $C_{28}H_{37}FO_7$ and a molecular mass of 504.6. It is widely known to have several media dependent polymorphs, including a BDP hydrate, and clathrates with a variety of solvents (British Pharmacopeia, 2012). Beclomethasone Dipropionate was supplied by 3M Healthcare (Loughborough, UK) unless otherwise specified.

2.2.1.3 Salmeterol Xinafoate

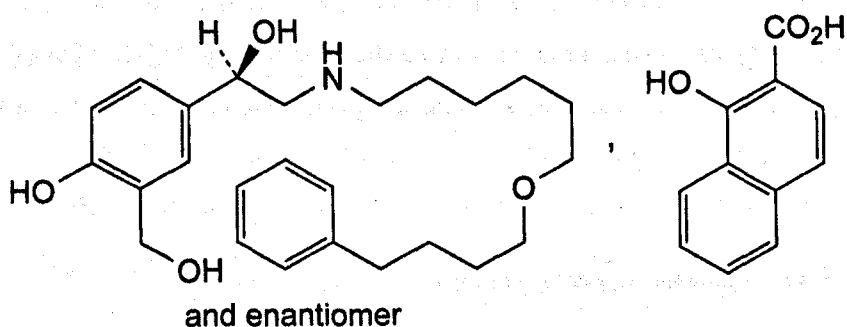


Figure 2.3 Salmeterol Xinafoate Monograph (British Pharmacopoeia, 2012).

Salmeterol Xinafoate is a beta₂-adrenoceptor agonist used as a long acting bronchodilator. It is a white or almost white powder, practically insoluble in water but soluble in methanol and slightly soluble in ethanol. It has a chemical formula of C₃₆H₄₅NO₇ and a molecular weight of 604. Salmeterol Xinafoate was supplied by 3M Healthcare (Loughborough, UK).

2.2.1.4 Fluticasone Propionate

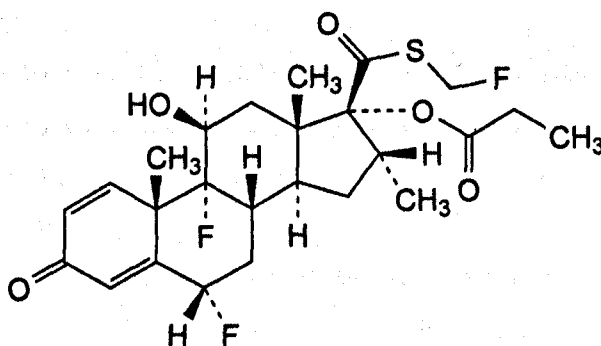


Figure 2.4 Fluticasone Propionate Monograph (British Pharmacopoeia, 2012).

Fluticasone propionate is a glucocorticoid used in prophylaxis against inflammatory airways conditions and to treat inflammatory skin conditions. It is a white or almost white powder practically insoluble in water but soluble in methylene chloride and slightly soluble in alcohol. It has the chemical formula C₂₅H₃₁F₃O₅S and a molecular weight of 500.6. Fluticasone Propionate was supplied by 3M Healthcare (Loughborough, UK).

2.2.1.5 Budesonide

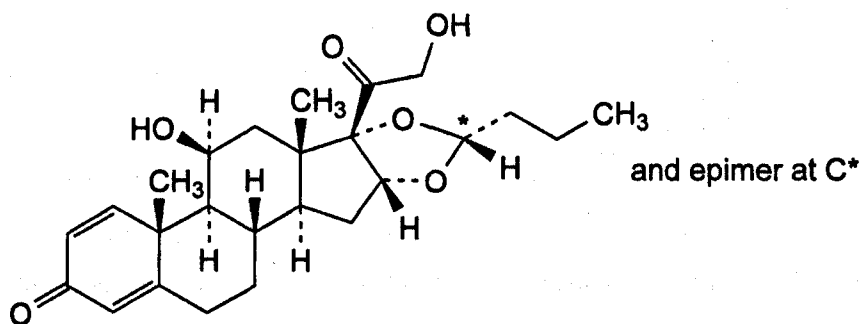


Figure 2.5 Budesonide Monograph (British Pharmacopoeia, 2012).

Budesonide is a glucocorticoid used in prophylaxis against inflammatory airways conditions and to treat inflammatory conditions of the bowels. It is a white or almost white crystalline powder practically insoluble in water but freely soluble in methylene chloride and sparingly soluble in ethanol. It has the chemical formula $C_{25}H_{34}O_6$ and a molecular mass of 430.5. Budesonide was supplied by 3M Healthcare (Loughborough, UK).

2.2.1.6 1,1,1,2-tetrafluoroethane (HFA 134a)

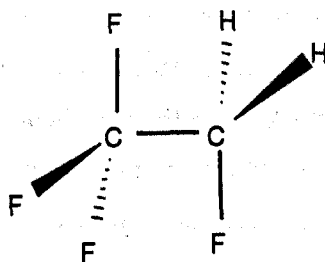


Figure 2.6 Structure of HFA134a

1,1,1,2-tetrafluoroethane (HFA134a) is a chlorine free alkane with no ozone depleting capabilities (Brindley 2003) widely used as a propellant in most modern pMDI devices as a replacement for the previously banned CFCs. It is utilised as a clear liquefied gas under pressure and with a boiling point of -26.5°C is also a colourless gas post actuation. HFA134a was supplied

by 3M Healthcare (Loughborough, UK) and BOC (Surrey, UK) as specified in the individual methods.

2.2.2 Pressurised Metered Dose Inhaler Components

Several pMDI components were used through this course of this study, either as part of a complete pMDI assembly for formulation handling and actuation or as representative substrates for force balance work. They key components with special consideration are as follows:

2.2.2.1 Aluminium Canister (Un-coated) and Fluorinated Ethylene Propylene Coated Canisters

A pMDI canister is the housing unit for the inhalation formulation to be delivered. As such it acts as a store for the API and excipient blends, either dissolved into or suspended within the chosen propellant. Its primary functional requirements are therefore to withstand the pressures of the liquefied gases (~1500k kPa), to avoid interacting with the formulation components, and to protect the formulation from either escape, or contamination from ingress (i.e. moisture) (McDonald, Martin, 2000). The most widely used containers are made from aluminium alloys due to their light weight, strength, compactness and low interactivity with traditional formulation materials (Munroe, Cripps, 2007). Stainless steel and glass canisters can be used in rare circumstances. As the largest surface area in contact with the formulation it is the most likely to experience interactions with the chemical constituents, and therefore will be considered as a surface of primary interest when assessing API-pMDI component adhesions and force balances. Some canisters are coated with sub-micron layers of modifying chemicals in an attempt to reduce surface-formulation interactions (Ashayer et al., 2004). One example is the use of fluoropolymers like fluorinated ethylene propylene (FEP). Such a coated canister was therefore chosen for comparison to the un-coated canister in terms of adhesive contact force with the respective APIs investigated.

Trimline aluminium un-coated and FEP coated pMDI canisters used in this study were provided by 3M Healthcare (Loughborough, UK) unless otherwise specified.

2.2.2.2 Metering Chamber

The metering valve in a pMDI is one of the most design critical elements in an aerosol formulation delivery system. It can be considered not as a singular part, but rather a collection of independent components that work in combination to achieve a goal. This is to measure and reproducibly deliver the formulation out of the canister upon actuation, whilst also forming the seal on the top of the canister that prevents loss of the pressurized contents. The metering chamber is perhaps the most critical component of the valve, as it serves to portion and contain the exact quantity of formulation needed to deliver an established aerosolized dose. A typical MDI metering valve operates in a stem down position and consists of two coupled valves placed on either side of a volumetric metering chamber. When the valve stem is depressed, the inner valve must close to isolate the rest of the formulation from the environment, while the outer valve opens to discharge the contents of the metering chamber (Munroe, Cripps, 2007). As such the metering chamber is nearly always in contact with the formulation, and by the very nature of its function, any interaction with the formulation can induce critical changes in the delivered dose efficacy of the API (McDonald, Martin, 2000). The metering chamber was therefore chosen as a device substrate for force based work.

Bespak 50 μ l metering valve assemblies (Bespak Europe Ltd, King's Lynn, UK) were used on all occasions within this thesis.

2.3 Methods

2.3.1 Atomic Force Microscopy

The science and extended applications of Atomic Force Microscopy (AFM) have been explored and explained in detail in chapter 1 and readers are directed to this section (1.11) for a full briefing on the experimental theory and its application to interparticulate interaction determination.

2.3.2 Time of Flight Secondary Ion Mass Spectrometry and Multivariate Analysis

2.3.2.1 ToF-SIMS

If a solid surface is bombarded with energetic primary particles (electrons, ions, neutrals or photons) that surface will, as a product of a collision cascade and energy transfer, yield secondary particles. Where the primary ions and the surface undergo collision there is extensive fragmentation and bond breaking leading to the emission of atomic particles. Further from the collision site however, the direct and indirect (knock-on) collisions become less energetic and are less able to exceed all bond energies, resulting in less fragmentation and more molecular fragments (Belu et al., 2003). As a result the emitted secondary particles may in turn be electrons, neutral species atoms and molecules or indeed atomic and cluster ions. While the vast majority of these particles will be neutral, a fraction is ionized and the mass spectrometry of these secondary ions (SIMS) allows a detailed chemical determination of the surface area (Grams, 2007). ToF-SIMS is a particularly popular application of the SIMS technique, and conceptually a simple means of mass separation used in SIMS analysis. In this instance, pulses of the generated secondary ions 'sputtered' from the analytical surface are accelerated to a given potential (usually 3 to 8 keV) so that all the ions possess the same kinetic energy, and are then allowed to drift through a field free space before striking an ion detector. As the heavier masses travel slower than lighter masses through this space, the ions strike the detector at differing times and the detector can then calculate impact intensity as a function of time of flight, with a direct correlation to ion mass as indicated by equation 2.1:

$$t = L \left(\frac{m}{2zV} \right)^{1/2} \quad (2.1)$$

Where t is the measured flight time of ions of mass to charge ratio (m/z) accelerated by a potential (V) down a flight path of length (L) (Vickerman, 1997). Figure 2.7 highlights the principle at work in a ToF-SIMS field free flight tube:

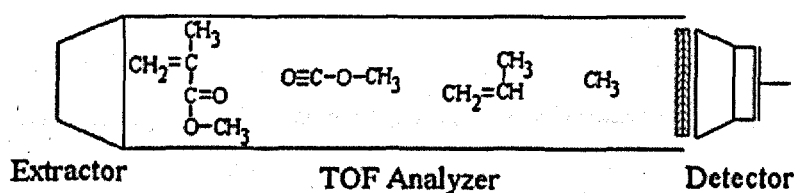


Figure 2.7 Schematic representation of ion mass separation in the ToF field-free drift tube

(Belu et al., 2003)

ToF-SIMS can either be run in a 'static' or 'dynamic' mode. The dynamic mode exploits the destructive nature of the incident primary ion beams to analyse the secondary ions emitted as a function of sputtering depth. This technique is very useful in either detecting trace deposits of elements, investigating the sequential composition of a material and layer composition, or simply in removing a surface layer in order to analyse those below. However the more modern static SIMS approach uses much lower primary ion doses, in an attempt to maintain sensitivity to the surface of the analyte. Often chemical surface specificity is of the greatest interest, as it is this interface that governs the largest component of physicochemical interactivity. Static SIMS better preserves the surface layers, albeit with a significant reduction in secondary ion yield and a loss of confidence in ion quantification (Grams, 2007). Significantly, by rastering the primary ion beam in a static mode across a surface of interest, it is also possible to develop a spatial set of SIMS spectra that can then be used to create elemental or chemical state images of a given

scan area. This process of ion imaging allows the relation of chemical analysis to surface topography and morphology. Figure 2.8 shows the basic experimental assembly of ToF-SIMS apparatus:

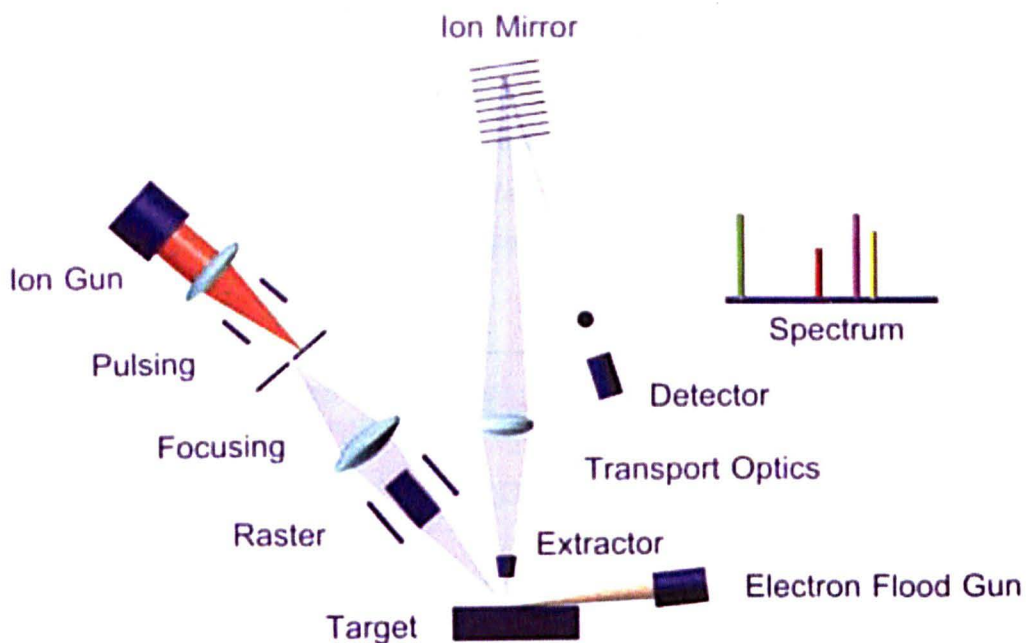


Figure 2.8 Schematic of a ToF-SIMS analysis (ION-TOF GmbH)

The primary ion source in a ToF-SIMS set up can be customised with respect to the mode of SIMS to be run and the specific aims of the experiment at hand. Field ionizing liquid metal ion guns generating gallium (Ga^+) or Bismuth (Bi_3^+) allow for spatial resolutions down to $1\mu\text{m}$ and below (although maintaining static conditions below this threshold is very difficult, and therefore this is practically not often the case) (Belu et al., 2003). Alternatively by thermally exciting elements such as caesium (Cs^+) or carbon₆₀ (C_{60}) coated metal sources, much larger single ion or cluster ions can be generated giving rise to much more destructive surface bombardments, ideal for surface sputtering and analysis.

The principle advantage of ToF-SIMS is therefore the versatility to perform both high sensitivity destructive and high spatial resolution surface sensitive chemical analysis of organic and inorganic materials. In particular the potential to move beyond high sensitivity individual spectra, to map a given topography on an ion by ion specific basis as a chemical image, is of fantastic potential in relating chemical composition to surface localisation. Such a technique has great value in identifying API localisation with respect to other excipients or APIs on an impacted surface, such as post actuated ACI plates.

2.3.2.2 Multivariate Analysis

One of the limitations of ToF-SIMS is that being a high energy process, fragment ions are dominant in the resultant spectra rather than whole molecular ions. This means that higher levels of data processing are required to identify accurate chemical composition (Scurr et al., 2010). Furthermore SIMS chemical images have the capacity to have generated a complete ion spectrum per pixel point (e.g. 256x256 pixels per image). This may amass to millions of spectra on an ion mass by ion mass basis, generating a vast hyperspectral data pool for analysis. This is complicated further with the fact that as a consequence of the low primary ion count and reduced acquisition times static SIMs employs to reduce surface degradation, there is often a low signal to noise ratio (Krzanowski, 2000). This means that with increasing spatial resolutions there is a decrease in available ion signal, and that noise from the counting statistics of the detector become much more significant (Lee, Gilmore, 2012). As a consequence, univariate analysis of this mass of subtle data, where each variable (secondary ion mass in this instance) is treated independently and analysed separately becomes very complicated and hugely time consuming. It is very easy for small chemical features that may still have great importance to be missed. Hence a multivariate approach to analysis is often employed in order that such data, with a huge number of dependent variables, can be considered in its entirety and then summarised using a smaller number of statistical variables. This has the benefit of allowing for a simpler, more rapid and holistic interpretation of the results (Lee, Gilmore, 2012).

In essence multivariate data analysis is a tool of chemometric pattern recognition, and can be described as organising results into groups based on their position within a multivariate dataspace (Belu et al., 2003). This is achieved by using matrix mathematics to arrange the

variables of a given set of experimental measurements, and then vector mathematics to describe these arrangements into a multidimensional graphical model (Krzanowski, 2000). It is then possible using one or several of a range of specifically chosen multivariate approaches (e.g. principal component analysis, multivariate curve resolution, maximum autocorrelation factoring etc.) to attempt to describe these modelled matrices in terms of 'factors', or directions in the virtual dataspace that account for the original dataset (Lee, Gilmore, 2012). Further statistical techniques can in turn be employed to calibrate, quantify and or cluster the datasets as per the desire of the experimental set up, but in basic terms all such algorithms will look to identify and summarise relationships between the multivariate data sets.

2.3.2.3 Principal Component Analysis (PCA)

Principal component analysis (PCA) is one form of factor analysis that tries to find the directions of greatest variation in the multivariate space defined by the data. As with other types of factor analysis it is employed to reduce the matrices of data to their lowest meaningful dimensionality, by describing them with the smallest number of factors, or 'principle components' possible (Lee, Gilmore, 2012). These directions are then used to define a new set of axes that explain how the samples and variables relate to each other, i.e. picking out the variates that correspond to the greatest degree of variability between data sets. Consequentially samples that are diversely spread along these new axis show less similarity than those that are grouped together with respect to that principal component (Belu et al., 2003). Figure 2.9 shows an example graphical representation of PCA, where data for 28 samples over two variables (x_1 and x_2) has been described by two principal components (PCA 1 and PCA 2). PCA 1 describes the factor with the greatest variance, and PCA 2 is orthogonal to PCA 1 and picks up the largest remaining variation (Lee, Gilmore, 2012). In this fashion, it is possible to redefine the samples along the 'new' axes in the data space by the principal components, and thereby determine the key contributions to the co-variance of the data. However whilst PCA can be used in its own right to look for trends in data variability, it is often used as a 'pre-processing' tool as a means of data reduction. As we infer higher and higher factors, it is possible to discard those that show the least variance as variability due to noise. This has a positive impact on analysis as it will reduce the dimensionality of the data, thereby reducing the expression of highly correlated and theoretically less desirable data trending (Krzanowski, 2000).

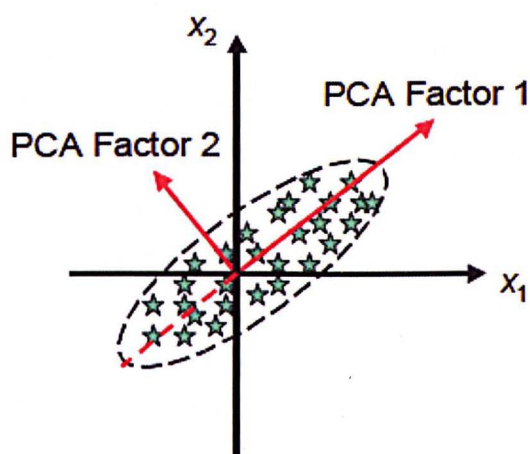


Figure 2.9: 2D representation of a principal component analysis (PCA) (Lee, Gilmore, 2012)

For example if we consider figure 2.9, we can ask whether it is necessary to describe the data in terms of the two factors (PCA 1 and PCA 2), or rather if the scatter observed is due to experimental noise. If the latter can be deduced or assumed, then the information in PCA 2 can be discarded and all the relevant chemical data can be provided by the projection of the data onto PCA 1. This is of benefit, as data that originally contained two variables can now be described by one factor and the most influential samples identified or the compacted data passed on for further modelling. As such PCA is a tool that can have a significant benefit if run before subsequent image analysis techniques like multivariate curve resolution in defining the number of factors to model for (Rao et al., 2012).

2.3.2.4 Multivariate Curve Resolution

While PCA factors describe variance within a hyperspectral dataset, they can sometimes be difficult to interpret and may not necessarily describe chemical images in particular, with any desirable pattern. This is because while the technique identifies combinations of chemical spectra that reflect the correlations and anti-correlations of a variety of components across the image, certain chemical components may be projected onto multiple factors and therefore become difficult to categorise entirely. Multivariate curve resolution (MCR) is another multivariate data processing technique that is of more particular use in the analysis of hyperspectral ToF-SIMS images (Scurr et al., 2010). With particular reference to SIMS spectra, it

assumes that each spectrum can be described as a linear sum of contributions, (MCR scores) from individual chemical components, each associated with a given spectral profile (MCR loading). While this is by no means guaranteed in a ToF-SIMS environment, as there are many other influences on ion peak position and intensity besides chemical composition, MCR does have the benefit of being able to resolve, identify and localize original chemical spectra from a multi-component mixture where very little is known about the composition. (Lee, Gilmore, 2012). The technique uses an 'iterative least squares' algorithm to extract solutions, while applying particular constraints, most notably one of non-negativity. This particular constraint applied to the loadings and scores matrices, ensures the MCR solution obtained better resembles the raw SIMS spectra, which has to return positive values. Consequentially MCR does not require the projected factors to be mutually orthogonal in the same way PCA does (Lee, Gilmore, 2012). Figure 2.10 shows a 2D representation of a MCR solution and it can be seen that all of the samples can be described by a positive mixture of the MCR factors MCR 1 and MCR 2, which themselves are positive descriptors of the original axes x_1 and x_2 .

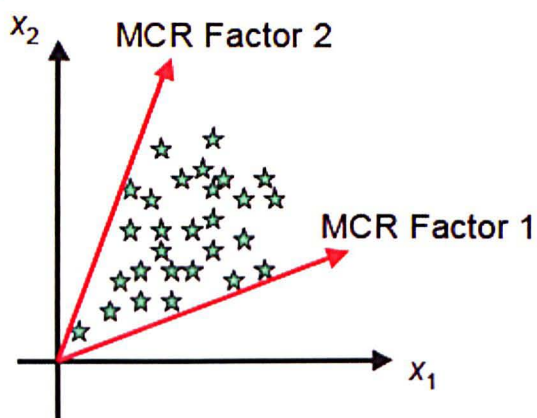


Figure 2.10: 2D representation of multivariate curve resolution (Lee, Gilmore, 2012)

These attributes make MCR a very useful tool in chemical image analysis, to pull out individual chemical contributions with respect to a given topography. However it should be borne in mind that MCR is a much more computationally demanding technique than PCA. And unlike PCA, MCR solutions are not unique for each data set, and are strongly open to bias from the initial user defined estimates, constraints and other pre-processing criteria. The accuracy of the MCR solution relies upon pixels or samples with contributions from only one chemical component,

and as a consequence peaks for intense components may appear in spectral profiles resolved for weaker contributors (Lee, Gilmore, 2012). However, the technique if appropriately controlled, offers the capacity to define the variation in components of a chemical map with respect to the localization of constitutional secondary ions involved i.e. map the key chemical variations across a topography of interest.

2.3.3 Raman Spectroscopy

Raman spectroscopy is utilised to describe the unique vibrational modes of molecules, generating a specific fingerprint spectrum through which the molecule or compound can be identified. While capable of simply generating individual series of spectra for identification and comparison, it also has the capacity in newer devices, to be used hyperspectrally as a chemical mapping tool in the analysis of a material surface. The flexibility of the Raman set up can allow the technique to model either general or site mapped changes in vibrational behaviours relating to numerous variables, principally (to date) temperature and time dependent stability, particularly with respect to phase and crystallinity changes.

The technique monitors the interaction between a defined monochromatic light source, and the molecular vibrations of the material being analysed. In essence the technique is based upon the 'inelastic' interaction between a photon and a molecule causing the returned photon to have gained or lost a vibrational quantum of energy (Larkin, 2011). More specifically a given molecular vibration can be excited by a given frequency of incident light to a higher virtual energy state by absorbing some of that light (M.Pelletier, C.Pelletier, 2010). This higher energy state will (almost always) relax back to a lower energy state, but while this is usually elastically to its original energy state (Rayleigh scattering), it may also be to a different vibrational energy level (Raman scattering) generating the release of a photon with an altered frequency to its incident state (Larkin, 2011). Figure 2.11 highlights the different potential changes in energy state in the differing scattering processes:

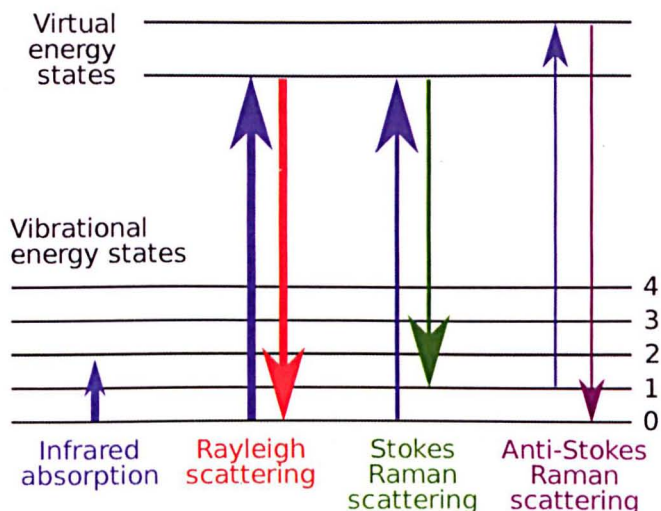


Figure 2.11 Possible energy state changes of the different scattering processes

Rayleigh scattering is much more common place than Raman scattering and the scattered intensity is about 10^{-3} less than the incident radiation (Larkin, 2011). It is considered elastic because there is no change in energy i.e. occurs at the frequency of incident radiation. Raman scattering however, is less common, with a scattered intensity of about 10^{-6} less than the incident radiation (Larkin, 2011). As figure 2.11 shows, there are two types of Raman scattering, Stokes and Anti-Stokes. Stokes Raman scattering, produces photons with lower energies than the incident photons, as a consequence of a relaxation to a higher than previous vibrational energy level. Anti-Stokes Raman scattering produces photons with increased energies than those from the light source, due to relaxation of the vibrational energy level to one lower than the previous (M.Pelletier, C.Pelletier, 2010). While both are important and measurable, the proportional ratio of Stokes to Anti-Stokes scattering is dependent upon the temperature and energy difference between the ground and excited energy states of a sample. In general Stokes scattering is most often explicitly measured as it usually exceeds Anti-Stokes scattering. This is because most samples are analysed at ambient temperatures with molecular vibrational modes at a ground state and less likely to subsequently loose energy by relaxation to a lower energy state. Subsequently, a Raman spectrum is built by measuring the changes in photon energy between incident and scattered light by plotting the scattered light intensity against the shift in light frequency and wavelength (the Raman shift). Stokes scattering will give rise to reductions

in frequency that can be related to the specific molecular vibrations in the compound being analysed, which can then be solved to identify or characterize the material.

A Raman system will usually consist of one or several monochromatic light sources (lasers), ranging from the ultraviolet (UV), visible (Vis) or near-infrared range (NIR) to offer a variety of incident wavelengths. These laser sources will be transmitted to the sample via an optics system, sometimes containing a series of optical filters and pinhole apertures to further refine the incident wavelength and illumination volume. Most systems will use an optical microscope to deliver the radiation to the sample and also collect the backscattered Raman light. Dielectric interference filters or holographic notch filters are often used to remove the Rayleigh scattered light from the detection signal before the filtered light is presented to light dispersion or frequency isolation devices and then the detector (Nelson, Treado, 2010). Raman spectroscopy has several key features as a chemical mapping apparatus. Notably it is a non-invasive process that does not require any special sample preparation, and although shorter wavelengths of incident light can sometimes cause energetic damage to a sample, astute choices of laser and exposure times allow even biological samples to be run in an instrument. It can be run in a wide range of conditions (i.e. temperature humidity and pressure), or indeed with the appropriate sample holders/chambers while varying these parameters for real time data collection. Background species such as water or carbon dioxide will not interfere with spectra as their Raman signal is very weak (Nelson, Treado, 2010). Finally by having a motorised stage it is possible to 'step by step' analyse a given topography, and generate a hyperspectral image of a sample, that can then be mapped according to already known pure spectra, or to those identified in the analysis. Theoretically the spatial resolution of the Raman instrumentation could be the wavelength of the incident light.

Raman spectroscopy does have weaknesses in use as mapping tool however. Firstly very high spatial resolutions are not always easily possible for a multitude of reasons. In attempting to generate a hyperspectral chemical map of a surface, a spectrum will be gathered at every specified period across the chosen image area. In most cases sample topographical analysis is often macroscale, and therefore attempting to analyse large areas with an attempted spatial resolution under $1\mu\text{m}$ would lead to huge numbers of spectra, that because of the slow (relative) speed in analysing the scattering spectrum can lead to long mapping times. Similar to the processing of ToF-SIMS data, even once achieved, this is very time consuming and difficult to

analyse univariately, although multivariate analysis can be applied. Raman microscopes also require the sample to be in the vertical focus of the microscope lens delivering the radiation. This incurs two problems, firstly, significant surface topography requires repetitive realignment of the lens relative to the surface to maximise focus. While this can be achieved by using the Raman signal as a basis for automatic or manual alignment, this again can significantly prolong a mapping procedure. While mapping speeds can be increased by reducing exposure times and repeat measurements, this leads to an increase in signal to noise ratio and susceptibility to anomalous feedback, and it is this that will determine image quality, not spatial resolution. Also because a microscope lens is used, if large mapping periods are required and automatic alignment is not used, focal drift can occur which can have a significant impact upon the Raman signal feedback. Finally but probably most significantly, Raman spectroscopy can suffer from significant interference from fluorescence (M.Pelletier, C.Pelletier, 2010). While originating from a different mechanism than Raman scattering it can occur at the same time, and the broad and intense nature of the phenomenon can easily dwarf the Raman signal obtained if it occurs in the same spectral window. While most fluorescent effects occur in the near-UV to visible range, moving to the NIR region can eliminate the effect, but as Raman intensity is proportional to the fourth power of the laser wavelength, this comes with a consequent reduction in Raman signal and therefore an increase in acquisition time. Furthermore in the NIR region the typical silicon CCD detectors show a reduction in detection efficiency.

2.3.4 Scanning Electron Microscopy

Scanning electron microscopy (SEM) is an imaging technique used to visualise sample surfaces with high depth of field and lateral resolutions of around 1-20nm (Butt et al., 2003). A fine beam of electrons is used to scan across the specimen surface in synchronism with the spot of a display cathode ray tube (CRT) (Chescoe, Goodhew, 1990). Unlike its sister instrument the transmission electron microscope (TEM) where electron transmission through the sample is analysed, SEM monitors the intensity of a chosen secondary signal consequent to the interaction of the primary electron beam on the sample surface. Such secondary signals may be in the form of secondary electrons, backscattered electrons, Auger electrons, cathodoluminescence or even x-rays, depending upon operational desires. However the

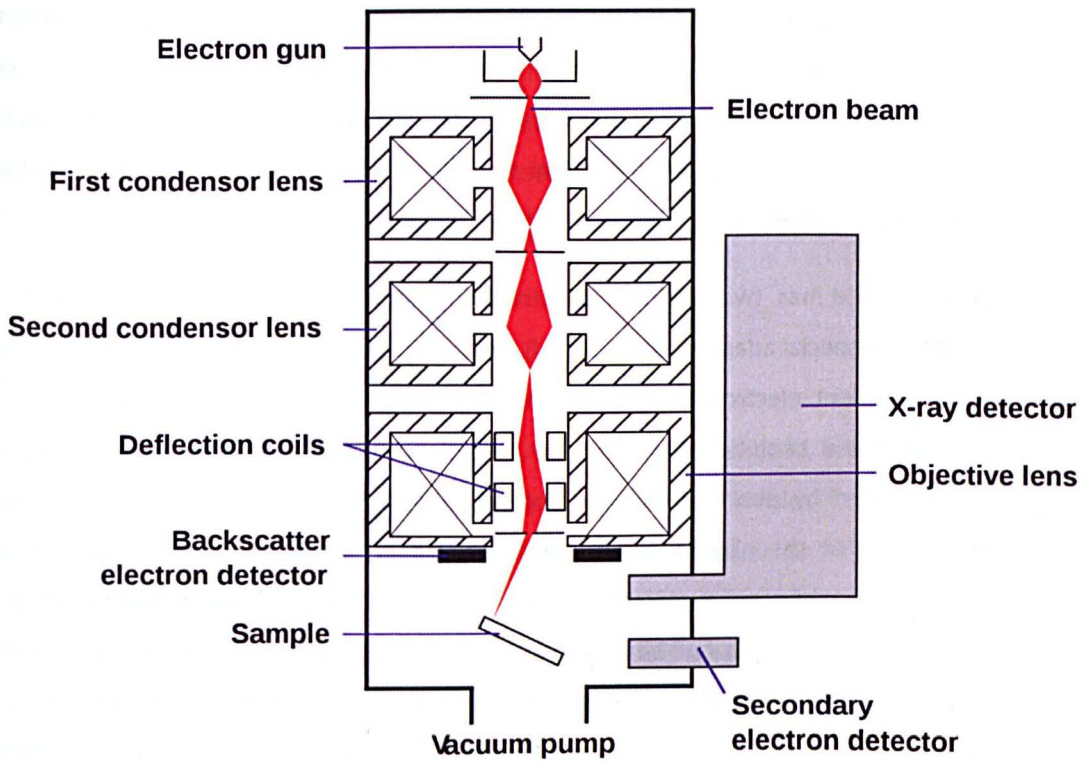


Figure 2.12 Schematic of a scanning electron microscope

principle remains largely the same, that if the intensity of emitted secondary signal changes across the specimen, then the contrast is seen by adjusting the brightness of the CRT spot by the amplified version of this detected signal (Watt, 1997). Figure 2.12 shows a basic schematic of an SEM system. In SEM the primary electron beam may be emitted thermionically from a heated filament tip within an electron gun. Tungsten, lanthanum or cerium hexaboride filaments are heated to exceed the surface potential of the constitutional metal, increasing the ioncore vibrations and inducing increasing electron collisions (Chescoe, Goodhew, 1990). Alternatively field emission gun (FEG) sources are also in use, where a strong electric field is used to extract electrons from a metal filament. In both cases electrons will be given off by a filament, and can in turn be accelerated (10 – 400 kV) towards and through an anode to the condenser system of the microscope. Here using multiple lenses (usually three) the microscope first varies the strength of illumination in the specimen plane to suit the sample and magnification desired and then focuses the suitability diminished electron beam to the sample surface (Watt, 1997). The

secondary ions produced by the primary electron beam raster, are usually collected by a cathode biased Everhart-Thornley scintillation secondary ion detector (Chescoe, Goodhew, 1990). This in conjunction with a subsequent photomultiplier reconverts the created light impulses to an electrical signal that can then be displayed versus the position of the primary beam on the sample surface (Watt, 1997).

Critically SEM has two principal constraints. Firstly it must be carried out under vacuum conditions (special adaptations excluded). This is because it is essential to prevent gas scattering of the incident electron beam travelling from the electron gun to the specimen. It is also because these conditions prevent the specimen, apertures or the electron gun becoming contaminated by debris in the microscope column (Hayat, 1974). Secondly, it is typically necessary that the objects being imaged are conductive at the surface; otherwise electric charging can take place as electrons are unable to dissipate under the incident beam (Butt et al., 2003). This means that non-conductive or poorly conductive surfaces are often coated with a thin layer of metal, usually gold or carbon, to enable improved sample visualisation and imaging. However whilst this process allows for superior SEM imaging to take place without charging, it is a destructive process that prohibits the subsequent use of the material after imaging, and can in itself lead to topographical artefacts that may show up upon imaging. It is however possible with newer SEMs to operate the microscope in what is called a 'low voltage' mode. Here the beam voltage is decreased to the equilibrium point where no charging will occur. In this fashion charging is avoided and less conductive materials can be imaged without coatings. However this comes at the cost of a reduced secondary ion count and a reduction in spatial resolution. Some SEMs (Environmental SEMs) have the capability to image while using low gas pressures (~30 mbar) in the sample chamber. This allows less-conductive surfaces to be visualised without metallization, as positively charged gas ions neutralise excess negative charge that would otherwise build up at the surface (Butt et al, 2003).

The SEM's spatial resolution is dependent directly upon the spot size of the incident electron beam which in turn depends upon the electron beam wavelength and the interaction volume of the beam and sample (Hayat, 1974). The smaller the spot size the better the potential instrumental resolution, but as a consequence beam current will also decrease, reducing the production of the secondary signal (secondary electrons etc.) and increasing noise (Chescoe, Goodhew, 1990). While it is therefore possible to image to around the nanometre scale, this is

not often easily achievable, and unlike the TEM where shorter more penetrative wavelengths can be used and atomic resolutions become a possibility, this is unachievable with an SEM. However because secondary ions are low energy (~20eV) it is only those from the top layers of the specimen that can escape for detection, making SEM a very surface specific imaging tool (Butt et al., 2003) capable of imaging bulk materials.

2.3.5 Andersen Cascade Impaction

The use of an Andersen Cascade Impactor (ACI) has been described briefly in chapter 1. As already stated an ACI is one the most widely used means of inhaled formulation deposition analysis, particularly from pMDI formulations. It can be considered an '*in-vitro*' airways model that evaluates formulation performance in terms of aerodynamic particle sizing. An ACI consists of a stack of eight separate stages, each with precisely calibrated nozzle of diminishing size and area, as the stack progresses down. Each stage is removable, but on assembly they are all sealed with O-rings and clamped together, with inserted impaction plates 80mm in diameter below each grating. The topmost stage is attached via a pre-separation jet stage to a 'throat' induction port that loosely reflects the induction geometry of the upper airways. The base of the ACI possesses an outlet to which a vacuum pump can be attached. A schematic of a complete eight stage assembled ACI is shown in figure 2.13. The working principal is relatively simple. As a vacuum pump draws air through the whole ACI stack at a predetermined airflow rate, a pMDI (or DPI with some technical changes to the set up) is actuated into the impactor via a mouthpiece adapter. The aerosolized formulation contents will pass into and down the ACI, with material impacting throughout the whole system. As the particles pass further down the ACI stack they are forced to pass through smaller and smaller gratings, thus separating out the particles by size discrimination. Figure 2.14 highlights this principal.

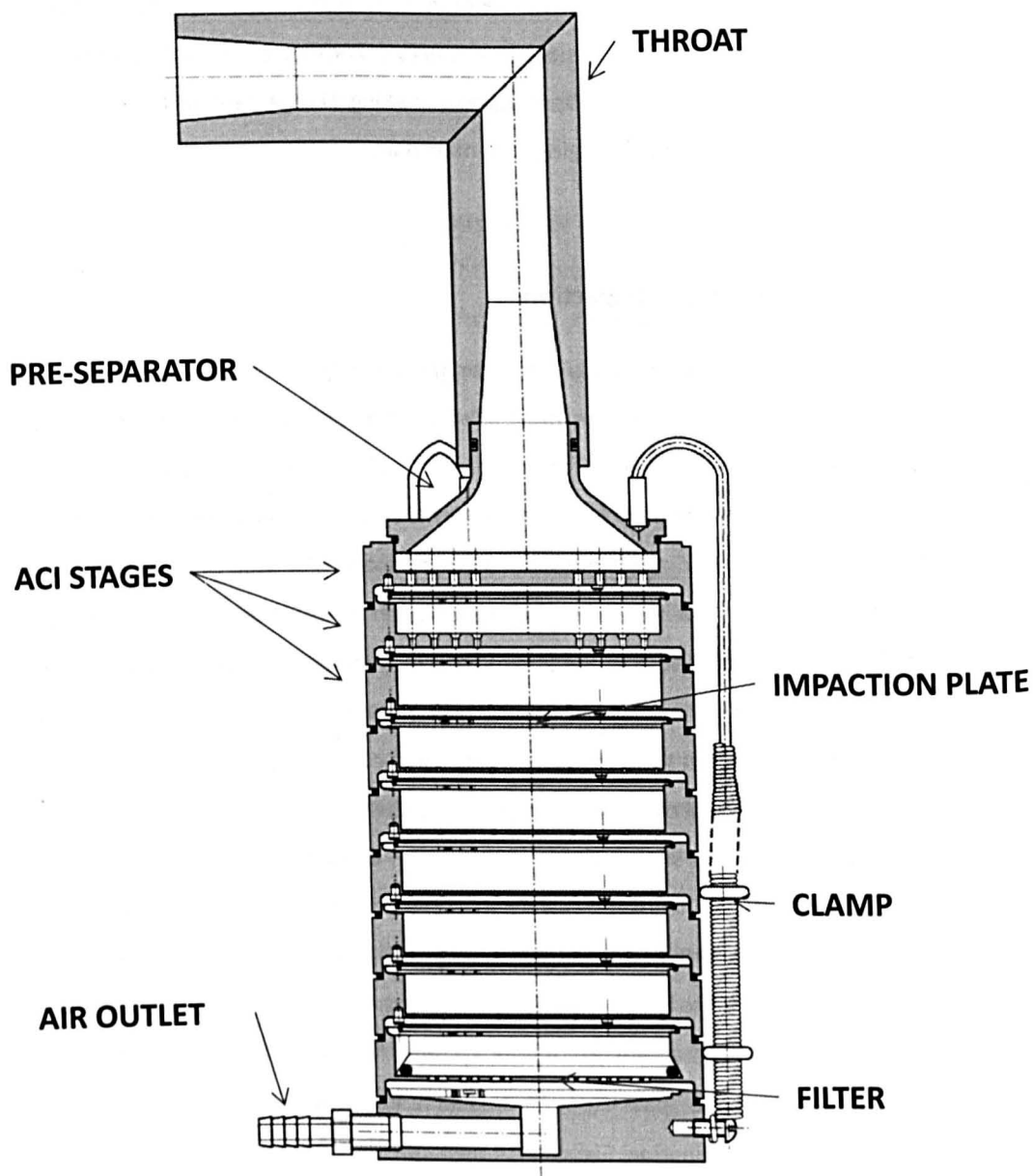


Figure 2.13 Schematic of an Andersen Cascade Impactor (European Pharmacopeia, 2012)

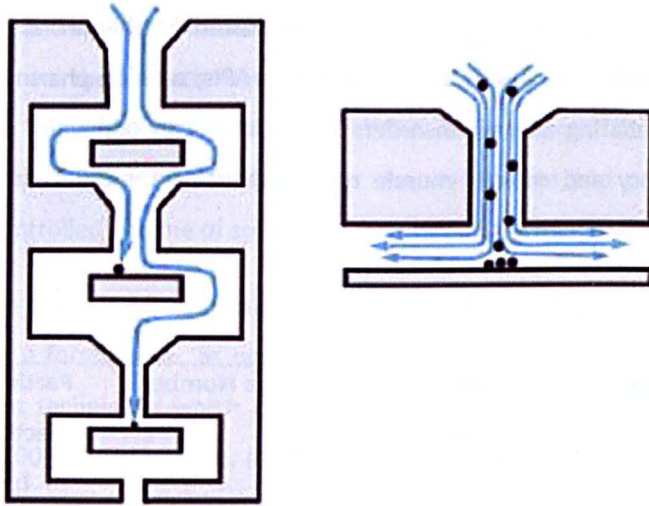


Figure 2.14 Aerodynamic particle separation in an ACI (Copley Scientific Ltd)

More precisely, for particles to impact on a plate they must have enough inertia to break from the travelling airstream. This can be explained by considering that when the direction of airflow changes, i.e. as when moving over an impaction plate, aerosolized particles will continue to move in the original direction of flow unless they lose inertia due to friction with the travelling gas molecules (Hickey, 1992). Because particle inertia is a function of particle density, shape and velocity, larger particulate masses will have sufficient inertia to escape from the airstream earlier than smaller particles, which must pass to lower levels with higher nozzle airstream velocities (Copley, 2008). Because at each stage, nozzle size and area decrease while total volumetric airflow remains constant, each subsequent nozzle airstream becomes more rapid as more air is forced through less spacious and numerous pathways. Therefore smaller particles that have less inertia higher in the stack will continue to relax into the airstream until they eventually pick up enough velocity to carry sufficient inertia to impact. Consequentially particles of larger aerodynamic diameters will impact on plates further up the ACI stack, while smaller particles may progress further down the stack before impacting on lower plates. In this fashion the ACI functions as a rough 'in-vitro' model of the progressing human airways. By subsequently removing each ACI stage and impaction plate it is possible to quantify the amount of material impacted on each surface. As each stage has a calibrated nozzle diameter this provides a

deposition profile of the formulation which reflects the aerodynamic particle sizing of that formulation post-actuation. As already indicated in chapter 1, this parameter is critical in influencing the clinical efficacy of inhalation APIs, as such pharmacological agents are of little use in combating airways disorders unless they can reach the deeper airways to modulate inflammatory and smooth muscle tone responses. Table 2.1 shows the standardised nozzle diameters used in an ACI.

ACI Stage	Nozzle Diameter (mm)	Nozzle Number	Particle Size Collection Band (μm)	Equivocal Airway Location
0	2.55 ± 0.025	96	9.0	Upper airways
1	1.89 ± 0.025	96	5.8 – 9.0	Upper airways
2	0.914 ± 0.0127	400	4.7 – 5.8	Pharynx
3	0.711 ± 0.0127	400	3.3 – 4.7	Trachea and primary Bronchi
4	0.533 ± 0.0127	400	2.1 – 3.3	Secondary Bronchi
5	0.343 ± 0.0127	400	1.1 – 2.1	Terminal Bronchi
6	0.254 ± 0.0127	400	0.7 – 1.1	Alveoli
7	0.254 ± 0.0127	201	0.4 – 0.7	Alveoli

Table 2.1: Standardized ACI stage definitions

As such, good formulation performance will see significant deposition on plates 4, 5 and 6. Poorer formulation performances will see increased deposition on the higher plates, or even on

the inhaler device, and pre-separation stages. Nano-scale residual matter may pass through all the stages and plates and is collected on a filter at the bottom of the stack. The ACI is not able to give real time data on the impaction of the formulation however, and analysis requires disassembly into the individual components and plates, before some form of quantification. Most usually this is via a variation of HPLC, after the wash down and perturbation of each component with a controlled volume of solvent.

The main advantages of compaction testing are that that it offers a specific means to quantify the API alone within a formulation, as opposed to techniques such as laser diffractometry or particle time of flight techniques which cannot differentiate between the API and accessory excipients (Copley, 2008). Furthermore, inertial impaction techniques should collect the total aerosolized dose across the experimental system, and therefore allow a user to investigate the localisation of an entire actuation. The technique also provides quantification of aerodynamic particle diameter which is much more pertinent than the calculated volume equivalent diameter which is often the measurement made by other techniques. There are issues with the ACI however, primarily the labour intensive nature of the technique. Automation of the apparatus is very difficult, and therefore manual operation is often necessary, and it may require a day's work just to deposition test four or five formulations. Furthermore nozzle damage or wear can lead to a significant impact on deposition performance as it upsets airflow dynamics. While stage mensuration is performed regularly in the pharmaceutical industry to validate nozzle parameters, it is undeniable that the whole concept of inertial impaction is dependent upon the calibration of the ACI apparatus, and any deviation will bias results. It is also worth highlighting that while the technique is often considered as an '*in-vitro*' lung model, it is actually far from representative. There is no accommodation for the principal variants of humidity, temperature changes, and flow rate variability that are significant factors '*in-situ*' inhaler use. However this should not be considered a critical shortcoming, as the facility to identify aerodynamic particle diameter remains a significant tool in assessing the promise of a inhalation formulation (and device).

The ACI in particular was designed for testing of pMDIs at a standardized flow rate of 28.3 L/min and therefore is suited particularly for work with this inhaler type. DPI testing with an ACI is less frequent as the requisite higher flow rates (~60 L/min) requires modification of the device, but is still possible. Other variations on impactors do exist, such as the more modern Next Generation

Impactor (NGI) and Multi Stage Liquid Impinger (MSLI). Each has its own benefits and drawbacks but the standardisation of the ACI by both the United States Pharmacopeia (USP) and European Pharmacopeia (EP) for inhalation formulation testing has made it a rock bed of regulatory and therefore investigatory testing.

2.3.6 High Performance Liquid Chromatography

High-performance liquid chromatography (HPLC) is a technique used for the quantitative analysis of drug formulations. As a chromatography procedure HPLC relies on the controlled separation of chemical mixtures. The technique begins with a liquid mobile phase, pumped at pressure through a small diameter column (3-10 μ m) filled with a specific stationary phase. The analyte of interest is passed through the column after injection into the mobile phase and separation of the mixture occurs according to the relative ease of progression of the analyte components through the stationary phase. The column elute is then analysed by UV spectroscopy (or other means) and the peaks corresponding to the constituents of the mixture can be solved and quantified according to their separation as function of run-time (Watson, 2005). Figure 2.15 shows a schematic of a basic HPLC set up and an example chromatogram.

The progression an analyte through the HPLC column is dependent upon the physicochemical properties of the solute in relation to the stationary phase and the environmental conditions (Lough, Wainer, 1996). There are several different separation mechanisms that HPLC can employ. Common variations include, normal phase liquid chromatography (hydrophilic stationary phase with non-aqueous mobile phase), reversed phase liquid chromatography (hydrophobic stationary phase with a polar aqueous mobile phase), ion-exchange liquid chromatography (charged stationary phase for charge based separations) and size-exclusion liquid chromatography (stationary phase based pore size exclusion of analyte). Tailored to the separation mechanism employed, a variety of other variables can be altered to best separate and define a pharmacological compound including mobile phase composition and flow rate. The mobile phase is normally pumped through the column at flow rates of between 1-10ml/min, and if the composition of this phase is kept constant then the method is termed 'isocratic'. However it is possible to alter the composition with time to generate a 'gradient' elution, if retention times of the various components in an analyte would otherwise show dramatically

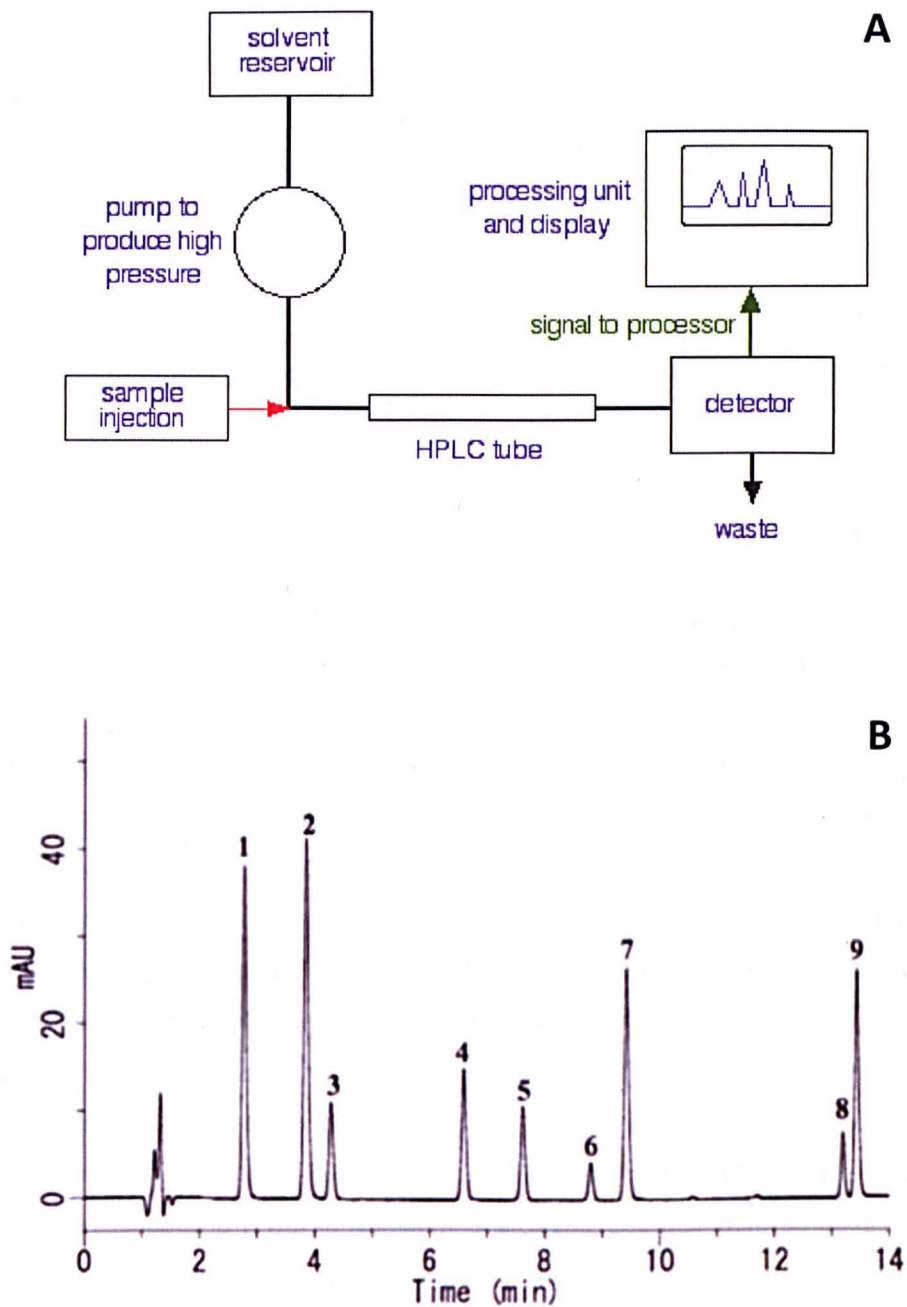


Figure 2.15 A) Schematic of HPLC apparatus and B) an example chromatogram

different retention times i.e. by increasing the polarity of a solvent during normal phase liquid chromatography to speed up the elution time of polar solutes (Lindsay 1992). HPLC is a readily automated process that allows for a very precise and controlled sample introduction which in turn ensures quantitative precision. With a variety of column types and easily adjustable flow and environmental conditions it has a wide application in pharmaceutical quantification. However there is the prerequisite that samples be extracted from their formulation prior to analysis i.e. into solution, which rules out an 'in-situ' or as received measurement of inhalation products. Furthermore to best elucidate the quantities of multiple components of increasingly complex chemical mixtures requires more and more significant method development.

2.3.7 Desorption Electrospray Ionization Mass Spectrometry

Desorption Electrospray Ionization Mass Spectrometry (DESI) is a mass spectrometry technique where either solid or liquid samples can be ionized under ambient conditions without any special sample preparation. The technique is based around the use of an electrospray emitter to generate a cloud of charged microdroplets of a chosen solvent. This is in turn directed by a high velocity gas jet at a surface of a sample of interest. Subsequently the molecules at the surface of the sample are desorbed and ionized before being desolvated and drawn up into a mass spectrometer (Chernetsova, Morlock, 2011). This principle is highlighted in figure 2.16. The facility to raster the sample stage, allows that the technique be employed to produce a chemical image map of an untreated or unaltered surface area. Similar to ToF-SIMS mapping analysis, a hyperspectral image can be generated as the electrospray is directed across the sample surface, from the mass spectrometry data. However the technique does suffer limitations in a role as an imaging tool. Its predominant use has been in bioanalytical work with a heavy emphasis on method development and small signal mapping. In terms of broader pharmaceutical research there are some barriers to its use. Fundamentally due to the nature of the technique being based around incident solvent droplets, there are several issues relating (particularly) to the surface desorption process. Firstly electrospray generation may obliterate the analytical surface (i.e. pharmaceutical powders) via the inert gas propulsion or simply via extensive solvent

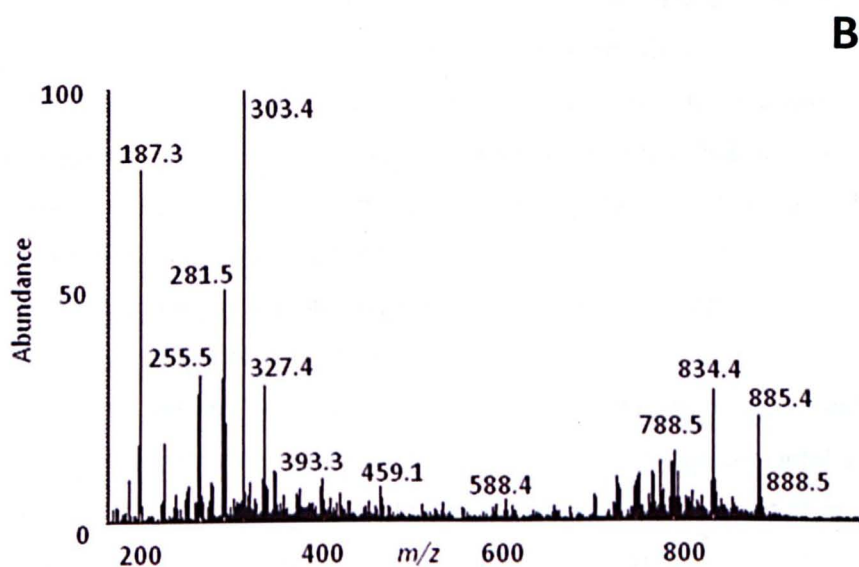
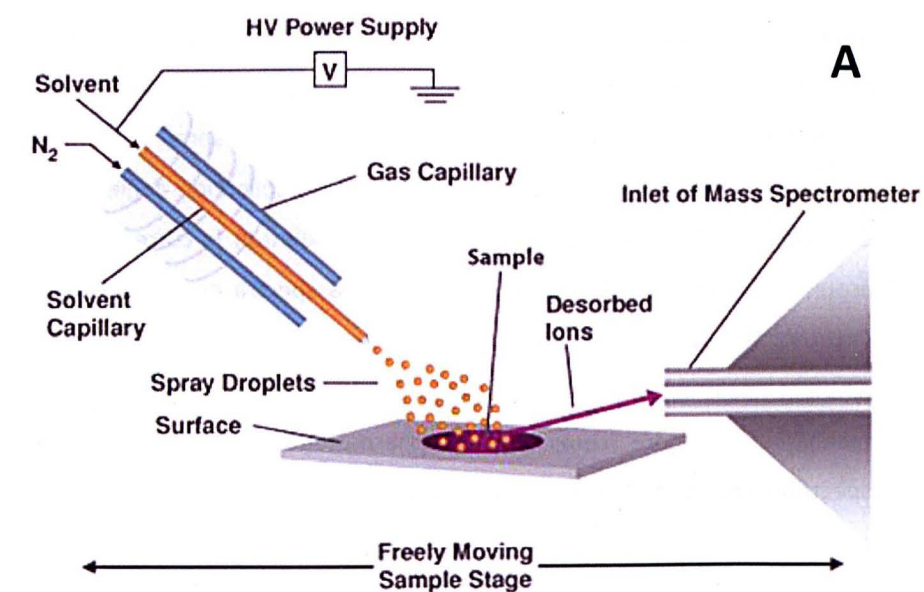


Figure 2.16 A) Schematic of DESI in operation (Prolisa Inc.) and B) an example point mass spectrum (Rao et al., 2012)

desorption. The technique can be tailored to try and reduce this effect, and with method refinement samples may only lose subnanogram amounts. But more problematic is the consistency of the desorption process. There is a heavy dependence of electrospray dynamics on numerous experimental variables (solvent choice, spray to sample distance, sample to spectrometer distance, gas pressure, spray angle, collection angle and solvent flow rate etc.). One particular consequence is that spatial resolution is currently not capable of exceeding around 200-250 μ m at best, and that the mass spectra produced may differ unpredictably by virtue of the electrospray to surface interactions (Chernetsova, Morlock, 2011). However an ambient mass spectrometry mapping facility can be seen as very useful complimentary technique to more commonplace pharmaceutical analytical methods such as Raman spectrometry, atomic force microscopy and ToF-SIMS.

2.3.8 Differential Scanning Calorimetry

Differential scanning calorimetry (DSC) is a thermoanalytical technique used to identify changes in the physical state of a material by its concurrent release or absorption of heat. It is a useful tool in looking at the phase transitions a material undergoes, as a means of event qualification or indeed quantification (enthalpies). It can be applied simply to look for differences in sample to sample behaviour, or in more sophisticated fashions to investigate very subtle physical changes and material behaviours. Modern differential scanning calorimeters function by measuring the differential heat flow required to maintain a sample of interest and an inert reference at the same temperature. The sample and reference are heated by different heat sources, and as a scanning temperature gradient is increased at a pre-determined rate, any differences in temperature between the two that develop as a result of exothermic or endothermic physical transitions (of the sample) are accommodated for by adjusting the heat flow to the sample to remove this difference. By plotting the difference between the heat flow to the sample and reference, against time or temperature a DSC thermogram can be produced (figure 2.17) that will identify the physical transitions the sample underwent through heating.

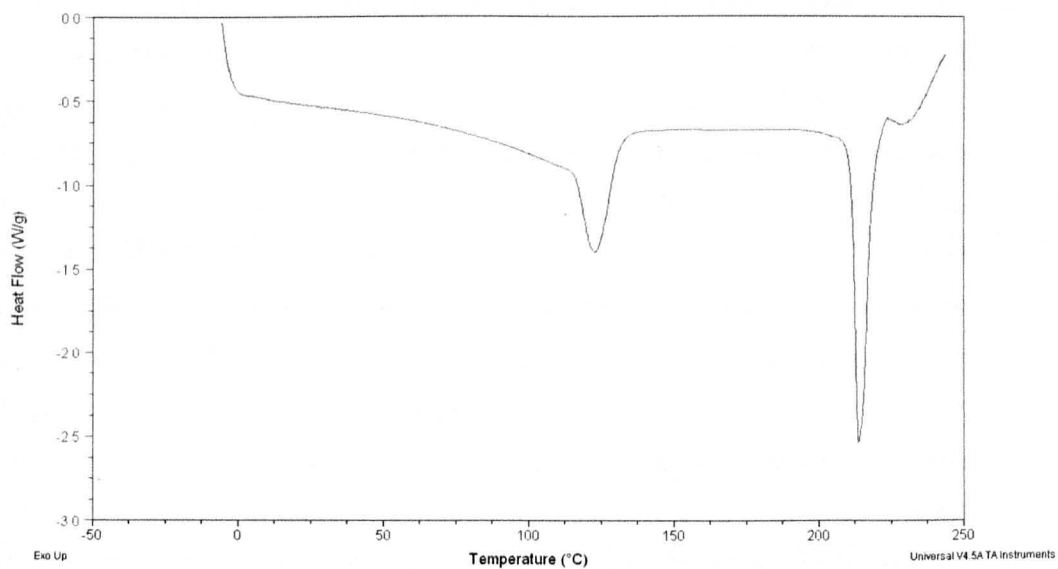


Figure 2.17: A DSC thermogram of Beclomethasone Monohydrate, showing the scanning differential heat flow adjustment to the sample with respect to a blank reference.

In this figure, endothermic transitions are observable as downward peaks and exothermic transitions would be seen as upward peaks. The temperature at which these peaks occur can be associated with phase transition events, such as the melting point of a substance, and it is possible to measure the enthalpy of these events. However more succinct changes in physical state can also be identified such as the molecular rearrangement of a material, for example glass transition and crystallization events, chemical reactions such as fusion reactions or decomposition behaviours such as desolvation etc. The reversibility of the events observed may also be investigated by cycling the temperature range through an event before cooling, and repeating the temperature ramp, and in so doing better defining the events under consideration.

2.3.9 X-Ray Powder Diffractometry

X-ray powder diffractometry (XRPD) is a technique that is employed to reveal detailed information about the chemical composition and often the crystallographic structure of pharmaceutical powders. X-rays are short-wavelength (0.01 to 10nm), high energy, electromagnetic pulses (waves). As such, they can be described as an oscillating electric field with a perpendicular oscillating magnetic field (Jenkins, Snyder, 1996). The oscillating electric field can couple to charged electrons surrounding atoms and cause them to accelerate (or sometime decelerate). If any of the incident energy is reradiated (as accelerated electrons decelerate according to quantum physics) scattering has occurred. It is possible to observe the diffraction of the incident X-rays as a consequence of scattering. If the scattering of photons is elastic in nature i.e. resultant photons are of the same energy as the incident photons (Thompson or coherent scattering) then it becomes possible to collect the scattered X-rays as a function of the angle of incidence (*theta*) and use this data to infer the chemical and crystallographic structure of a powder (Jenkins, Snyder,1996). Scattered waves from different atoms will interfere constructively or destructively depending upon the spatial arrangement between the scattering atoms and the wavelength of incident light. Highly organised crystal structures (i.e. 3D crystal lattices) with a series of parallel planes with material specific distances between them, will induce much more co-ordinated interference, subject to Bragg's Law, giving rise to a unique pattern of well-defined peaks as theta changes. As such it is possible to determine from the level of interference observed, the degree of ordered structure (crystallinity) but also from where these peaks occur as theta varies to infer the specific polycrystalline elements that define the unique form of the powder being analysed.

2.4 References

- R.Ashayer, P.F.Luckham, S.Manimaaran, P.Rogueda. (2004) Investigation of the molecular interactions in a pMDI formulation by atomic force microscopy. *European Journal of Pharmaceutical Sciences*; 21:533
- M.Belu, D.J.Graham, D.G.Castner. (2003) Time-of-flight secondary ion mass spectrometry: techniques and applications for the characterization of biomedical surfaces. *Biomaterials*; 21:3635-3653
- A.Brindley. (1999) The chlorofluorocarbon to hydrofluoroalkane transition: The effect on pressurized metered dose inhaler suspension stability. *Journal of Allergy and Clinical Immunology*; 104:S221-S226
- British Pharmacopoeia (2012) *British Pharmacopoeia Commission, London, UK*
- H-J.Butt, G.Karlheinz, M.Kapfl. (2003) Physics and chemistry of interfaces. *Wiley-VCH, Weinheim, Germany*
- E.S.Chernetsova, G.E.Morlock. (2011) Ambient desorption ionization mass spectrometry (DART, DESI) and its bioanalytical applications. *Bioanalytical Reviews*; 3:1-9
- D.Chescoe, P.J.Goodhew. (1990) The operation of transmission and scanning electron microscopes. Microscopy Handbook No.20. *Oxford University Press, New York, USA*
- M.Copley. (2008) Cascade Impactors: Theory, design and practical design for optimal testing. *Inhalation Magazine*; 1-5
- European Pharmacopoeia (2012) [viewed May 2012] European Directorate for the Quality of Medicines and Healthcare. Available from <http://www.edqm.eu>
- J.Grams. (2007) New Trends and Potentialities of ToF-Sims in Surface Studies. *Nova Science Publishers Inc. New York, USA*
- M.A.Hayat. (1974) Principles and techniques of scanning electron microscopy. Biological applications. *Van Nostrand Reinhold Co., Michigan, USA*

A.J.Hickey. (1992) Methods of Aerosol Particle Size Characterization. In: A.J.Hickey Pharmaceutical Inhalation Aerosol Technology; 219-253. Marcel Dekker INC, New York, USA

R.Jenkins, R.L.Snyder. (1996) Introduction to X-ray Powder Diffractometry. *John Wiley & Sons Inc., New York, USA.*

W.J.Krzanowski. (2000) Principles of Multivariate Analysis; A User's Perspective. Revised Edition. *Oxford University Press Inc., New York, USA.*

P.J.Larkin. (2011) Infrared and Raman Spectroscopy; Principles and Spectral Interpretation. *Elsevier, Waltham, MA, USA*

J.S.Lee, I.S.Gilmore. (2012) The Application of Multivariate Data Analysis Techniques in Surface Analysis. In: J.C.Vickerman, I.S.Gilmore. Surface Analysis: The Principal Techniques. 2nd Edition. *John Wiley & Sons Ltd, Chichester, UK*

S.Lindsay. (1992) High Performance Liquid Chromatography. 2nd Edition. *John Wiley & Sons Ltd, Chichester, England.*

W.J.Lough, I.W.Wainer. (1995) High Performance Liquid Chromatography; Fundamental Principles and Practice. *Blackie Academic & Professional, London, UK*

K.J.McDonald, G.P.Martin. (2000) Transition to CFC-free metered dose inhalers – into the new millennium. *International Journal of Pharmaceutics; 201:89-107*

S.J.M.Munroe, A.L.Cripps. (2007) Metered Dose Inhalers. *Encyclopedia of Pharmaceutical Technology*

M.P.Nelson, P.J.Treado. (2010) Raman Imaging Instrumentation. In: S.Sasic, Y.Ozaki. Raman, Infrared and Near-Infrared Chemical Imaging. *John Wiley & Sons, Hoboken, NJ, USA*

M.J.Pelletier, C.C.Pelletier. (2010) Spectroscopic Theory for Chemical Imaging. In: S.Slobodan, Y.Ozaki. Raman, Infrared and Near-Infrared Chemical Imaging. *John Wiley & Sons, New Jersey, USA. pp 1-20*

W.Rao, D.J.Scurr, J.Burston, M.R.Alexander, D.A.Barrett. (2012) Use of imaging multivariate analysis to improve biological and anatomical discrimination in desorption electrospray ionization mass spectrometry imaging. *Analyst;137:3946-3953*

Chapter 2 – Materials and Methods

D.J.Scurr, T.Horlacher, M.A.Oberli, D.B.Werz, L.Kroeck, S.Bufali, P.H.Seeberger, A.G.Shard, M.R.Alexander. (2010) Surface Characterization of Carbohydrate Microarrays. *Langmuir*; 26(22): 17143-17155

J.C.Vickerman, I.S.Gilmore. (2012) Surface Analysis: The Principal Techniques. 2nd Edition. *John Wiley & Sons Ltd, Chichester, UK*

D.G.Watson. (2005) Pharmaceutical Analysis. 2nd Edition; A Textbook for Pharmacy Students and Pharmaceutical Chemists. *Elsevier, Philadelphia, USA.*

I.M.Watt. (1997) The Principals and Practice of Electron Microscopy. 2nd Edition. *Cambridge University Press, Cambridge, UK*

3.0 Application of the CAB Approach to Inhalation Materials with 'Non-Ideal' Surfaces

3.1 General Introduction

3.1.1 Limitations of the Cohesive Adhesive Balance

The CAB approach, as highlighted in chapter 1, is subject to limitations in its analytical application to inhalation technologies. It cannot be forgotten that the CAB is based on AFM methodology and therefore suffers the same inadequacies which distort all AFM results such as drift, hysteresis, creep, etc. (Butt et al, 2005). However outside of experimental error, what can be considered the most significant limitation of the approach is the necessity for smooth (typically crystalline) surfaces to perform measurements upon (Jones et al, 2008a). The fundamental principle of the CAB approach demands that the surfaces of cohesion and adhesion should be morphologically identical. This is so that with the same particulate tip, the same geometry of contact is achieved across both surfaces and therefore the only remaining variable in force determination will be chemical attraction (Bekat et al, 2004a). The only way to ensure this has been to use crystalline material with validated surface homogeneity and surfaces not exceeding a root mean square roughness of 1nm (R_q). I.e. this negates the impact of geometry on particle-surface force interaction, and validates the CAB approach as a means of force quantification in an 'ideal' model but is problematic when applied to rougher surfaces and materials with multiple crystalline faces of different surface properties.

3.1.2 pMDI Formulation Topographies

Crucially such CAB methodology is not an accurate representation of particle morphologies '*in-situ*'. Firstly as described in chapter 1, real particles in inhalation formulations are typically micronized to generate a respirable particle size. As a consequence of the destructive nature of the micronization processes commonly used, there are generated many particles of high surface area, increased amorphous content, high surface energies and cohesive tendencies (Lohrmann et al, 2007). Importantly these resultant particles also exhibit significant topographical roughness. It is therefore possible that a CAB balance developed using model crystalline

substrates, may not be a realistic appreciation of a force balance '*in-situ*' because of the inherent lack of accommodation for the geometries of the particle-particle or particle surface contact regimes that are occurring. Secondly, the device materials used to house the inhalation formulations are of prime consideration when considering critical particle surface contacts in formulation. Poorly controlled adhesive interaction between the components of pMDIs, such as the API and device materials (valve components, metering chamber, canister walls etc.) or other excipients can lead to flocculation in suspension systems, crystallization in solution systems, and inappropriate respirable particle size upon actuation. (Begat et al, 2004b, Traini et al, 2006, Traini et al 2005, James et al, 2007, Eve et al, 2002). Equally within DPIs, uncontrolled interactions between a carrier particle and API may lead to heterogeneous powder mixing, poor dose uniformity or ineffective association/dissociation of the carrier and API on inhalation. Such problems have long been recognised by manufacturers of inhalation formulations and significant work has gone into first describing and then combating inappropriate interactions within formulations and between the formulation and delivery devices. Various techniques have been employed, and regarding the potential for device-formulation interactions, strategies such as canister wall coatings have been developed. The principle here is that a tough but chemically and electrically inert, smooth coating to the metalwork, will reduce interactions with the formulation components, reduce dose loss, and as a consequence improve dose reproducibility. One such example is the use of a fluorinated ethylene propylene (FEP) canister coating (3M Healthcare Ltd). In this instance the fluorocarbon derived polymer coating will show greater stability due to the many carbon-fluorine bonds (partial ionic character), and will be highly chemically resistant through a reduction in dispersive van der Waals forces. This reduction is due to the electronegativity of the fluorine atoms rendering the molecules much less susceptible to transient polarization and dipole formation. However, despite the performance improvements such coatings, or selective material components can offer, they remain macroscale surfaces, that are factory made and will never exhibit uniform surface roughness on a microscale equivalent to that of a molecular crystal face.

As such the CAB approach cannot be utilized in its purest form to model the force balances between APIs and inhaler components. It would be particularly useful if the model could be adapted from model pharmaceuticals to the materials that compose the device and formulation themselves. In such fashion the efficacy of various coatings and indeed other device materials

could be examined with respect to the cohesive-adhesive tendency of a particular API or excipient.

3.1.3 Interpreting data from Recrystallized Substrates

Being unable to account for the influence of contact geometry within the CAB approach is tolerated because a fundamental force balance based on chemical attraction can thereby be extracted from the materials in use. This should in principal be a constant driving factor behind the adhesive or cohesive interaction between two components. However beyond the disparity between real material surfaces and recrystallized model surfaces in terms of developing reproducible contact geometries, there is also the possibility that recrystallized API surfaces used to model API force balances can in themselves be misleading in deriving a 'true' force of adhesion or cohesion. Different crystal faces exhibit different surface energies depending upon the molecular orientation at that given surface (Muster & Prestidge, 2002). The presentation of these surfaces will depend upon the crystal habit of the material being processed, which is in turn known to develop depending upon a multitude of variables inherent to the recrystallization process such as the levels of supersaturation, level of impurities, crystallization process parameters (e.g., stirrer speed) and the solvents and antisolvents utilized in crystallization (Mullin, 2001). Of particular note Hooton et al. (2008) showed that by using two different solvents, N,N-dimethyl-formamide (DMF) and ethanol, two distinct habits of budesonide crystals could be formed. These two habits exhibited dominant faces of different molecular presentations, which in turn showed significantly different CAB ratios, although not rank affinities, when probed with a range of carrier APIs. The dominant face of the DMF solvated crystal exhibited a CAB ratio approximately twice that of the dominant face from the ethanol solvated crystal. Therefore it is apparent that the force balance acquired using the CAB approach and model crystal substrates may be very sensitive to the recrystallization process used to develop the substrates.

It would therefore be expected that AFM measurements on the different energy faces of model crystalline substrates could underestimate or overestimate the fundamental forces of cohesion and adhesion (Jones et al, 2008a). This has wider implications in that, as has been alluded to in several studies, the very handling of the tip material and substrate will in itself lead to changes

in the force measurements made. This may be through providing different crystal habits (Hooton et al, 2008) or any other chemical or physical difference (Jones et al, 2008b). Whilst the CAB technique has already proven that it is capable of deriving functional adhesive relationships that can be linked to '*in-vitro*' performance data in model systems, this is only of limited use if it cannot be applied to materials in a functional state. The assumption that a CAB approach has a prerequisite for molecularly flat surfaces, is justified theoretically, but what is not known is to what extent increases in surface roughness can be accommodated. Whilst a purely accurate chemical force balance description may not be generated if rougher surfaces are used, it remains possible that the a CAB plot might still hold true enough to imply a linear relationship that can function to describe the force balance in a 'non-ideal' formulation better than that from a recrystallized model system.

3.1.4 Clathrates

Drug particles in the presence of CFCs or HFAs, have a tendency to form clathrates over time within formulation (Phillips, Byron, 1994). Clathrates are solid solutions that occur through the hydrogen bonding of host molecules within a structure that, via the creation of cavities in the crystal lattice, are capable of encaging a variety of guest molecules (Englezos, 1993). They are considered an 'inclusion compound' where two molecular species have arranged themselves so that one entraps the other (Englezos, 1993). The host molecules hydrogen bonding forms a regular 3D network with repetitive cavities, while an appropriate guest molecule will occupy a cavity either completely or partially and contributes to the physiochemical nature of the compound (Plumridge, Waigh, 2002). Previous work into the stability and energetics of clathrates in inhaler formulations has identified that the clathration of propellant molecules within an API has led to greater thermodynamic stability of the compound and reduced surface energy (Bouhroum, 2009). This raises the possibility that certain clathrates may in fact be the most desirable polymorph for formulation development in inhaled products. Furthermore it is known that certain clathrates crystallize with large flat accessible surfaces e.g. Beclomethasone Dipropionate CFC-11 clathrate (Bouhroum, 2009). There is therefore interest and on-going work into the potential of clathrates in aerosol based formulation development, and significantly these molecular entities may offer an appropriate substrate for investigatory CAB studies.

3.2 Chapter Aims and Objectives

3.2.1 Chapter Aim

The aim of this chapter was to investigate the application of the CAB approach to a broader range of 'non-ideal' inhalation based products, including clathrated entities, assessing whether a useful force balance could still be generated and if the CAB approach would still hold true. In such fashion, to determine to what extent the approach can help better characterize interparticulate interactions within inhalation formulations on an API-API / excipient or API-component basis.

3.2.2 Chapter Objectives

The objectives of this chapter were as follows:

- To investigate the surface morphological properties of a common API, Beclomethasone Dipropionate, and two of its polymorphs; a CFC-11 and IPA clathrate
- To investigate the surface morphological properties of three key pMDI components; an FEP coated canister wall, an uncoated canister wall and the metering chamber.
- To investigate the force of interaction between the BDP APIs and the pMDI components.
- To determine whether the CAB approach can be applied to such as received 'non-ideal' micronized powders and inhaler components and generate a legitimate force balance.
- To assess the necessity for molecularly flat surfaces in validating the CAB approach.
- To characterize the structure and physicochemical behaviour of clathrated APIs

3.3 Materials and Methods

3.3.1 Materials

Beclomethasone Dipropionate (BDP) was chosen for use within this study due to its frequent use as an ICS in inhalation formulations and its known ability to clathrate in a variety of solvents. Micronized anhydrous BDP was purchased from Sicor (UK). The two solvents chosen for use were trichlorofluoromethane (CFC-11), supplied by Arkerma (UK), and isopropyl alcohol (IPA), supplied by Sigma-Aldrich Company Ltd (UK). These two solvents were known to generate inclusion compounds with BDP (Bouhroum, 2009). All other chemicals were purchased from Sigma Aldrich unless otherwise specified. The inhaler components used (uncoated aluminium canisters, fluorinated ethylene propylene (FEP) coated aluminium canisters and stainless steel metering chamber) were supplied by 3M Healthcare Ltd (Loughborough, UK).

3.3.2 Methods

3.3.2.1 Preparation of BDP Clathrates

The preparation of clathrates was based on the process described by EM Philips (Philips, Byron 1994). Both the 1.67% w/w BDP CFC-11 clathrates, and 3% BDP IPA clathrates were synthesized at room temperature by suspending the anhydrous BDP in the relevant propellant in a pressure resistant vial. This mixture was then shaken using a Stuart SF1 Flask Shaker at 800 oscillations per minute for 2 hours. The resulting suspension was refrigerated for 24 hours before repeat vacuum filtration through a Buchner filter to obtain the crystals. Excess propellant was removed passively by evaporation for 24 hours at room temperature.

3.3.2.2 AFM Tip Functionalization

Contact mode DNP-S (short, thick) tips (BrukerNano, Coventry, UK) were used for functionalization. These tips are designed to have low spring constants ($k \sim 0.35$ N/m) for very sensitive surface responses. In this study they were chosen because it was assumed that the v shaped cantilever would perform better as a functionalization scaffold, and that the lower

spring constant would be more sensitive to the functional particle-surface interactions. The resonant frequency and Q values of each tip were determined using the in-built AFM software (DI EnviroScope, NanoScope IIIa Controller, NanoScope version 5.30 software, BrukerNano, Coventry, UK) for each cantilever before they were functionalized and the spring constants calculated by Saders method (Sader et al, 1999). Nine functionalized tips were prepared in total, 3 with anhydrous BDP, 3 with BDP CFC-11 clathrates and 3 with BDP IPA clathrates. In each instance the cantilevers were functionalized using the EnviroScope AFM. An epoxy resin (Loctite, Henkel Ltd, Hatfield, UK) was applied to a silica disk and placed onto the AFM stage. A sacrificial AFM tip was used to draw thin lines of the adhesive from bulk. The blank cantilevers were placed in the tip holder and manually lowered on to these glue strands until contact was observed via laser deflection or visually, then removed. The resin substrate was then removed and replaced with the appropriate powder sample. Using the AFM microscope small individual powder particles/crystals were resolved, identified and aligned with the position of the tip. The cantilever was then lowered manually onto the powder particles for attachment and then removed. The functionalized tips were left to dry for 24 hours. Successful tip functionalization was confirmed by low vacuum SEM imaging as described below.

3.3.2.3 Scanning Electron Microscopy (SEM)

The particle sizes and morphology of the anhydrous BDP, the BDP IPA clathrates and the BDP CFC-11 clathrates were imaged by a JEOL JSM-6060LV scanning electron microscope (JEOL Ltd, Tokyo, Japan) at various magnifications under vacuum. Powder samples were sprinkled onto carbon stubs, lightly pressed with a glass cover slip, then nitrogen gassed to remove any excess. These stubs were sputter coated (Balzers Benchtop Sputter Coater SCD 030) with gold in an argon atmosphere (50Pa) at 30 mA for 4 minutes before SEM imaging. The pMDI components (FEP coated aluminium canister, uncoated aluminium canister and stainless steel metering chamber) were cut from bulk and then attached directly to carbon stubs and imaged in the same apparatus but without sputter coating, to preserve the samples for use. Imaging was therefore carried out in low vacuum mode. All the BDP CFC-11, BDP IPA and anhydrous BDP functionalized tips (3 of each) were also imaged both prior to and after use in the SEM, to characterize successful functionalization and subsequent changes to morphology that might influence results. The tips were placed on a sliver of silica gel attached to a carbon stub. These

were not sputter coated to allow use after imaging, and subsequently low vacuum mode was used.

3.3.2.4 Differential Scanning Calorimetry (DSC)

A TA Instruments DSC 2920 differential scanning calorimeter (TA Instruments, Delaware, US) was used to perform all DSC work. The DSC was used to help confirm the BDP clathrate synthesis, and the purity of the parent sample. This was achieved by determining the phase transitions of anhydrous BDP, BDP CFC-11 clathrates and BDP IPA clathrates. Accurately weighed samples of about 6 mg were sealed in aluminium hermetic pans, equilibrated at 0°C, kept isothermal for 3 minutes and then heated at 10°C per minute under nitrogen to 300°C. DSC cycles were also performed on BDP CFC-11 clathrates and BDP IPA clathrates to check for reversibility of the phase transitions observed. In these instances accurately weighed samples of the two clathrate powders were again placed in sealed aluminium hermetic pans. The DSC was then equilibrated at 0°C for three minutes and ramped at 10°C per minute to 150°C, at which point the temperature was then cooled by 20°C per minute to 0°C before re-heating at 10°C per minute to 220°C. Thermograms produced were analysed using TA universal analysis –NT software (TA Instruments, Delaware, US).

3.3.2.5 X-Ray Powder Diffraction (XRPD)

A Bruker D8 diffractometer (Bruker AXS, Madison, WI, USA), operating in a Debye-Scherrer geometry, was used to collect XRPD patterns of the synthesized BDP clathrates. A ceramic X-ray tube with a copper target, wavelength $\lambda = 1.54059 \text{ \AA}$, equipped with a scintillation detector was operated at 40kV, 40mA to generate x-rays. Samples were filtered through a 1 μm sieve before loading into a 0.7mm capillary tube. These tubes were then attached to a goniometer and visually aligned, before placement in the diffractometer. A BDP CFC-11 clathrate sample was analysed by XRPD to compare with the reported crystal structure and calculated diffractogram (Cambridge Structural Database) to prove synthesis. The sample was run for 24 hours, collecting 1 diffractogram per hour. These diffractograms were plotted, merged and analysed using Xmgrace (Grace Development Team, Boston, US).

3.3.2.6 Atomic Force Microscopy (AFM)

AFM imaging was carried out using an EnviroScope AFM with a NanoScope IIIa Controller (BrukerNano, Coventry, UK) on the surface of all the CAB substrates to visually qualify surface topography and morphology before quantifying the microscale roughness. Images were performed in tapping mode AFM using TAP300 tips (BrukerNano, Coventry, UK). Images were taken at a scan size of $5\mu\text{m} \times 5\mu\text{m}$, and at a scan rate of 1Hz. Surface roughness was determined using NanoScope 7.3 software (BrukerNano, Coventry, UK) and quantified using the arithmetic mean (R_a) and the root mean square (R_q) of the average height deviations measured from the topographical data.

AFM force data acquisition was performed on the same apparatus. In this instance the environmental chamber was used to maintain a relative humidity as close to 0% RH as possible to minimize the influence of capillary forces (Hooton et al, 2004). At no point was the humidity allowed to rise above 5% RH. The functionalized tips were placed into the tip holder, optically aligned and then challenged to five sample surfaces using a defined set point voltage once the humidity chamber had reduced the humidity to an acceptable value. The samples were ordered as follows; the corresponding powder sample of the tip material (first cohesive measurement), followed by the FEP coated aluminium canister, the uncoated aluminium canister, the stainless steel metering chamber (adhesive measurements) and then a repeat of the powder sample. This repeat cohesive measurement was used to either identify any significant changes that might implicate tip destruction or alteration, or highlight critical inherent variability of adhesive force genesis. Ten force curves were collected per tip at randomly selected sites over the sample surface at a scan rate of 1Hz. The F_{adh}/F_{coh} was recorded by ramping the substrate surface into and out of contact with the cantilever and measuring the deflection of the cantilever. Hooke's law was then applied to the recorded values with the calculated spring constants of the tips and a quantitative measurement of the forces of adhesion/cohesion obtained. The cohesive and adhesive forces were then analysed using Begat et al's (2008a) cohesive-adhesive balance approach outlined previously.

3.4 Results

3.4.1 Characterization of Beclomethasone Dipropionate and the Beclomethasone Dipropionate Clathrates

3.4.1.1 SEM Analysis

SEM images of the anhydrous BDP, the BDP CFC-11 clathrate and the BDP IPA clathrate are shown in figures 3.1, 3.2 and 3.3 respectively. The scales presented are not consistent due to the significantly different particle sizes between the BDP particulates, but were chosen to best illustrate and allow description of the powder morphologies and topographies. The anhydrous micronized BDP (fig. 3.1) shows the most irregular and amorphous particle structure, with a particle size distribution of between 2 μ m - 40 μ m and consistent aggregation. The BDP CFC-11 clathrate (fig. 3.2) is readily identifiable as repeating hexagonal crystals with a large size distribution of 5 μ m-85 μ m and what appear to be well defined smooth surfaces. Some small cracks in these crystal faces can be seen across a large number of the particles imaged, and these were found at various sites across the sample in multiple images. Notably, these well-defined crystals have distinct faces, namely a predominant hexagonal face (fig. 3.2 BDP CFC 3) and a lateral more rectangular crystal face (fig. 3.2 BDP CFC 4). The BDP IPA clathrates demonstrated a much less reproducible crystal structure with a flatter, fractured plate, irregular and more clustered morphology. Particle size distribution was in the region of 2-30 μ m (fig. 3.3).

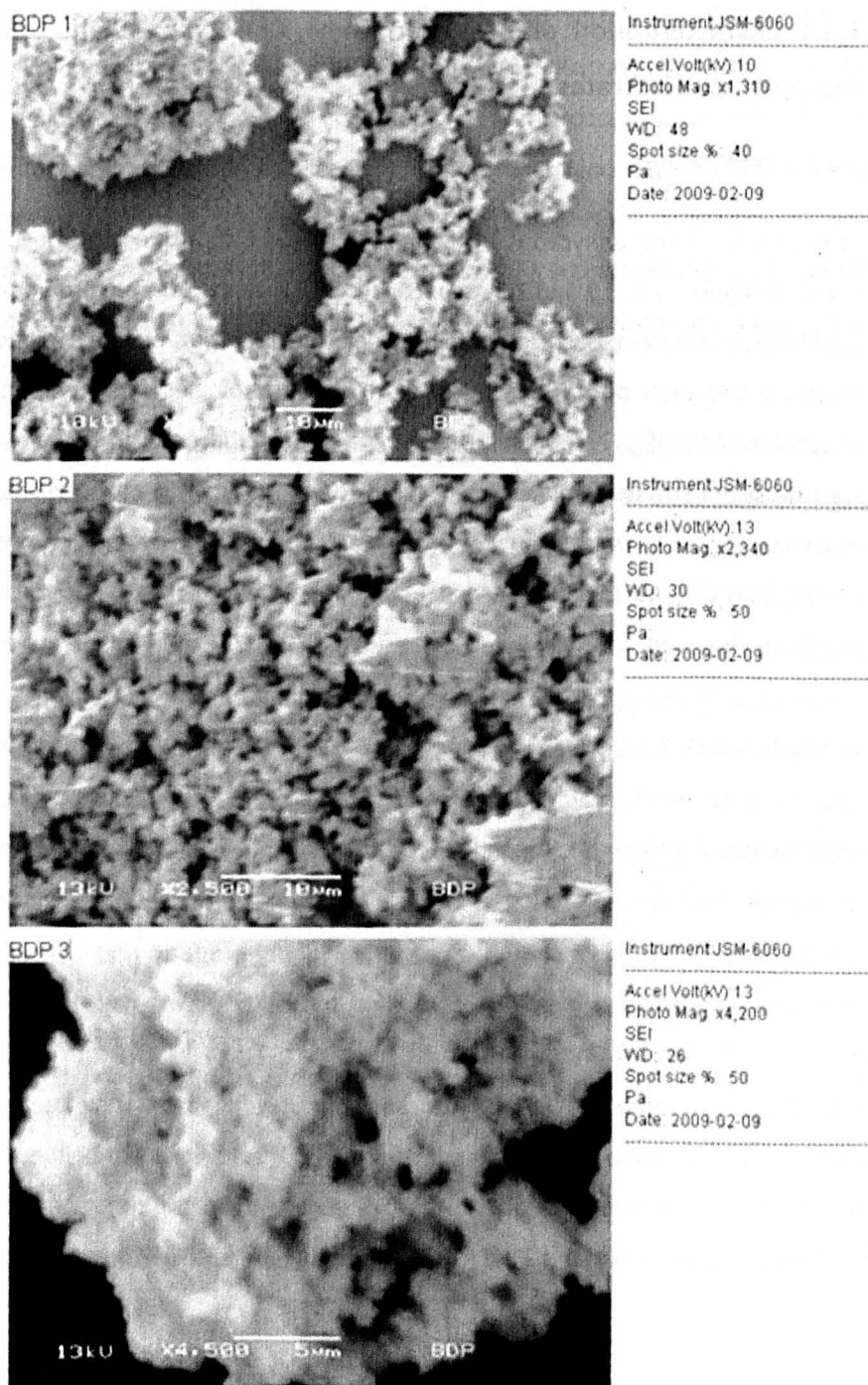


Figure 3.1 SEM images of the Anhydrous Beclomethasone Dipropionate powder particles at various magnifications (as labelled)

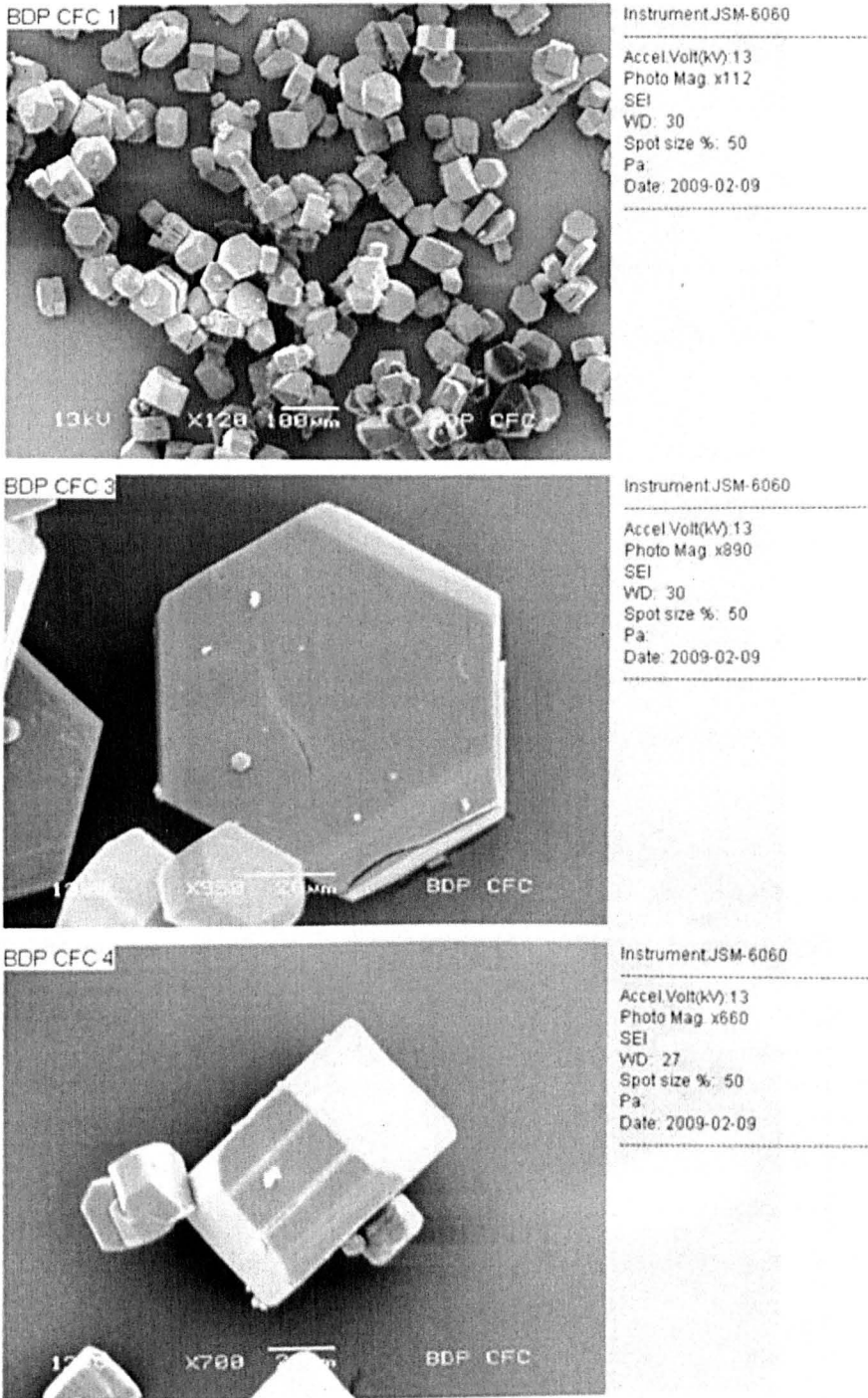


Figure 3.2 SEM Images of the synthesized BDP CFC-11 Clathrate powder particles at various magnifications (as labelled)

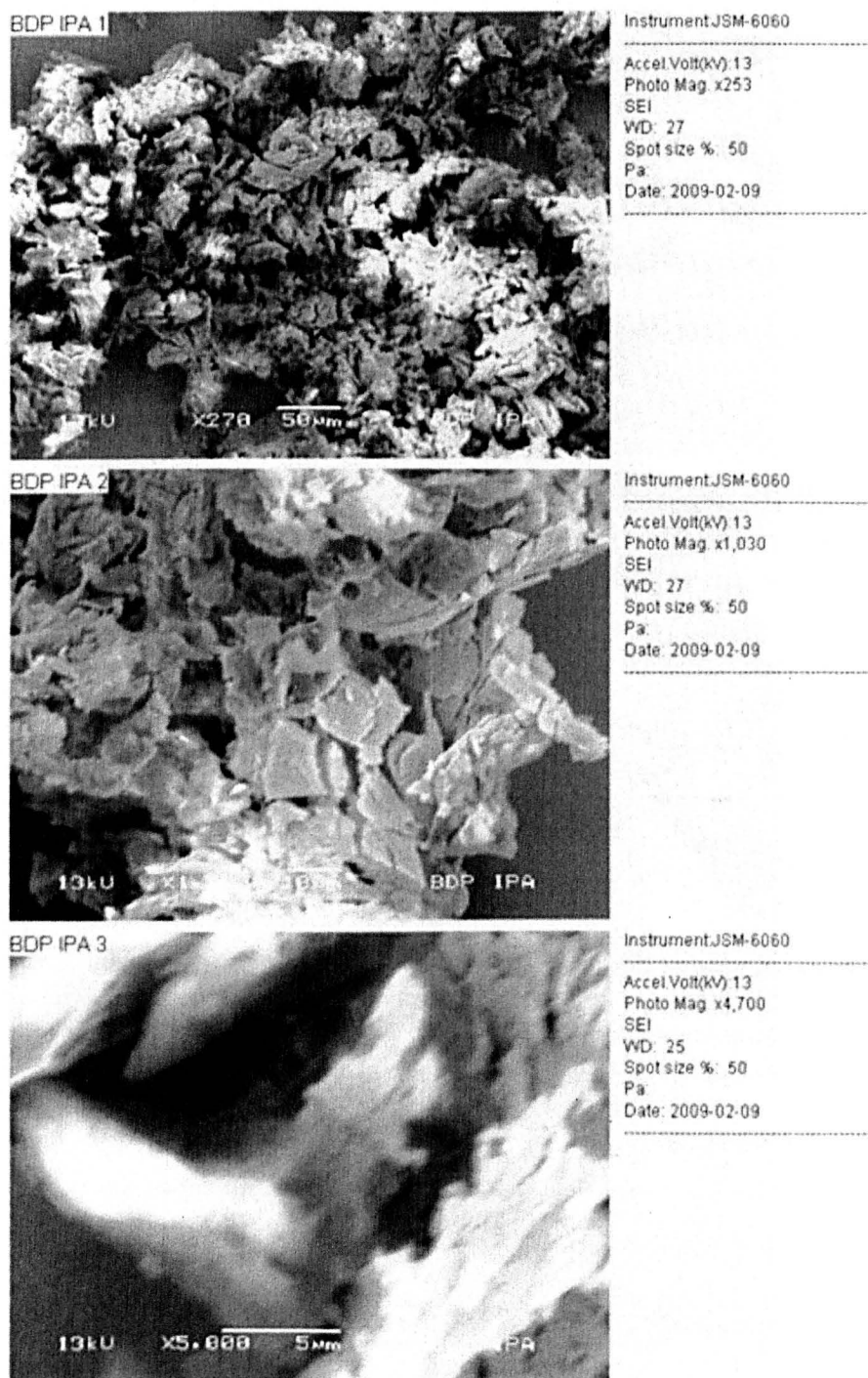


Figure 3.3 SEM images of the synthesized BDP IPA clathrate powder particles at various magnifications⁵ (as labelled)

3.4.1.2 X-Ray Powder Diffraction Analysis

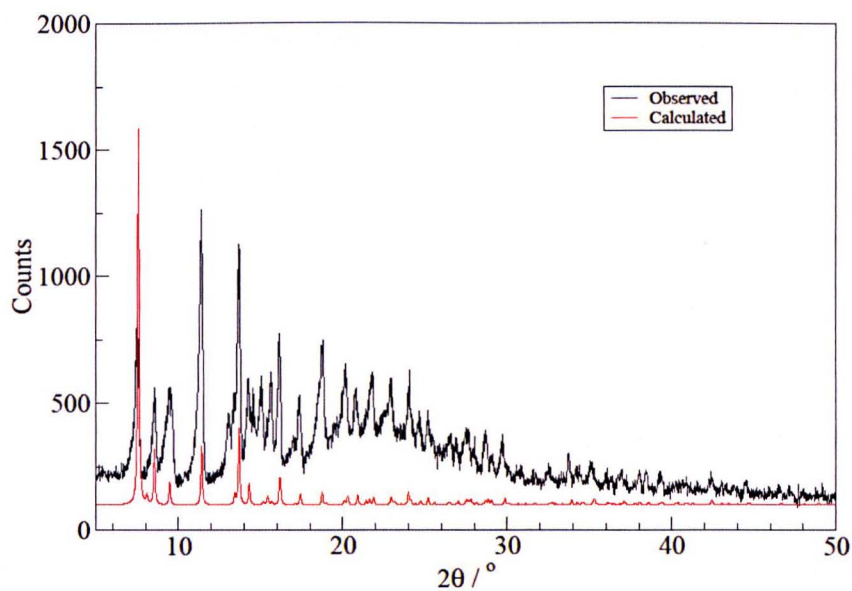


Figure 3.4: X-Ray Powder Diffractograms for the observed synthesized BDP CFC-11 Clathrate and the calculated Cambridge Structural Database reference.

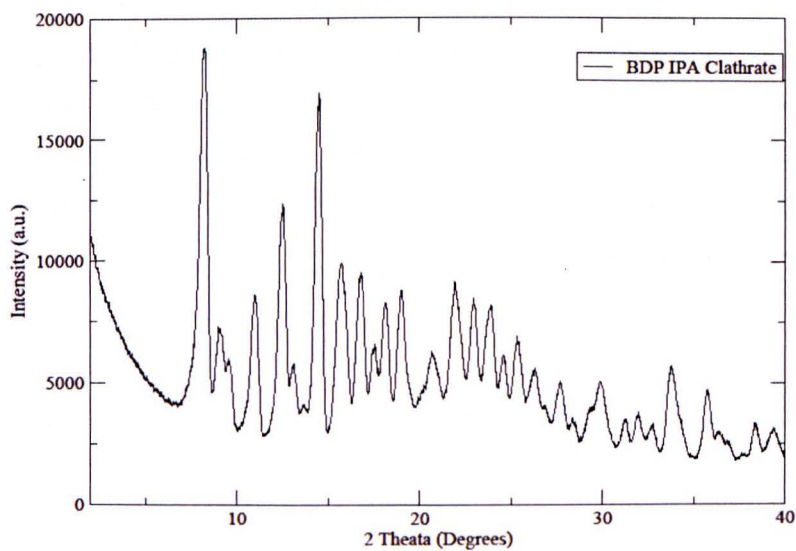


Figure 3.5: X-Ray Powder Diffractogram for the synthesized BDP IPA Clathrate

A merged diffractogram (compiled from 24 diffractograms of 1 hour run time each) of the synthesised BDP CFC-11 clathrate is presented in figure 3.4. The calculated diffractogram from the Cambridge Structural Database is presented alongside as a reference to validate successful synthesis. Characteristic peaks for the BDP CFC-11 clathrate are known, and can be seen on the reference diffractogram to be at 2 Theta values of 7.2, 8.5, 9.6, 11.2, 13.8, 16.8 and 18.5°. While an x-ray powder diffractogram was compiled for the BDP IPA clathrate in fig 3.5 there does not exist a reference diffractogram for comparison, which would have allowed confirmation of synthesis.

3.4.1.3 Differential Scanning Calorimetry

Representative DSC thermograms for anhydrous BDP, BDP CFC-11 clathrate and BDP IPA clathrate are shown in figure 3.6. All traces for anhydrous BDP show a single endotherm at around 213°C (fig. 3.6 A), which corresponds to the literature melting point of BDP (212°C). The traces for the BDP CFC-11 clathrates (fig. 3.6 B) exhibit this melting event, but also a consistent exothermic event at 91.2°C, immediately before another endotherm at 94.6°C. The BDP IPA thermograms (fig. 3.6 C) also show the melting endotherm and another broader endothermic transition maximizing at about 142°C, although no exothermic event was evident prior to this. Figure 3.7 shows cycled DSC traces where samples of the BDP CFC-11 clathrate and BDP IPA clathrate were heated to just below the observed melting point of BDP, before the temperature was cycled back to 0°C and then re-ramped to sample melting. This process was designed to investigate whether the energetic events seen prior to melting in both samples, were reproducible or irreversible. As can be seen in these traces, these events did not reoccur upon the reheating process.

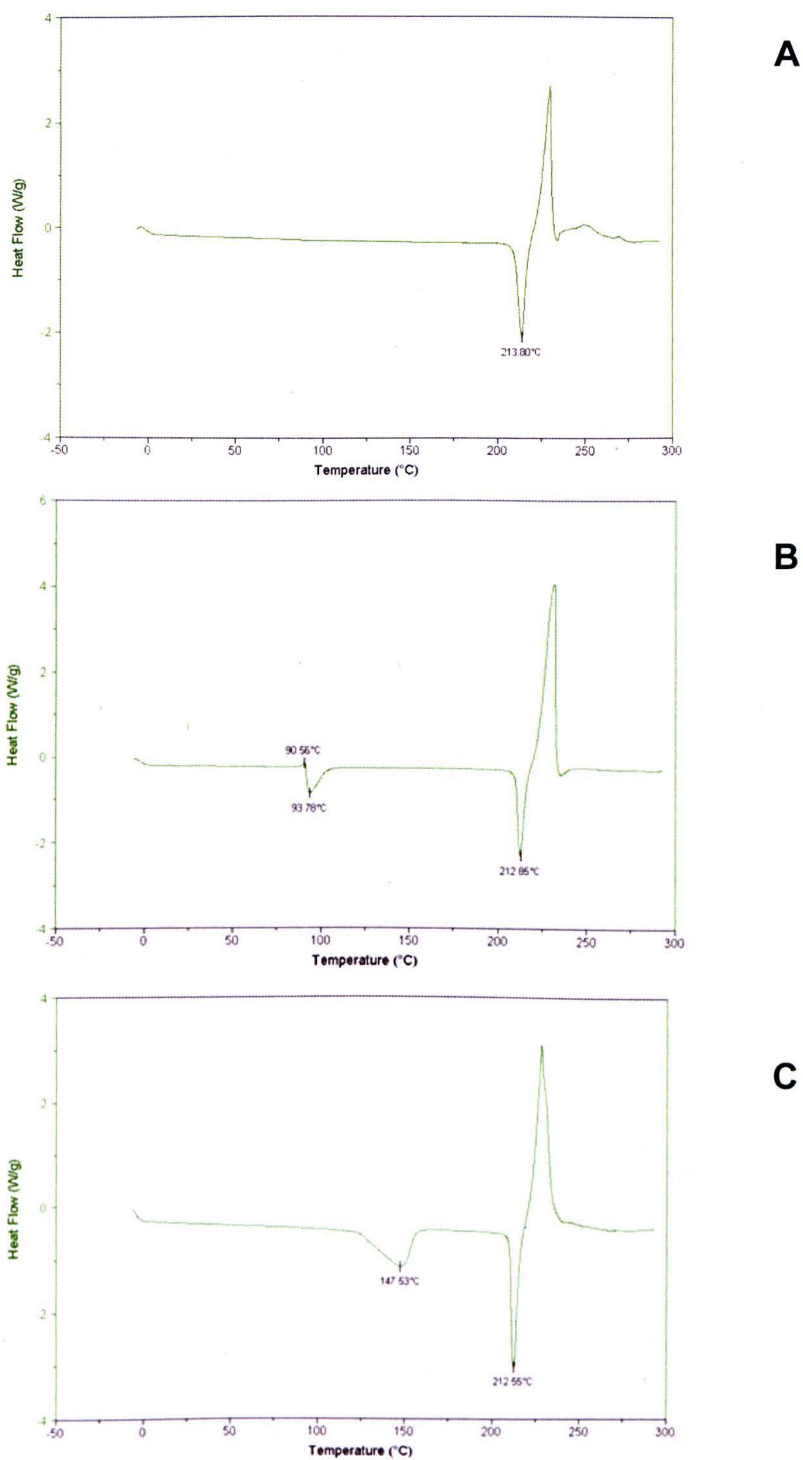


Figure 3.6: DSC heating thermograms of (A) anhydrous BDP, (B) BDP CFC11 clathrates and (C) BDP IPA clathrates.

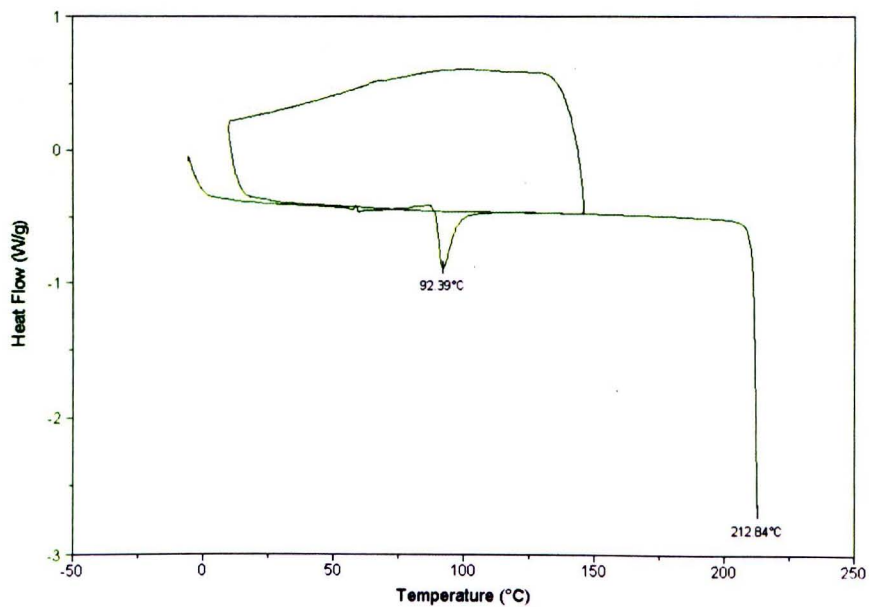
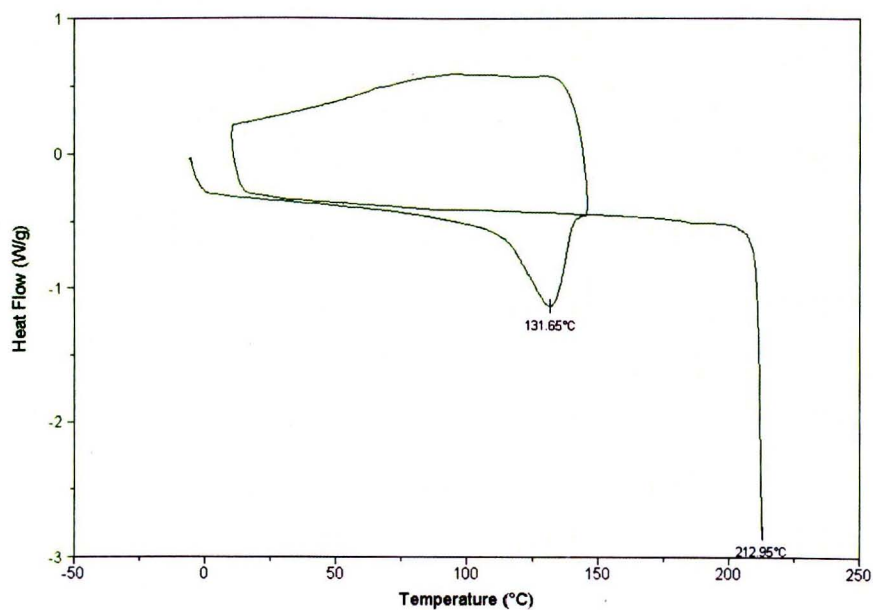


Figure 3.7 Cycled DSC heating thermograms of (A) BDP IPA Clathrate and (B) BDP CFC-11 Clathrate

3.4.1.4 Atomic Force Microscopy Imaging

Height and phase tapping mode AFM images of the BDP clathrates and anhydrous BDP are shown in figure 3.8. These images were all captured over a spatial area of $5\mu\text{m} \times 5\mu\text{m}$, to allow a direct comparison in root mean square and arithmetic mean roughness values as calculated by the instrument software. As observed in the SEM images the BDP CFC-11 clathrate has two very distinct crystal faces (dominant hexagonal face and lateral rectangular face) these were therefore both imaged separately to report any differences in surface roughness. The average calculated root mean square (R_q) and arithmetic mean roughness (R_a) values derived from the image analysis are displayed in table 3.1. The R_q roughness is generally accepted as being the most reliable indicator of surface roughness and is a statistical measure of the magnitude of a varying height. It was determined from the topographical AFM images by the instrument software via the following equation (James et al, 2008):

$$R_q = \sqrt{\frac{1}{n} \sum_{i=1}^n y_i^2} \quad (3.1)$$

Where n is the number of points in the topography profile, i is the asperities and y_i is the distance between the asperities. The R_a is less often used in AFM based work but has been applied in many other fields and reflects the mean of the height variation around a zero point on a sample surface and is given by the following equation (James et al, 2008):

$$R_a = \frac{1}{n} \sum_{i=1}^n y_i \quad (3.2)$$

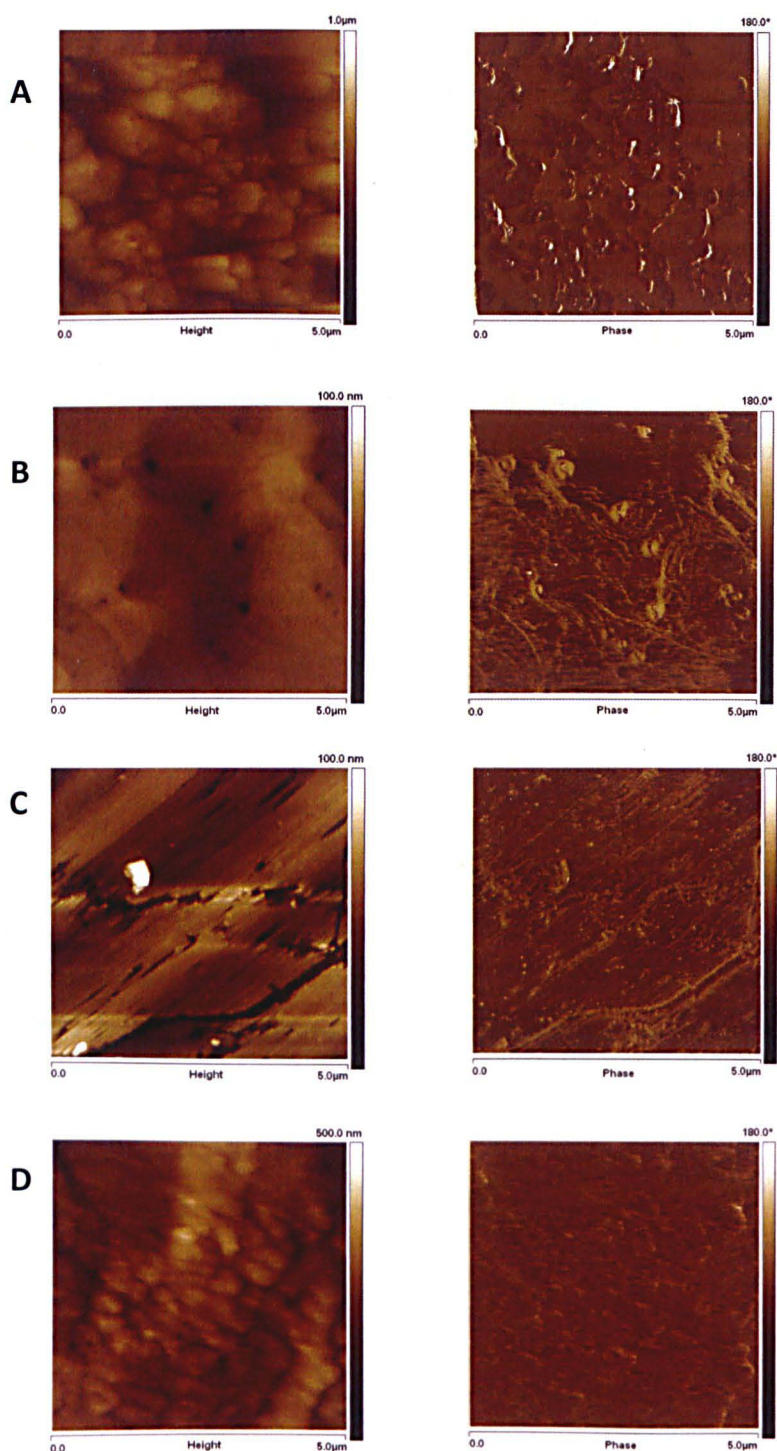


Fig 3.8: 5µm x 5µm Tapping mode AFM height (left) and phase (right) images of (A) Anhydrous BDP powder bed, (B) BDP CFC-11 clathrate particle main face, (C) BDP CFC-11 clathrate particle lateral face and (D) BDP IPA clathrate particle face

SAMPLE	ARITHMETIC MEAN ROUGHNESS (R_a) (nm \pm SD)	ROOT MEAN SQUARE ROUGHNESS (R_q) (nm \pm SD)
ANHYDROUS BDP	91.9 \pm 39.0	117.6 \pm 53.1
BDP CFC-11 CLATHRATE (COMBINED FACES)	9.7 \pm 7.7	12.0 \pm 8.7
BDP IPA CLATHRATE	22.3 \pm 6.6	29.5 \pm 7.0

Table 3.1: Arithmetic mean roughness and root mean square roughness values for Anhydrous BDP, BDP CFC-11 Clathrates and BDP IPA Clathrates over a 5 μ m x 5 μ m area.

Both the lateral and main faces of the BDP CFC-11 clathrates were seen to be very flat with little variation in surface topography; all of the topographical features were 100nm or less in height (figs. 3.8 B, 3.8 C). On the main face of the crystal, small spherical indents could be seen in the topographic image, and these features showed a difference in phase. These indents were consistent across the set of images and did not appear to be artefacts of the imaging technique. On the lateral face a series of linear fractures can be seen topographically on an otherwise smooth surface. There is little phase difference, and it is likely these are attributable to either cracks in the crystal face corresponding with those seen on the SEM images of the BDP CFC-11 clathrates (fig. 3.2) or features related to steps in the crystalline surface. The images of the BDP IPA clathrate crystals (fig. 3.8 D) showed a consistent topography of irregular nanoscale undulations in the region of 500nm. Anhydrous BDP showed a similar topographical pattern to that of the BDP IPA clathrates, with repeating rising and falling plateaus (fig. 3.8 A). The size of these features were however larger than those of the BDP IPA clathrate, with a maximum variability of 1 μ m. The data in table 3.1 shows the calculated average R_a and R_q roughness values from the set of AFM images collected for each of the three API materials. From this data it is apparent that the anhydrous BDP has by far the roughest surface (R_q 117.6nm), with the clathrated samples showing somewhere between a 5-10 times smoother microscale topography. The BDP CFC-11 clathrate had the smoothest surface (R_q 12.0nm) in agreement with the SEM images obtained (fig 3.2), and the BDP IPA clathrate remained significantly

topographically smoother (R_q 29.5nm) than the parent powder, in conjunction with the larger more regular crystal shape that was apparent. Both the clathrates also showed significantly less variability in surface roughness across images than the anhydrous parent powder, as demonstrated by the standard deviations about the mean R_q values.

3.4.2 Characterization of the pressurized metered dose inhaler components

3.4.2.1 SEM Analysis

SEM images of the selected pMDI components (FEP coated canister, uncoated canister and metering chamber) are shown in figure 3.9. The FEP coated canister (fig. 3.9 A) shows a very homogenous microscale surface with few surface artefacts on the surface coating. The layering of the FEP coating can be seen as a sweeping effect across the images with some small degree of height variability. However, it is worth noting that the fluorinated coating was not always continuous across all images and in some cases, a degree of absence was recorded, leading to a rougher surface with significant depressions. The uncoated canister (fig. 3.9 B) displayed a rougher surface with more consistent topographical variability. Some regions of the canister appeared rougher than others with evidence of significant microscale imperfections in the metal working. However of the three materials the metering chamber appeared to have the least homogeneous surface by SEM analysis (fig. 3.9 C). Multiple micrometre sized holes, scratches and other surface defects can be seen, probably introduced by the manufacture or finishing process of the component. However although more frequent and irregular than the features seen on the canister samples, it is difficult to define the depth of these defects given the limitations of an SEM image in evaluating three dimensional variability. While these defects were much more common on the metering chamber than the two canister samples, they were not uniformly distributed, and while there were areas on the macroscale that showed significant surface heterogeneity, there were also others that were much less variable in the extent of their topographical features.

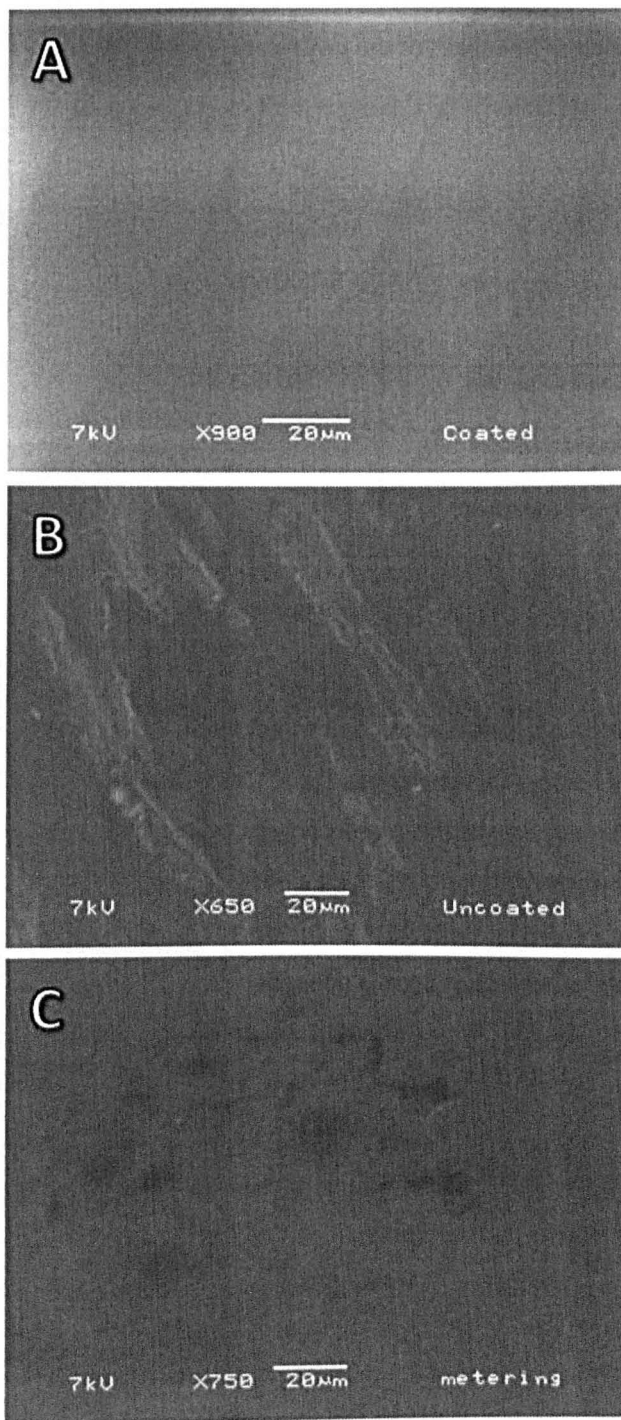


Fig 3.9: SEM images of A) FEP coated pMDI canister B) Uncoated pMDI canister and C) pMDI stainless steel metering chamber

3.4.2.2 Atomic Force Microscopy Imaging

Tapping mode AFM images of the pMDI components are shown in figure 3.10 and the calculated R_q and R_a values are given in table 3.2. The R_q and R_a values were ascertained as described above from images of $5\mu\text{m} \times 5\mu\text{m}$.

SAMPLE	AVERAGE ARITHMETIC MEAN ROUGHNESS (R_a) (nm \pm SD)	AVERAGE ROOT MEAN SQUARE ROUGHNESS (R_q) (nm \pm SD)
<i>FEP Coated Canister</i>	18.1 \pm 1.3	24.7 \pm 1.33
<i>Uncoated Canister</i>	29.8 \pm 9.4	40.0 \pm 9.3
<i>Metering Chamber</i>	15.5 \pm 6.4	22.8 \pm 8.4

Table 3.2: Average mean roughness (R_a) and root mean square roughness (R_q) values for pMDI components over a $5\mu\text{m}^2$ area

Surprisingly the stainless steel metering chamber reported the smoothest surface of all the components across this image size (R_q 22.8nm). The asperities seen on the surface appear to be sharper and less consistent in morphology than the features on the canister wall samples (fig. 3.10 C). However, with only reaching a maximum of 100nm in height they appear less prominent than some of the features that occur on the canister samples. The FEP coated canister wall shows irregular asperities upon a generally smooth surface (fig. 3.10 A). The reported roughness values were slightly larger than those seen with the metering chamber (R_q 24.7nm), but significantly the standard deviations were much less, showing reduced variability across images. Some of these isolated 'islands' of topography reach a maximum of around 300nm in height. Both the coated canister and metering chamber reported smoother surfaces across this surface area than the uncoated canister (R_q 40.0nm), which shows a more repetitive undulating topography with surface features again reaching around 300nm (fig. 3.10 B).

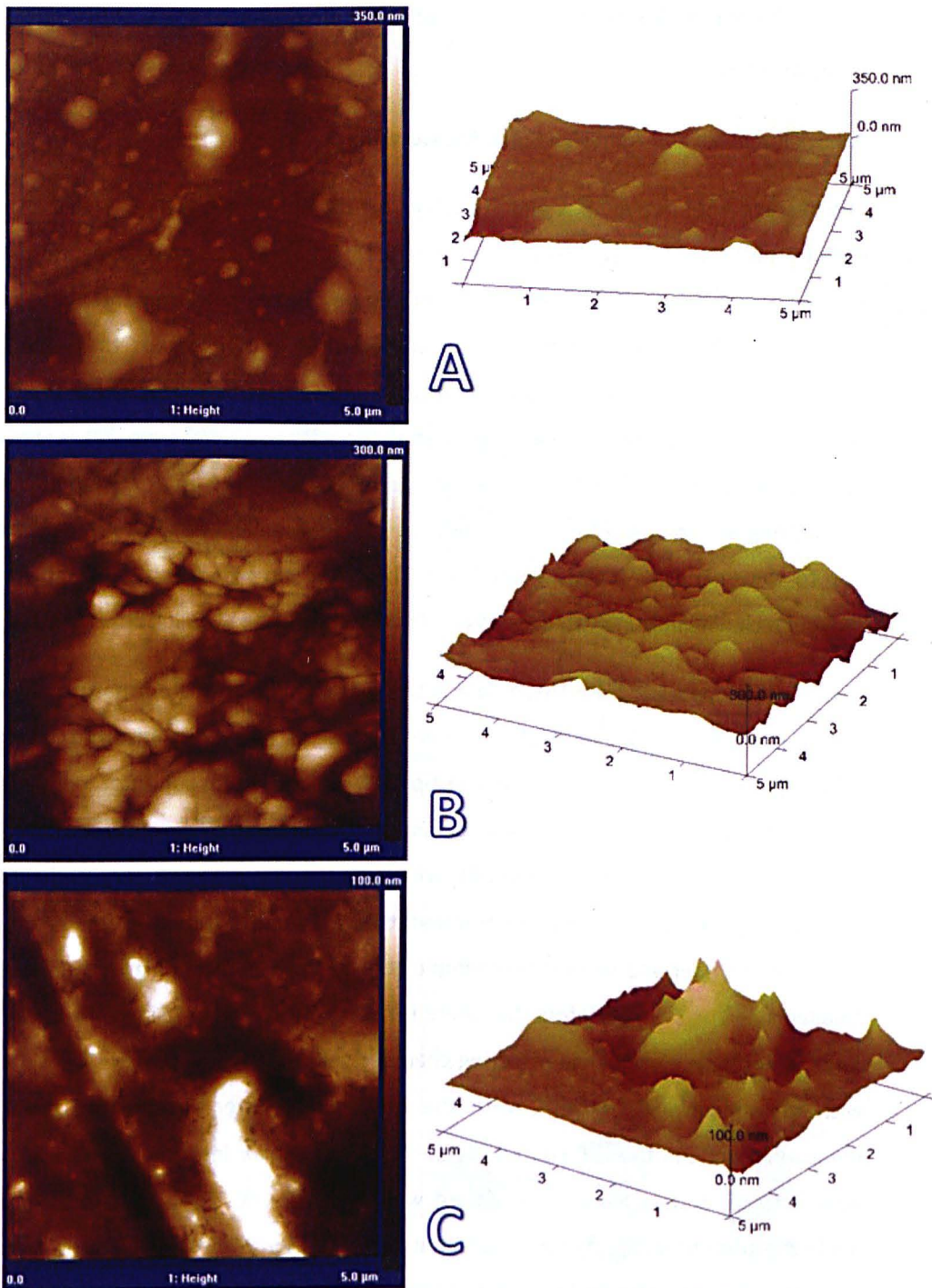


Figure 3.10: AFM height and 3D interpretation of (A) FEP Coated Canister, (B) Un-coated Canister and (C) Metering Chamber. *NOTE vertical scales are NOT identical but as labelled.*

3.4.3 Cohesive Adhesive Balance of the Beclomethasone APIs and the pMDI components.

3.4.3.1 Cohesive and Adhesive Force Measurements

The average AFM derived F_{adh} and F_{coh} values for the anhydrous BDP, BDP CFC-11 clathrate and BDP IPA clathrate tip sets are shown in figure 3.11, 3.12 and 3.13. In each figure the first average F_{coh} measurement is placed leftmost on the figure. These measurements were made prior to adhesive measurements on the inhaler components and represent the force of attraction between the functionalized tip and a surface composed of the same API as the tip particle. A second average F_{coh} measurement taken after the adhesive measurements is shown on the far right of the figures. Absolute values of adhesion/cohesion are only of importance when considering an individual tip's cross material interactions, and largely irrelevant from tip to tip due to the unknown contact geometries. The tip to tip trends within a set are however of particular significance in comparison.

Immediately apparent from these data is the range, and inconsistent nature of the interactive forces. The trend of adhesion/cohesion between one tip was rarely mirrored consistently by the other tips in the same series, with one tip showing an increase in interactive force from one material to another and a subsequent tip showing a decrease. The anhydrous BDP tips (fig. 3.11) for example show two separate trends, where on the first BDP and uncoated canister samples the three tips increase in force measurement from 1st to 3rd. However, for the coated canister, metering chamber and second BDP samples the 1st tips interactions are larger than the 2nd but smaller than the 3rd. This infers that there is not a consistent compliance to a ratio of adhesion force generation. Overall the metering chamber substrate showed the largest interactive force with the anhydrous BDP tips, with the uncoated canister second and the two cohesive measurements and the FEP coated canister showing similar interparticulate interactivities. The inconsistency in data trend is continued with the BDP CFC-11 clathrate tips (fig. 3.12). Here, while the tips show slightly more continuity in rank adhesion forces from tip 1 to tip 3, across the CAB substrates, the deviation around the average adhesion forces is very large, as shown by the error bars (as standard deviation). This implicit variability makes it difficult to confirm to the rank adhesions with confidence and hints at significant variability around the forces of particle-

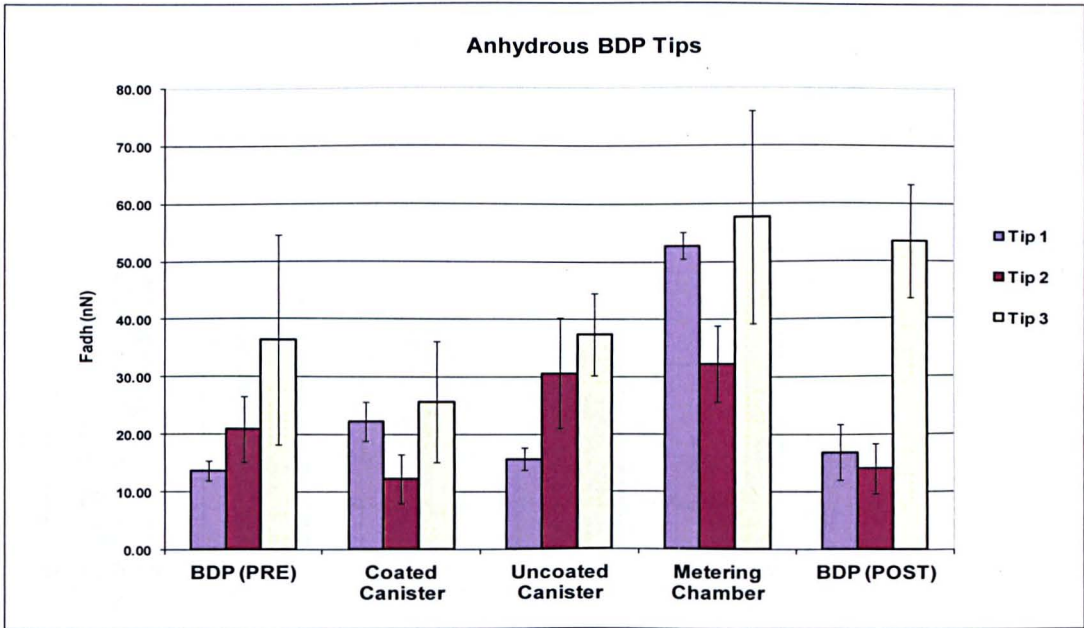


Fig 3.11 Mean Cohesive and Adhesive Force Values of Anhydrous BDP tips against CAB substrates

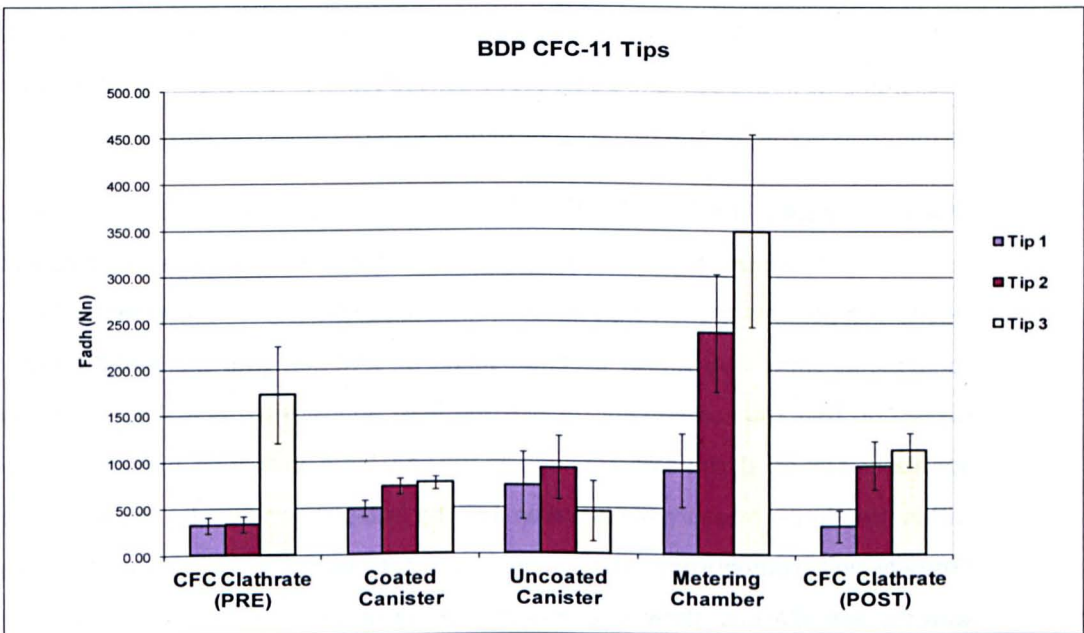


Fig 3.12 Mean Cohesive and Adhesive Force Values of BDP CFC-11 tips against CAB substrates

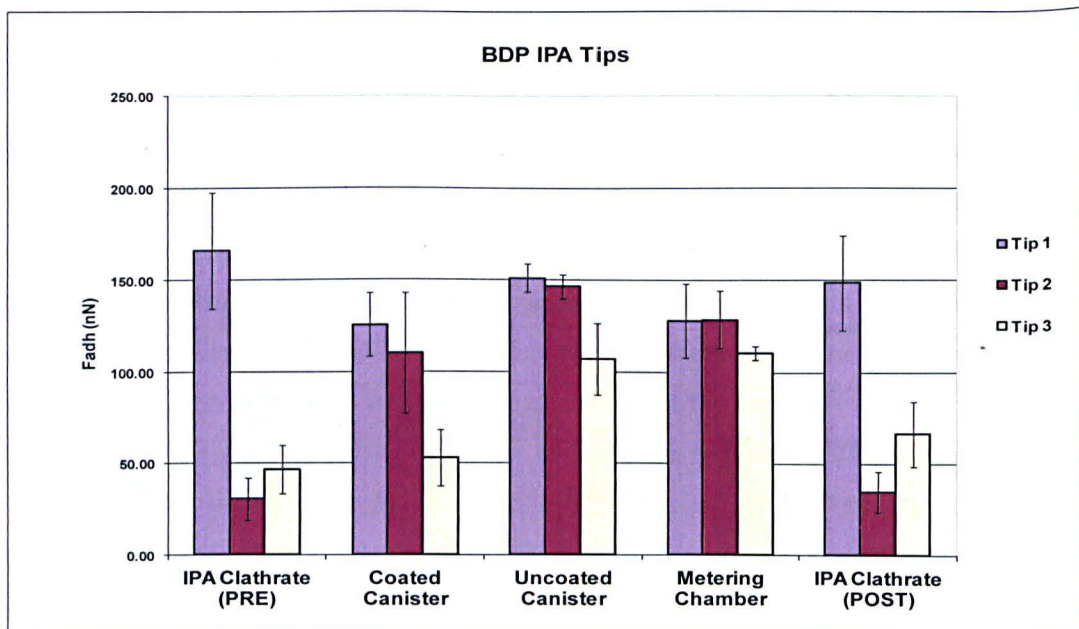


Fig. 3.13 Mean Cohesive and Adhesive Force Values of BDP IPA tips against CAB substrates

surface contact. In general the absolute forces of adhesion are significantly larger than those with the anhydrous BDP tips, in the region of two to four times greater. The metering chamber measurements in this BDP CFC-11 tip set evidenced significantly larger F_{adh} values than the other tip materials in comparison to the other sample surfaces especially with tips 2 and 3.

When considering the BDP IPA (fig. 3.13) tip data, tips 1 and 3 show a consistent force relationship, however tip 2 does not conform consistently and the adhesive ratios with the three inhaler components are not replicated with the two cohesive measurements. All three inhaler components show very similar absolute values of adhesion with the BDP IPA tips, with some suggestion that the coated canister was the least adhesive surface. Once more the standard deviations around all the data are consistently very large, indicating a massive spread of values within the force measurements taken on the sample surfaces by the functionalized tips. Critically while comparison of the F_{coh} measurements made before and after F_{adh} measurements with the BDP IPA tips, show a reproducible trend of tip to tip cohesion on similar scales, the anhydrous BDP and BDP CFC-11 clathrate tips do not mimic this. Instead there is a change in rank tip adhesion to the cohesive surface, albeit with large standard deviations that could range to redefine this.

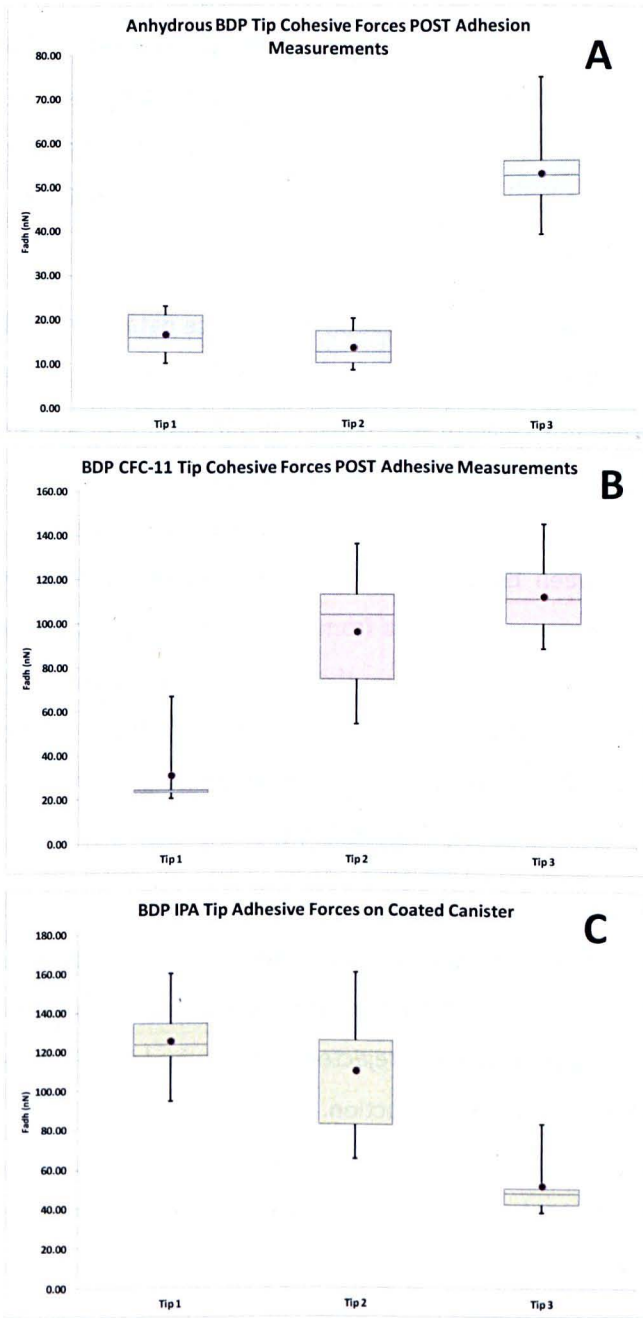


Fig 3.14 Example box plots showing force data from A) Anhydrous BDP tips on anhydrous BDP (post adhesion measurements), B) BDP CFC-11 tips on BDP CFC-11 (post adhesion measurements) and C) BDP IPA tips on the FEP coated canister

Figure 3.14 shows some selected box plots describing the force data generated from given tip sets on given substrate surfaces. These were compiled for all the tip to surface relationships to display and analyse the difference between the tip data sets without making an assumption of the statistical distribution of the F_{adh} data. In each plot, the bottom and the top of the box represent the 1st and 3rd quartiles and the band within the box is the median (2nd quartile). The dot represents the mean of the data, and the ends of the whiskers represent the minimum and maximum force values within the data set.

Figure 3.14 A shows the representation of the force data from the three anhydrous BDP tips on their second set of cohesive measurements (post adhesion measurements). In this plot the mean is consistently close to the median for all three tips, and the range of the force data is about 10nN for the first two tips and 40nN for the last. Figure 3.14 B shows the force data from the BDP CFC-11 tips on their second cohesive measurement. Here there are significant differences between both the mean and median of the first two tips and of the quartile measures to the range of the data from all three tips. Tip 1 shows that the mean lies above the 3rd quartile. Figure 3.14 C shows the force data from the BDP IPA tips on their adhesive measurements on the coated canister. While tip 1 has a relatively close mean to median relationship, tips 2 and 3 do not. There is again a very great dissimilarity in the range of the data sets in comparison to the quartile measures.

Figure 3.15 shows some example cohesive force curves from the functionalized AFM tips. Column A shows example force curves of all three tip types that were used to calculate the F_{adh} between the tips and their respective cohesive surface. Column B shows example force curves of all three tip types that were rejected and required to be repeated. The blue line is the tip approach while the red is tip retraction.

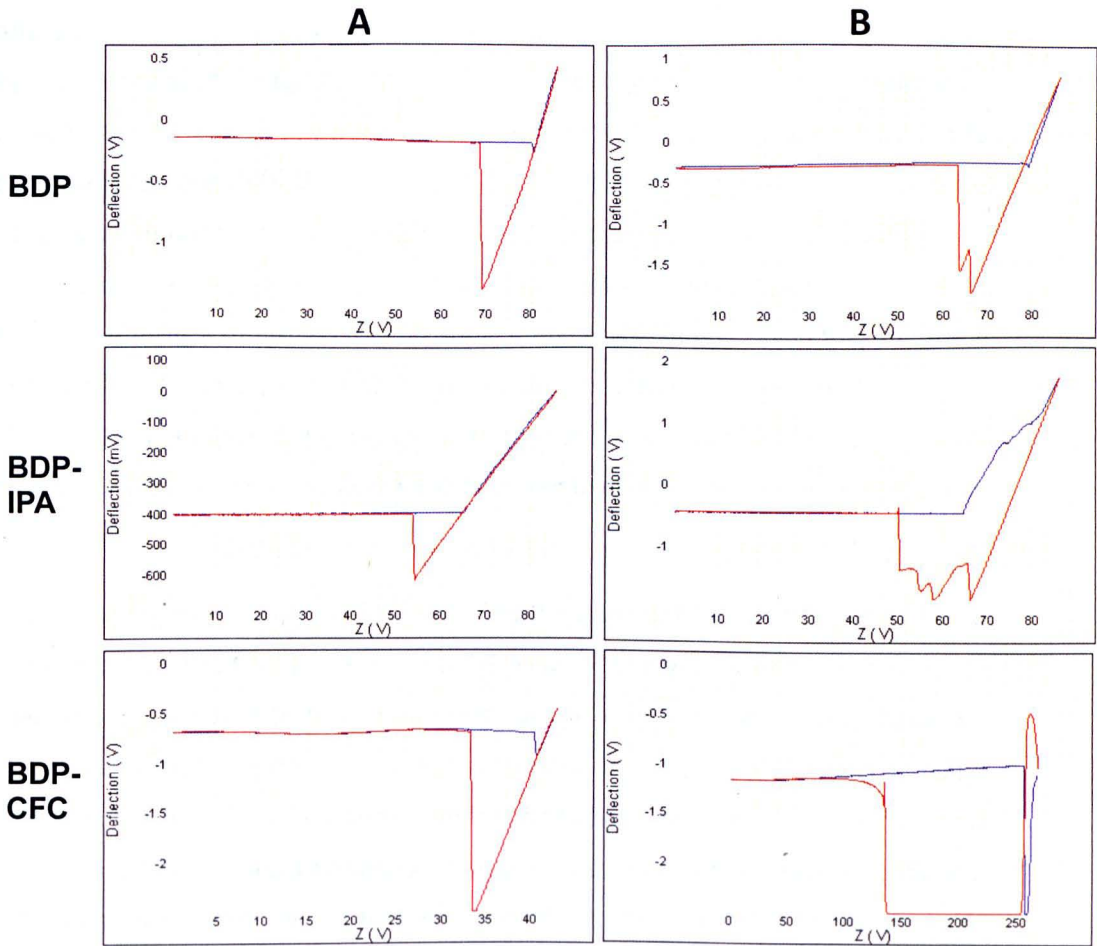


Fig 3.15 Example cohesive force curves from functionalized anhydrous BDP tips, BDP-IPA tips and BDP-CFC11 tips A) Accepted force curves and B) Rejected force curves.

3.4.3.2 CAB Plots

By plotting the average adhesion values of each tip against the average cohesion values of that same tip, a CAB plot can be produced as described earlier. The cohesive values used for the plots were an average of the cohesive measurements made both prior to and after inhaler component force measurements with an individual tip. CAB plots showing the average F_{adh}/F_{coh} of the anhydrous BDP and the BDP clathrates are shown in figures 3.16, 3.17 and 3.18. The bisecting line on each plot represents parity between adhesive and cohesive forces, where above this line cohesion is dominant ($F_{coh} > F_{adh}$) and below, adhesion dominates ($F_{adh} > F_{coh}$). Once the adhesive force values from each tip have been plotted against their cohesive force value, the plot points were analysed for a linear fit with respect to a given substrate. Each fit is graphically labelled and displayed with the coefficient of determination (R^2) and graphical equation (CAB ratio / gradient of linear fit) to show firstly how well the linear model fitted the data points and secondly what the dependent CAB ratio of that linear regression for tip material to surface was.

Figures 3.16, 3.17 and 3.18 show that there is very little compliance to a linear fit across any of the data sets. There is only one R^2 value in excess of 0.7, with the remainder below 0.5. The anhydrous BDP tip series (fig. 3.14) has two tips (2 and 3) that show more cohesive than adhesive character on the coated canister but then the other (tip 1) then shows the opposite trend (R^2 0.41, $y=1.31x$). Two tips (1 and 2) show more adhesive character than cohesive on the uncoated canister but, the other tip (3) again reverses this trend (R^2 0.59, $y=0.95x$). Notably in this instance tip 1 lies very close to the bisection that represents adhesive and cohesive force parity. All three tips do show greater adhesive character than cohesive with respect to the metering chamber, but these plots still do not show a good linear relationship and have the worst coefficient of determination out of the three APIs (R^2 0.33, $y=0.55x$). The CAB plots for the BDP CFC-11 tips (figs. 3.17) follow a similar pattern where 2 tips of the three (1 and 2) for both the coated (R^2 0.41, $y=1.27x$) and uncoated (R^2 0.59, $y=0.95x$) canister lie on the adhesive side of the intersection but with the 3rd tip lying on cohesive side. The un-coated canister has all three tips well across the intersection on the adhesive side and on this occasion the linear fit of these plot points show a better correlation (R^2 0.89, $y=0.33x$). The BDP IPA tips (fig. 3.18) show the least consistency in tip adhesion relationship. Two tips on the coated canister (1 and 3) are cohesively dominated, with one (2) that shows more adhesive character (R^2 0.27, $y=0.86x$). Two

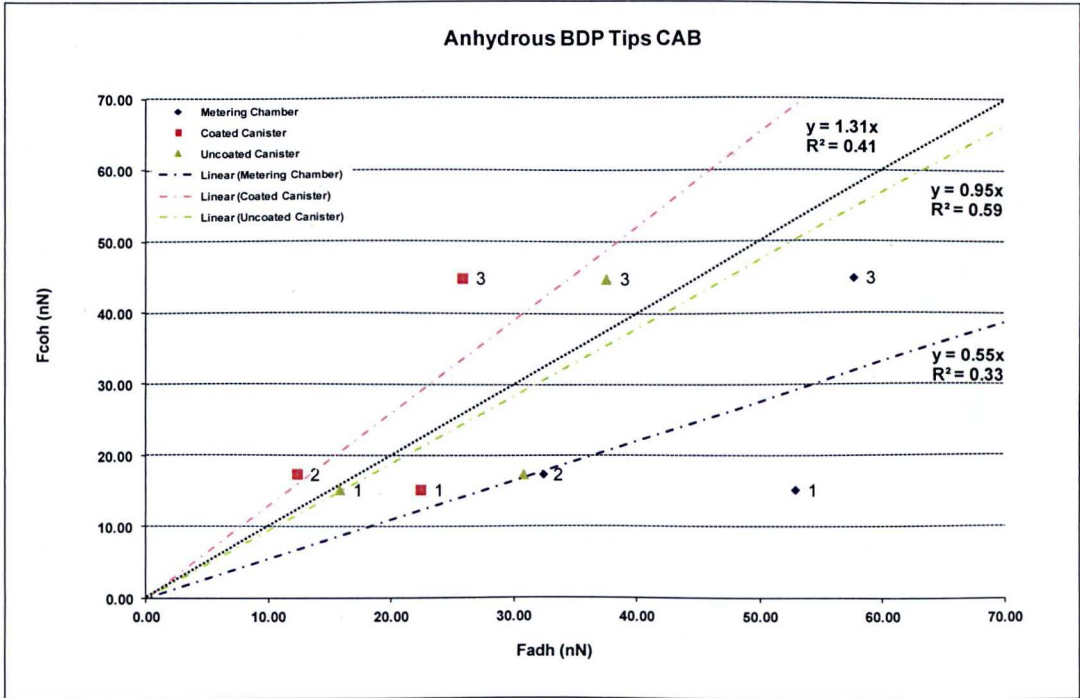


Fig 3.16 CAB plot for anhydrous BDP tips against pMDI components

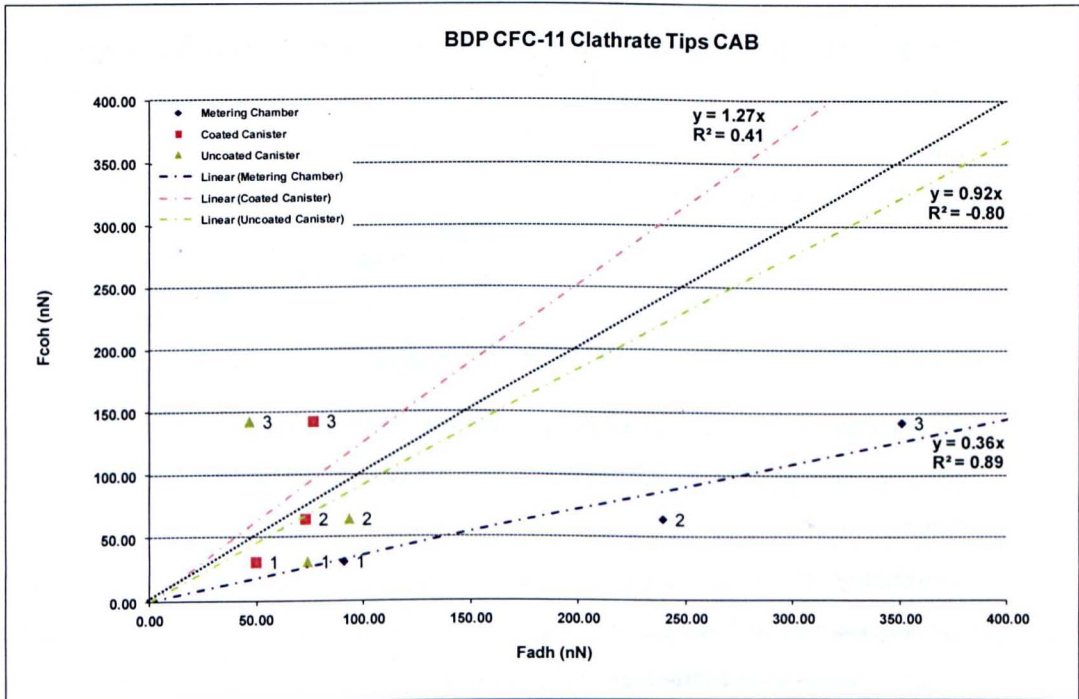


Fig 3.17 CAB plot for BDP CFC-11 tips against pMDI components

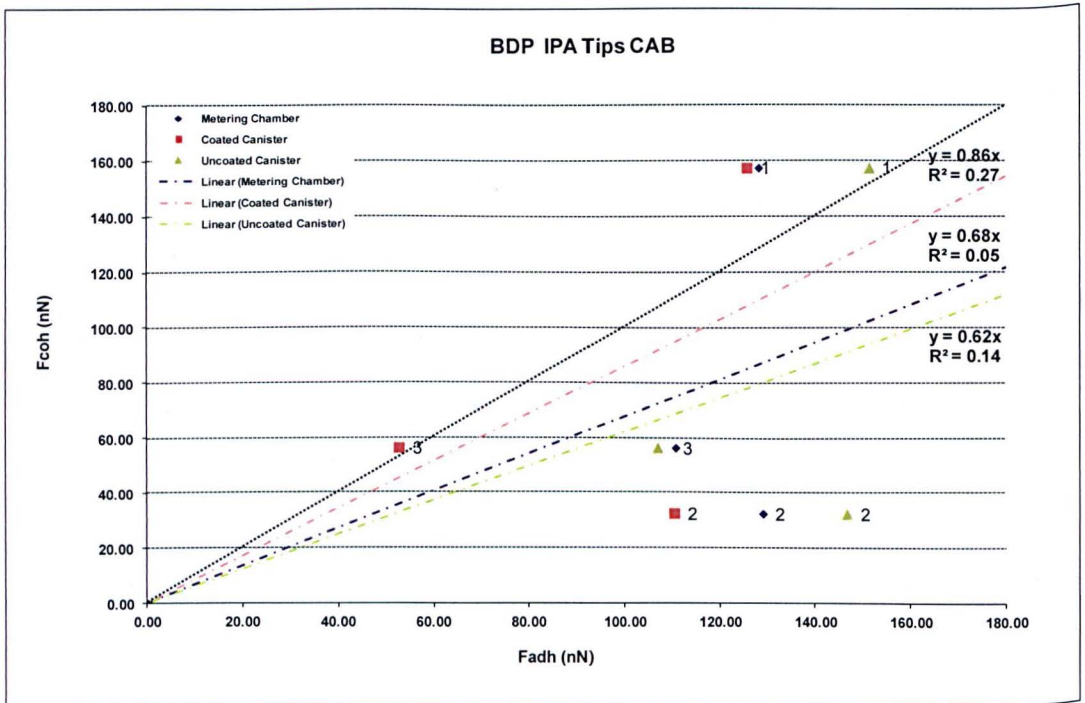


Fig 3.18 CAB plot for BDP IPA tips against pMDI components

tips on the uncoated canister (2 and 3) show adhesive tendency with one again (tip 1) reversing this trend (R^2 0.14, $y=0.14x$), and in this instance while two tips (2 and 3) show significant adhesive dominance on the metering chamber, one (tip 1) shows an unexpected cohesive favourability (R^2 0.05, $y=0.68x$).

3.4.3.3 SEM Characterization of Functionalized Tips

Figure 3.19 shows SEM images of one of the functionalized tips of each BDP tip material both prior to, and after force data acquisition. This was performed to both confirm successful tip functionalization and also allow for identification of any obvious changes to tip particle morphology that might suggest a critical failure of the contact regime. All 9 functionalized tips were confirmed as having been functionalized successfully. Notably all three particles are very large in comparison to the blank tips, especially the BDP CFC-11 clathrate which occupies a large area of the DNP-S cantilever. In all cases, while some contamination of the rest of the cantilever

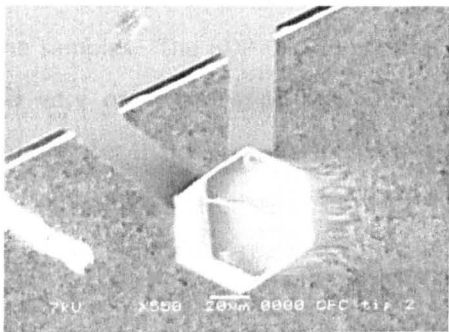
A1



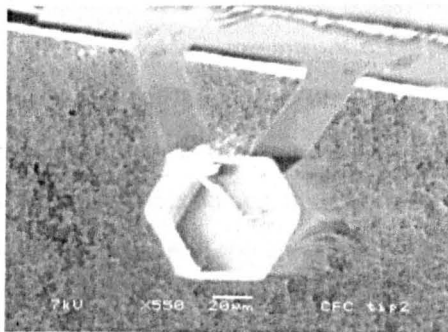
A2



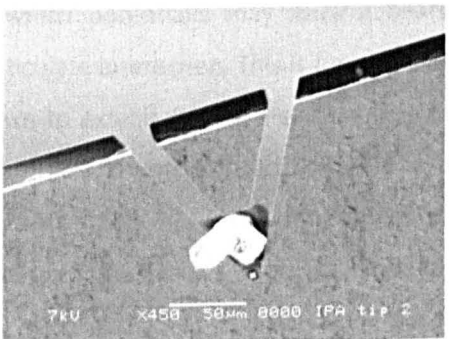
B1



B2



C1



C2

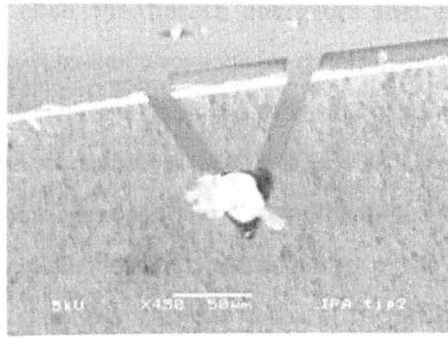


Fig 3.19: Low Vacuum SEM images of functionalized tips of A) Anhydrous BDP, B) BDP CFC-11 Clathrate and C) BDP IPA Clathrate both prior to (1) and after (2) AFM force curve acquisition

chip by particulate matter can be seen, there is was no obvious critical change to the functional particle morphology. However two of the tips did pick up contaminant material near the functional particle (fig 3.19 A2, C2) during use, and while this does not look to have impacted the assumed contact area this cannot be guaranteed. Furthermore on the SEM images of some tips the resin used for particle attachment was visible (fig. 3.19 C1, C2) beneath the functional particle. Because this was topographically hidden it was deemed acceptable and unlikely to cause any interference in the force data acquisition. These images were typical of the whole set of the functionalized tips.

3.5 Discussion

3.5.1 Characterization of Beclomethasone Dipropionate and the Beclomethasone Dipropionate Clathrates

3.5.1.1 SEM and AFM Analysis

The morphological differences seen between the powder samples in the SEM images (fig. 3.1, 3.2 and 3.3) were as expected. Typical micronization procedures where larger particles are smashed up and broken down, render inherently more cohesive, smaller particles with increased surface energies as exemplified by the anhydrous BDP micronized sample (fig. 3.1). The AFM images of the anhydrous BDP (fig. 3.8 A) support this view, by showing a rough and inconsistent surface, with some areas having roughness values around 10 times in excess of the crystalline samples. The BDP CFC-11 clathrate particles (fig. 3.2) were in contrast crystals that exhibit a very organized appearance with smooth flat surfaces that are consistent with particulate matter that has crystallized into an ordered structure. However, while the BDP CFC-11 clathrate particles showed consistent shape and surface morphology, they were very diverse in size and in general the particles were much larger than those of the anhydrous BDP and BDP IPA clathrate.

The ordered structure of this sample highlighted the different crystal faces that exist, as shown above, which potentially may have a bearing upon the surface energetics that influence interparticulate interaction. This is for the reasons described above where different crystal faces are known to exhibit different surface energies dependent upon the molecular orientation at that crystal face (Hooton et al, 2008). This ordered crystalline structure is well reflected in the AFM data (figs. 3.8 B, 3.8 C) with consistently homogeneous and flat topographies with low extracted roughness values (table 3.1). Indeed the CFC clathrate was the flattest of the samples by AFM, with an R_q and R_a about half the IPA clathrate. The two faces of the BDP CFC-11 clathrate showed small differences, where although both were smooth and equally as flat (R_q and R_a data was merged) there appeared differing surface artefacts. The lateral face showed some degree of grading and a higher proportion of what appear to be surface fractures. While the main face did show a lesser degree of fracturing, it also showed some small, rounded depressions. The cracks and fractures were attributed to small degrees of propellant escape in synthesis. It is unlikely that they are the result of sputter coating prior to SEM imaging because

the same fractures can be seen on the particles that were attached to the AFM tips and imaged without sputtering. The depressions however are currently unexplained but presumably reflect defects in the crystalline structure. These features were not considered significant, as the apparent integrity of the particles was upheld and the DSC traces that followed showed a suitable consistency.

The BDP IPA clathrate particles show less apparent order than the BDP CFC-11 clathrate particles. Although the SEM images of the BDP IPA clathrates (fig. 3.3) show plate-like crystals with flat surfaces, these particles show less reproducibility in particle shape. Particle size does however, seem more consistent than the BDP CFC-11 clathrate and although the particles are morphologically different from the micronized precursor they are not excessively larger. The AFM images (fig. 3.8 D) suggest that the IPA clathrate has a surface with features between the micronized BDP and the BDP CFC-11 clathrate. There is an obvious decrease in height variation compared to the precursor, but unlike the CFC clathrate, there is still some ridging and particulate heterogeneity. Importantly, however the SEM images distinguished the size difference between the CFC clathrate and the IPA clathrate, where on a $5\mu\text{m} \times 5\mu\text{m}$ image we are almost certainly on the face of a single CFC clathrate, whilst with the IPA clathrate and the anhydrous BDP the particle size range falls into this resolution, and it is not possible to rule out a multi-particle image of both which would lead to an increase in the estimation of surface roughness. However the roughness ranking of the API powders are consistent with what would be expected from the SEM images.

Notably the R_q values established for all the API powders are significantly larger than those of the model substrates used in previous CAB studies ($\sim 1\text{nm } R_q$) (Hooton et al, 2006, Jones et al, 2008a etc.). All the powders have to be used as a cohesive surface for a CAB and therefore their own surface roughnesses across particle contact areas are important. The BDP CFC-11 clathrate was the least rough of the substrates, but remained in the region of 10x rougher than the recrystallized crystals manufactured for use in model systems. The anhydrous BDP is in the order of 100x rougher than an ideal substrate and the IPA clathrate 20x so. It could be expected therefore that the CFC-11 clathrate would show the most promise at providing a consistent cohesive surface at the very least, and that the anhydrous BDP is the least likely powder substrate to show microscale parity in contact geometry.

3.5.1.2 XRPD and DSC

The observed XRPD traces shown in figure 3.4 help prove the synthesis of the BDP CFC-11 clathrate, and rule out the presence of other polymorphs. The expected diffraction peaks calculated from the single crystal structure at 2 theta values of 7.2, 8.5, 9.6, 11.2, 13.8, 16.8 and 18.5° can be distinguished. There is therefore an appropriate correspondence to the calculated diffractogram of the clathrate, distinguishing the BDP CFC-11 clathrate from other BDP polymorphs. The intensities are lower and the peaks are broader in the observed sample, but this is not unexpected, due to the potential for some disorder in the crystal structure to exist as introduced in the process of synthesis, handling, sample preparation and presentation. Any physical impurity, can lead to a broadening in diffractogram peaks and it is important to note that the CFC-11 within the host molecules, is not accounted for in the calculated single crystal structure. The existence of the propellant in the molecular structure elicits the broad peaks after 18.5° 2 theta as the guest molecule shows significant disorder in differing orientations within the host BDP. Hence figure 3.4 suggests a sample with good phase purity. This data was therefore accepted in proving the BDP CFC-11 clathrate synthesis. The process could not be repeated for the BDP IPA clathrate because the structure has not been solved and therefore no reference exists. However an XRPD diffractogram was compiled (fig 3.5) and the peaks were similar in nature to the CFC-11 clathrate up to 18.5° 2 theta with small differences beyond. The DSC traces performed also go some way into proving this was a clathrated structure as described below.

The DSC traces obtained in figure 3.6 prove several key points. All the samples show a consistent endotherm that corresponds to the melting point of BDP at around 213°C (Vervaet, Byron, 1999). The thermograms for the BDP CFC-11 clathrate and the BDP IPA clathrates show energetic events not present in the anhydrous BDP sample. Distinct exotherms around 91°C are followed rapidly by endotherms at around 95°C in the BDP CFC-11 clathrate sample. The BDP IPA clathrate samples also show a significant broad endotherm prior to melting at around 142°C, although no exothermic event can be distinguished prior to this. It is proposed that these events relate to a solid state rearrangement of the clathrates, or rather declathration, where the propellant is released as the caged structure changes (Bouhroum et al, 2009). At a certain temperature the molecular structure of the clathrate changes in response to the thermally induced increased molecular freedom. The loss of the typical caged structure is accompanied by

a release of the encaged propellant. The loss of the propellant corresponds to the exothermic event, whilst the solid state rearrangement is endothermic. Considering the BDP CFC-11 clathrate samples, both such events can be seen, although interestingly the exotherm precedes the endotherm. This suggests that the increasing molecular mobility of the CFC-11 with temperature, reaches a point where the molecules can simply escape clathration, and that this loss of the encaged molecules leads to a collapse of the molecular structure of the BDP and subsequent re-arrangement. However, the BDP IPA clathrate thermograms do not evidence such an exotherm prior to a 'rearrangement endotherm'. This may be related to the fact that propellant release and solid state rearrangement will occur almost simultaneously, and that if the critical temperature at which declathration occurs is higher (as it appears in the BDP IPA clathrate) then the process may be more instantaneous and the endothermic transition will mask the propellant release. Alternatively, the DSC traces for the IPA clathrate show that the rearrangement endotherm is much broader than that of the CFC clathrate, and may reflect a more complicated or drawn out change in chemistry. What is however clear from the cyclic DSC traces of the clathrated samples (figs. 3.7 A and B), is that these processes are irreversible. This is indicative of a non-reversing phase transition that supports the notion of a solid state rearrangement and the loss of propellant.

3.5.2 Characterization of the pMDI Components

The SEM and AFM imaging of the pMDI components show significant differences between the three selected inhaler component surfaces. The effect of FEP coating of the canister wall can be seen quite clearly on SEM and AFM imaging. The SEM image (fig. 3.9 A) shows that on the microscale the FEP coat gives a very smooth surface, albeit with a layering effect that induces some small ridges across the surface. This homogeneity of the surface, coupled with the chemistry of the coating itself would be expected to significantly reduce interactions between the formulation and the canister wall, and provide a surface most capable of conforming to a CAB relationship. Critically however, the fact that the coating is not complete in some areas leads to a prospective duality in the reactive nature of the canister wall, as well as potentially inducing inconsistent tip surface contacts that would disturb a CAB. The AFM images (fig. 3.10 A) further suggested that while the coating appears to render large areas of flat and

homogeneous surface, there exist several induced surface asperities. These may possibly be explained as excessive deposits of coating, and in some cases these were very significant in scale, reaching in the region of 300nm above the relative surface structure. Most were also quite broad and contrasted with the sharper asperities seen on the metering chamber (fig. 3.10 C), but by virtue of inducing an increased level of surface roughness, would still be expected to alter the geometry of any particle contact at those points and increase the range of interaction scale across the surface.

The uncoated canister would be expected to offer more variability in interparticulate interactivity and contact geometry. This is because the surface was seen to possess many more obvious surface imperfections by SEM and AFM. The topographical variation by surface rutting, scratching and folding is very evident and although the AFM measurements (fig. 3.10 B) of these features suggest that they are of a similar size to those features on the coated canister they are much more frequent. SEM images of the metering chamber seemed to suggest it was the roughest surface with a multitude of topographical features and significant surface heterogeneity (fig. 3.9 C). However the smaller scale AFM images (fig. 3.10 C) are not convergent with the SEM images collected over a larger area. The AFM images appear to suggest that the surface morphology and topography at the microscale shows significantly different consistency than that on the macroscale, and this is borne out by the AFM derived roughness values seen in table 3.2.

These values reflect this unexpected observation by suggesting the metering chamber is of a similar roughness (R_q) to the coated canister wall. The larger deviations around the R_q and R_a of the metering chamber correspond to a lack of consistency within the surface features, but this is still surprisingly low considering the SEM images. The uncoated canister is in the region of 1.5 to 2 times rougher than both the other pMDI components and would therefore seem to be the least suitable surface substrate for CAB assessment. The metering chamber, despite the low R_q assessment would still be expected to conform less well to a CAB balance than the coated canister because of the microscale inconsistency that would deter an as consistent surface contact model. The R_q values calculated for all three pMDI components were in excess of the ideal substrates used in previous CAB studies by some distance. Even the coated canister showed an R_q of 20x larger than the 1nm standard. Therefore, combined with the roughness measurement of the powder samples it would suggest that a CAB balance would be severely

stretched to provide a useful model on these 'non-ideal' materials, but that if any relationships were to hold true, the balance between the BDP CFC-11 clathrate and coated canister would theoretically be the most likely.

3.5.3 The Cohesive Adhesive Balance of the BDP APIs and pMDI Components

The force data that was acquired with the functionalized tips was very diverse and variable. As established earlier, because each individual tip presents a different and uncharacterized contact regime, even with a flat surface, the absolute adhesion values cannot be compared directly between tips and powder samples. However the different tips should elicit the same proportionality of adhesive response from surface to surface, if the contact geometry for a normalizing cohesive measurement is the same as for an adhesive measurement. This is because with reproducible interparticulate forces in a controlled environment, the only variation in interaction will be the contact area. Assuming flat substrates, this variation is limited to the topography of the individual tip, and the contact geometrics of that topography would be the same across all the substrates. Therefore any increase in adhesion from surface to surface, should be proportionally mirrored by each tip the same series. However from the average force data acquired in figures 3.11, 3.12 and 3.13 it can be seen that this is obviously not so in these data sets, and that in all three tip types, several samples have very dissimilar tip to tip proportionalities. The CAB plots (figs.3.16, 3.17 and 3.18) reflect this same variability in results as they are simply a graphical representation of the ratio of the adhesive forces to the cohesive. With tip to tip values varying disproportionately from substrate to substrate, there is little linearity in any of the tip plots as highlighted by the consistently low R^2 values and wide point scatter. If the balance was to have held true for these particulate and component samples then some suggestion of a linear fit would have been the consequence of a close to proportional movement in adhesion from tip to tip with cohesion. This immediately suggests a failure of any consistency in contact area for tip material contact. This is not totally unexpected but provides a level of quantification to the level of roughness that cannot be accommodated in the CAB analysis approach. Such a failure could be a sign that the functional tip has been changed over time and the effective contact area differed, resulting in adhesion force differences. The SEM images before and after force data acquisition suggest there were no obviously critical

differences in the tip morphologies, although as the SEM is limited to a 2D microscale assessment it is unclear whether the actual nanoscale point of contact on the functional tips was subject to wear or collapse etc. There is also the impact on AFM force measurements of technical inaccuracies.

This is plausible when we consider the large relative size of the functional particles on the cantilevers. The assumption that the cantilever can function correctly under the weight and dynamics of functionalization is not as yet known. Indeed with the BDP CFC-11 clathrate in particular the DNP-S cantilever is dwarfed by the particle and on several occasions, deflection and hysteresis could be observed on the AFM outside of surface to surface contact. Figure 3.15 BDP CFC shows two force curves (A and B) that were recorded using a BDP CFC-11 functionalised tip. BDP CFC A was a useable trace that shows a large but analysable adhesion. Even in this instance however the tip approach is not smooth, with some undulation that may reflect either some scattered laser light hitting the photodiode, or cantilever flex under the weight of the functional particle. This has the effect that the deflection signal from the AFM that defines the adhesion of the tip to surface is subject to large errors based in the cantilever's modified behaviour. The difficulty in recording a force curve with such functionalized tips was further typified by the high output of unusable traces such as fig. 3.15 BDP CFC B. The adhesion in this instance was so big as to prevent the full and proper movement of the tip through its approach and retract cycle. Here the particle tip appears to have made a massive jump in and remained 'stuck' to the surface for vast majority of the remaining tip motion. The large nature of these particulate tips means that the effective contact area of the tip is increased significantly beyond that of a bare tip. Although this causes no problems theoretically, it does have the significance of leading to such large adhesions that they have the potential to exceed the capability of the cantilever to quantify completely, or as above, prevent an entire force curve from completing. Indeed in several cases such as fig. 3.15 BDP CFC B, the adhesions were so large that they exceeded maximal cantilever deflection (that can be sensed by the AFM photodetector), which forced the analysis (where possible at all) to be based upon an extrapolation of the force curve recorded. This adds error into the assessment of adhesion and might help further explain the disparity of the force results from this model. As a consequence there was only a relatively low number of force curves collected for each tip on each surface. By limiting the number of curves used, the longevity of each tip was preserved, but as a consequence the data collected was

more likely to suffer from anomalous results, which may reflect some of the more obscure values seen.

However it is more than likely that the largest influence on the force data is the combined effect of the roughness of the substrates. The values collected by the AFM suggested that the materials ranged from 10 to 100 times rougher than the CAB standard of 1nm R_q , and that the influence of asperities or depressions may well be significant even on this scale. Figure 3.20 shows particle surface contacts on a smooth and rough surface. A particle contacting a smooth surface has much more accurately calculable and reproducible contact geometry. A particle contacting on a rough surface however has a multitude of differing contact regimes dependent upon the site of interaction (Rabinovich et al, 2000a, Rabinovich et al, 2000b). Indeed multiple asperities smaller than the particle may reduce the contact area and the adhesion force, while a variety of asperities larger or of a given orientation can serve to induce a variety of increased contact areas (Beach et al, 2001). This situation is complicated further when we introduce the concept of a non-spherical tip particle; where the geometric possibilities widen. Even with the smoothest cohesive and adhesive surfaces (the BDP CFC-11 clathrate and the coated canister wall) very variable and inconsistent data was recorded. This would seem to indicate that even nanoscale roughness in the region of 10-20nm (R_q) has led to significant alterations in contact geometries, capable of disrupting the CAB process beyond a workable limit. However there is a possibility, specifically in this case, that the large functional tip plays a significant role in this perturbation.

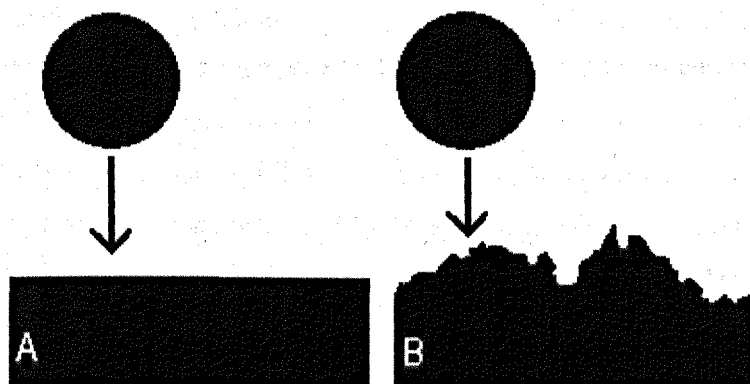


Fig 3.20 Hypothetical Spherical Particle Contact on A) Smooth and B) Rough surfaces

The fact the CFC-11 clathrate particle attachments were in the region of 20 μ m to 60 μ m and relatively smooth, means that the potential contact area was far beyond a 5 μ m square area. Combining the nanoscale roughness measured by AFM, the macroscale topographical variability seen on SEM and such large tip surface areas, this adds up to an unavoidably significant amount of surface to surface contact heterogeneity, even with low local R_q values. This may account for the significantly larger force values obtained with the BDP CFC-11 clathrate tips and the large degree of force variability seen. With the suspect contact mechanics of the functionalized tip, it would appear that the practical nature of the CFC clathrate as a functional tip may be a very limiting feature.

However fig. 3.15 BDP B and fig. 3.15 BDP IPA B also show two other rejected force curves from the other two tip materials where there was evidence of multiple points of adhesion and pull off points that compromised the F_{adh} assessment. The existence of these, would inherently suggest that a consistent adhesive and cohesive surface area was impossible, unless the same contacts were seen on all the force measurements with that tip. But as fig 3.15 BDP A and fig 3.15 fig BDP IPA A show they were not. The most likely explanation for the inconsistent occurrence of these traces is therefore the combination of tip particle and substrate roughness leading to highly variable contact regimes, with some multiple point contacts, depending on localisation. The very inability of the cohesive measurements prior to, and after adhesive force measurement, to produce consistent results, is particularly indicative of the challenge of applying a standard CAB approach to non-ideal materials.

Figure 3.14 shows some example box plots of the F_{adh} data from the three tip types on given substrates. These plots were used to make a non-parametric assessment of the force data. In so doing the mean and median of the data could be compared, and the key quantile values of these data sets with respect to the range of the data could be analysed. Principally, on a crystalline smooth surface, force distributions (given a consistent contact geometry) should appear Gaussian. In such instances it would be expected that the mean and median averages were the same. The further that parity is parted from, the further away from a Gaussian distribution the data will have moved. The further away from a Gaussian distribution the force data is, it would suggest a more and more inconsistent contact regime. As figure 3.14 A shows, the set of anhydrous BDP tips produced a box plot of reasonable consistency on their second cohesive measurements. As described above there was no expectation that absolute F_{adh} should

be similar due to the expected differences in contact geometries between tips, but the mean and median averages were relatively close and the 1st and 3rd quartiles showed a similar relationship to the extremes of the data (with the exception of tip 3). From this we could infer that these tips had a reasonable reproducible contact regime and that a close to Gaussian distribution of the adhesive forces was complied.

However as figure 3.14 B and 3.14 C show, this was not the case with other tip to substrate sets. The BDP CFC-11 tips second cohesive data set (fig. 3.14 B) shows that the first tip had a massive disparity between the median and mean average F_{adh} . In fact due to the huge range generated by the F_{adh} point extremes, the mean was dragged above the 3rd quartile. The 2nd tip also shows quite a difference from the 2nd quartile to the mean, while the 3rd tip is somewhat closer. The BDP IPA tip example (fig. 3.14 C) again shows a large variation, tip to tip, in the coherence of the statistical descriptors. This was common to many of the other tip to surface sets. What this further describes is that the contact regimes of the individual tips were not just inconsistent from substrate to substrate, but also between measurements on the same surface. The disparity of the mean from the median in many of the tip to surface cases renders the mean as a largely invalid descriptor in these instances. However as already identified, the impact of tip and substrate roughness was so extreme as to visibly render the CAB data uncorrelated.

Yet, despite the challenged nature of the CAB data, and the lack of many linear regressions with good fits to the tip data, it is still possible to suggest some basic underlying trends. From these trends there are still some prospective conclusions that can be drawn about the interacting tip materials and inhaler surface components. Firstly from the data collected the relative affinity of each tip material for the inhaler components can be described as indicated by the data spread from the CAB plots (fig. 3.16, 3.17 and 3.18):

Anhydrous BDP tips:

Stainless steel metering chamber > Uncoated aluminium canister > FEP coated aluminium canister

BDP CFC-11 tips:

Stainless steel metering chamber > Uncoated aluminium canister > FEP coated aluminium canister

BDP IPA tips:

Uncoated aluminium canister > Stainless steel metering chamber > FEP coated aluminium canister

Despite the variability of these data, and the difficulty therein of drawing firm conclusions from them, these trends were much as expected prior to the study. Consistently across all three tip materials the FEP coated canister seemed to be the least adhesive surface, with most plot values for all tip types lying on or above the CAB plot intersection (i.e. $F_{coh} > F_{adh}$). This would infer that the powders were more interactive with themselves than the coating, which would be a significant benefit in an inhaled formulation and fits to the manufacturer's purpose. Furthermore the implied CAB ratios of 1.31, 1.27 and 0.86 with the anhydrous BDP, BDP CFC-11 and BDP IPA tips respectively were consistently higher than for the same tip sets on the other CAB substrates. Equally there is some evidence that the metering chamber was the most adhesive component with respect to all the powders, as virtually all the plot values lie well below the intersection ($F_{adh} > F_{coh}$) and for both the anhydrous BDP and BDP CFC-11 tip sets, linear fitting gave a significantly more adhesive CAB than for the fits for the coated and uncoated canisters (CAB ratios of 0.55 and 0.36 respectively). The CAB ratio extracted for the BDP IPA tip set on the metering chamber was also 0.68, although this was a less adhesive balance than with the uncoated canister in this instance. Importantly, the only good linear fit seen between a tip set, was that between the BDP CFC-11 tips on the metering chamber (fig. 3.17). Here the three tips showed a linear regression with a coefficient of determination of 0.89 and a CAB ratio of 0.33. This could be said to be a more confident indicator that the BDP CFC-11 tips had a very adhesively dominated relationship with the metering chamber and would be

likely to preferentially adhere to this surface in-device. However, the lack of consistency across the other tip sets renders this definition slightly obsolete, as there is no confident comparator.

This suggestion of an adhesive force balance may reflect a more adhesive chemical interaction between the metering chamber surface and the tip materials. Yet it is worth noting that using R_q roughness assessments can be somewhat misleading. This is because surfaces of very different topographies may measure close to the same R_q as all that is reported is the variability of height, around the mean height of a sample (i.e. the R_q of a flat surface with many depressions can equal a flat surface with many peaks). In this respect the similar R_q values calculated for the metering chamber and the BDP CFC-11 clathrate may have disguised the potential for each surface to generate consistent surface contact geometries, or as already highlighted simply been too small in scale to properly predict the tip particle surface contact regimes. Therefore it would seem that in agreement with visual characterization the metering chamber appears to have been the most variable of the substrates, with inconsistent surface topography leading to high variability in contact geometry and therefore F_{adh} .

The uncoated canister is the most ambiguous surface and little can as yet be suggested about the data plots for this material. The anhydrous BDP tips and BDP CFC-11 tips produced CAB ratios of 0.92 and 0.95 (fig 3.16, 3.17), very close to the centre line of 1 ($F_{coh} = F_{adh}$). Whilst this might have suggested a generally neutral or slight adhesive preference for these powders, the R^2 value of the anhydrous tip regression was 0.59, suggesting only a weak fit, and for the BDP CFC-11 tip regression -0.8, which infers no linear trend at all. Furthermore the BDP IPA tips (fig 3.18) show one tip that sits just above this intersection again, but then has two tips registering very adhesive values, that lead to a CAB ratio 0.62 and an R^2 value of 0.14. As such it is very difficult to draw any conclusions about this tip material.

3.6 Conclusion

It is apparent that the CAB approach, whilst offering a unique assessment of interparticulate adhesion in model formulations cannot be easily applied to 'non-ideal' materials. This is due to inherent surface topographies, even on small spatial scales, that render dissimilarities in cohesive and adhesive surface geometries that give rise to a collapse of the model. Whilst flat surfaces were hypothetically required to apply the model, to what extent this could be circumvented to reflect real pharmaceutical powders and device components was unexplored. It would appear however that with respect to the materials chosen in this study, the inherent surface roughnesses and large functional tip particles combined to exceed the limits of the cohesive adhesive balance approach and while to a limited degree expected trends could be identified, these remained statistically unproven. Certainly clathrated BDP particles, while offering relatively smooth surfaces, are not viable to work in a CAB study. Despite the reduced surface roughnesses, the large particle sizes formed in synthesis exaggerate particle contact regimes and serve to introduce critical variability in contact area genesis. Furthermore such particle sizes would seem to prove too large and inflexible to give accurate and sensitive tip functionality, with negative consequences upon AFM cantilever function. Hence while these molecular entities may be of interest and show lower surface energies than other polymorphs (Bouhroum et al, 2009), the CAB approach is not suited to qualifying or quantifying their interaction with pMDI components.

It could be suggested that despite the collapse of the CAB study with the materials investigated here, there is evidence to show that the FEP coated canister is effective at reducing interparticulate interactions with APIs. It may shift a marginally adhesively dominated relationship between the un-coated canister and APIs to a cohesively dominated relationship. This would of course be of large benefit in pMDI inhalers in avoiding dose loss to the inhaler housing. However due to the variable nature of the data collected and the problems outlined above, particularly with respect to the uncoated canister, this suggestion cannot be confirmed. Further work to establish whether the benchmark 1nm R_q marker used in previous studies is the maximal limit is appropriate and on-going alongside other refinements of the limits of a CAB approach and how it can be linked to other studies of formulation assessment. It remains unclear whether the CAB approach can be applied to 'real' materials in their entirety but it does

seem that such an approach may only work with very strict morphological controls of both tips and surface, or with some adaptation to the process yet to be developed.

3.7 References

- E.R.Beach, G.W.Tormoen, J.Drelich, R.Han. (2002) Pull-off force measurements between rough surfaces by atomic force microscopy. *Journal of Colloid and Interface Science*; 247:1:84-99.
- P.Begat, D.A.V.Morton, J.N.Staniforth, R.Price. (2004a) The Cohesive-Adhesive Balances in Dry Powder Inhaler Formulations I: Direct Quantification by Atomic Force Microscopy. *Pharmaceutical Research*; 21:9:1591-1597
- P.Begat, D.A.V.Morton, J.N.Staniforth, R.Price. (2004b) The Cohesive-Adhesive Balances in Dry Powder Inhaler Formulations II: Influence on Fine Particle Delivery Characteristics. *Pharmaceutical Research*; 21:10:1826-1833
- A.Bouhroum, J.C.Burley, N.R.Champness. R.C.Toon, P.A.Jinks, P.M.Williams, C.J.Roberts. (2010) An Assessment of Beclomethasone Dipropionate Clathrate Formation in a Model Suspension Metered Dose Inhaler. *International Journal of Pharmaceutics*; 391:98-106
- H-J.Butt, B.Cappella, M.Kappl. (2005) Force Measurements with the atomic force microscope: Technique, interpretation and applications. *Surface Science Reports*; 59:1-152
- P.Englezos. (1993) Clathrate Hydrates. *Industrial and Engineering Chemistry Research*; 32:7:1251-1274
- J.K.Eve, N.Patel, S.Y.Luk, S.J.Ebbens, C.J.Roberts. (2002) A study of single drug particle adhesion interactions using atomic force microscopy. *International Journal of Pharmaceutics*; 238:17-27
- J.C.Hooton, C.S.German, S.Allen, M.C.Davies, C.J.Roberts, S.J.B.Tendler, P.M.Williams. (2004) An Atomic Force Microscopy Study of the Effect of Nanoscale Contact Geometry and Surface Chemistry on the Adhesion of Pharmaceutical Particles. *Pharmaceutical Research*; 21:6:953-961
- J.C.Hooton, M.D.Jones, R.Price. (2006) Predicting the Behaviour of Novel Sugar Carriers for Dry Powder Inhaler Formulations via the Use of a Cohesive-Adhesive Force Balance Approach. *Journal of Pharmaceutical Science*; 95:6:1288-1297
- J.C.Hooton, M.D.Jones, H.Harris, J.Shur, R.Price. (2008) The Influence of Crystal Habit on the Prediction of Dry Powder Inhalation Formulation Performance Using the Cohesive-Adhesive Force Balance Approach. *Drug Development and Industrial Pharmacy*; 34:974-983

J.James, B.Crean, M.Davies, R.Toon, P.Jinks, C.J.Roberts. (2008) The surface characterization and comparison of two potential sub-micron sugar bulking excipients for use in low-dose, suspension formulations in metered dose inhalers. *International Journal of Pharmaceutics*; 361:209-221

M.D.Jones, H.Harris, J.C.Hooton, J.Shur, G.S.King, C.A.Mathoulin, K.Nichol, T.L.Smith, M.L.Dawson, A.R.Ferrie, R.Price. (2008a) An investigation into the relationship between carrier-based dry powder inhalation performance and formulation cohesive-adhesive force balances. *European Journal of Pharmaceutics and Biopharmaceutics*; 69:496-507

M.D.Jones, J.C.Hooton, M.L.Dawson, A.R.Ferrie, R.Price. (2008b) An Investigation into the Dispersion Mechanisms of Ternary Dry Powder Inhaler Formulations by the Quantification of Interparticulate Forces. *Pharmaceutical Research*; 25:2:337-348

M.Lohrmann, M.Kappl, H-J.Butt, N.A.Urbanetz, B.C.Lippold. (2007) Adhesion forces in interactive mixtures for dry powder inhalers – Evaluation of a new measuring method. *European Journal of Pharmaceutics and Biopharmaceutics*; 67:579-586

J.W.Mullin. (2001) Crystallization (4th edition) Butterworth-Heinemann, Oxford, UK

T.H.Muster, C.A. Prestidge. (2002) Face Specific Surface Properties of Pharmaceutical Crystals. *Journal of Pharmaceutical Science*; 91(6): 1432–1444.

E.M. Phillips, P.R.Byron. (1994) Surfactant promoted crystal growth of micronized methylprednisolone in trichloromonofluoromethane. *International Journal of Pharmaceutics*; 110:9-19

T.H.Plumridge, R.D.Waigh. (2002) Water structure theory and some implications for drug design. *Journal of Pharmaceutics and Pharmacology*; 54:9:1155-1179

Y.I.Rabinovich, J.J.Adler, A.Ata, R.K.Singh, B.M.Moudgil. (2000a) Adhesion between Nanoscale Rough Surfaces I: Role of Asperity Geometry. *Journal of Colloid and Interface Science*; 232:10-16

Y.I.Rabinovich, J.J.Adler, A.Ata, R.K.Singh, B.M.Moudgil. (2000b) Adhesion between Nanoscale Rough Surfaces II: Measurement and Comparison with Theory. *Journal of Colloid and Interface Science*; 232:17-24

J.E.Sader, J.W.Chon, P.Mulvaney. (1999) Calibration of rectangular atomic force microscope cantilevers. *Review of Scientific Instruments*; 70:3967-3969

D.Traini, P.M.Young, P.Rogueda, R.Price. (2005) The Use of AFM and Surface Energy Measurements to Investigate Drug-Canister Material Interactions in a Model Pressurized Metered Dose Inhaler Formulation. *Aerosol Science and Technology*; 40:227-236

D.Traini, P.M.Young, P.Rogueda, R.Price. (2006) In Vitro investigation of Drug Particles Interactions and Aerosol Performance of Pressurized Metered Dose Inhalers. *Pharmaceutical Research*; 24:1:125-135

C.Vervaet, P.R.Byron. (1999) Drug-surfactant-propellant interactions in HFA-formulations. *International Journal of Pharmaceutics*; 186:13-30

4.0 Application of the CAB approach to, and Characterization of Semi-Model Inhalation Substrates

4.1 General Introduction

4.1.1 Semi-model Substrates for CAB studies

Chapter 3 showed that the surface roughness constraints of the CAB approach are not sufficiently flexible to be extrapolated to unrefined API or device surfaces. Whilst a pure CAB was not possible without smooth crystalline surfaces, it was unknown as to whether a rough force balance characterisation could be performed that might better describe the materials used in real inhalation formulations. The general shortcomings of the CAB performed using the materials described in chapter 3 were indicative that substrate roughness and large functional particle sizes, stretched the model beyond its workable limits as defined by the contact region. However the concerns described relating to the viability of a pure CAB study in describing real formulation character still remain. It is therefore of interest as to whether an approach somewhere in the middle ground between these two extremes (i.e. crystal surfaces and micronized particulates) could bridge this gap. As such, if better considered functional particles and flatter and more consistent (topographically) CAB surfaces were able to yield a simple description of adhesive balance character, for a given API combination, this may still prove useful in relating to further '*in-vitro*' indicators of real formulation performance. Any links could then be potentially extrapolated to provide the basis of a quick and simple screening or characterization tool.

4.1.2 Modification of CAB materials

In modifying the failed CAB technique application to raw surfaces from chapter 3, there is a desire to account for the two identified critical factors. Firstly the particulate tips should be of a size conducive to controlled cantilever contact mechanics. They should generate particle to particle contact on as small a scale as possible, (ideally one to one) to reduce topographical variability being exaggerated. Secondly CAB surfaces should be made to be as topographically smooth as possible so as to reduce unavoidable differences in contact geometries. It is also

important to determine whether any alterations to the CAB materials in achieving these effects occur without significantly compromising the physicochemical makeup of the material form i.e. the inducement of polymorphism etc. Otherwise the distinction between a 'real' surface and a 'model' surface is reduced. This therefore dictates that the surface chemistry should not be changed, surface contamination should be avoided and environment specific behaviours eliminated. This therefore limits the approaches that can be used to better 'idealise' the real material surfaces, but protects the validity of so doing so. In this chapter the investigatory approach adopted was to compress the free powder of a range of inhalation APIs into a powder disc. In so doing to attempt to generate a semi-model substrate with improved topographical character and investigate the process as a means of generating an API surface that is better suited for a CAB experiment than the raw powder yet without needing a recrystallization process. This chapter therefore proceeds by looking at the effect of such compression on API surface roughness, whether this will allow a more consistent evaluation by AFM methodology and more specifically, a fundamental CAB assessment of two APIs.

4.2 Chapter Aims and Objectives

4.2.1 Chapter Aim

The aim of this chapter was to characterize and investigate the use of 'semi-model' processed APIs as a substrate for AFM investigations and in particular as a means to perform a CAB study between designated combinations of inhalation APIs. In so doing to examine the functionality of a compromise between 'model' crystalline surfaces and the 'non-ideal' formulation materials in providing an assessment of the force balance between two APIs.

4.2.2 Chapter Objectives

The objectives of this chapter were as follows:

- To examine the impact of API powder compression upon the ease of application to AFM based imaging and force based investigations.
- To determine the effect of API compression in reducing API surface roughness.
- To determine the effect of API compression upon surface specific morphologies, topographies and physicochemistry.
- To attempt to extract a rough force balance between combinations of compressed APIs using a modified CAB methodology.

4.3 Materials and Methods

4.3.1 Materials

4.3.1.1 Active Pharmaceutical Ingredients

Beclomethasone dipropionate (BDP), salbutamol sulphate (SS), budesonide (BUD), salmeterol xinafoate (SX) and fluticasone propionate (FP) were chosen for investigation due to their prominence of use within inhaler formulations in modern medicine, and both the subtle and significant chemical differences between the APIs within their classes, and between their classes respectively. The micronized powders were all provided by 3M Healthcare (Loughborough, UK). All other reagents and accessories were provided by Sigma Aldrich Company Ltd (Gillingham, UK).

4.3.2 Methods

4.3.2.1 API Powder Compression

The API powders were compressed using a manual hydraulic Specac IR press model 15011 (Specac Ltd., Kent, UK) to provide significantly smoother API surfaces for CAB experimentation while still retaining strong physicochemical similarities with the parent free powder. Sufficient powder to form a solid compress was filled onto a stainless steel pellet fitted within a 13mm cylindrical IR die. This was sealed off with a second steel pellet after minor damping of the powder and removal of any excesses and spillage. The assembly was then attached to a base unit with an air outlet feeding from the die. The entire cast was loaded into the press housing, where a metal punch was loaded into the cast column and manually lowered onto the topmost pellet. By using an adjustable upper bolster on the punch, maximum manual compression was applied, before a vacuum pump was attached to the air outlet at the bottom of the cast. The vacuum pump was then activated and the desired pressure on the system was induced via a manual pumping process. The API discs produced were formed using a 10 ton pressure application for two minutes. The discs were carefully removed from the die and placed into a

desiccator until required for use. The discs were mounted to a double sided sticky carbon stub attached to an SPM specimen disc before SEM or AFM imaging and force interrogation.

4.3.2.2 SEM Imaging

SEM images of the morphology and topography of the powdered and compressed APIs were collected by a JEOL JSM-6060LV scanning electron microscope (JEOL Ltd, Tokyo, Japan) at various magnifications under vacuum. Powder samples were sprinkled directly onto a double sided sticky carbon stub mounted on an SEM sample holder before being compressed lightly with a sterile glass coverslip and nitrogen gassed to remove excess deposits that might detach in the sample chamber. Compressed powder discs were mounted directly onto the carbon stubs. All API material samples were sputter coated in gold using a Balzers Benchtop Sputter Coater SCD 030 in an argon atmosphere (50Pa) at 30 mA for 4 minutes before SEM imaging took place. The functionalized AFM cantilevers were also imaged by SEM prior to force balance determination in order to confirm the functionalization process and examine the attached particulates. The tips were placed on a sliver of silica gel attached to a carbon stub and were not sputter coated to allow their use after imaging. Subsequently low vacuum mode was used to allow SEM images of these cantilevers without charging.

4.3.2.3 Differential Scanning Calorimetry

A TA Instruments DSC 2920 differential scanning calorimeter (TA Instruments, Delaware, US) was used to perform all DSC work. DSC was used to compare the pre- and post- compressed API powders in order to identify any obvious differences in physical transition that might suggest a significant impact to the physicochemical state of the APIs by the compressive force used in the powder compression process. Accurately weighed samples of about 6 mg were sealed in aluminium hermetic pans, equilibrated at 0°C, kept isothermal for 3 minutes and then heated at 10°C per minute under nitrogen to just above the reference melting points of each of the APIs (250°C for BDP and SS, 350°C for FP and 160°C for SX). Disc samples were collected and analysed after deliberate fragmentation of compressed API discs. Thermograms produced were analysed using TA universal analysis –NT software (TA Instruments, Delaware, US).

4.3.2.4 AFM Imaging and Roughness Measurements

AFM images were acquired in a tapping mode operation with TAP300 (BrukerNano, Coventry, UK) tips using a Dimension 3000 AFM (BrukerNano, Coventry, UK). Each tip was loaded into the tip holder and then optically aligned, before the resonant frequency was determined using the operating software. Height and phase images were then collected using the calibrated resonant frequency over spatial distances of $5\mu\text{m} \times 5\mu\text{m}$ and $10\mu\text{m} \times 10\mu\text{m}$ at between 1.5 - 2Hz for topographical and morphological visual characterization and surface roughness comparison between APIs and the pre- and post-compressed powder forms. 5 images were collected at both scan sizes across the same API samples (powder or compress) with a minimum of $50\mu\text{m}$ spatial difference in either x or y. Images were flattened and noise reduced before presentation using Nanoscope 7.3 (BrukerNano, Coventry, UK). Roughness measurements were made using the same software but prior to any image processing so as to avoid any bias to the raw data. The roughness measures used were the root mean square roughness (R_q) and the arithmetic mean roughness (R_a) alongside the maximum surface feature height (R_{max}) which was included to identify the extent of idiosyncratic feature occurrence and variability, even if unrepresentative of the bulk of the surface topography. The derivation of the former roughness parameters was discussed in chapter 3, while the R_{max} represents the maximum height deviation from the average surface level across a given surface area.

4.3.2.5 AFM Work of Adhesion and Surface Energy Measurement

Surface energy measurements were carried out on the compressed API pellets using three silicon nitride DNP-S (short, thick) tips (BrukerNano, Coventry, UK). These tips were chosen due to their low spring constants and therefore high sensitivity to adhesion forces. The force of adhesion (F_{adh}) between each tip and the substrates was measured by collecting 25 force curves on each material after deflection sensitivity calibration on a non-deforming silicon wafer, and prior to tip self-imaging on a TGT-1 tip grating (NT-MDT, Moscow, Russia). The F_{adh} and tip radii were then calculated using Nanoscope 7.3 (BrukerNano, Coventry, UK) software using the force curves and tip images obtained. Using the following equation it was then possible to calculate the work of adhesion (W_A):

$$W_A = \frac{2F_{adh}}{3\pi R} \quad (4.1)$$

Where R is the radius of the contacting tip. (This equation assumes the Johnson-Kendall-Roberts model of contact). The surface free energy (γ_1) of the API substrate could then be calculated using the following relationship:

$$W_A = 2\sqrt{\gamma_1\gamma_2} \quad (4.2)$$

Where γ_2 is the surface free energy of the silicon tip, assumed to be a reference 42mJ m^{-2} (James et al, 2008).

4.3.2.6 AFM Tip Functionalization

Contact mode DNP-S (short, thick) tips (BrukerNano, Coventry, UK) were used for functionalization by the same practical method as indicated in chapter 3. However in this instance they were functionalized using a Multimode AFM with a Nanoscope V controller and Nanoscope version 8.10 software (BrukerNano, Coventry, UK). The spring constant of each tip was determined by the AFM software using a thermal noise method (Hutter, Bechhoefer, 1993). Ten functionalized tips were prepared in total, 5 with micronized (anhydrous) beclomethasone dipropionate and 5 with salbutamol sulphate. An epoxy resin (Loctite, Henkel Ltd, Hatfield, UK) was applied to a silica disk and placed onto the AFM stage. A sacrificial AFM tip was used to draw thin lines of the adhesive from bulk several times until a very thin strand of adhesive was accessible. The blank cantilevers were placed in the tip holder, optically aligned to allow their spring constant to be calculated and then manually lowered on to these glue strands until contact was observed via laser deflection or visually, before removal. The resin substrate was then removed and replaced with the appropriate powder sample. The powder samples were sprinkled onto double sided sticky carbon stubs mounted on an SPM specimen, and blown down with a nitrogen tap to remove any excess powder. Using the AFM microscope small individual powder particles or agglomerates were resolved, identified and aligned with the position of the tip. The cantilever was then lowered manually onto the powder particles for attachment and

then removed. Great care was taken to identify small and isolated particulates to minimize the chance of multiple uptake or excessively large functional masses. The functionalized tips were left to dry for 24 hours. Successful tip functionalization was confirmed by low vacuum SEM imaging as described above.

4.3.2.7 Cohesive Adhesive Balance Measurements

AFM based CAB force measurements were carried out using an EnviroScope AFM (BrukerNano, Coventry, UK) with a NanoScope IIIa Controller according to largely the same methodology as described in chapter 3. In this instance 100 force measurements were taken by each functionalized tip on both the adhesive and cohesive surfaces and both the powder compress surfaces were given positive and negative ion bombardment via a antistatic gun (Milty Zerostat 3, Fisher Scientific, Loughborough, UK) to eliminate electrostatic build up as a consequence of the compression process. Force measurements were performed after automatic raster of the sample relative to the tip, by steps of $1\mu\text{m}$ in the x and y direction after each individual measurement. This was to examine the adhesive force spread across a larger area of the substrates and avoid any bias to anomalous regions of topography or contamination etc. Humidity was again kept as close to 0% RH as possible to minimize capillary interaction, with no rises above 5% during operation tolerated. Once the F_{adh} and F_{coh} had been extracted from the force curves these values were averaged and then plotted against each other on a tip by tip basis to generate a CAB plot for each API tip type. Linear fitting was then applied to each tip set to attempt to identify any trend appreciable as a CAB.

4.4 Results

4.4.1 AFM Derived Surface Free Energy Determination of Compressed APIs

Figure 4.1 shows the AFM calculated average surface free energies (γ) of the inhalation APIs beclomethasone dipropionate (BDP), salmeterol xinafoate (SX), salbutamol sulphate (SS), fluticasone propionate (FP) and budesonide (BUD) after compression in an IR press. Table 4.1 breaks down these results to the force of adhesion (F_{adh}), work of adhesion (W_A) and surface free energy of the APIs as ascertained by each of the individual AFM tips. Figure 4.1 shows that of all the APIs investigated SS showed the greatest surface free energy with an average $45.3\text{mJ/m}^2 (\pm 5.7)$. The other beta₂-agonist SX, averaged $37.1\text{mJ/m}^2 (\pm 3.9)$, but was superseded by BDP with an average surface energy of $39.2\text{mJ/m}^2 (\pm 2.9)$. Both these APIs did however show greater consistency between the three tip measurements than SS, with smaller standard deviations. The two remaining corticosteroids FP and BUD showed reduced average surface energies at $27.7\text{mJ/m}^2 (\pm 6.6)$ and $29.9\text{mJ/m}^2 (\pm 8.3)$ respectively. Notably both these APIs showed large inconsistencies in measurement, and BUD in particular showed a significantly exaggerated standard deviation in calculated W_A and surface energy between the AFM tips, predominantly between the first and remaining two (table 4.1).

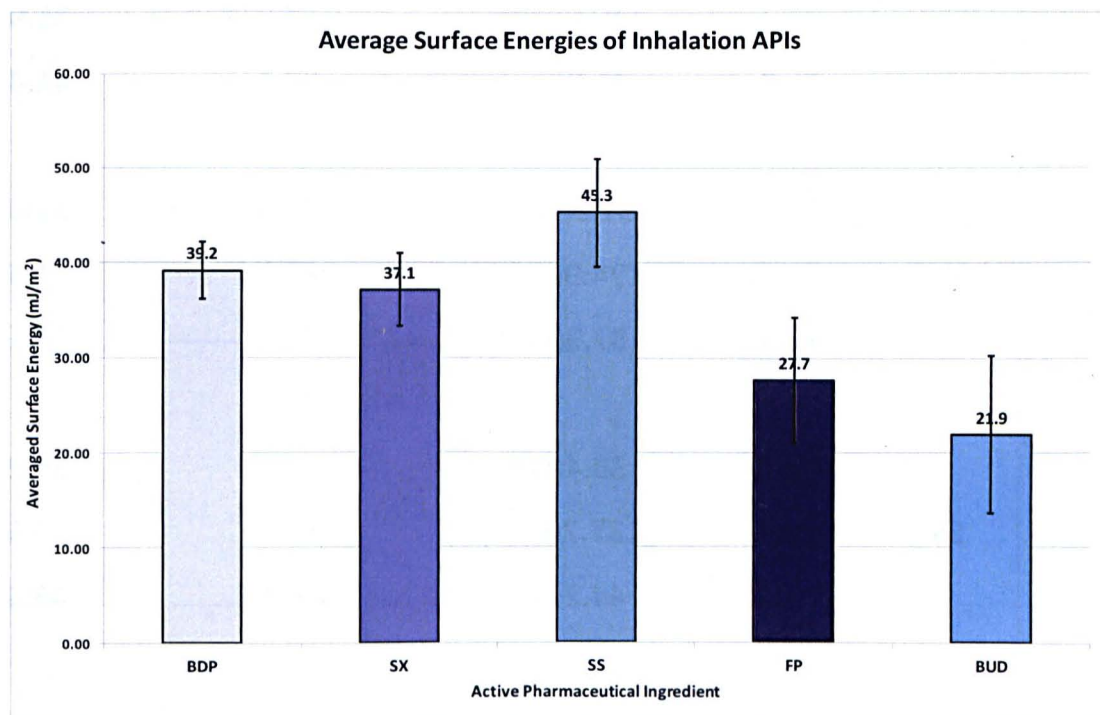


Figure 4.1: Average surface energies of compressed Beclomethasone Dipropionate (BDP), Salmeterol Xinafoate (SX), Salbutamol Sulphate (SS), Fluticasone Propionate (FP) and Budesonide (BUD) as determined by AFM

API	Tip	Force of Adhesion (F_{adh}) nN	Work of Adhesion (W_A) mJ m ⁻²	Surface Energy (γ) mJ m ⁻²
BDP	<i>Tip 1</i>	33.9(±15.2)	82.4	40.4
	<i>Tip2</i>	116.0(±37.2)	77.6	35.9
	<i>Tip3</i>	41.8(±8.4)	83.4	41.4
SX	<i>Tip 1</i>	31.9(±12.4)	77.5	35.8
	<i>Tip2</i>	124.9(±33.2)	83.5	41.5
	<i>Tip3</i>	37.9(±7.2)	75.7	34.1
SS	<i>Tip 1</i>	33.4(±7.1)	81.20	39.2
	<i>Tip2</i>	137.7(±14.2)	92.06	50.5
	<i>Tip3</i>	44.2(±6.4)	88.24	46.4
FP	<i>Tip 1</i>	31.7(±15.8)	77.0	35.3
	<i>Tip2</i>	94.4(±39.8)	63.1	23.7
	<i>Tip3</i>	31.9(±6.8)	63.6	24.1
BUD	<i>Tip 1</i>	18.8(±7.97)	45.6	12.4
	<i>Tip2</i>	102.5(±42.2)	68.6	28.0
	<i>Tip3</i>	32.7(±9.12)	65.3	25.4

Table 4.1: The force of adhesion, work of adhesion and surface energy of inhalation APIs as determined by AFM

4.4.2 Differential Scanning Calorimetry Analysis on the Effects of API Compression

Figure 4.2 shows the overlay of three individual differential scanning thermograms of the pre-compressed API powders BDP, SS, FP and SX. The three BDP samples all showed a consistent melting point at around 212°C. Crucially no other thermodynamic event was seen on the thermograms for any of the samples that might suggest polymorphic impurities such as the common hydrate formation. The three SS samples were also consistent showing a broad melting point endotherm beginning at around 190.98°C. The three SX samples all showed a large endotherm at around 123°C and a subsequent smaller endotherm at 139°C. The FP samples were the least consistent, but still all evidenced a single melting point endotherm at about 290°C.

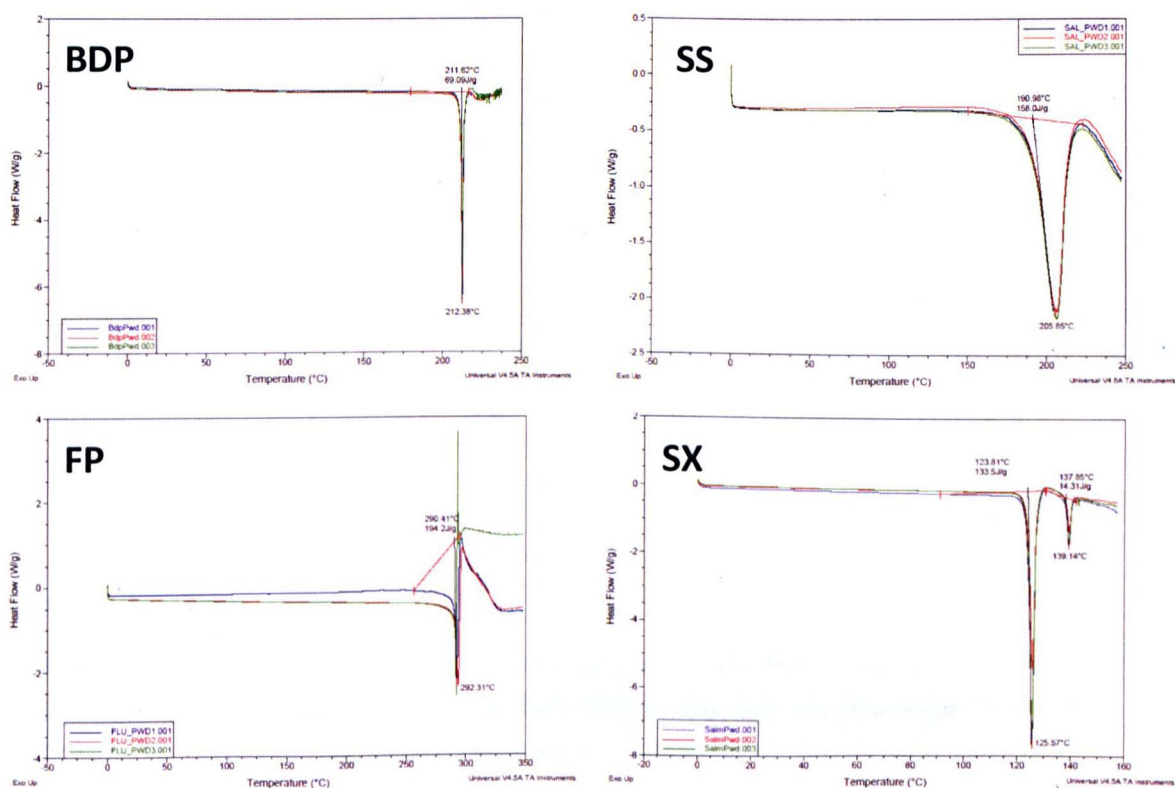


Figure 4.2: Differential scanning calorimetry thermograms of the pre-compressed powders of Beclomethasone Dipropionate (BDP), Salbutamol Sulphate (SS), Fluticasone Propionate (FP) and Salmeterol Xinafoate (SX)

Figure 4.3 shows the thermograms of the same four APIs after compression by IR press use. The figure shows that the three BDP samples had almost identical melting endotherms at about 209°C again with no other obvious events in the rest of the trace. The SS samples showed a single but very broad melting endotherm maximizing at around 202°C, but beginning nearer 180°C. The FP samples showed a repetitive melting endotherm at 296°C, with no other thermodynamic transitions. The SX samples all showed the two endotherms as described pre-compression with a larger transition at 124°C and a smaller endotherm at 138°C.

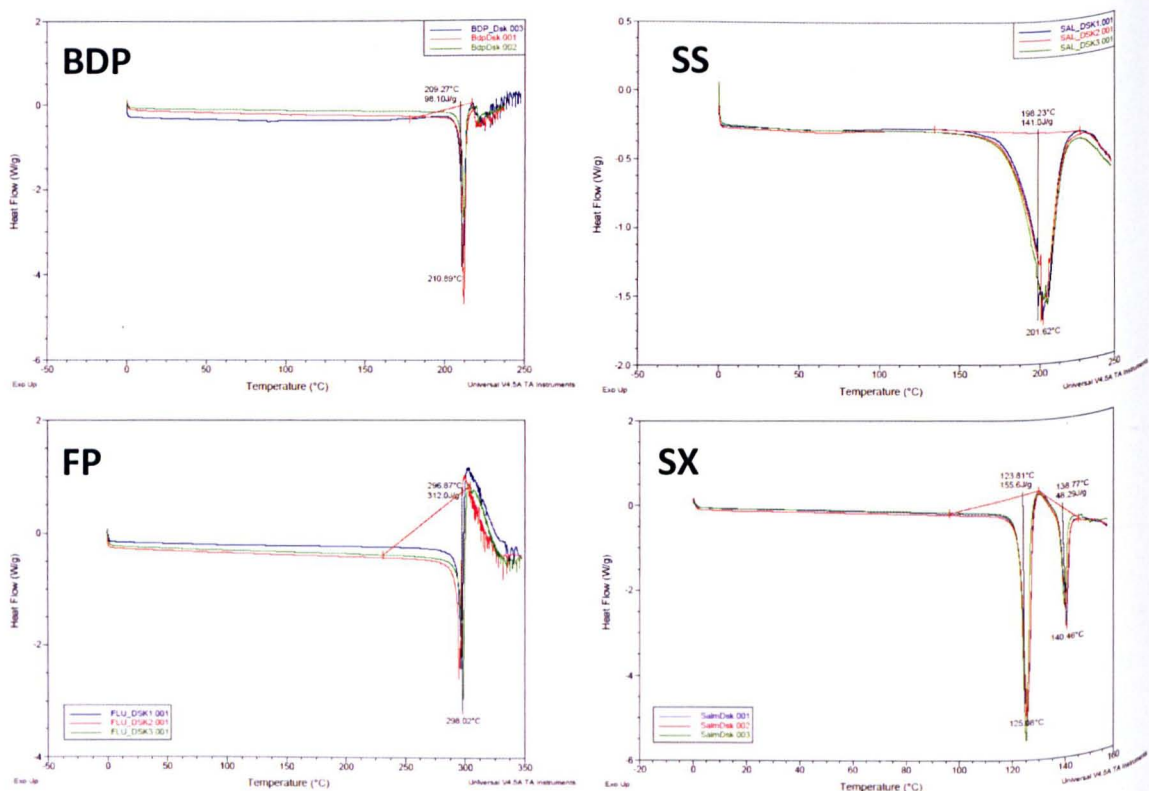


Figure 4.3: Differential scanning calorimetry thermograms of the compressed powders of Beclomethasone Dipropionate (BDP), Salbutamol Sulphate (SS), Fluticasone Propionate (FP) and Salmeterol Xinafoate (SX)

Figure 4.4 shows the two sets of thermograms overlaid for comparison. The pre-compressed API powder traces are in blue with the post-compressed disc samples in red. The figure shows that while the size of the endothermic transitions witnessed do appear to change between the sample sets, particularly with regards the two beta₂-agonists, none of the samples show any significant deviation in the onset of the transitions observed or any developed or unique transitions corresponding to one set and not the other.

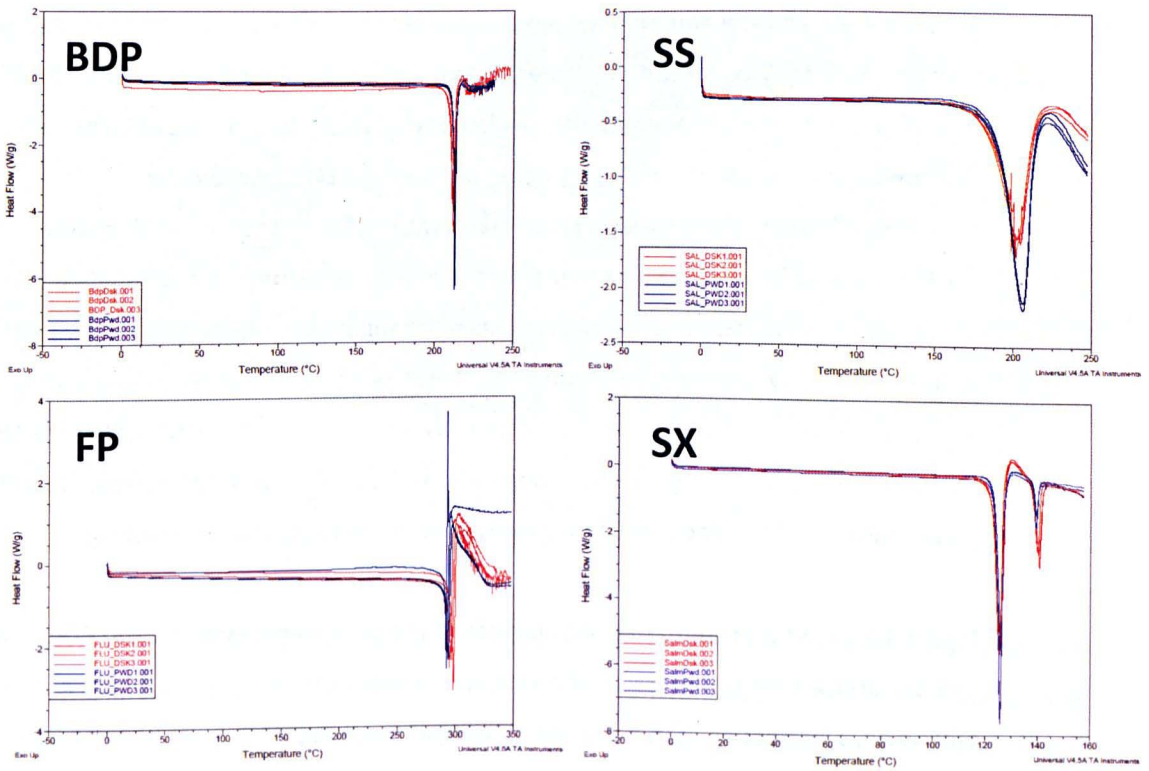


Figure 4.4: Comparison of the differential scanning calorimetry thermograms of the pre-compressed and post compressed powders of Beclomethasone Dipropionate (BDP), Salbutamol Sulphate (SS), Fluticasone Propionate (FP) and Salmeterol Xinafoate (SX)

4.4.3 The Cohesive Adhesive Balance of Salbutamol Sulphate and Beclomethasone Dipropionate using Compressed Powder Substrates

4.4.3.1 SEM and AFM Topographical Analysis

Figure 4.4A shows representative SEM images of the pre-compressed SS and BDP powders at two magnifications. The micronized salbutamol sulphate powder appears to show an irregular plate-like particulate structure at larger magnifications (fig 4.4A SS B), with individual particle sizes varying from less than a micron up to several microns. Some of these particles can be seen to be co-associated with surrounding particles into larger particulate agglomerates several microns in diameter. Over larger areas (fig 4.4A SS A) these agglomerated masses can also be differentiated, and the variation in agglomerate size can also be discerned as progressing from submicron up to 5 or 10 μm in diameter. The surface of the powder is therefore inherently 'rough' with irregularly shaped particle agglomerates stacked and localized to generate a surface with macroscale variability in topographic profile. The BDP powder (fig 4.4A BDP B) shows a distinctly different particulate morphology, with more spherical and smooth micronized particles ranging in size from less than 0.5 μm and less frequently up to around 4 μm in diameter. These spherical particles are however again arranged into agglomerates, with the smaller particles distinctly visible within coherent larger particulate bodies in generating irregularly arranged composites that overlay each other. Over larger areas (fig 4.4A BDP A) the SEM images give the impression of significant topographical variability with appreciable depressions and elevations caused by wide spread irregularly coordinated agglomerate stacking.

Figure 4.5 shows representative SEM images of the post-compressed SS and BDP powder discs. The SS surface post compression shows a very smooth topography (fig 4.5 SS A) that is scored with various impression marks and the occasional particulate debris. At higher magnification (fig 4.5 SS B) it can be identified that the distinction of individual particulates or agglomerate masses is lost and the surface shows a softly undulating but homogenous nature, with the occasional depression or debris based feature. The BDP compress shows a macroscale (fig 4.5 BDP A) surface that appears generally topographically smooth, but with a wide spread 'paving' effect, where a distinct repetitive micro-scale pattern can be seen to cover the majority of the surface. Notably the disc surfaces are littered irregularly with particulate debris, some of which are 25 to 50 μm in diameter. At further magnification (fig 4.5 BDP B) the compressed BDP samples can be

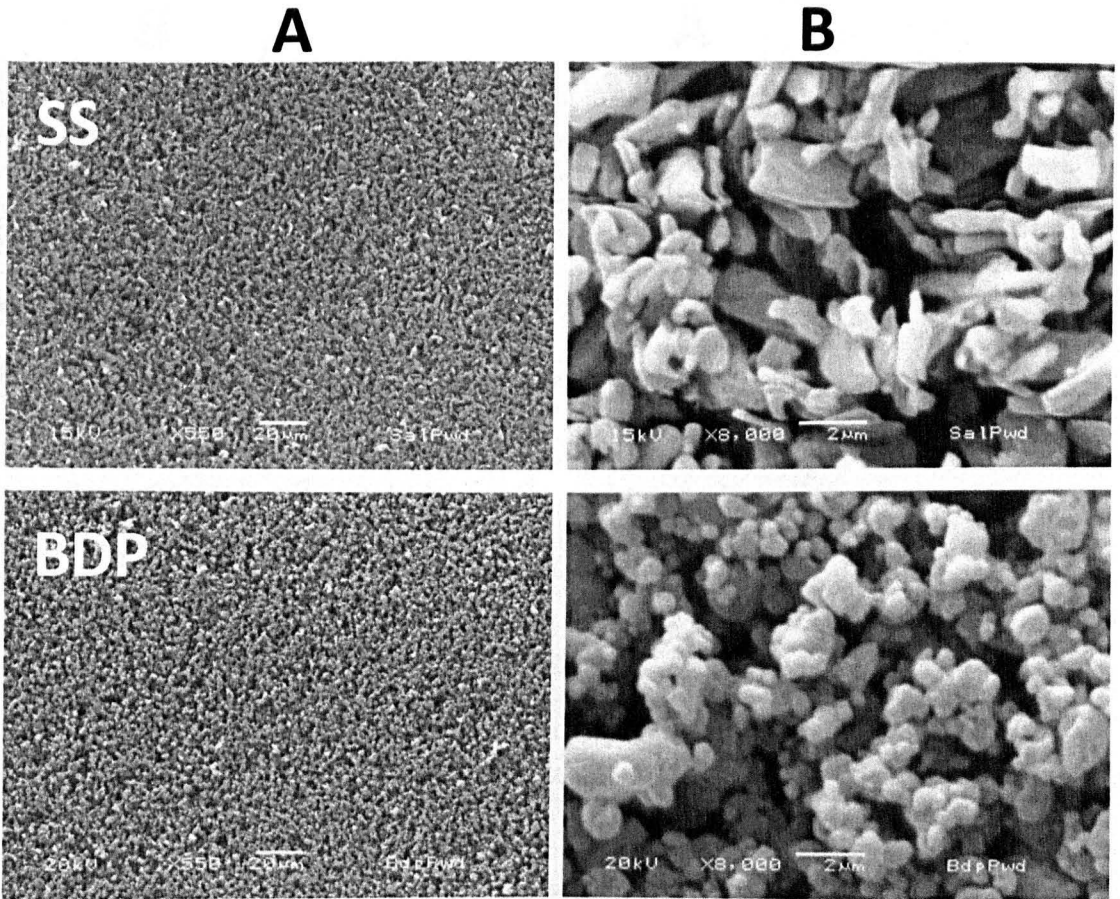


Figure 4.4A: SEM images of Salbutamol Sulphate (SS) and Beclomethasone Dipropionate (BDP) micronized powders before compression at A) 550x magnification and B) 8,000x magnification. Scaled as indicated.

seen to consist of still quite well defined particulate associations, with 'squashed' agglomerates and particulate matter of varying sizes interlocking and overlaying to give rise to the paving effect observed at lower magnifications across the majority of the compress surface. These agglomerates show a small degree of topographical variability, with some protruding from the mean surface into mounds or as distinct particulate extrusions. The particle and agglomerate sizes appear consistent with the pre-compressed powder, although the quantity of larger particulate associations seems to have increased under compression. The spherical or rounded particle shape is maintained, and the surface topography reflects this with repetitive spherical

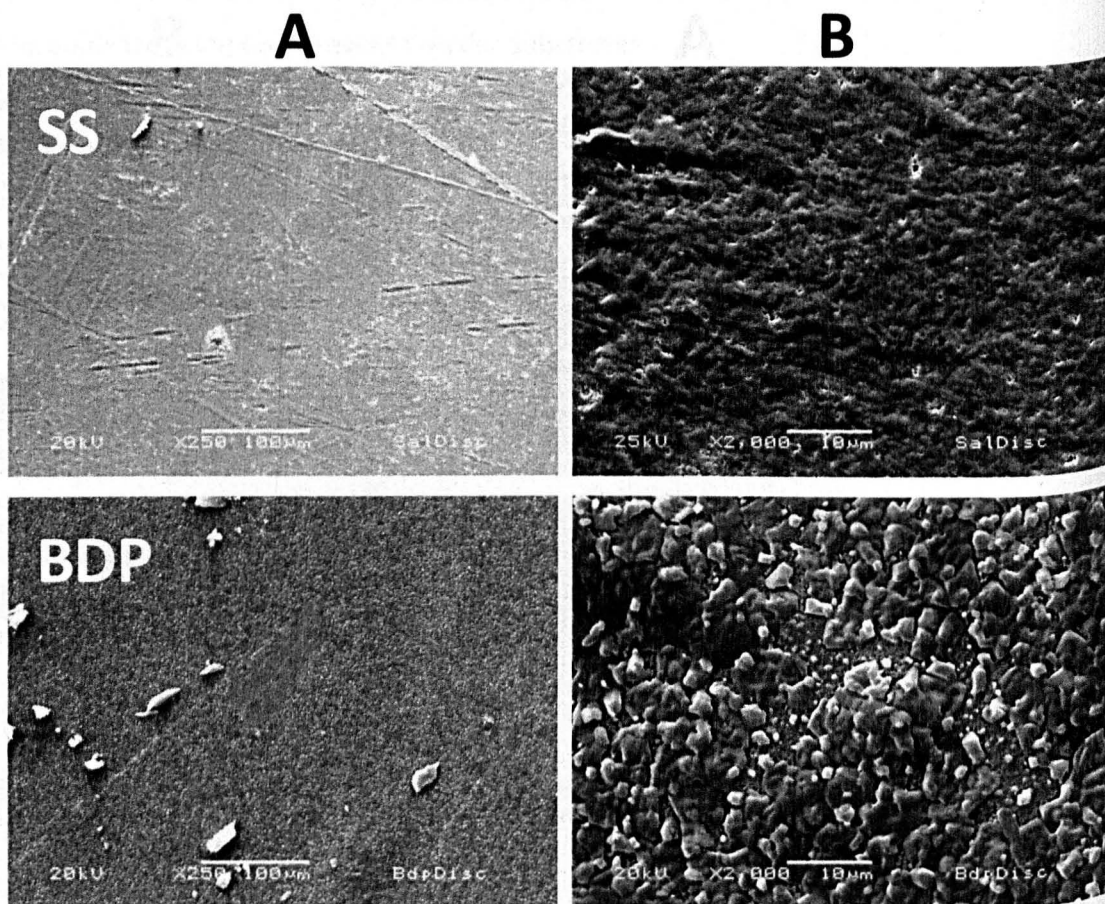


Figure 4.5: SEM images of Salbutamol Sulphate (SS) and Beclomethasone Dipropionate (BDP) powders after compression at A) 250x magnification and B) 2,000x magnification. Scaled as indicated.

arrangements. Figures 4.6 and 4.7 show tapping mode AFM topographic images powders at a $5\mu\text{m} \times 5\mu\text{m}$, and $10\mu\text{m} \times 10\mu\text{m}$ scan size of the pre- and post-compressed BDP and SS respectively. The pre-compressed SS powder shows an irregularly shaped particulate arrangement. There is a predominance of larger ($2\text{-}5\mu\text{m}$ diameter) particles, but there are some smaller particles ($0.5\text{-}1\mu\text{m}$ diameter) observed, frequently in the spaces associated with these larger interlocking 'plate' type particles. When the SS powder is compressed the subsequent AFM images show a surface with a significant reduction in topographical features. The $5\mu\text{m} \times 5\mu\text{m}$ scan size (fig 4.7 SS A) shows that some degree of individual particle character can be identified, albeit on a sub-micron scale, along with some small surface cracks. There are no evident larger particulate masses, although some of the surface cracks appear to define larger

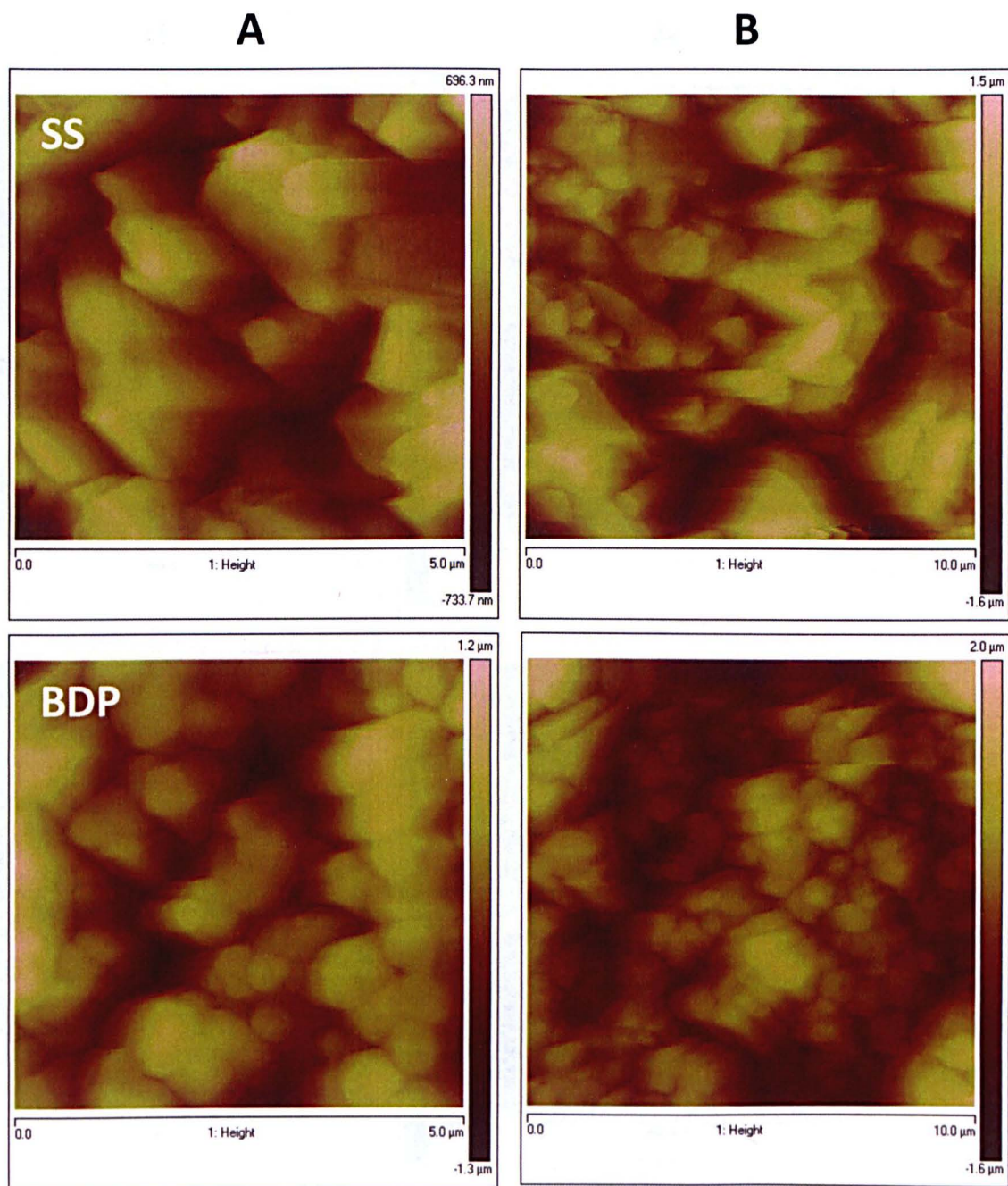


Figure 4.6: Example tapping mode AFM images of Beclomethasone Dipropionate (BDP) and Salbutamol Sulphate (SS) pre compression at 5µm x 5µm (A) and 10µm x 10µm (B) scan sizes.

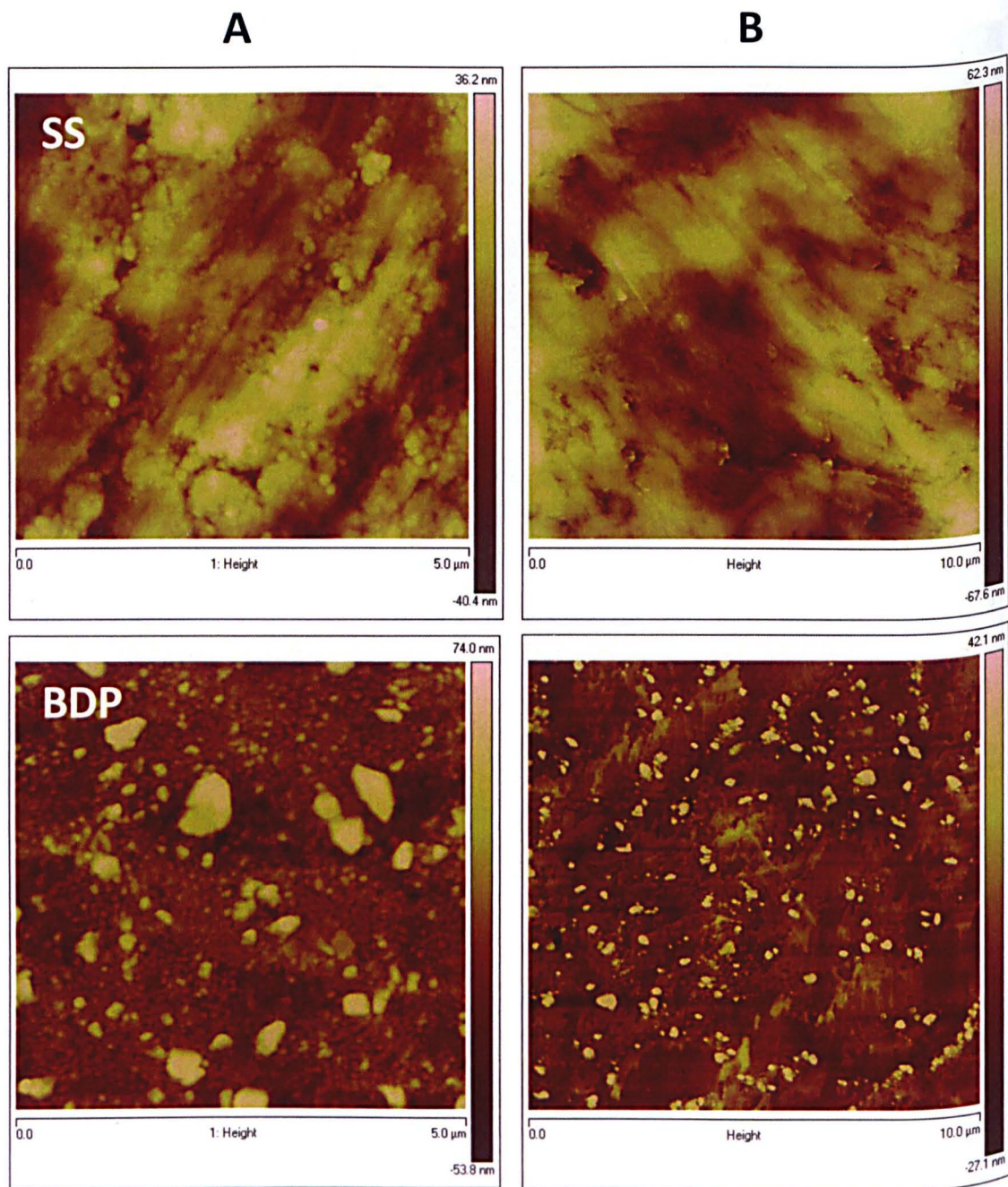


Figure 4.7: Representative tapping mode AFM images of Beclomethasone Dipropionate (BDP) and Salbutamol Sulphate (SS) after compression at 5µm x 5µm (A) and 10µm x 10µm (B) scan sizes.

plate like subsections of the API surface. At this scale and more prominently over the $10\mu\text{m} \times 10\mu\text{m}$ scan size images, the surface appears to be largely topographically homogeneous apart from some areas of material bunching (i.e. into small peaks of between $5\text{-}50\mu\text{m}$) or areas with small surface cracks. The surface of the SS compresses also appears to have a unidirectional surface specific sweeping pattern across larger areas. The BDP powder prior to compression shows an arrangement of more rounded particles, varying in size from $0.25\mu\text{m}$ up to $2\mu\text{m}$ (fig 4.6 BDP A). These particles appear to be co-associated into groups or agglomerates, better defined in the larger scan size (fig 4.6 BDP B). These collections of smaller particles overlay into broader topographical features, that generate rises and falls in the powder surface. After compression the BDP (fig 4.7 BDP A) shows a smoothed sub-micron particle littered surface with significant larger particle fragments ($1\text{-}4\mu\text{m}$) spread across this underlay. The sub-micron particles are visible as co-associated rounded elements forming the broader surface structure. When the larger scan size is viewed (fig 4.7 BDP B) this can be seen to be consistent across a larger area, with little co-ordination of the large particle protrusions from a lightly undulating background surface topography. The protruding particles from the BDP surface appear to be in the region of $30\text{-}40\text{nm}$ proud of the general surface structure.

4.4.3.2 AFM Derived Roughness Measurements

Table 4.2 and table 4.3 show the calculated root mean square (R_q), arithmetic mean (R_a) and maximum feature height (R_{max}) of the BDP and SS pre-compressed powders and their corresponding powder compresses across the $5\mu\text{m} \times 5\mu\text{m}$ and $10\mu\text{m} \times 10\mu\text{m}$ scan sizes respectively. For each sample 5 tapping mode images were collected and while tables 4.2 and 4.3 show the breakdown of the individual image analysis, figure 4.8 shows the collated data in terms of the R_q average for each sample type. As table 4.2 documents, when considering the $5\mu\text{m} \times 5\mu\text{m}$ scan size images, the BDP pre-compressed powder returned an average R_q of 352nm , and an average R_a of 282nm . The R_{max} values for the images analysed ranged from 1585nm up to 2718nm . In comparison the BDP powder compress showed an average R_q of 25.4nm and R_a of 15.0nm with R_{max} values ranging from 170nm to 430nm . The SS powder pre-compression showed an average R_q of 230nm and R_a of 182nm with R_{max} values starting at 1278nm and peaking at 2257 while its powder compress averaged an R_q of 11.8nm an R_a of 9.4nm . When the $10\mu\text{m} \times 10\mu\text{m}$ scan size is considered, table 4.3 shows that the BDP powder averaged an R_q of 541nm , with an average R_a of 433nm and R_{max} values ranging from 2982nm to

API	AFM Image Number	Root Mean Square Roughness (R_q) nm	Arithmetic Mean Roughness (R_a) nm	R Maximum (R_{max}) nm
BDP Powder	1	394	313	2702
	2	351	280	2373
	3	411	340	2122
	4	244	197	1585
	5	360	278	2718
	Average	352	282	2300
BDP Disc	1	19.9	12.1	253
	2	20.0	13.7	184
	3	17.5	12.3	170
	4	38.2	19.8	430
	5	31.3	16.9	384
	Average	25.4	15.0	284
SS Powder	1	270	210	2257
	2	251	201	1442
	3	202	160	1278
	4	207	164	1372
	5	218	177	1419
	Average	230	182	1557
SS Disc	1	13.1	10.3	124
	2	11.3	9.1	87.2
	3	13.8	11.2	99.2
	4	10.5	8.2	86.2
	5	10.4	8.0	99.4
	Average	11.8	9.4	99.2

Table 4.2: 5µm x 5µm tapping mode image R_q , R_a and R_{max} Roughness analysis of Beclomethasone Dipropionate (BDP) and Salbutamol Sulphate (SS) powders before and after compression

API	AFM Image Number	Root Mean Square Roughness (R_q) nm	Arithmetic Mean Roughness (R_a) nm	R Maximum (R_{max}) nm
BDP Powder	1	525	421	3837
	2	438	349	2982
	3	432	344	3042
	4	565	459	3740
	5	743	594	4532
	Average	541	433	3627
BDP Disc	1	10.2	6.55	209
	2	17.9	13.6	179
	3	15.3	10.1	308
	4	15.2	10.1	284
	5	19.5	14.7	324
	Average	15.6	11.0	261
SS Powder	1	455	367	3023
	2	671	523	4672
	3	398	313	2954
	4	581	476	4210
	5	486	380	3134
	Average	518	412	3599
SS Disc	1	19.8	15.6	258
	2	17.6	13.8	158
	3	18.7	13.8	143
	4	16.2	13.0	96
	5	14.4	11.4	109
	Average	17.3	13.5	153

Table 4.3: 10µm x 10µm tapping mode Image R_q , R_a and R_{max} roughness analysis of Beclomethasone Dipropionate (BDP) and Salbutamol Sulphate (SS) powders before and after compression

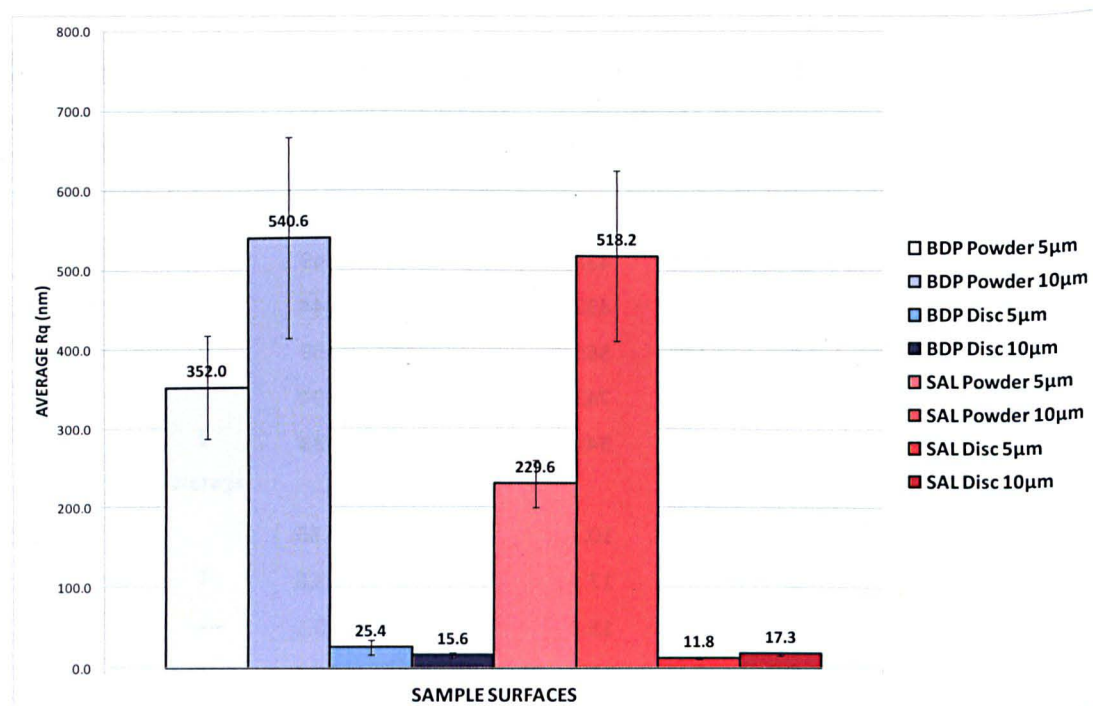


Figure 4.8: Comparison of the average root mean square roughness of Beclomethasone Dipropionate (BDP) and Salbutamol Sulphate (SS) powders pre- and post-compression as derived from 5µm x 5µm and 10µm x 10µm tapping mode AFM images

4532nm. The compressed beclomethasone in comparison showed an average R_q of 15.6nm and R_a of 11.0 with R_{max} values ranging from 179nm to 324nm. The salbutamol powder across this scan size had an average R_q of 518nm and an average R_a of 412nm, with R_{max} values from 2954nm to 4672nm. The SS compress however returned an average R_q of 17.3nm, with an average R_a of 13.5nm and R_{max} values starting at 96nm and topping at 258nm. Figure 4.8 displays the average R_q values for both the compressed and un-compressed API samples at both scan sizes for comparison. Notably the SS roughness values are lower than the BDP samples for all but the 10µm x 10µm compressed disc topography scans. There is approximately a 14x decrease in surface roughness by R_q between the BDP samples at 5µm x 5µm, increased to a 34x decrease when considering the same samples at 10µm x 10µm. The SS powder compress shows a 19x decrease in surface roughness by R_q over 5µm x 5µm, with a 30x decrease across the 10µm x 10µm images. Importantly, the un-compressed samples also showed significantly more

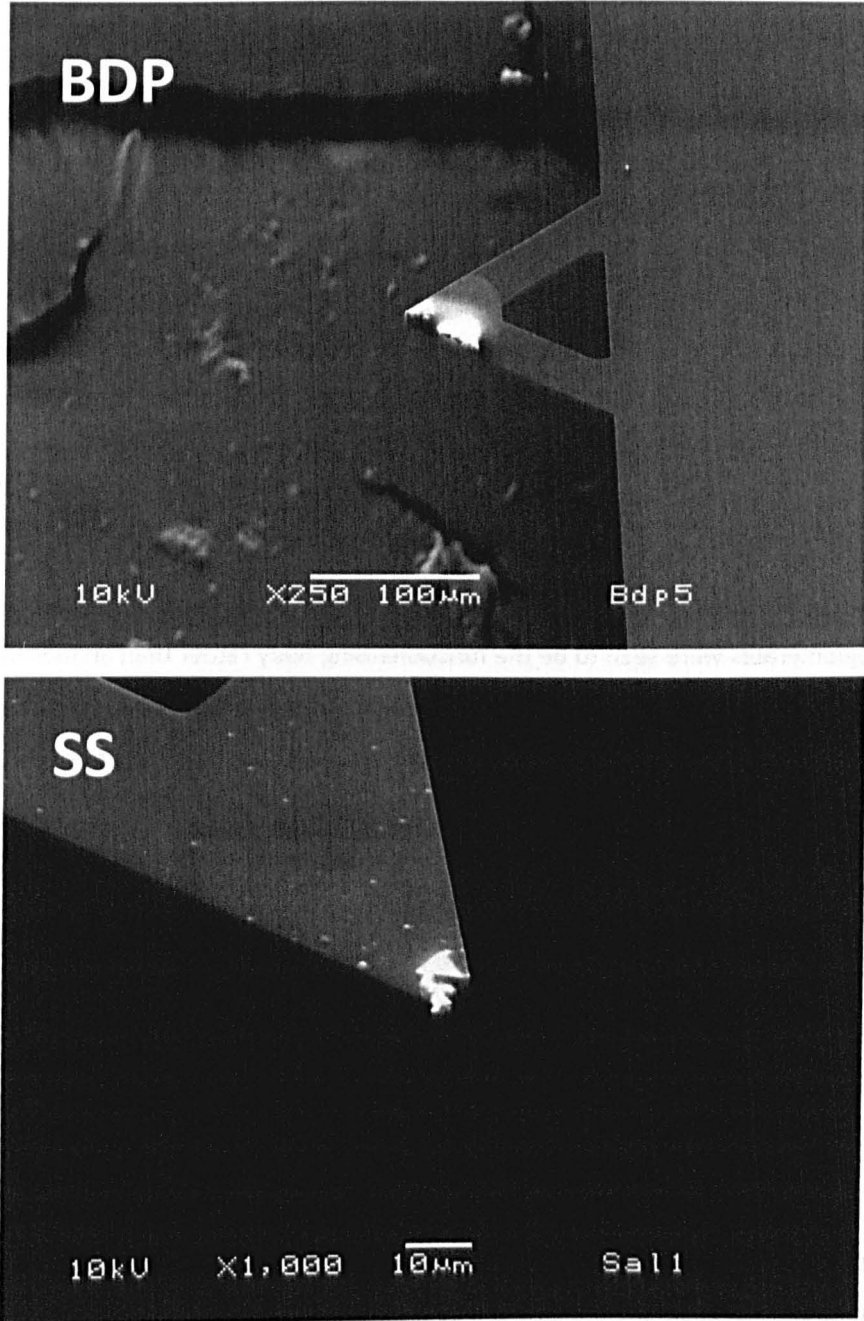


Figure 4.9: Example SEM images of functionalised AFM tips with Beclomethasone Dipropionate (BDP), and Salbutamol Sulphate (SS) particulates. Magnification as stated.

variability (as standard deviation) of their roughness measurements, exaggerated when the scan size was increased.

4.4.3.3 SEM Imaging of Functionalized AFM tips

Figure 4.9 shows two example SEM images of the functionalised DNP-S cantilevers prior to CAB based force probing. SEM was used to ratify that successful functionalization had occurred. Figure 4.9 shows representative images of both a BDP functionalised and SS functionalised tip. Three tips from the original functionalization procedure (2 BDP and 1 SS) were found to have been either unsuccessfully functionalised or inappropriately contaminated with excess API or adhesive. These tips were therefore discarded and replacements created; further SEM imaging confirmed that all subsequent tips had been functionalised successfully. These tips were then used for force curve genesis on the API powder compresses. As figure 4.9 shows, small particulate attachment could be confirmed visually for both APIs. In all instances particle agglomerates were seen to be the functionalising body rather than an individual particle. As the BDP example shows (fig 4.9 BDP) areas of bare adhesive could sometimes be identified in some SEM images, although this was only considered problematic if the imaging suggested significant functional particle coverage. As the SS tip also indicates (fig 4.9 SS) there was also often additional particle debris introduced to the rest of the cantilever in the attachment process, though this was considered acceptable as long as it did not interfere with the prominent particle or offer potentially multiple contact sites.

4.4.3.4 Cohesive Adhesive Balance using Powder Compress Substrates

Figures 4.10 and 4.11 show the resultant CAB plots based on the average adhesion and cohesion force AFM data from 100 force measurements using five BDP functionalised tips and SS functionalised tips respectively. Figure 4.10 indicates that all five BDP tips registered adhesion/cohesion plots below the xy intersect. The five tips could be described by a linear fit with a $y = 0.35x$ gradient and an R^2 value of 0.57. Conversely the five salbutamol tips (fig 4.11) all lay above the xy intersect with a linear fit that reads a $y = 1.69x$ gradient and a 0.57 R^2 value.

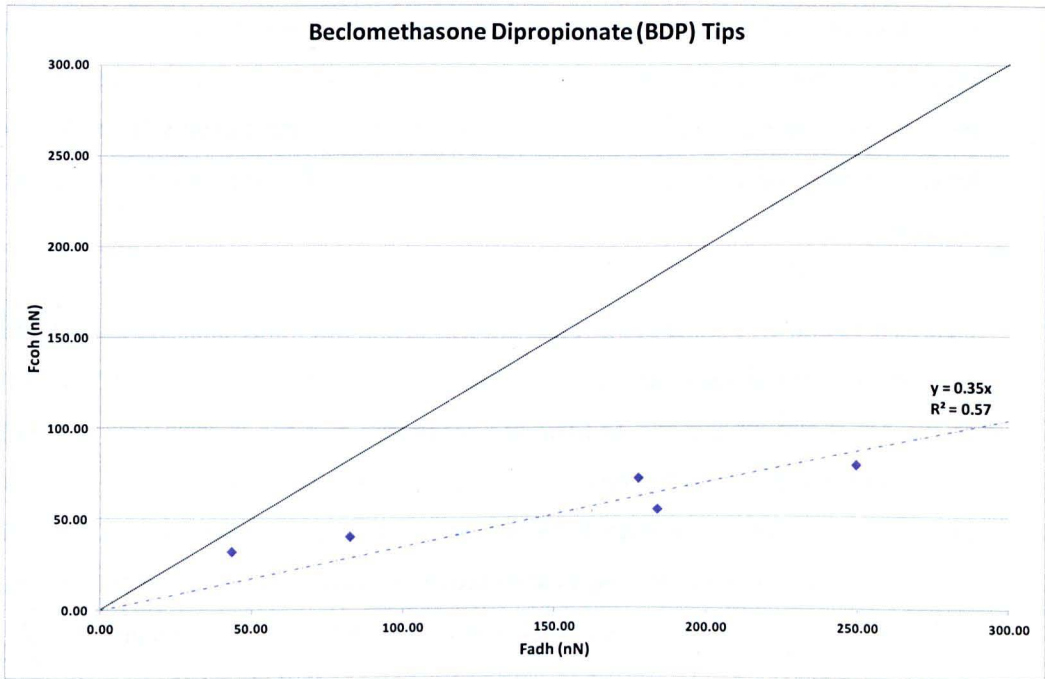


Figure 4.10: CAB plot for Beclomethasone Dipropionate (BDP) tips with Salbutamol Sulphate (SS)

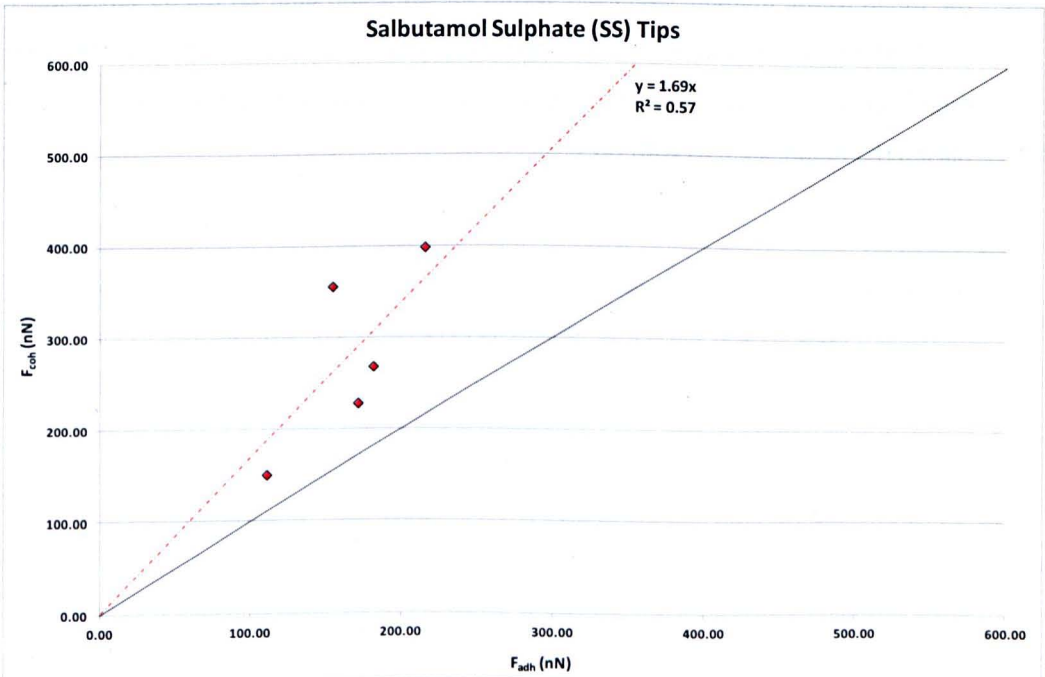


Figure 4.11: CAB plot for Salbutamol Sulphate (SS) tips with Beclomethasone Dipropionate (BDP)

Chapter 4 - Application of the CAB approach to, and Characterization of 'Semi-Model' Inhalation Substrates

Figure 4.12 shows example cohesive and adhesive force curves obtained with the same SS and BDP functionalised tips respectively. The blue trace is the extension curve and the red line the retraction. The example BDP traces show a smaller adhesion by cohesive (BDP-BDP) measurement than by adhesive measurement on a SS surface. Conversely the SS traces show a larger adhesion on cohesive measurement (SS-SS) than on adhesive measurement on a BDP surface.

Figures 4.13 and 4.14 show the box plots of the SS and BDP functionalised tip force data on both the cohesive and adhesive surfaces. The bottom of the boxes represent the 1st quartile, the top of the boxes the 3rd quartile and the line inside the box the median (2nd quartile). The dots represent the mean, and the ends of the whiskers represent the maximum and minimum F_{adh} recorded. Fig 4.13 shows that both the adhesive and cohesive data sets from the SS tips showed good consistency between the mean and median with only a couple of small discrepancies (tip 4 cohesive data, and tip 3 adhesive data). The ranges of the tip data sets are variable with some showing evidence of extreme minimums or maximums that dwarf the quartile measures. Fig 4.14 shows that the same is true of the BDP tips force data, with a generally tight agreement of the mean to the median, especially within the adhesion data on the SS substrate. Tips 1 and 2 within the cohesive data show the largest disparity. The range of each tip substrate data set is more consistent, but there remains evidence of outlying maxima and/or minima that have biased the mean, such as with tip 1.

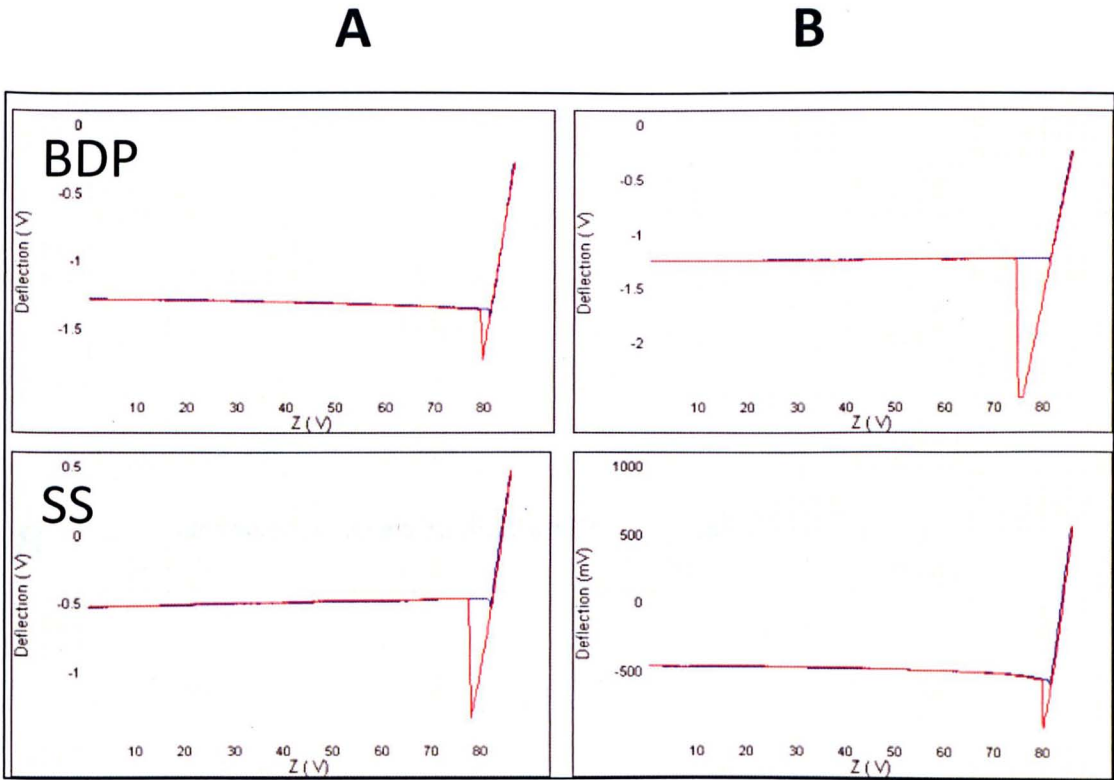


Figure 4.12: Example A) cohesive and B) adhesive force curves using the same Beclomethasone Dipropionate (BDP) and (SS) functionalised tips respectively

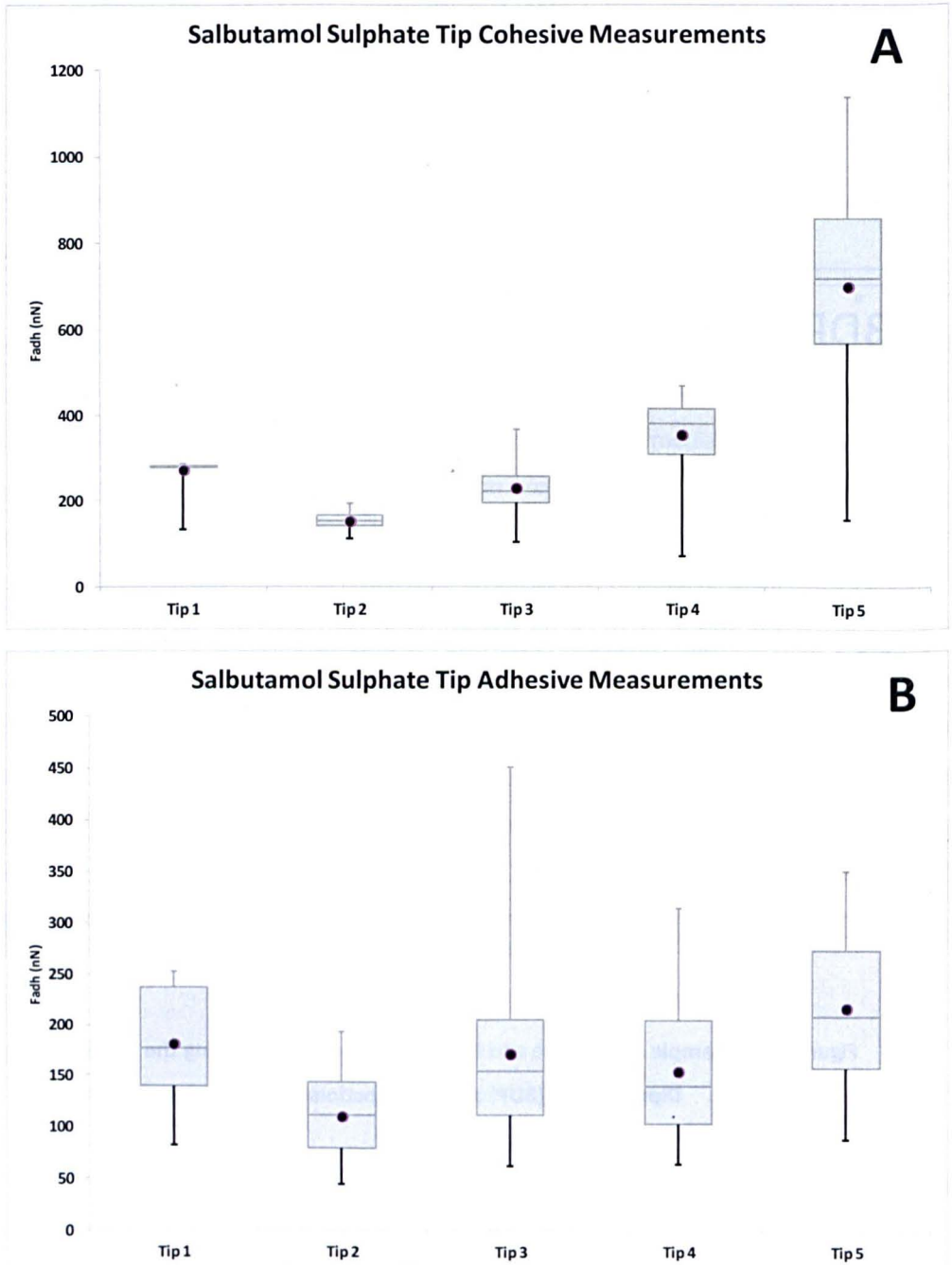


Figure 4.13: Box plots of the force of adhesion measurements of Salbutamol Sulphate tips on a A) Salbutamol Sulphate substrate and B) Beclomethasone Dipropionate substrate

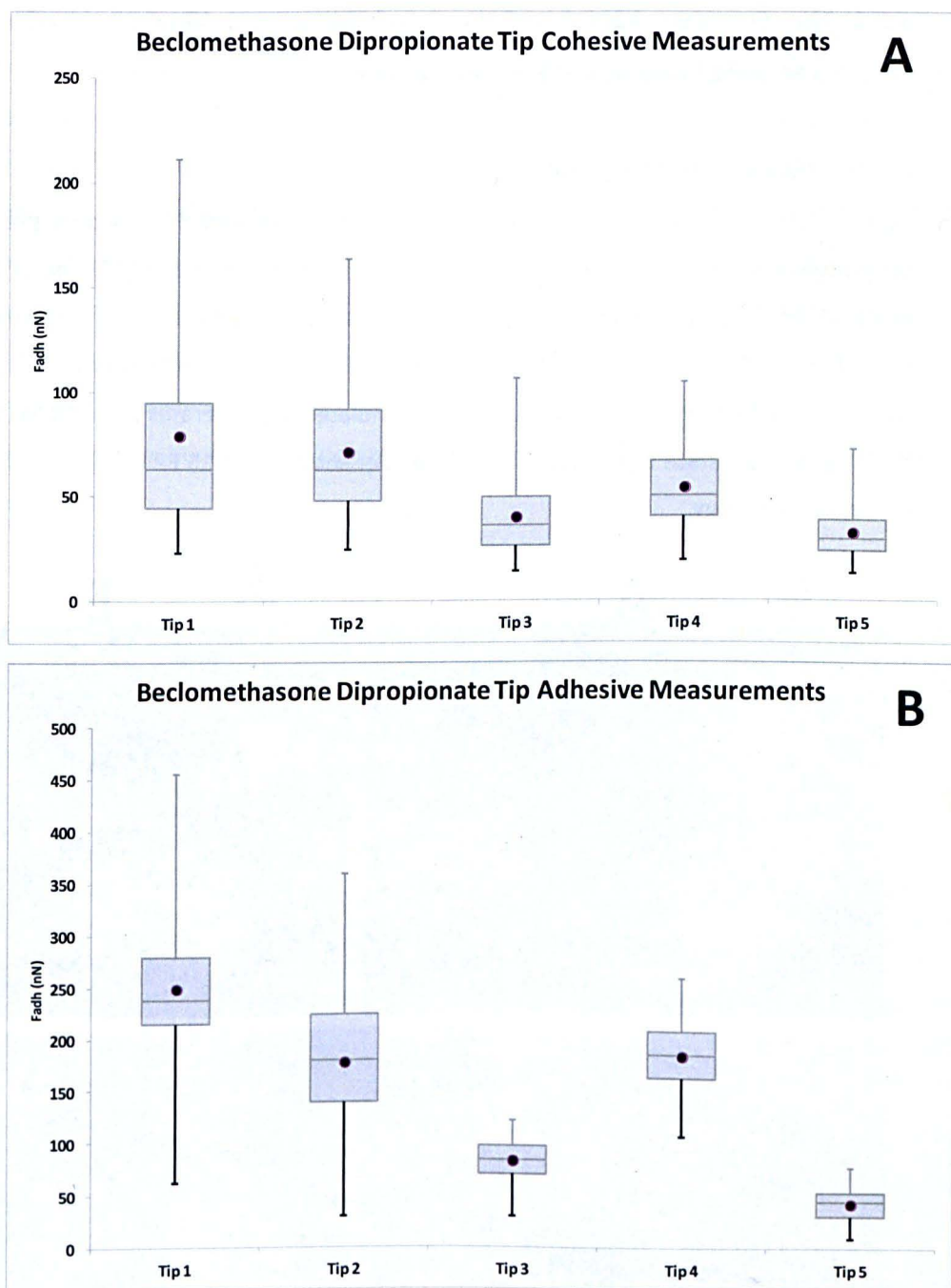


Figure 4.14: Box plots of the force of adhesion measurements of Beclomethasone Dipropionate tips on a A) Beclomethasone Dipropionate substrate and B) Salbutamol Sulphate substrate

4.4.4 The Cohesive Adhesive Balance of Salmeterol Xinafoate and Fluticasone Propionate using Compressed Powder Substrates

4.4.4.1 SEM and AFM Topographical Analysis

Figures 4.15 and 4.16 show the SEM images of the SX and FP powders pre- and post-compression respectively. The un-compressed SX powder (fig 4.15 SX B) shows an irregular elliptical, or shard-like particulate morphology. Particles are generally long and thin with a size range from 1-5 μ m in length and 1-2 μ m in width. These particles can be seen over larger areas to have clustered into irregularly shaped and accumulated agglomerates (fig 4.15 SX A) creating a heterogeneous surface topography. The FP powder shows (fig 4.15 FP B) shows more consistent particle morphology.

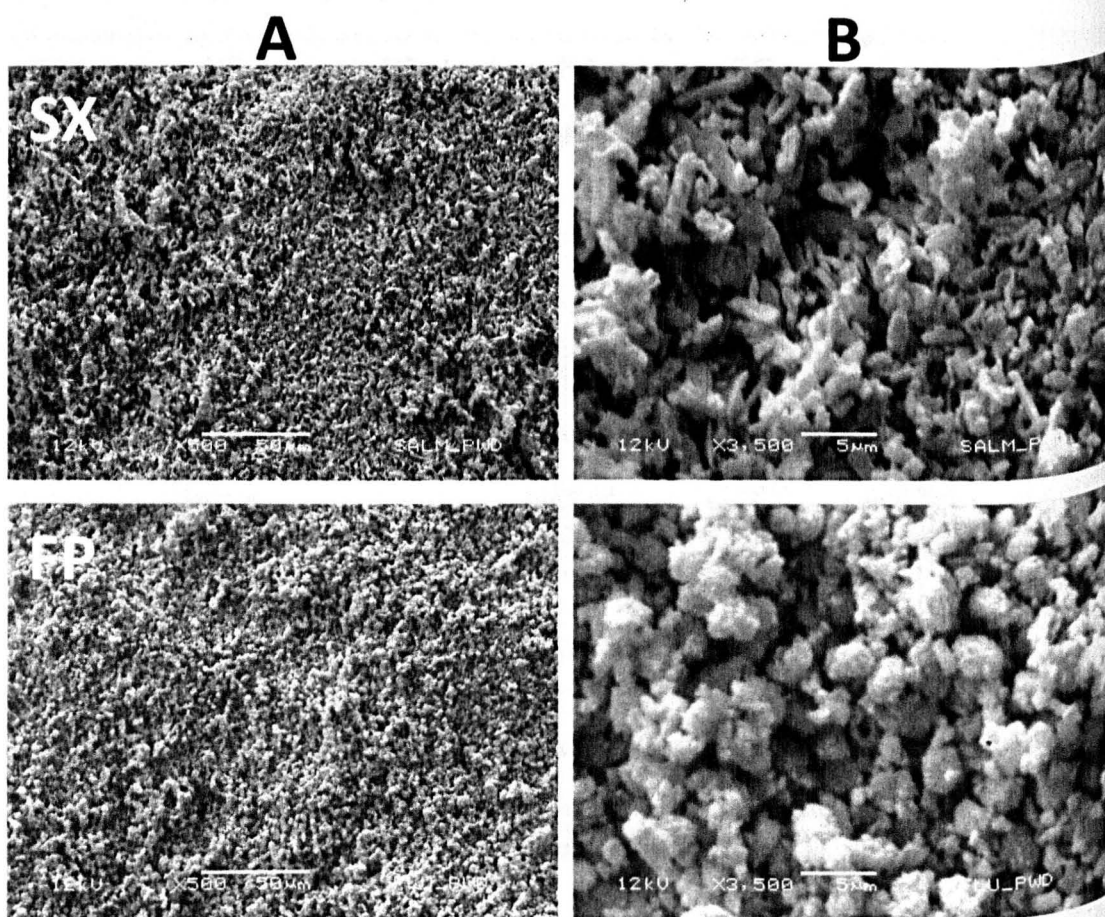


Figure 4.15: SEM images of Salmeterol Xinafoate (SX) and Fluticasone Propionate (FP) micronized powders before compression at A) 500x magnification and B) 3,500x magnification. Scaled as indicated.

Particles are generally spherical but rough and nodular. They have a particle size range of between 1-2 μ m in diameter, and can be seen (fig 4.15 FP A) to aggregate to some extent over larger areas into peaks and troughs of particle coverage. Again the surface can be seen to be rough and tumultuous, with particle overlay leading to elevations and depressions in topography. The compressed SX powder (fig 4.16 SX B) shows a distinct flattening of topographical features. Individual particle character is largely lost, giving a broadly homogeneous and optically smoothed surface. Some small undulation seen at larger magnifications hints at compressed particle overlay. Over both larger areas (fig 4.16 SX A) and with increased magnification to smaller areas (fig 4.16 SX B) distinct surface disruption can be seen, with unidirectional surface demarcation as surface ridging or surface depression stretching across images.

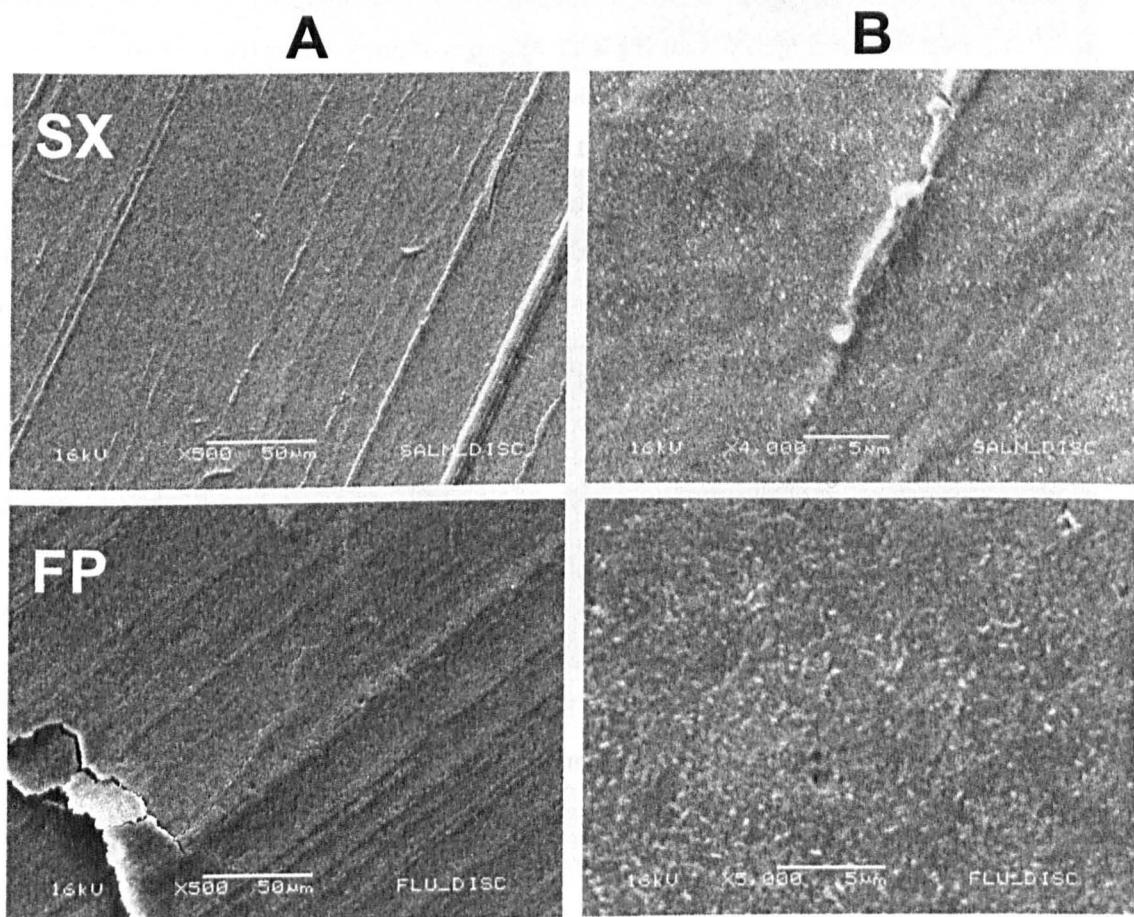


Figure 4.16: SEM images of Salmeterol Xinafoate (SX) and Fluticasone Propionate (FP) micronized powders after compression at A) 500x magnification and B) 4000-5000x magnification. Scaled as indicated.

These features run consistently across all images, dissecting the otherwise planar powder bed. Some surface debris can also be seen to be scattered inconsistently across the surface. The compressed FP (fig. 4.16 FP A) powder shows a largely homogenous surface, with repetitive unidirectional ridging inter-dispersed with occasional areas of surface fracture or collapse (fig 4.16 FX A). Here surface cracks ranging from the nanoscale up to several microns can be identified and at some points the surface layers can be seen to have separated entirely. Some have either inverted or risen over each other. At larger magnifications (fig 4.16 FX B) the powder compact can be seen to have an irregularly patterned surface with some distinction of original particle morphology. Some minor surface protrusion can be seen, with the occasional depression or surface crack.

Figure 4.17 shows the associated tapping mode AFM images of the compressed SX and FP powders over a $5\mu\text{m} \times 5\mu\text{m}$ (fig 4.17 A) and a $10\mu\text{m} \times 10\mu\text{m}$ (fig 4.17 B) surface area. Both powder compresses show identifiable individual particle definition, in particular over the smaller surface area. The SX images (fig 4.17 SX A, B) seem to show a mildly undulating surface with unidirectional tracking. Over the larger scan size, whilst there does appear frequent particulate protrusion, these are of a small scale ($<1\mu\text{m}$ diameter), maximising at 60nm proud and consistently far below this. In general the topography appears widely homogenous. The FP compress (fig 4.17 FP A, B) shows frequent individual particle protrusion from the surface bed. The protrusions regularly extend up to 80nm from the surface, are between $1\mu\text{m}$ - $3\mu\text{m}$ in diameter, occur at irregular angles and show extensive coverage over the larger scan sizes. The topography of the FP compact therefore appears more heterogeneous than the SX compact.

Figure 4.18 presents the average root mean square roughness analysis of the FP and SS powder compacts as derived from the collected tapping mode AFM images. The FP powder compact averaged an R_q of 20.0nm over the $5\mu\text{m} \times 5\mu\text{m}$ images and 23.6nm over $10\mu\text{m} \times 10\mu\text{m}$ images. The SX powder compact averaged an R_q of 13.9nm over the $5\mu\text{m} \times 5\mu\text{m}$ scans and 17.4nm over the $10\mu\text{m} \times 10\mu\text{m}$ scans. The image to image roughness deviation was greatest across the smaller scan size images than the larger.

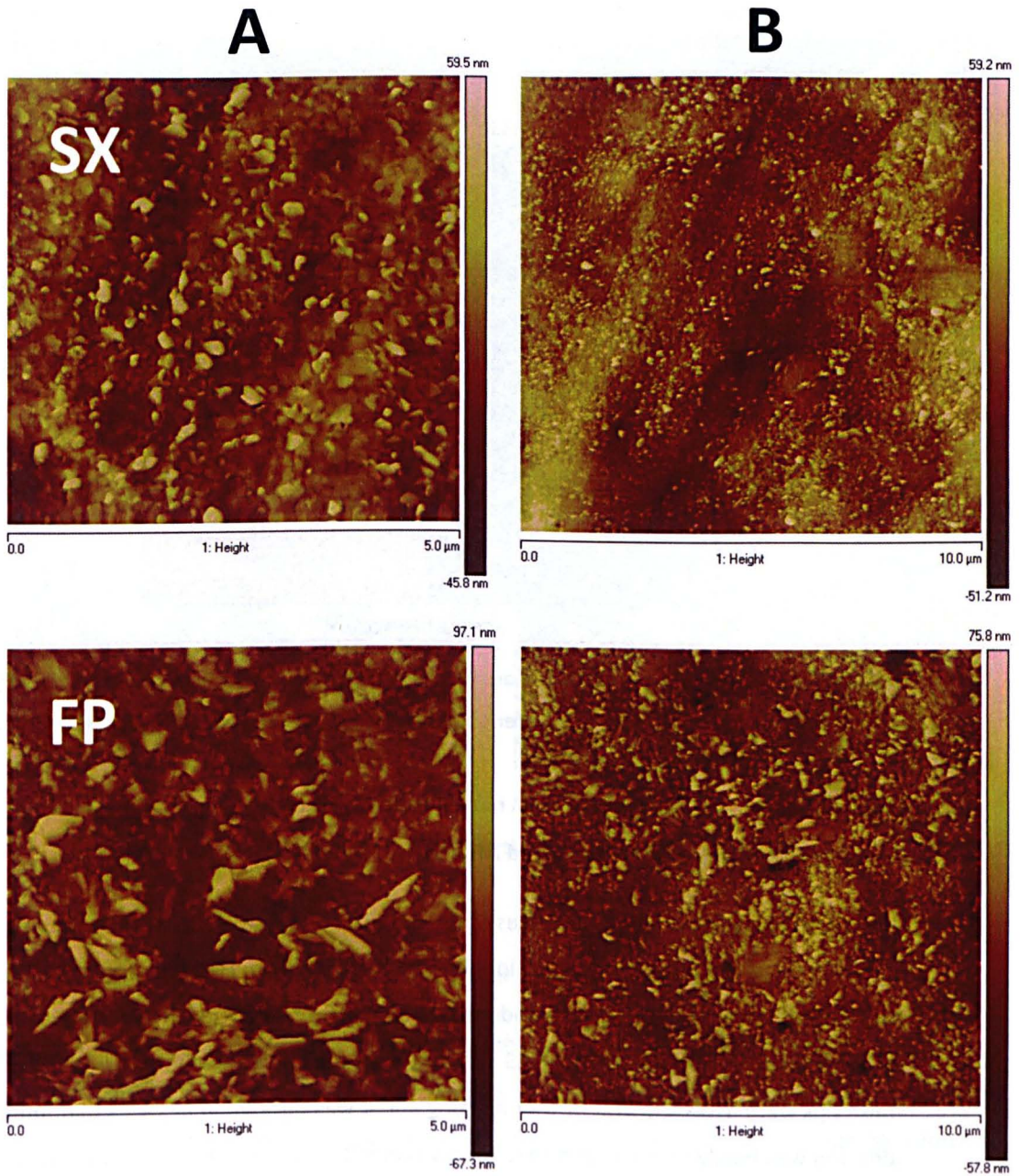


Figure 4.17: Representative tapping mode AFM images of Salmeterol Xinafoate (SX) and Fluticasone Propionate (FP) after compression at 5µm x 5µm (A) and 10µm x 10µm (B) scan sizes.



Figure 4.18: Average Root Mean Square Roughness Analysis of Fluticasone Propionate (FP) and Salmeterol Xinafoate (SX) Powder Compacts at 5µm x 5µm and 10µm x 10µm scan sizes.

4.4.4.2 SEM Imaging of Functionalized AFM tips

Figure 4.19 shows example SEM images of functionalised SX and FP DNP-S AFM tips. All ten AFM tips were seen to have been functionalised successfully on the first attempt. In all cases functional particle masses could be identified at the tip site. Often these were multi particle agglomerates. In some images (fig 4.19 SX B) multiple particle attachment masses could be seen. These tips were assessed with further imaging and it was decided in all cases that multiple point adhesion was highly unlikely, and that the tips could be used for the subsequent force balance. In a couple of instances excess bare adhesive could also be identified. Again following further functional particle assessment it was deemed that this would not contaminate the particle surface interaction in any way.

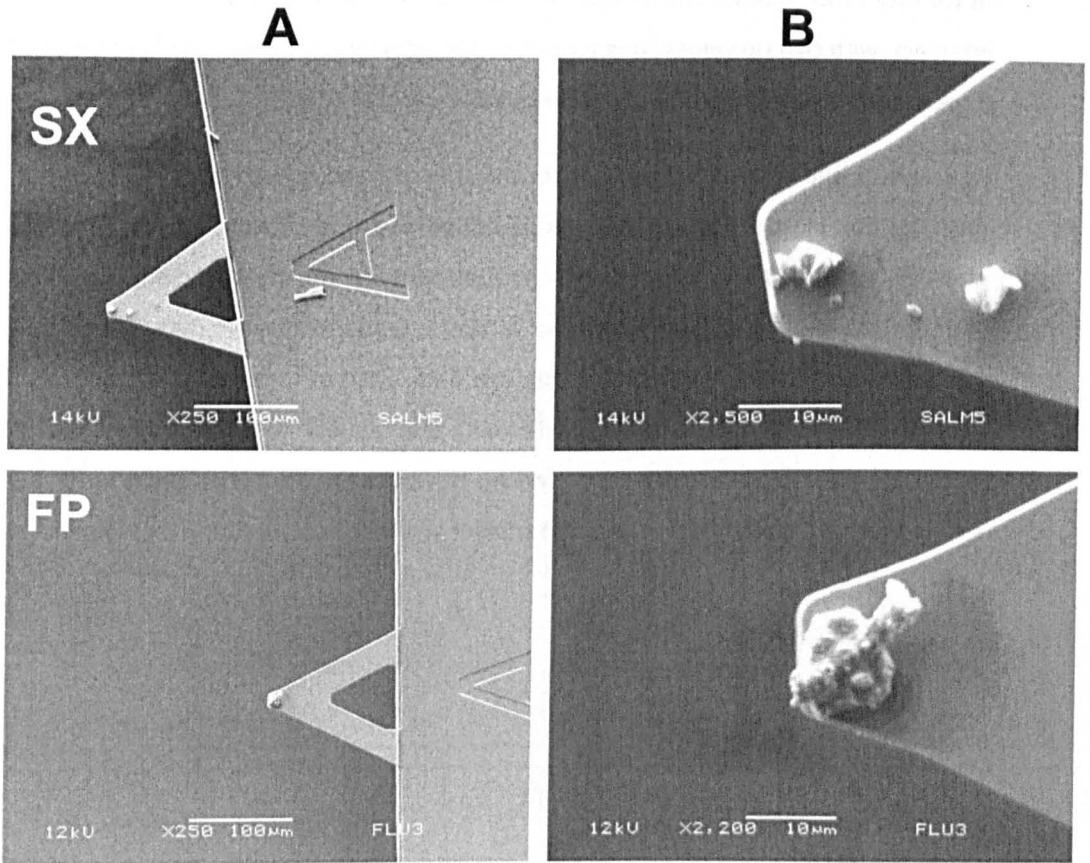


Figure 4.19: Example SEM images of functionalised AFM tips with Salmeterol Xinafoate (SX A B), and Fluticasone Propionate (FP A B) particulates at various magnifications.

4.4.4.3 Cohesive Adhesive Balance using Powder Compress Substrates

Figure 4.20 shows example force curves using the same functionalised FP and SX tips on both cohesion and adhesion substrates. The blue line is representative of tip extension and the red line is tip retraction. The FP tip can be seen to have a larger adhesion on the SX substrate (adhesive measurement) than on the FP substrate (cohesive measurement). The SX tip shows the reverse with a larger adhesion on the cohesive SX measurement over that on the FP surface.

Figures 4.21 and 4.22 show the CAB plots established from the F_{adh} derived from 100 force curves using the FP tips and SX tips respectively on the compacted powder surfaces of adhesion and cohesion. Figure 4.17 shows that the FP tips' plot points all lie on the adhesive side of the xy intersect, with a linear fit giving a coefficient of determination of 0.81. The gradient of this linear

Chapter 4 - Application of the CAB approach to, and Characterization of 'Semi-Model' Inhalation Substrates

fit (or CAB ratio) is 0.63. The SX tips force balance plot points (fig 4.21) all lie just above the xy intersect, with two tip values lying almost on the intersect itself. A linear fit of these points gives a coefficient of determination of 0.97 with a CAB ratio of 1.05.

Figures 4.23 and 4.24 show box plots for the cohesive and adhesive force data of the SX and FP tips. The box plots are constructed as identified above in section 4.4.2.4 for the SS and BDP plots. Both figures show some small disparities between the mean and median within some tip surface data, most particularly with the SX tips 1, 2 and 4 cohesive data, the FX tip 2 cohesive and adhesive data and the FX tip 4 adhesive data. Each of these tip substrate sets show large maxima or minima F_{adh} values (as whiskers) that appear to have skewed the mean some distance either above or below the median. However the other tips seem to have a generally strong agreement of both averages and smaller and more balanced force extremes.

A

B

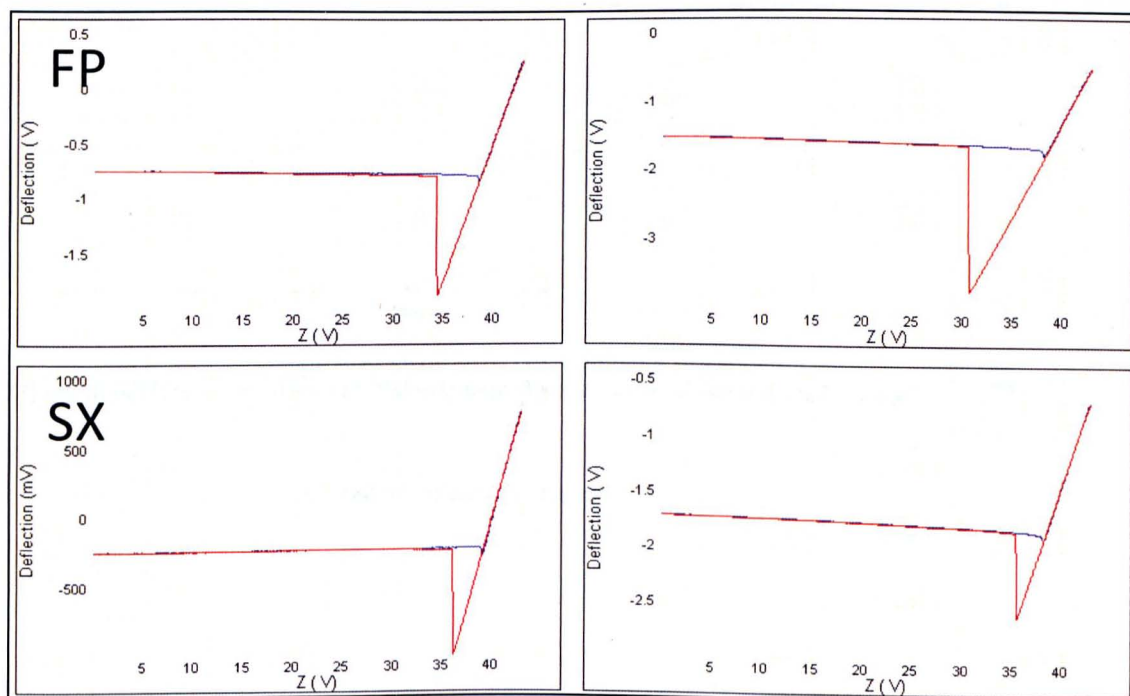


Figure 4.20: Example A) cohesive and B) adhesive force curves using the same Fluticasone Propionate (FP) and Salmeterol Xinafoate (SX) functionalized tips respectively

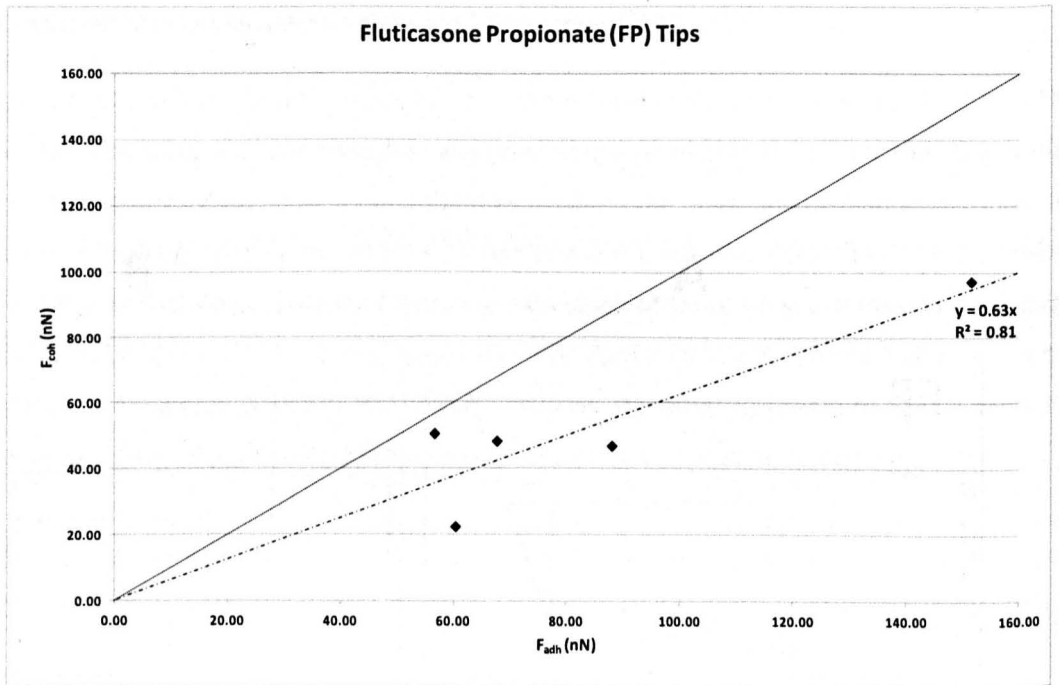


Figure 4.21: CAB plot for Fluticasone Propionate (FP) tips with Salmeterol Xinafoate (SX)

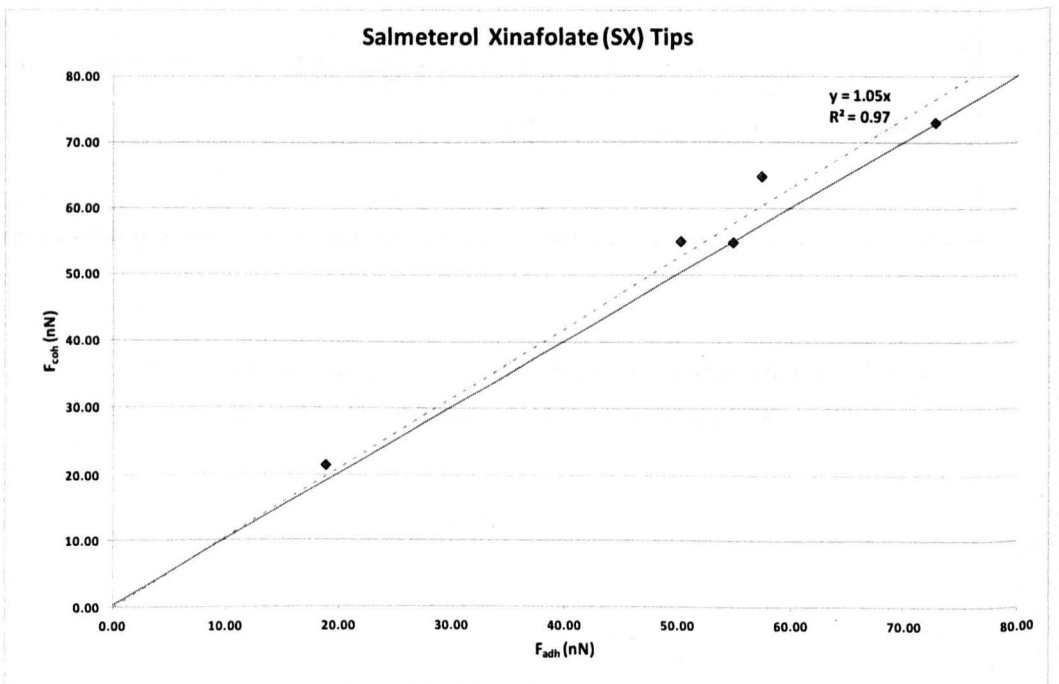


Figure 4.22: CAB plot for Salmeterol Xinafoate (SX) tips with Fluticasone Propionate (FP)

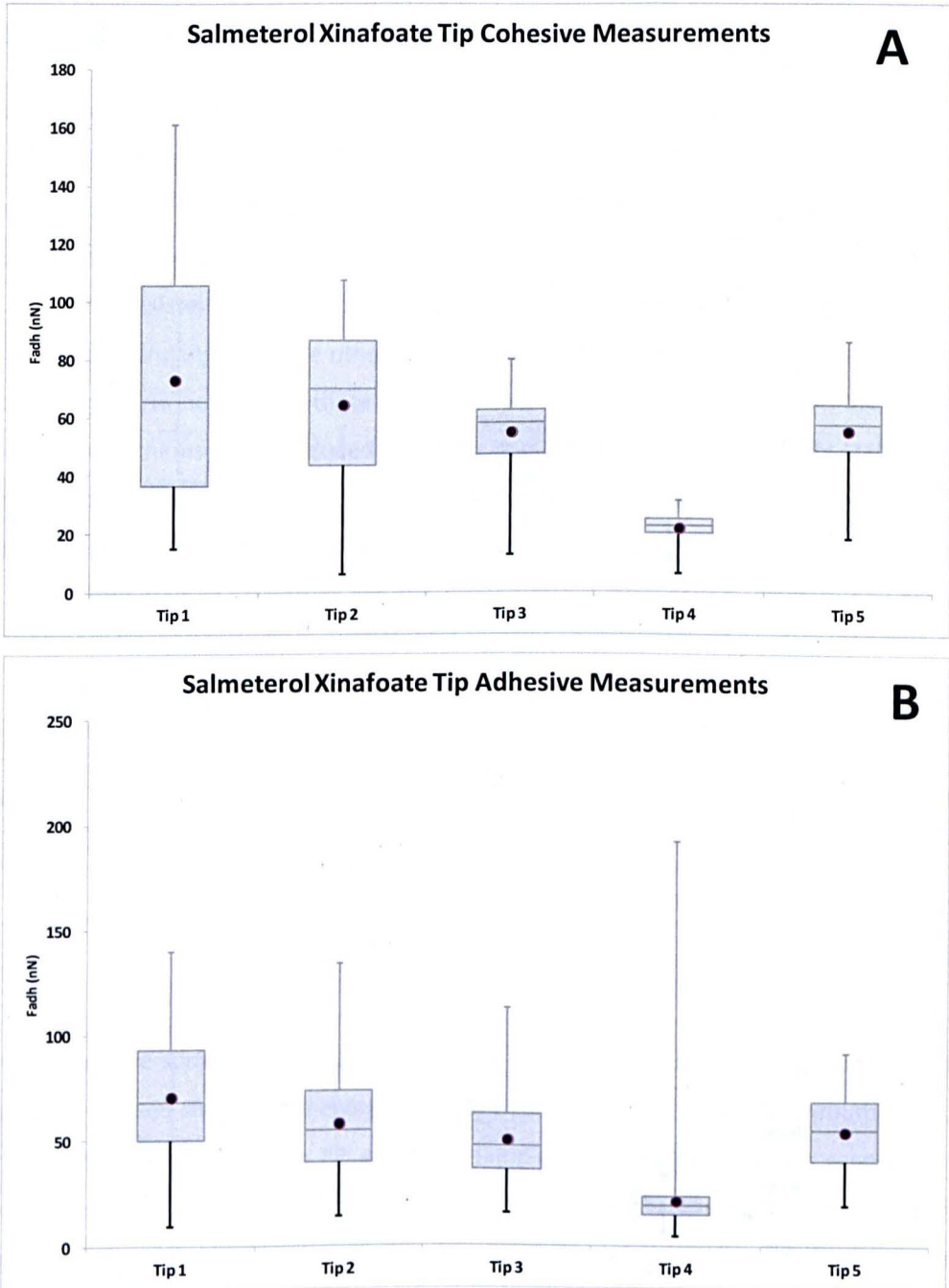


Figure 4.23: Box plots of the force of adhesion measurements of Salmeterol Xinafoate tips on a A) Salmeterol Xinafoate substrate and B) Fluticasone Propionate substrate

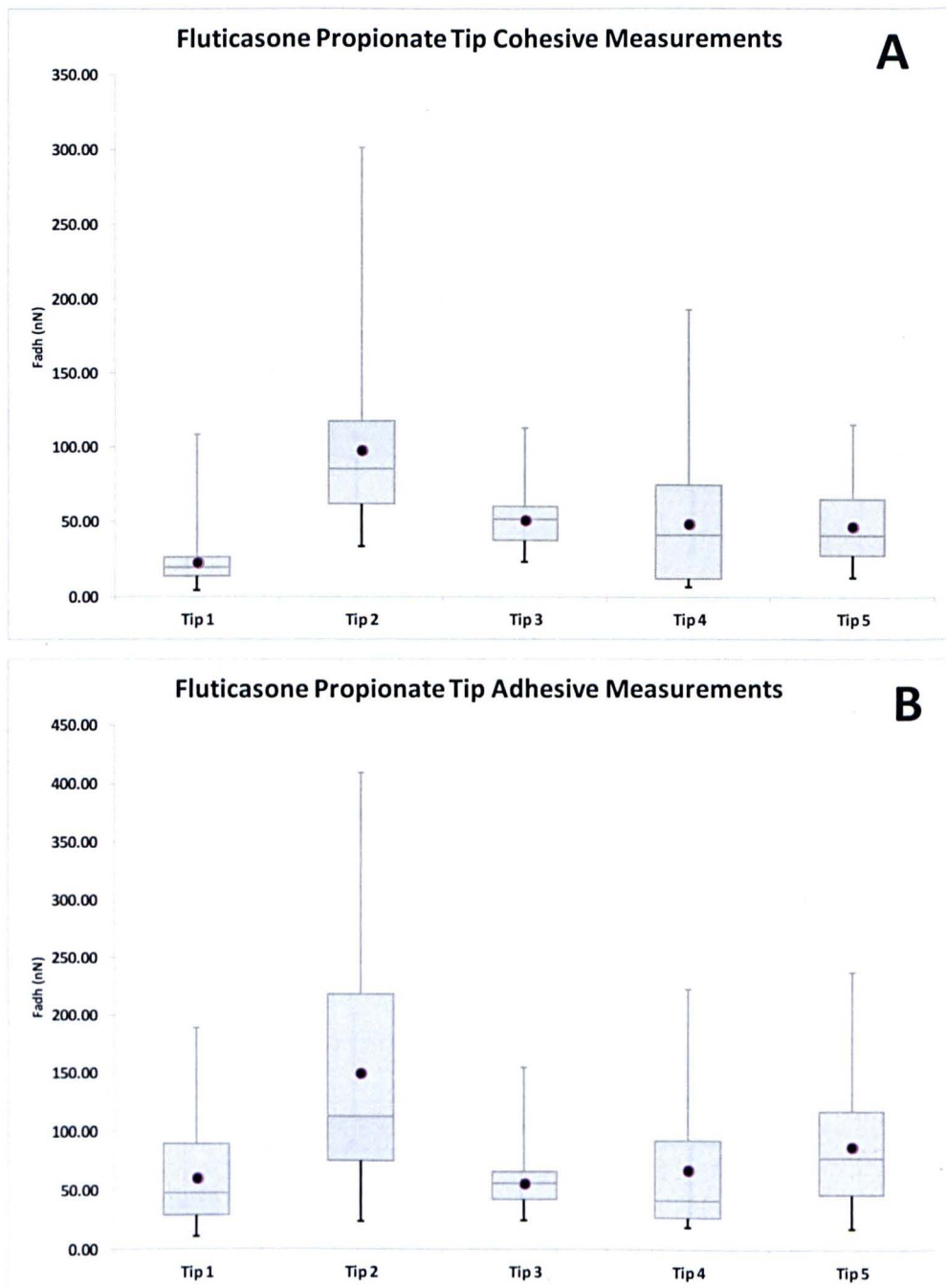


Figure 4.24: Box plots of the force of adhesion measurements of Fluticasone Propionate tips on a A) Fluticasone Propionate substrate and B) Salmeterol Xinafoate substrate

4.5 Discussion

4.5.1 Characterizing the API Power Compresses

4.5.1.1 Surface Energy Analysis and Differential Scanning Calorimetry

The compression of the API powders into powder pellets was largely a success in providing coherent substrates intended for further AFM based work. All of the APIs produced succinct and structurally solid powder 13mm discs after compression in the IR press with the exception of BUD. This API consistently produced a structurally unstable, fractured compress easily disrupted with minimum handling. Both the other corticosteroids, BDP and FP did produce useable pellets although it is worth noting that these were both significantly more friable than the two beta₂-agonists, which themselves produced distinctly homogeneous and structurally stable powder discs. Once these discs had been manufactured the next step was to investigate whether the compression process itself had induced any obvious changes in the physicochemical state of the APIs, and through an investigation into the surface free energy of the resultant powder discs, determine both their suitability for force based AFM work and an appreciation of their rank interactivity.

As table 4.1 and figure 4.1 illustrate, the rank order of surface free energy as determined by AFM ran as follows:

$$\text{SS} > \text{BDP} > \text{SX} > \text{FP} > \text{BUD}$$

The values for the surface free energy levels observed were broadly similar to those extracted by other AFM based surface free energy experiments (James et al, 2008, Bouhroum et al, 2009 etc.) with the exception of the FP and BUD samples. Both these samples recorded lower surface free energies than previously documented, (although it is worth noting significant variability in the recorded values). These two substrates were the most difficult samples to generate force data from with quite visible and tactile degeneration of the compress surfaces. Most specifically the BUD sample as a compact, was very fragile and fell apart readily. This led to a great deal of difficulty in identifying appropriate regions upon which to make force measurements, and as a consequence of the poorly homogeneous surface structure led to

several force curves of unusable nature. The degree of surface heterogeneity is most probably why the budesonide sample showed the greatest standard deviation within the three AFM tips employed (fig 4.1, table 4.1). Because of the difficulty using the BUD compress it was decided that this API would not be put to further use within further CAB based experimentation. FP, although generating a fragile compact was still proven capable of standing up to handling and force based experimentation albeit with a persistent degree of variability between and within the individual AFM tips. The three other powder discs were much more versatile and the beta₂-agonists in particular generated apparently topographically smooth and stable compacts. The BDP compact was not quite as stable as the SS and SX samples, and appeared less homogeneous topographically, with some areas of surface splintering and protrusion. It was of interest that the corticosteroid should have a calculated surface free energy between the two beta₂-agonists as it was expected that the two distinct chemistries of the different API classes would generate a class specific divide. It is however possible that the BDP sample showed a greater surface free energy than the SX compress due to increased variability in adhesion forces arising from a less consistent topographical surface. While figure 4.1 shows that the BDP samples showed the least variance between the AFM tips, when considering table 4.1 the adhesion force data for BDP had a larger deviation than the SS and SX. This may infer increased surface roughness, leading to a greater variability in contact regimes between probe to surface contacts. Notably the SS substrate showed the greatest consistency within each tip's adhesive force data measurements, but a greater degree of deviation between the tips than both the SX and BDP compress samples. This may reflect both a short range homogeneity and lack of surface roughness of the salbutamol sample but with wider topographical heterogeneity.

From figures 4.2, 4.3 and 4.4 we can compare the basic thermodynamic assessment of the API powders before and after compression. As indicated BUD was not used due to the failure of the API to produce a workable powder compact. However the other four APIs were analysed by DSC to identify any induced thermodynamic events in the compressed sample, or changes to the extent or occurrence of previously identified transitions. What can be seen, especially in figure 4.4, is that for all the samples, there was no obvious induction of any new phase transitions, or displacement of the existing (primarily melting) endotherms. Whilst this suggests that the APIs had not been significantly contaminated or undergone radical polymorphic changes it is worth noting that the DSC runs for these samples would not be expected to pick up very subtle

alterations to API physicochemical states such as crystallization behaviours etc. without further methodology refinement. In particular any surface changes which may be insignificant in terms of percentage mass (and hence undetected by DSC) may have a significant impact on AFM based measurements. What was evident however was that there were some changes to the behaviour of the compressed APIs. SX showed consistent thermograms prior to compression with a large endotherm at around 124°C and a second smaller endotherm at 138°C. Very obviously after compression the first endotherm had reduced relative to the second. These endotherms can be associated with the melting of two polymorphs of the beta₂-agonist, the stable form I (124°C) and the meta-stable form II (138°C) (Tong et al, 2001, Beach et al, 1999). Subsequently it can be concluded that the compression process may have changed the polymorphic balance of SX, with more form II being formed. This is important as it suggests the compression process has affected the API, and may have led to different molecular orientations which could impact a CAB. This will warrant further investigation, such as the use of techniques such as FT-IR or confocal Raman so as to ascertain the extent and location of any polymorphic change which was beyond the scope of this current work.

4.5.1.2 SEM and AFM Roughness Analysis of Beclomethasone Dipropionate and Salbutamol Sulphate Powder Compacts

From the surface energy data and the DSC thermograms collected it was decided to further analyse the SS and BDP by SEM and AFM. While these two APIs would not be considered in a real formulation together due to their different clinical frequencies of use and speed of respective physiological effects, they proved to be the two highest surface energy APIs, which would give them the greatest chance of developing significant forces of adhesion and cohesion that could be identified within a CAB model (adapted to rougher surfaces). More fundamentally they are APIs from two different drug classes with distinctly different chemistries between which it would be of interest to explore in a force balance approach.

As the data in figure 4.4A and figure 4.6 shows, both powders had very distinctive morphologies prior to compression. The AFM and SEM images were in agreement that the SS powder presents as a series of irregular plate-like particulates that co-associate to some extent. The particle size

Chapter 4 - Application of the CAB approach to, and Characterization of 'Semi-Model' Inhalation Substrates

was in the region of 2-5 μm in diameter, however some smaller particulates can be seen especially by SEM (fig. 4.4A). The existence of several even larger agglomerated particle masses on the scale of 5-10 μm can also be identified. The BDP powder showed a very different morphology, with both the SEM and AFM images showing much more spherical particles, generally smaller (~0.5-1 μm in diameter) than the SS particles with some larger exceptions. Quite evidently however these smaller particles are broadly all aggregated into larger and irregularly spread agglomerates that span across the powder bed. From the SEM images (fig 4.4A BDP, SAL A) it can be seen that the BDP powder looks rougher than the SS powder, with more topographical variability as the irregular agglomerates stack to generate frequent particle protrusions and crevices between the aggregates. The SS powder bed looks smoother in comparison but in a similar fashion there are some obvious topographical features developed by the arrangement of the larger particles and smaller particles associated with these into aggregate mounds and depressions between them. This suggests both powder beds are inherently much rougher than the target sub to low nanometre constraints of a pure CAB study, and the AFM imaging bears this out (fig. 4.6).

Crucially tables 4.2 and 4.3 define the roughness of these powders and show that they are both too rough for use as a CAB substrate, with roughness values in excess of the failed CAB substrates in chapter 3. It was considered important to look at two scan sizes for the roughness calculations, as the roughness parameters defined and used in tables 4.2 and 4.3 are specific to the surface area to which they refer and significantly, powder surfaces will often not be uniform, i.e. topographical variability will usually increase over larger surface areas. So while a 5 μm x 5 μm scan area may better represent the locale where a single particle contact may occur, the 10 μm x 10 μm scan size gives a better idea of how consistent that surface character is. This is a particularly significant consideration when there is an intention to perform force based measurements across a surface, as such force based surface characterization is much more representative of that material if wider areas are sampled. The surface roughness values of the SS powder across both scan sizes were 230 nm R_q over 5 μm x 5 μm and 530nm R_q over 10 μm x 10 μm . The BDP powder had an average R_q over 5 μm x 5 μm of 352nm and over 10 μm x 10 μm of 541nm. Significantly this data backed up the visual appreciation that the BDP powder was rougher than the SS at both scan sizes, however interestingly, the BDP powder had not increased in roughness (54% increase) to the same extent as the SS powder (130% increase).

This is perhaps explained by the average R_{max} values of both powders, where the increase between the two scan sizes for BDP was from 2300 nm to 3627nm, where SS was from 1557nm to 3599nm. This suggests that smaller particle agglomerates of the BDP powder generate larger surface topographical variability at smaller scales, but that the larger particles of SS will orient and render more significant roughness over larger areas, as irregular large particulate agglomerates protrude from the surface or generate surface depressions.

After compression the SEM images (fig 4.5) show the dramatic changes to the API surface morphologies and consequent topographies. The SS compress shows an almost complete loss of individual particle definition at higher magnifications (fig 4.5 SS B). The surface now appears consistently mildly undulating with some very small irregular depressions. The macroscale surface (fig 4.5 SS A) appears flat and homogeneous apart from some distinct surface defects such as scoring and the occasional fragment contaminant. The scoring marks are likely the result of surface defects of the stainless steel IR die pellets that compress the powders, causing an imprint to be generated on the powder compact. The fragments are also probably the result of some surface destruction in the compress removal or handling process. Both these surface features are not consistent in their coverage of the powder compact. Some areas suffer heavy incidence while others remain largely homogenous and topographically consistent. The beclomethasone compact still shows some individual particle character (fig 4.5 BDP B) in the SEM images, as it appears the small spherical particles have been compacted as multi-component agglomerates into each other. The surface appears significantly smoother, but the compressed particle agglomerates create a 'paving' pattern with some degree of protrusion shown by the electron micrograph. Over the larger areas (fig 4.5 BDP A) this paving effect can still be seen, and in similar fashion to the SS powder disc, there is evidence of some surface scratches and fractured powder debris inconsistently spread across the surface. This debris appears more regularly on the BDP images, suggesting the more friable powder was more susceptible to damage on production and handling than the SS.

The AFM images (fig 4.7) again are largely consistent with the SEM images with respect to the compacted discs. The SS disc shows evidence of some individual particle, or individual agglomerate character at the smaller scan size. Here some surface cracks and powder demarcations suggest the overlap of the original particulate matter. These are not significant in

scale, often only a few nanometres in width and one or two micron in length at most. However when looking at the larger scan size, these features are much less discernible and the surface appears very homogenous, scattered irregularly with small peaks and surface folds. The vast majority of the surface appears to bear a unidirectional sweeping pattern, which again is most likely the imprint of the stainless steel pellet used to compress the APIs. The AFM images of the BDP pellet highlight the paving effect of the compressed particles seen in the SEM images. Notably, while the height differential is actually quite small (10s of microns) the AFM images at both scan sizes define the surface as a compacted multiparticulate background with frequently dispersed larger particle protrusions. This spread is best seen at the larger scan size and contrasts distinctly from the SS disc on which larger images make it less obvious to define individual particle situation.

From both the SEM and AFM images of the two compacts it is evident that a significant reduction in surface roughness was achieved, and this is most obviously proven in tables 4.2 and 4.3 and figure 4.8. Figure 4.8 shows most graphically the extent of the surface roughness decrease between the free powders and their associated compacts, with close to a 14x and 19x reduction in average R_q at the $5\mu\text{m} \times 5\mu\text{m}$ scan size for beclomethasone and salbutamol respectively, and a 34x and 30x decrease in average R_q at $10\mu\text{m} \times 10\mu\text{m}$. The average roughness values (R_q) for both compacts across both scan sizes are much closer to the target roughness values that would allow a semi-model CAB to be performed (25.4nm and 15.6nm for BDP and 11.8nm and 17.3nm). As expected an increase in topographical consistency of the powder compacts is related to a reduction in the standard deviation about the roughness measurements made on the samples. The inherently rough and irregular powder sample AFM images individually show a range of R_q values and maximum topographical features, while the powder compact images are significantly more consistent with less variation from location to location in terms of absolute R_q or R_{max} . Despite this significant improvement it should still be borne in mind that this represents a 10x-20x greater roughness than a single crystal face. The only unexpected result from the roughness analysis is the lower average R_q for the BDP compact across the larger scan size than the smaller scan size. This may simply be related to the increased deviation about the BDP $5\mu\text{m} \times 5\mu\text{m}$ measurements, with two slightly raised R_q values skewing the data. What can also be seen is that the SS compacts were smoother than the BDP compacts over the lower scan size and that this was reversed over the larger areas.

Certainly the compression process can be seen to have dramatically reduced the surface roughness of both the APIs, generating substrates which would be much more suitable for a force balance experiment. The surface morphology of both has also been altered, significantly more so with the beta₂-agonist than the corticosteroid. This has facilitated the topographical normalization but it is unclear as to whether subtle surface specific physicochemical changes have occurred which would affect the validity of force measurements.

4.5.2 The Cohesive Adhesive Balance of Salbutamol Sulphate and Beclomethasone Dipropionate using Semi-Model Substrates

4.5.2.1 AFM Tip Functionalization

The AFM tip functionalization process was carried out with great care to generate only small functional tips. This was in an attempt to reduce the size of the contact regime in the force balance and avoid the impact that such large functional particles (such as the clathrates in chapter 3) had in multiplying the effect of substrate roughness. In this fashion, with particular care to use only minimal volumes of adhesive and attach only individual particles (or particle agglomerates) the AFM tips were all characterized by SEM to confirm successful functionalization (fig 4.9). From the SEM images obtained it was possible to see that all the functional particulates were attached to the AFM tip, with no critical contaminants on the rest of the cantilever. On two occasions excluding the rejected tip (e.g. fig 4.9 BDP) multiple particulates were seen on the same tip, however it was obvious from both images that because of the morphological difference in the particles, only one would make surface contact as the functional particle and hence these tips were accepted. This differed from the rejected tip where multiple particles presented quite possibly multiple sites of surface contact. On a couple of tips there was also concern about larger amounts of adhesive being present than intended. However as the functional particulates were not seen to be coated in the adhesive, it was assumed this would not be a practical issue upon force measurement.

4.5.2.2 The Cohesive Adhesive Balance

Figure 4.10 shows the CAB plot representing the force data for the BDP functionalized probes. Significantly it can be seen that all the plot points lie on the adhesive side of the xy intersect. Furthermore, these plot points all appear to be well correlated, and indeed a linear fit gives a CAB ratio of 0.35, with an R^2 value of 0.57. Figure 4.11 shows the CAB plot for the SS functionalized tips. Conversely in this instance all the probes return force results that lie above the xy intersect, or in the cohesive domain. These plots again appear reasonably well correlated with perhaps one exception (154,355), and a linear fit models a CAB ratio of 1.69 with a coefficient of determination again of 0.57.

These results are significant in a multitude of ways. Firstly the very co-association of all the plot points in both figures 4.10 and 4.11 onto one side of the CAB plot is strong evidence for a general classification of the two materials into a force balance descriptor. This would suggest that the BDP tips induced a greater adhesive force with the SS substrate than the cohesive force from the BDP substrate, and that the SS tips interacted to a greater extent with the cohesive substrate than the adhesive substrate. In essence this reflects that SS is more interactive with itself than BDP but that BDP is more interactive with SS than itself. This could be considered an expected trend, as it is consistent with the surface energy measurements made in figure 4.1. Here the API with the higher surface energy measurement dominates the force balance with respect to the API with a lower recorded surface energy. However the realization of this relationship as a quantifiable force balance could be of huge significance if these two APIs were co-formulated, as this relationship may lead to an influence on a multitude of parameters, from solubility issues, to aerodynamic particle genesis and the resulting deposition profile. Furthermore the reasonable linear correlation of the data points, would support confidence in the balance data.

Figure 4.12 shows some example force curves from both a SS and BDP tip on a cohesive and adhesive surface respectively. The consistency seen with the force curves in this instance was far superior to that seen in the previous chapter and there was no rejected force curves due to technical failings. The example adhesions seen in figure 4.12 were representative of the data as a whole and support the inference of the CAB plots that BDP has a larger force of adhesion with SS than it does with itself and vice versa.

Figures 4.13 and 4.14 go further towards supporting the significant improvement in surface contact area consistency. The box plots of the two tip materials show a generally good compliance of the mean to the median average of the tip-surface data. This is important as it suggests a broadly Gaussian distribution of the force data that would be the expected distribution on a molecularly smooth surface. While there are some slight discrepancies, such as the SS tip 4 adhesive data the SS tip 3 cohesive data (fig 4.13) and the BDP tip 1 and 2 cohesive data, these have been caused by some extreme outliers. The existence of such outliers may be attributed to the remaining surface and tip roughness combinations causing more discreet but still palpable alterations to F_{adh} genesis. However in comparison to the pure material runs in chapter 3 the compliance of the two averages and the visibly more symmetrical statistical arrangements of these box plots serves to confirm that compression of the substrates, and small particle tip functionalization had a significantly positive impact on contact regime consistency. Furthermore in this instance these plots validate to the most part the use of the mean as the data descriptor within the CAB plots.

Hence, it can be suggested in light of the range of data above that the compression of the APIs was sufficient to allow a CAB to function broadly. While topographical variability is obviously still an issue, as evidenced with the small spread from a linear fit observed and the statistical arrangements shown by the box plots presented, the close to 60% confidence in the CAB ratios extracted lends itself to the success of the semi-model substrates as a middle ground for CAB assessment. This is again potentially of importance, as if we determine the semi-model substrates are better characteristic of the 'in-situ' APIs then such a CAB may better define the relationship of the real materials or offer a less work intensive means to assess this force balance.

There is a significant improvement in terms of a correlation over the previous results and suggests that the semi-model substrates and smaller functional tips have sufficiently reduced the geometric variability in the contact regime to allow the broad application of a CAB approach. While a pure CAB remains impossible with such materials, the improved confidence in such correlation is adventitious in providing a quantification of the balance. This was beyond the expected classification of the API force balance simply into an adhesive or cohesive domination and allows for a direct comparison with future force balances.

4.5.3 The Cohesive Adhesive Balance of Salmeterol Xinafoate and Fluticasone Propionate using Semi-Model Substrates

4.5.3.1 SEM and AFM Characterization of the Powder Compacts

Having seen that a force balance was successfully carried out using BDP and SS powder compacts, it was decided to investigate whether another force balance could be established with a second combination of APIs using the same modified substrate approach. The second combination of APIs chosen was that of SX and FP. These two were another combination of a beta₂-agonist and corticosteroid, but with subtly different chemistries. Furthermore this combination has widespread clinical use, as both a DPI and pMDI formulation for the treatment of asthma and other inflammatory respiratory diseases (Seretide[®] Inhalers). In this instance therefore the combination of APIs is a more realistic one than that experimented with using BDP and SS and still presents an interesting combination of chemistries. While the success of the compression process in reducing powder roughness and increasing surface suitability had already been proven and characterized using the BDP and SS data, it was still considered important to broadly characterize the SX and FP powders using imaging techniques to account for any variation in effect the individual APIs might show as a result of their unique chemistries.

Before compression figure 4.15 shows the particle morphologies of the two APIs as seen by SEM imaging. The SX and FP powders show different particle shapes and sizes. The FP particles are significantly more spherical, with nodular rough surfaces. At larger magnifications (fig 4.15 FP B) these particles show a strong tendency to cluster into agglomerates. They are smaller in length than the SX particles in general but broader. The SX powder (fig 4.15 SX B) shows more irregular particle morphology with more elliptical, long, thin and smoother particle characteristics. These appear to have agglomerated less consistently at higher magnifications over smaller areas. However, lower magnification (fig 4.15 SX A) images show agglomerate development, with distinct particle bodies creating an irregular surface by particle clustering and overlay. By contrast the SEM images of the compressed powders show significant topographical smoothing. The FP powder compact (Figure 4.16 FX) now shows a much more consistent topography. Individual particle character has been generally reduced, although some definition of the individual particles can still be seen as a pattern of slight protrusions away from the average surface, and demarcations of particle outlines. The SX compact similarly shows some small signs

of individual particle character (fig. 4.16 SX B) at higher magnifications, although not so pronounced as with the FP disc. Over larger areas at lower magnifications (fig. 4.16 FP SX A) both discs show no distinctive pattern to identify the original particulate localization. Both show significant smoothing with large areas of a consistent surface. However both discs also show surface features consistent with the SS and BDP samples, in the unidirectional track marks across the images. Again these are likely to be the impression left by the die casting process. In SX's case these are less obvious, but where visible show significant topographical impact, leading to bunching of the API material and small pieces of surface debris in secluded areas. The FP disc shows far more consistency of these imprints, with many leading to small surface cracks and some to entire fissures.

The AFM images of the powder compacts support the impressions given by the SEM image assessment (fig. 4.17). Both the FP and SX discs show a spread of particles protruding from the surface, but these are more significant in terms of scale and frequency on the FP disc. Both samples seem to evidence the same undulation of the surface as the probable consequence of the press imprint, but the SX disc looks broadly more homogenous, with the FP surface less consistent with far more irregular associations of prominent particles. The roughness analysis of the compacted API powders performed on the AFM images is shown in figure 4.18. A comparison with the free powder was not done, as it was not considered necessary to further characterize the scale of roughness reduction, as the flattening process was plainly evident from the SEM images collected. Importantly though, figure 4.15 highlights that the compaction process has generated surfaces with similar a roughness to the two previous APIs. This suggested that these powder compacts were suitable for use as CAB substrates. The SX compact can be seen to give a smoother average R_q than the FP compact over both scan sizes (13.9nm R_q at 5 x 5 and 17.4nm R_q at 10 x 10 compared to 20.0nm R_q 5 μm x 5 μm 23.6nm R_q 10 μm x 10 μm). This again shows the beta₂-agonist as smoother on compression than the corticosteroid. This may suggest, in line with some of the features seen optically and the general handling of the compacts, that the corticosteroid surfaces are more fragile, and fracture prone, less flexible to the compression process. However the increase in roughness from small scan area to larger presents a bigger percentage increase by R_q with respect to the SX powder (25%) than the FP powder (18%). This in turn may indicate the FP powder has a more consistent topography over larger areas than SX powder. However, from the SEM images analysed the FP disc can be seen

to be subject to several surface collapses (cracks, inversions etc.) that will not be factored into the AFM data on these scan sizes and by scan area selection.

4.5.3.2 AFM Tip Functionalization

The SEM images of SX and FP tip functionalization (fig 4.19) were consistent with those seen with the BDP and SS tips. In this instance no tips were seen to have failed the functionalization process or were rejected. There were similar issues regarding multiple particulate attachments, and some excess areas of adhesive, but these were again investigated with further imaging and accepted as non-critical. In general the FP particle attachments were larger than the SX attachments, but all were of a significantly decreased particle size to the failed functional particles in chapter 3.

4.5.3.3 The Cohesive Adhesive Balance

The CAB of SX and FP using the powder compacts further proved that the semi-model substrates could be utilized successfully in describing the force balance of a combination of APIs. For both API tip types a strong linear relationship between all the tip plot points could be seen. This suggests that proportionality was broadly maintained between F_{adh} and F_{coh} from tip to tip. The implications of such are that the contact geometry between the tips and the cohesive and adhesive surface was not changing critically so as to bias the basal chemical forces. In this instance the confidence in the fit was compounded by coefficients of determination that were even stronger than those with the SS and BDP powders, (0.81 for FP tips and 0.97 for SX tips). This supports the success of the compaction process in providing substrates suitable for use with a CAB approach in defining a broad force balance of two APIs. The FP tips (fig. 4.21) all lie in the adhesive domain of the CAB plot, and when fitted linearly generate a CAB ratio of 0.63. This therefore infers that FP has a stronger force of adhesive interaction with SX than the force of auto-adhesion. Conversely the SX tips (fig 4.22) all plot force points just above and very close to the xy intersect where $F_{adh} = F_{coh}$. The gradient of the linear fit of these points gives a CAB ratio of 1.08. This would therefore indicate that SX has a very slight cohesive tendency i.e. it undergoes larger interactive forces when contacting itself than when contacting FX. However, this CAB ratio is only just above the cohesion/adhesion parity, and therefore this balance may

reflect that SX largely interacts on a similar scale with both itself and FP and has a neutral force balance. When this balance is compared to the one performed between SS and BDP the same broad trend can be seen, i.e. that the beta₂-agonist has a cohesively dominated relationship with the corticosteroid and the corticosteroid an adhesively dominated relationship with the beta₂-agonist. However with the SX FP force balance this is far less pronounced. Visually both the FP and SX balances lie closer to the xy intersect than the SS BDP balances. The CAB ratios for the two beta₂-agonists are 1.69 and 1.08 for SS and SX while for the two corticosteroids are 0.57 and 0.63 for BDP and FP respectively. Broadly the force balances sit according to what might be expected in line with the surface energy assessment of the APIs. However interestingly, the implied difference between SX and FP in surface free energy (37.1 mJ/m² to 27.7 mJ/m²) was very similar to that between SS and BDP (45.3 mJ/m² 27.7 mJ/m²). This would have suggested that based on a pure surface free energy basis, both balances would have shown similar cohesive and adhesive separations. It is possible that the deviation around the surface energy measurements on the FP compact hide the fact that it was closer to SX in surface free energy than the average suggested.

The example force curves in figure 4.20 were representative of the bulk of the force curves collected with all the functional tips used. Consistency was high and there were no rejected curves as a result of unusable traces. Again, as expected the general appearance of the curves is consistent with the CAB balance constructed from the mean of the data, showing larger adhesions between SX tips and SX than between SX tips and FP and the reverse with the FP tips. The box plots in figures 4.23 and 4.24 show a similar analysis to that of the SS BDP data. Broadly the mean and median of the tip-substrate datasets are roughly consistent, with some discrepancies arising where particularly large outliers appear to have pulled the mean away from the 2nd quartile. The fig 4.24 FP tip 2 cohesive and adhesive data is a good example of this, as is the FP tip 4 adhesive data and the fig 4.23 SX tip 1 cohesive data. In these examples it is reasonable to presume that this is still related to the roughness of the compressed substrates. Some variability in tip-surface contact geometries still occurs because the compressed substrates are not molecularly smooth. In some instances this is still generating contacts that are not equivalent in area, which leads to the genesis of exaggerated or suppressed F_{adhs} that stretch the data, and move away from the pure Gaussian distribution desired. Yet the SX adhesive tip data and most of the remaining tip-surface data shows a very good consistency of the mean to the median with balanced quartiles and whiskers. This infers a far more consistent

Chapter 4 - Application of the CAB approach to, and Characterization of 'Semi-Model' Inhalation Substrates

contact regime than with the pure materials trialled in chapter 3, which in turn gives rise to the far better correlations between the plot points in the CAB balance. That a linear regression of these points gives acceptable coefficients of determination is further support that the trends identified are not artificial. As with the SS BDP data, the box plots in figs 4.23 and 4.24 were assumed to provide suitable confirmation that the mean was a reasonable descriptor of the data for use in the CAB plots and that these CAB ratios were not overly biased by anomalous data.

4.6 Conclusions.

It has been shown that the compression of API powders for use as AFM substrates has been not only successful in allowing a series of investigations by AFM, including both imaging and force probing, but also (in conjunction with the considered selection of smaller functional particle probes) in allowing a broad CAB approach to be applied with success to two combinations of common APIs. The compression process has been shown to induce several changes in API morphology, topography and to an unknown extent the physicochemical makeup of the APIs. Some of these alterations are beneficial. Surface roughness of salbutamol sulphate and beclomethasone dipropionate powders have been reduced 15x to 30x fold depending upon the scan area considered, consistent with an obvious reduction in prominent particulate matter and surface smoothing. This has operationally facilitated conventional AFM measurements and allowed for the CAB approach to be applied without the model constraints being exceeded due to surface roughness induced contact regime alteration. The use of the compacts was further supported by the success of fluticasone propionate and salmeterol xinafoate compacts to perform further CAB analysis. Interestingly a slightly different force balance was identified that offers an interesting comparison to that of the salbutamol and beclomethasone.

However there are concerns raised that the induction of thermodynamic alteration as seen by DSC, such as the potential polymorphic shift between the ratio of salmeterol xinafoate form I and form II is an indicator that the solid state structure of the API maybe affected and hence should be taken into account in future measurements. This perhaps defeats to some extent the purpose of finding a middle ground between the excessively rough 'as received' micronized powder particles and the recrystallized API surfaces in establishing a force balance. However the other APIs do not show any obvious changes to, additional or omitted thermodynamic events that might suggest critical changes to phase behaviour (Although this must be tempered by the inability to assess crystallinity or other succinct changes in physiochemical form). The appearance, in particular of salbutamol sulphate, post-compression may infer a recrystallization process has occurred under pressure. This again would detract from the aims of producing a semi-model substrate. Further investigation and characterization of the precise impact of the compression procedure would be advisable but this is limited by the exact demands of certain technical procedures and more problematically sample availability. However despite this the excellent success of these modified substrates in generating CAB plots with significantly

improved linear force plot correlations, has allowed a rough quantification of the force balance in both a salbutamol / beclomethasone and salmeterol / fluticasone system. The distinct division between the pairing of the adhesively dominated beclomethasone and cohesively dominated salbutamol as well as the near neutral balanced salmeterol and adhesively dominated fluticasone offers an opportunity to investigate differing force balances and their association with formulation performance indicators.

4.7 References

E.R. Beach, G.W. Tormoen, J. Drelich, R. Han. (2002) Pull-off force measurements between rough surfaces by atomic force microscopy. *Journal of Colloid and Interface Science*; 247:1:84-99.

A.Bouhroum, J.C.Burley, N.R.Champness. R.C.Toon, P.A.Jinks, P.M.Williams, C.J.Roberts. (2009) An Assessment of in situ Beclomethasone Dipropionate Clathrate Formation in Suspension Metered Dose Inhalers. *LBSA, School of Pharmacy, University of Nottingham*

J.L.Hutter, J.Bechhoefer. (1993) Calibration of atomic force microscope tips. *Review of Scientific Instruments*; 64(7):1868-1873

J.James, B.Crean, M.Davies, R.Toon, P.Jinks, C.J.Roberts. (2008) The surface characterization and comparison of two potential sub-micron sugar bulking excipients for use in low-dose, suspension formulations in metered dose inhalers. *International Journal of Pharmaceutics*; 361:209-221

H.H.Y.Tong, B.Y.Shekunov, P.York, A.H.L.Chow. (2001) Characterization of Two Polymorphs of Salmeterol Xinafoate Crystallized from Supercritical Fluids. *Pharmaceutical Research*; 18(6):852-858

5.0 The Cohesive Adhesive Balance of Inhalation Formulations and their 'in-vitro' Deposition Performance

5.1 General Introduction

5.1.1 Associating Force Balances to 'in-vitro' Deposition Performance

Chapter 4 showed that using a compressed API surface it is possible to perform a descriptive CAB experiment between combinations of APIs. Whilst the exact effects of the compression process upon the physicochemical nature of the APIs requires further investigation, there was success in identifying a rough force balance between two sets of inhalation APIs, which was not achievable with raw materials. This offers an opportunity to investigate the links between the force balance of the primary components of an inhalation system and the performance attributes of that system. When considering inhalation formulations one of the principal attributes a device and formulation combination must achieve is a suitable deposition profile. As chapter 1 indicated, for an API to elicit a physiological effect it needs to reach the appropriate target site. This not only requires a particle size of between 1 and 5 μ m, but also a subsequently suitable aerodynamic particle character. One of the means to measure the aerodynamic particle size of a formulation is to use an Andersen Cascade Impactor (ACI). This device acts loosely as an 'in-vitro' model of the airways, and its complete description and fundamental principals are explained in chapter 2. In basic terms the ACI is a series of calibrated gratings of reducing nozzle size which, with a calibrated air through flow, can be used to separate out incumbent airborne particulates onto collection plates below each grating. The gratings are also attached to pre-grating components that link the pMDI or DPI to the ACI stack, and roughly mimic the upper airways. The collection plates and the surfaces of the attaching components can then be analysed for quantifiable assessment of particulate deposition. The proportion of deposition throughout the stack can be used as an assessment and measure of the aerodynamic particle sizing of a formulation. Ultimately the effective aerodynamic particle size is derived from many complex variables, and this is even more complicated in a pMDI system with the use of a volatile propellant. Nevertheless the fundamental driving force is the interparticulate or inter-surface interactivity of the formulation components. Thus it is highly likely that differing force balances between the primary components will result in alterations to the aerodynamic particle sizing

achieved. While it is overly simplistic to factor out the influence of solvent forces derived from API suspension in the propellant, being able to associate the force balance between two key components to given changes in deposition profile could prove invaluable in the assessment of current and prospective formulations. This chapter will therefore centre on performing ‘in-vitro’ deposition assessments of two API combinations using an Andersen Cascade Impactor, in an attempt to link changes in the profiles obtained to the CAB of the systems already performed.

5.2 Chapter Aims and Objectives

5.2.1 Chapter Aim

The aim of this chapter was to investigate the ‘in-vitro’ deposition performance of two binary pMDI formulations in HFA134a, namely salbutamol sulphate with beclomethasone dipropionate and salmeterol xinafoate with fluticasone propionate. In so doing to attempt to identify whether a basic API system CAB could be associated with beneficial or disadvantageous changes to the deposition character of the individual components of a propellant based inhalation system.

5.2.2 Chapter Objectives

The chapter objectives were as follows:

- To investigate the ‘in-vitro’ deposition performance of the two binary systems in comparison to the deposition performance of the individual APIs.
- To establish any link between the CAB balance of the API combinations and their deposition performance.

5.3 Materials and Methods

5.3.1 Materials

Beclomethasone dipropionate (BDP), salbutamol sulphate (SS), salmeterol xinafoate (SX) and fluticasone propionate (FP) were chosen for investigation in this chapter. BDP and SS were chosen to be used as a combination as a result of the CAB performed between the two APIs in chapter 4. This identified a clear force balance. BDP showing a strong adhesively dominated relationship with the beta₂-agonist and the SS showing a strong cohesively dominated relationship with the corticosteroid in return. Fluticasone and Salmeterol were chosen as comparators to be investigated due to both the clinical prominence of this combination within both DPI and pMDI inhaler formulations (Seretide®), and also as another combination of the same two drug classes with subtly different chemistries. The force balance between these two APIs showed FP with a mildly adhesive force domination with SX and that SX showed a marginal cohesive, if not neutral force relationship with FP in return. The micronized powders were all provided by 3M Healthcare (Loughborough, UK). A Ventolin® inhaler (containing salbutamol sulphate 100µg per actuation in HFA134a) was also provided by 3M Healthcare Ltd (Loughborough, UK) to run as a comparator to the salbutamol containing formulations. All pMDI components and accessories for manufacture were provided by 3M Healthcare Ltd (Loughborough, UK) unless otherwise stated. All other reagents and accessories were provided by Sigma Aldrich Company Ltd (Gillingham, UK).

5.3.2 Methods

5.3.2.1 Formulation of pMDI canisters

The pMDI formulations manufactured in this chapter were as follows:

SS 100:	Salbutamol Sulphate 0.165g, HFA134a 99.83g
BDP 100:	Beclomethasone Dipropionate 0.165g, HFA134a 99.83g
SS BDP 50:	Beclomethasone Dipropionate 0.0825g, Salbutamol Sulphate 0.0825g, HFA134a 99.83g
SS BDP 100:	Beclomethasone Dipropionate 0.165g, Salbutamol Sulphate 0.165 g, HFA134a 99.67g
FP 100:	Fluticasone Propionate 0.165g, HFA134a 99.83g
SX 100:	Salmeterol Xinafoate 0.165g, HFA134a 99.83g
SX FP 50:	Fluticasone Propionate 0.0825g, Salmeterol Xinafoate 0.0825g, HFA134a 99.83g
SX FP 100:	Fluticasone Propionate 0.165g, Salmeterol Xinafoate 0.165g, HFA134a 99.67g

In addition to the formulations manufactured above, a Ventolin® inhaler (salbutamol sulphate 100µg per metered dose provided by 3M Healthcare Ltd, Loughbourogh, UK) was used as a comparator to the SS 100 formulation to identify any obvious differences in deposition profile that might indicate critical formulation issues with the in-house pMDIs.

The above manufactured pMDI target systems were based on a HFA 134a density of 1.206g/ml and a 50µl metering valve. Each formulation was then designed to deliver the following masses of API per metered dose:

SS 100:	Salbutamol Sulphate 100µg
BDP 100:	Beclomethasone Dipropionate 100µg
SS BDP 50:	Beclomethasone Dipropionate 50µg, Salbutamol Sulphate 50µg
SS BDP 100:	Beclomethasone Dipropionate 100µg, Salbutamol Sulphate 100µg

FP 100:	Fluticasone Propionate 100µg
SX 100:	Salmeterol Xinafoate 100µg
SX FP 50:	Fluticasone Propionate 50µg, Salmeterol Xinafoate 50µg
SX FP 100:	Fluticasone Propionate 100µg, Salmeterol Xinafoate 100µg

For each system a bulk unit was prepared in a Trimline can (1 inch neck) by adding the required amount of API or mixture of APIs to the can. The can was then sealed and the required quantity of HFA 134a (DuPont, Stevenage, UK) was then injected through the 1 inch non-metering valve from a donor can using a PTFE transfer button, to the target weight. Each Trimline can was then sonicated in an ultrasonic water bath for 3 minutes to effect dispersion of the micronized powder. The cans were then chilled in a cryobath to -60°C to maintain the liquidity of the propellant without pressurization and a then a hole was punched with a nail at a point just beneath the valve crimp. To form a spout, a polythene Pasteur pipette was then pushed into the hole and then clipped off around 1cm away from the can. The chilled contents from the Trimline can were then sequentially decanted via the formed spout into 16ml FEP coated pMDI canisters (3M Healthcare Ltd, Loughborough, UK) which were immediately crimped with Bepak BK357 50mcl metering valves. This generated a total of 6 MDI units per system. All units were then water bath tested for leaks at 40 °C.

The formulated masses of SX and FP used in the formulations above are not representative of those in clinical use. SX and FP systems are usually dosed at a constant dose of 25µg per actuation of SX with a variable dose between 50µg to 250µg of FP per actuation. SS and BDP are not clinically used together due to the predominant use of SS as an ‘as required’ reliever, and BDP as a regular prophylactic. However usual doses of SS and BDP are in the region of 100µg per metered dose. The masses chosen in this chapter were used to allow an appropriate assessment of the force balance of the system. By mass matching this removes mass variance as a variable for deposition effects. Both combinations of APIs were produced as a 50µg per actuation (50µg API 1 and 50µg API 2) formulation and as a 100µg per actuation (100µg API 1 and 100µg API 2) formulation. By delivering 50µg of each API this meant that a total API delivery of 100µg was maintained, and could be compared both with the individual API formulations for consistency but also to the doubled mass formulation to examine mass based effects. No other excipients

were used in the formulation process, so as to rule out their impact on the surface interactions of the APIs under consideration. The formulations were therefore tested within a maximum of two weeks of manufacture to reduce the potential for degradation or instability issues.

5.3.2.2 Andersen Cascade Impaction

An eight stage Andersen Cascade Impactor (3M Healthcare Ltd, Loughborough, UK) was used for aerodynamic particle sizing and deposition profiling of the formulated aerosols. A schematic of the apparatus is given below in figure 5.1

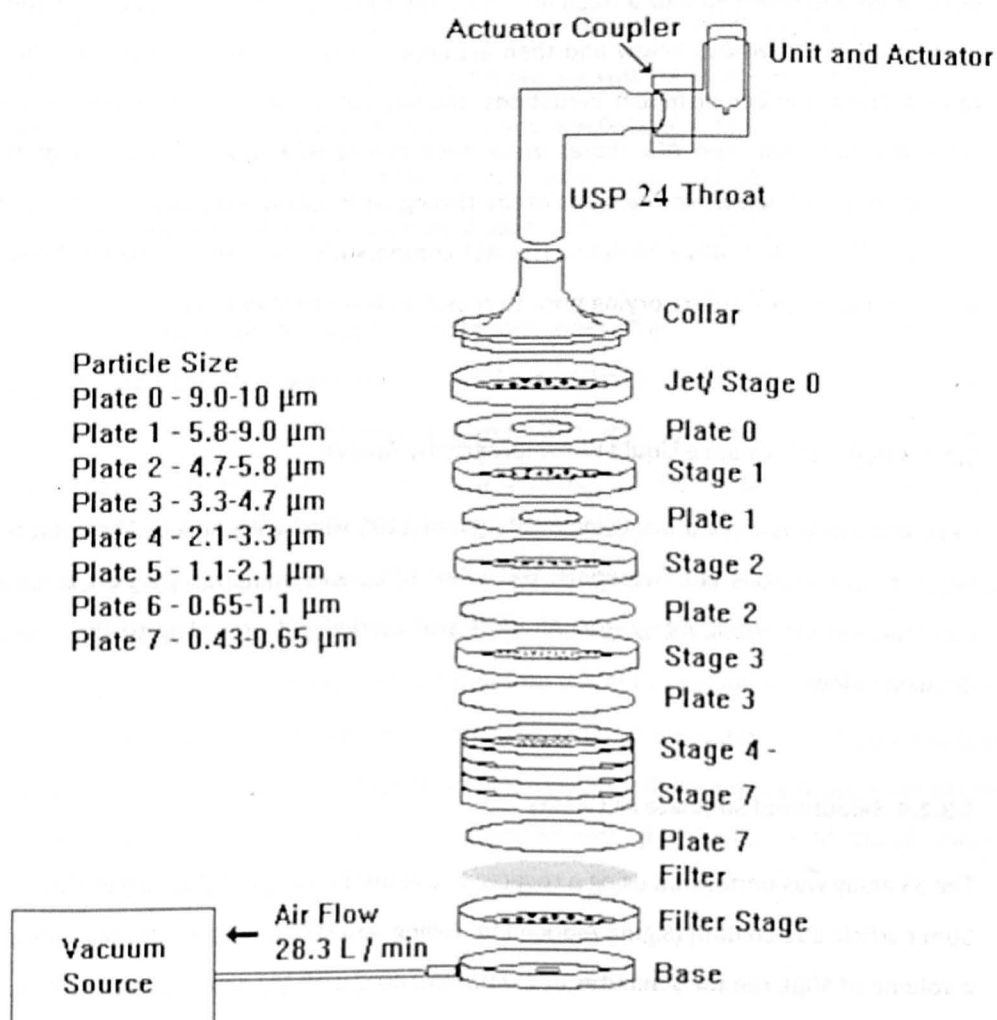


Figure 5.1: Schematic of an Andersen Cascade Impactor and associated particle size separation (3M Healthcare Ltd)

The ACI stack was assembled with all stages plated as shown, with silicone O-rings around each stage and Whatman grade 934-AH glass microfiber filter paper (Sigma Aldrich Ltd, Gillingham, UK) cut to size and fitted into the filter stage. A vacuum pump was used to draw airflow through the ACI stack at 28.3 l/min as per European Pharmacopeia standards for pMDI assessment (European Pharmacopeia, 2012). Airflow was calibrated by a DFM 200 flow meter (Copley Scientific, Nottingham, UK) attached via a mouthpiece adaptor, with a tolerance of ± 0.5 l/min. After airflow had been adjusted as necessary, formulation canisters were loaded into clean actuators. As per the ACI/HPLC methods described below these formulations were then pre-processed (waste firing, weight records etc.) as appropriate. After pre-processing, the canisters were dried and replaced into a fresh actuator. The formulations were shaken for the durations specified in the methods below and then actuated via an actuator coupler into the ACI stack. After a given number of repeat actuations, the vacuum pump was switched off, and the ACI stack disassembled. The ACI stages were each rinsed with given quantities of the sample diluents detailed below, and samples of the rinsing were taken and placed in HPLC autosampler vials for HPLC quantitative analysis. The ACI components were then washed thoroughly with water and methanol before drying prior to reassembly for further runs.

5.3.2.3 High Performance Liquid Chromatography Analysis

HPLC analysis was carried out using a HP Agilent 1100 HPLC with Agilent Chemstation software (Agilent Technologies Ltd, Stockport, UK). The HPLC was equipped with an autosampler, UV detector and electronic integrator. All work was carried out according to the assay protocols detailed below.

5.3.2.4 Salbutamol Sulphate ACI Assay

The SS assay was performed using a reverse phase methodology. A Supelco LC-18, 4.6 x 150mm, 5 μ m particle size column (Sigma Aldrich Ltd, Gillingham UK) was used. Samples were injected at a volume of 40 μ l, run for 6 minutes at 2.0ml/min, 40°C with UV detection at 225 nm. Two blanks and two reference samples were run before and after each sample set for system evaluation and calibration. The mobile phase was a mixture of 45% HPLC methanol: 55% triethylamine phosphate buffer with sodium dodecyl sulfate (pH 2.5). The triethylamine solution was prepared

by dissolving 1.442g sodium dodecyl sulfate into 980ml of HPLC grade water, then adding 6.8ml of phosphoric acid. The pH of the resulting solution was then adjusted to 2.5 with triethylamine (~11ml) and degassed for an hour. This generated a final buffer composition of 100 mM triethylamine phosphate with 5 mM sodium dodecyl sulphate. A binary solvent input was used on operation to obtain the requisite mobile phase constitution

The ACI stage sample diluent used was a mixture of *45% HPLC grade methanol: 55% 0.1% phosphoric acid (v/v)*. This was prepared by mixing 1ml phosphoric acid with 1000ml HPLC grade water, then combining 550ml of the resultant solution with 450ml methanol. SS reference standards were produced in duplicate. 43mg of SS was accurately weighed into a 100ml volumetric flask. This was dissolved into approximately 50ml of sample diluent, before sonication. After cooling the flask was diluted to volume with sample diluent. 2ml of the resultant solution was pipetted into a 200ml volumetric flask, diluted to volume and mixed well. 25ml of this solution was pipetted into a 50ml volumetric flask before dilution to volume and mixing. This gave a SS reference solution of approximately 2µg/ml (100µg/50ml).

Each SS formulation was actuated to waste four times after 10 seconds of appropriate shaking. The valve and valve stem were then cleaned with 10ml of water and 10ml of methanol before drying with a nitrogen tap. The canisters were then accurately weighed before returning to a new actuator. The ACI was operated at a standard 28.3l/min flow rate. The SS containing formulations were shaken appropriately for 10 seconds before coupling to the ACI via the mouthpiece adaptor, and actuation before 2 seconds from the end of shaking. The actuated unit was left for 30 seconds attached to the adaptor before removal and the process was repeated. Each device was actuated a total of five times into the ACI stack. After the final actuation the ACI stack was left running with the device attached at the mouthpiece for 30 seconds before the vacuum pump was shut down. The ACI was then disassembled into its constituent pieces which were all placed into sterile plastic bags pre-filled with given volumes of sample diluent. The volumes of sample diluents used were as follows:

Component / Plate	Rinse / Diluent (ml)
Valve Stem*	10
Actuator	50
Throat and Coupler	50
Jet, Plate 0 – Plate 3	10
Plate 4 – Plate 5	50
Plate 6 – Plate 7	10
Filter	10

Table 5.1 Salbutamol sulphate ACI stage diluent rinse volumes

After each component was placed into the bag, these were sealed and the pieces were agitated in the diluent using manual shaking for a minimum of 90 seconds. Each component was then rinsed down with the diluent volume using a disposable syringe before the further mixing to ensure homogeneity. Approximately 2ml of the diluent was then pipetted into a HPLC autosample vial. Notably the valve stem was an exception to this technique. It was not placed into a plastic bag but rather washed down inside and out with the 10ml of allocated diluent using a 5ml syringe and a needle into a clean beaker. The rinsing was mixed and then approximately 2ml was pipetted in a HPLC autosampler vial. The filter sample was first passed through a 0.45µm PTFE syringe filter to prevent any fibers from the filter paper itself contaminating the HPLC sample. The canister was then cleaned with water and methanol before drying and the recording of an accurate post run weight.

The API peaks from the HPLC chromatograms for were then integrated using the chemstation software to ascertain the area counts for quantification. The deposition mass on each stage was then calculated based on the calibration factors acquired from the standard solutions using the following equation:

$$SS_{Mass} = \frac{A_{sam}}{A_{std}} \times W_{std} \times \frac{P}{100} \times \frac{V_{sam}}{100} \times \frac{2/200}{1} \times \frac{25/50}{1} \times \frac{1000}{5} \quad (5.1)$$

Where SS_{Mass} is the mass of SS per actuation, A_{sam} is the area counts of the sample SS peak, A_{std} is the (average) area counts of the SS peak in the SS standard, W_{std} is the weight of the reference standard, P is the purity of the SS (%), V_{sam} is the volume of sample diluent used for the relevant sample stage, 2/200 and 25/50 represent the SS reference sample dilutions and 5 represents the number of actuations.

The mass of SS deposited on each component was then expressed as a percentage of the total recovered mass for deposition analysis. The mass of SS deposited on plate 3 to plate 7 was summed as the fine particle dose (FPD). This represents an aerodynamic particle size of $<5\mu\text{m}$ and is considered the target area for primary effect. The FPD can be expressed as a proportion of the total mass recovered of SS as the fine particle fraction (FPF). The mass median aerodynamic particle size (MMAD) for the formulation (the diameter at which 50% of the particles recovered by mass are larger and 50% are smaller) was then calculated from the ACI stack mass distribution using MMADcalculator (www.mmadcalculator.com, 2013). This calculation uses the calibrated nozzle sizes of the ACI in conjunction with the mass distribution of the formulation to plot cumulative masses versus aerodynamic diameters and statistically identify the median diameter. The geometric standard deviation (GSD) is then calculated in conjunction as a measure of the spread of the aerodynamic particle size distribution. Importantly both values apply with restriction to the calibrated ACI stack and do not account for mass lost to any un-calibrated pre-stack components (valve, actuator, throat etc.).

5.3.2.5 Beclomethasone Dipropionate ACI Assay

The BDP assay could not be performed from the same samples as the SS analysis due to the difficulty finding a method to separate the two APIs from each other in an adequately accurate, and time conservative manor. As such all the BDP assays were performed on separate runs, which was a limitation to a direct comparison of deposition performance. A Supelco LC-18, 4.6 x 150mm, $5\mu\text{m}$ particle size column (Sigma Aldrich Ltd, Gillingham UK) was used to run 20 μl aliquots of the samples. These were run at a 2.0ml/min flow rate, at 60°C for 12 minutes with UV detection at 238nm. The mobile phase was a mixture of 55% HPLC grade acetonitrile : 45% HPLC grade water. This was achieved using a binary solvent input. Standard solutions of BDP were produced in duplicate. 50mg of BDP (anhydrous) was accurately weighed into a 100ml

volumetric flask, dissolved in approximately 50ml of acetonitrile with sonication. After cooling the solution was diluted to volume. 2ml of this solution was pipetted into a 200ml volumetric flask which was diluted to volume with acetonitrile to give a standard solution of 5µg/ml BDP. Acetonitrile was used as the sample diluent. ACI operation parameters, sample diluent volumes and HPLC quantification was carried out in identical fashion to that described for SS in 5.3.1.4. The mass of BDP per stage was then expressed as a percentage of the total weight recovered for analysis, and the FPD and FPF of each BDP containing formulation documented.

5.3.2.6 Salmeterol Xinafoate and Fluticasone Propionate ACI Assay

An ACI assay for SX and FP was used that allowed for both APIs to be separated and detected using the same HPLC methodology. An ACE 5 C18, 75 x 4.6mm 5µm particle size HPLC column was used for analysis. Samples were run for 8 minutes (15 for jet stage and filter) isocratically at 40°C with a flow rate of 1.0ml/min. Injection volumes of 20µl were used from each sample and the detector was set to record UV absorbance at 228nm. The mobile phase for this assay was a mixture of *63% HPLC grade methanol: 37% ammonium acetate Solution (0.6% w/v): 0.05% trifluoroacetic acid (TFA)*. This was prepared by first accurately weighing 6g of ammonium acetate, and dissolving in 1000mL of HPLC grade water. 370ml of this resultant 0.6% w/v solution was then mixed with 630mL of HPLC grade methanol and 0.5ml of TFA to generate the mobile phase. Sample diluent for the ACI stage dissolution was prepared as a mixture of *85% HPLC grade methanol: 15% ammonium acetate solution*, produced by mixing 850ml of methanol with 150ml of the 0.6% ammonium acetate solution.

SX and FP standards were prepared in duplicate. 30mg of FP was accurately weighed into a 100ml volumetric flask. About 50mL of HPLC grade methanol was added, and the contents were sonicated until the API had completely dissolved. After the solution had cooled to room temperature, the flask was diluted to volume with methanol and mixed well giving a FP concentration of approximately 300µg/ml. 30mg of SX was accurately weighed into a 200ml volumetric flask. Approximately 100ml of HPLC grade methanol was added and the contents sonicated to complete dissolution. After equilibration to room temperature the flask was diluted to volume with further methanol and mixed well giving an SX concentration of 150µg/ml (103µg/ml salmeterol base). Using volumetric pipettes, 4ml of the fluticasone stock and 3ml of the salmeterol stock was measured into a 100ml volumetric flask. This was diluted to volume

with sample diluents and mixed well giving a standard solution with an FP concentration of 12µg/ml and an SX concentration of 4.5µg/ml (3.1µg/ml salmeterol base). ACI operation was identical to that as described for SS in 5.3.1.4 with the exception that 6 total actuations were used per formulation and that the following volumes of sample diluent were used for the relevant stages:

Component / Plate	Rinse / Diluent (ml)
Valve Stem*	10
Actuator	20
Throat and Coupler	50
Jet, Plate 0 – Plate 2	10
Plate 3 – Plate 4	20
Plate 5 – Plate 7	10
Filter	10

Table 5.2 Salmeterol xinafoate and fluticasone propionate ACI stage diluent rinse volumes

An example chromatogram of a SX FP sample solution is presented below in figure 5.1A showing the expected elution times and peak occurrences of the two APIs:

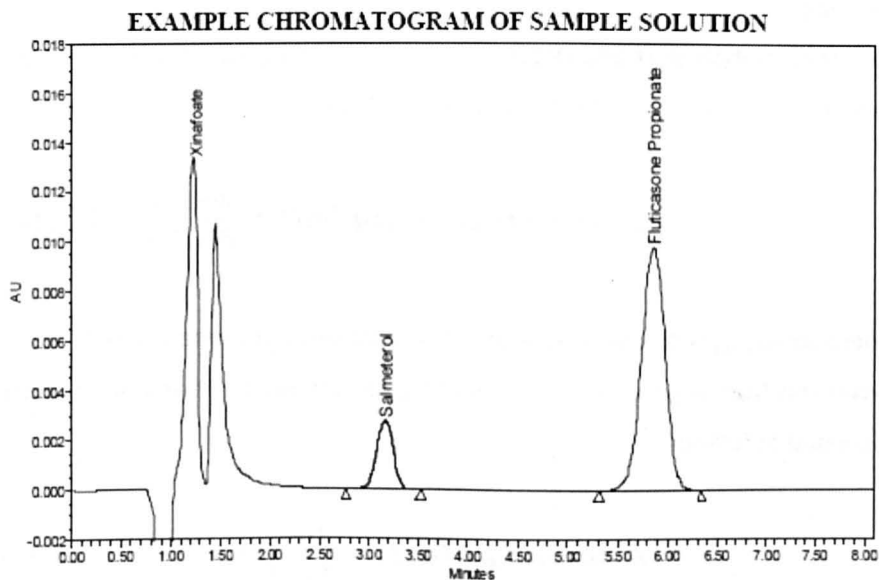


Figure 5.1A: Example chromatogram of salmeterol xinafoate and fluticasone propionate sample solution (3M Healthcare Ltd).

The API peaks were again integrated using the chemstation software to ascertain the area counts and the amount of each of the components was calculated based on the calibration factors acquired from the standard solutions. The SX calibration (B_{SX}) standard was calculated as follows:

$$B_{SX} = Area_{std} \div \left[\frac{(W_{std} \times P \times 0.6883)}{200ml} \times \frac{3ml}{200ml} \right] \quad (5.2)$$

Where $Area_{std}$ is the average peak area of the salmeterol peaks from quantification standards, W_{std} is the weight of SX used, P is the purity of the SX (1 for completely pure material), and 0.6883 is the molecular weight conversion from salmeterol xinafoate to salmeterol base. The remaining volumes represent the dilutions of the reference in production as described above. The calibration factor for FP (B_{FP}) was calculated as follows:

$$B_{FP} = Area_{std} \div \left[\frac{(W_{std} \times P)}{100ml} \times \frac{3ml}{200ml} \right] \quad (5.3)$$

Where $Area_{std}$ is the average peak area of the fluticasone peaks from the quantification standards, W_{std} is the weight of FP used and P is the purity of the FP (1 for completely pure material).

The concentration of SX and FP found on the valve stem, actuator, throat and couplet, jet stage, plates 0-7 and the filter could be calculated as follows:

$$Concentration (\mu g/ml) = \frac{Area_{sam}}{B_{SX}/B_{FP}} \times 1000 \quad (5.4)$$

Where $Area_{sam}$ is the peak area of the sample peak of interest, and the $\times 1000$ reflects the conversion from mg to μg . The amount ($\mu g/actuation$) of FP and SX on each component was calculated as follows:

$$Amount (\mu g/act) = \frac{Area_{sam}}{B_{SX}/B_{FP}} \times \frac{Dilution}{6} \times 1000 \quad (5.5)$$

Where **Dilution** is the volume of sample diluent used to rinse each stage respectively, **6** is the number of actuations per sample run and **x1000** is the conversion from mg to μg . In this fashion the amount of SX and FP deposited on each component could be calculated. The quantity of SX and FP deposited on plate 3 to plate 7 was summed as the fine particle dose (FPD). This represents an aerodynamic particle diameter of $<5\mu\text{m}$ and is considered the target area for primary effect. The FPD as a proportion of the total dose mass recovered is the fine particle fraction (FPF). The FPD may also be described as a proportion of the total expected dose delivered (i.e. $6 \times 100\mu\text{g FP} = 600\mu\text{g}$).

5.4 Results and Discussion

5.4.1 Deposition of the Solo and Co-Formulated Salbutamol Sulphate and Beclomethasone Dipropionate

5.4.1.1 Deposition Performance of Salbutamol Sulphate

Figures 5.2, 5.3, 5.4 and 5.5 show the individual stage by stage deposition of SS in a Ventolin® 100, SS 100, SS BDP 50 and SS with BDP 100 pMDI formulations respectively. These deposition profiles are expressed as percentages of the total collected dose of the respective APIs derived from the HPLC assay of the solvent wash offs of the ACI stack stages. Figure 5.6 shows all these deposition profiles for SS in combination for comparison. It can be seen that in all the SS formulation assays, there was a consistent general trend of deposition. High level deposition on the pre-ACI stages can be seen, most particularly the actuator and throat, where there was a consistent 50-60% of collected dose found in combination across all the salbutamol assays. There was then a subsequent decrease in deposition across the early stages of the ACI (jet stage to plate 1) before a subsequent increase to a 'second peak' starting at plate 2 and maximizing at plate 4, followed by a variable drop off in deposition to plates 5 and 6, with very little recovered mass on plate 7 or at the filter. Plate 4 was consistently the ACI plate with the most deposited material across all the formulations (16% Ventolin®, 13% SS 100, 13% SS BDP 50 and 13% SS BDP 100) with plate 5 consistently the next highest, followed by plate 3. This suggests that for all the formulations there were two significant areas of salbutamol deposition. Primarily this was the pre-stack surfaces, suggesting a high proportion of the emitted dose would be lost to the device or with respect to 'in-vivo' correspondence would be swallowed. However the second peak in deposition is in the respiratory target range or rather on the fine particle plates. These plates from plate 3 down to the filter represent an aerodynamic particle size of <math><5\mu\text{m}</math>, which is considered the ideal particle size range to reach the target airways and illicit the intended physiological responses.

Critically, however, it can be seen that the general trend in SS deposition is the same for all the formulations, with some distinct changes in the exact pattern. The salbutamol only formulations (Ventolin® and SS 100) shows a higher percentage deposition on the fine particle plates than the formulations co-formulated with BDP. This is coincident with what appears to be less

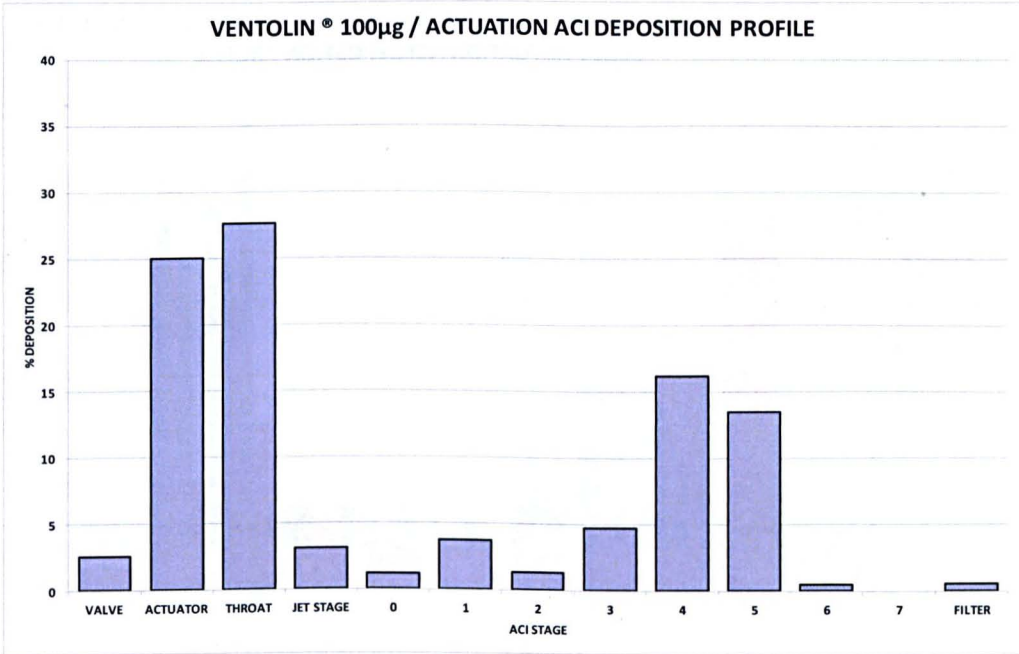


Figure 5.2: Percentage deposition profile across an Andersen Cascade Impactor of total collected dose of salbutamol sulphate from a Ventolin® pMDI formulation.

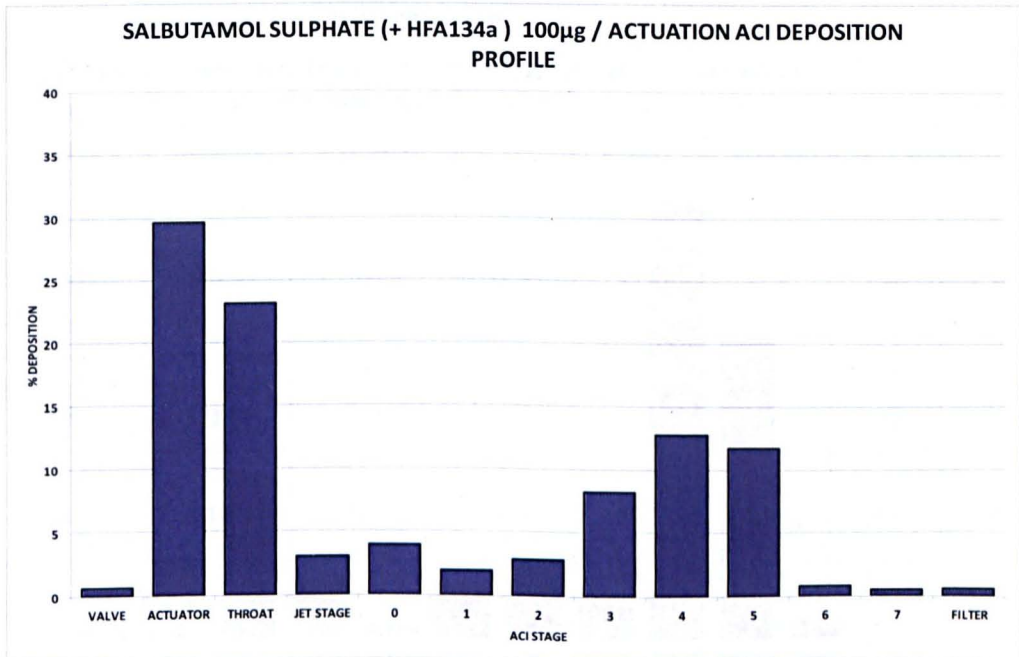


Figure 5.3: Percentage deposition profile across an Andersen Cascade Impactor of total collected dose of salbutamol sulphate from a salbutamol sulphate 100µg / actuation pMDI formulation.

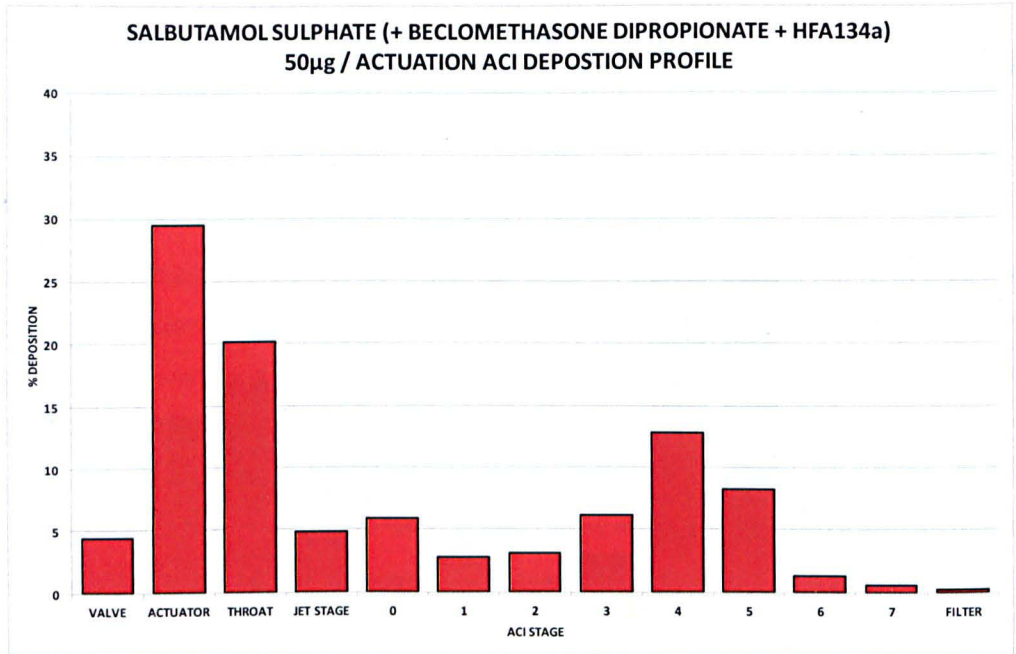


Figure 5.4: Percentage deposition profile from an Andersen Cascade Impactor of total collected salbutamol sulphate from a salbutamol sulphate and beclomethasone dipropionate 50µg / actuation pMDI formulation.

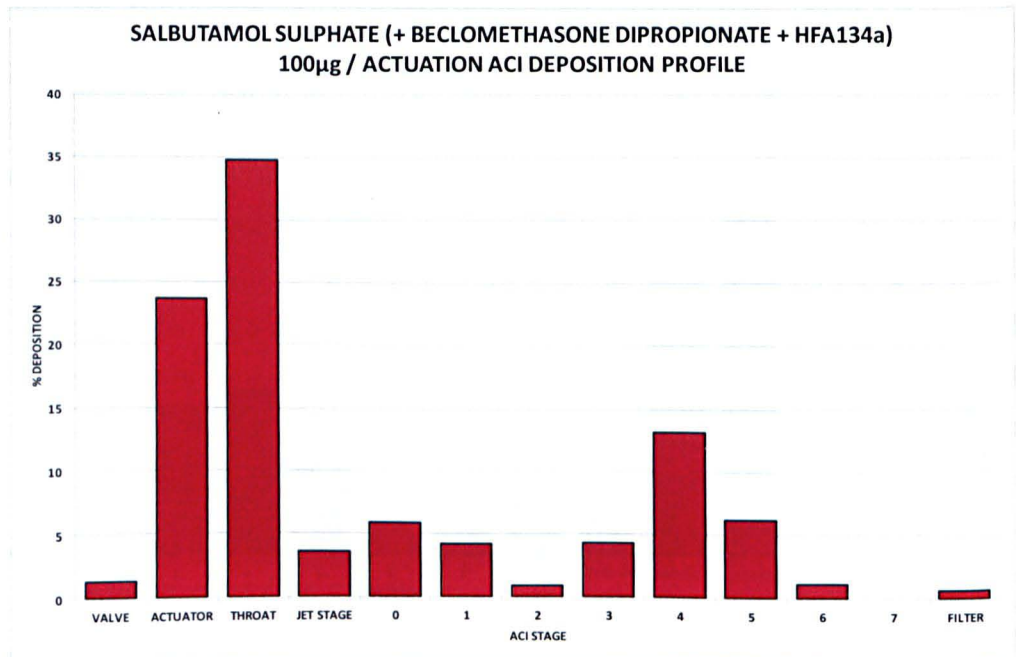


Figure 5.5: Percentage ACI deposition profile of total collected salbutamol sulphate from a salbutamol sulphate and beclomethasone dipropionate 100µg / actuation pMDI formulation.

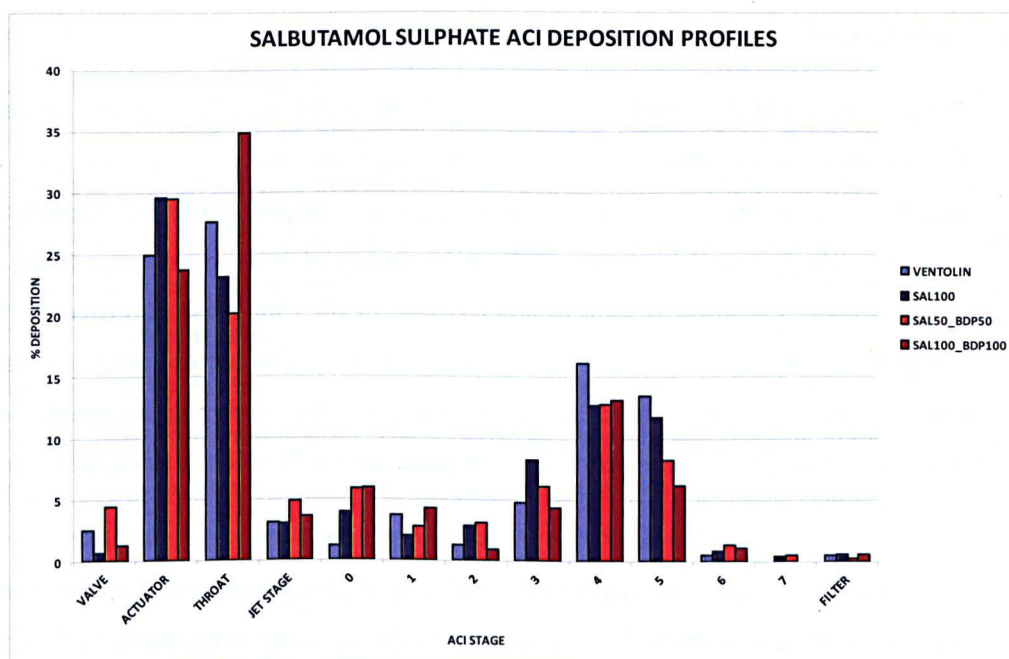


Figure 5.6: Percentage ACI deposition profiles of total collected dose of salbutamol sulphate from all formulations

Formulation (SS Weight / Actuation)	Average Weight SS / Actuation (µg)	Total Expelled Dose SS Recovered (%)	FPD SS (µg)	FPF Collected Dose SS (%)	FPF Expected Dose SS (%)	MMAD (µm)	GSD (µm)
Ventolin® 100µg	106.94	106.9	37.89	35.4	37.9	2.49	1.56
SS 100	112.91	112.9	39.22	34.7	39.2	2.80	1.82
SS + BDP 50	63.31	126.6	18.56	29.3	40.7	2.86	1.82
SS + BDP 100	90.43	90.4	23.00	25.4	23.0	3.02	1.59

Table 5.3: Salbutamol sulphate deposition indicators from ACI / HPLC data across all formulations

percentage deposition on the earlier stages, including the actuator and throat as well as the early ACI stack stages.

Table 5.3 highlights these differences further. It shows the critical indicators for each of these formulations with respect to SS deposition. These indicators include the total weight per actuation recovered, the percentage of this weight with respect to the total expected weight per actuation, the fine particle fraction (FPF) of the recovered dose per actuation (the weight of API reaching plate 3 or lower ($<5\mu\text{m}$) as a percentage of the total mass of recovered API) and the fine particle fraction of the expected dose per actuation (fine particle dose as a percentage of the expected mass of actuated material). In addition the mass median aerodynamic particle diameter (MMAD) and geometric standard deviation (GSD) of each formulation are shown as calculated.

The table shows that for every actuation, $37.89\ \mu\text{g}$ of SS in the Ventolin® pMDI reached the fine particle plates, compared to $39.22\ \mu\text{g}$ of SS from the SS 100 μg formulation, $18.56\ \mu\text{g}$ from the SS BDP 50 formulation and $23.00\ \mu\text{g}$ of SS from the SS BDP 100 formulation. When the total masses of SS recovered are used to normalize these values we can see that the fine particle fractions show a subsidence from the SS only formulations upon the addition of BDP. The Ventolin® and SS 100 formulations have similar FPFs (collected dose) of 35.4% and 34.7% each while the SS BDP 50 shows a reduction in FPF to 29.3%, and the SS BDP 100 formulation has the worst FPF, with 25.4%. This reduction in FPF is also mirrored by a gradual increase in MMAD. The S100 formulation reported a MMAD of $2.80\ \mu\text{m}$, which increases to $2.86\ \mu\text{m}$ with the SS BDP 50 formulation and then $3.02\ \mu\text{m}$ with the SS BDP 100 run. This suggests that the aerodynamic particle size distribution is becoming more biased towards larger particulates upon the co-formulation of SS with BDP. In effect this is indicative of a reduction in the frequency of smaller, more penetrative particle bodies and an increase in those with larger aerodynamic diameter. This is evidenced by the concurrent change in proportional deposition up the ACI plates. Interestingly the Ventolin® formulation had a MMAD of $2.49\ \mu\text{m}$ despite similar FPFs, which highlights the comparable increase in proportional mass reaching plates 4 and 5 over plate 3. The spread of the aerodynamic diameters as GSD was relatively quite similar across the formulations.

This data combined therefore seems to suggest that there is a negative impact on the deposition performance of SS by the addition of BDP. Such an effect on deposition may indicate an alteration to the SS aerodynamic particle formation by its interaction with the BDP particles either in formulation or on actuation. This negative effect on SS deposition may also be exaggerated with an increase in expelled total particle mass, as shown by the largest MMAD of 3.02 μ m and lowest FPF of 25.4% with the SS BDP 100 formulation. If we consider the average weight per actuation of each of the formulations we can see that the Ventolin[®], SS 100 and SS BDP 50 formulations all led to a greater than expected recovery of material. This was most significant with the SS BDP 50 formulation where 127% of the expected dose was recovered (i.e. 127 μ g for every expected 100 μ g). The SS BDP 100 formulation however shows a 10% under-recovery of the expected mass. Small differences in the total recovered dose to that expected from pMDI inhalers are often experienced, as the pMDI valve based means of dose measuring relies on precision engineering with small tolerances. In conjunction with the imprecise distribution of the suspended API within the HFA134a this can lead to over or under dosing. Greater than 15% deviations are generally considered critical, and would suggest some experimental failure. It is therefore clear that if we use the FPF of the expected total dose per actuation, this over- and under-recovery skews the trend in FPF effect. Therefore the FPF of the recovered dose appears a better measure; however it should be borne in mind that this is in turn slightly misleading as it implies a pattern of deposition without accounting for mass that may have been lost outside of the measureable system (i.e. device retention) or simply in the process of handling.

5.4.1.2 Deposition Performance of Beclomethasone Dipropionate

Figures 5.7, 5.8 and 5.9 show the individual stage by stage deposition of BDP in a BDP 100, SS BDP 50 and SS BDP 100 pMDI formulations respectively. Figure 5.10 shows these deposition profiles in combination for comparison while table 5.4 shows the deposition indicators for the BDP recovered from the formulations. What is immediately noticeable from the individual graphs and in combination, is a significantly poorer fine particle performance with respect to the salbutamol assays. There is a significant deposition of again 50-60% recovered BDP dose on the actuator and throat, and while there is on all three formulation assays a small increase in percentage deposition over plates 3, 4 and 5 this is not on the same scale as the SS assays. The dominant fine particle plate in each of the individual formulations varies, with plate 3 (8%)

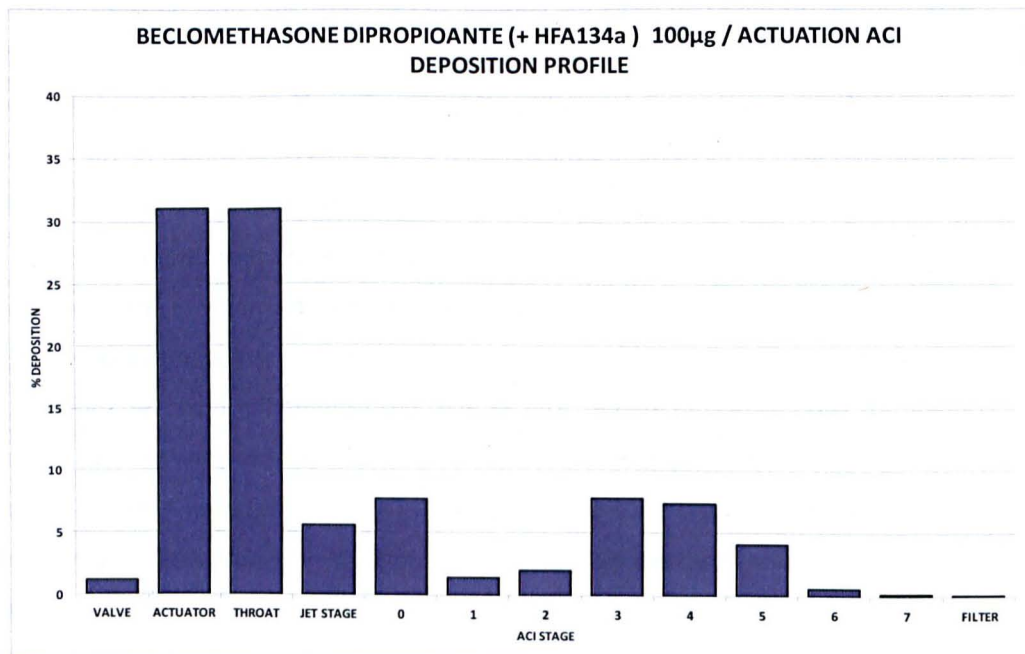


Figure 5.7: Percentage ACI deposition profile of total collected beclomethasone dipropionate from a beclomethasone 100µg / actuation pMDI formulation.

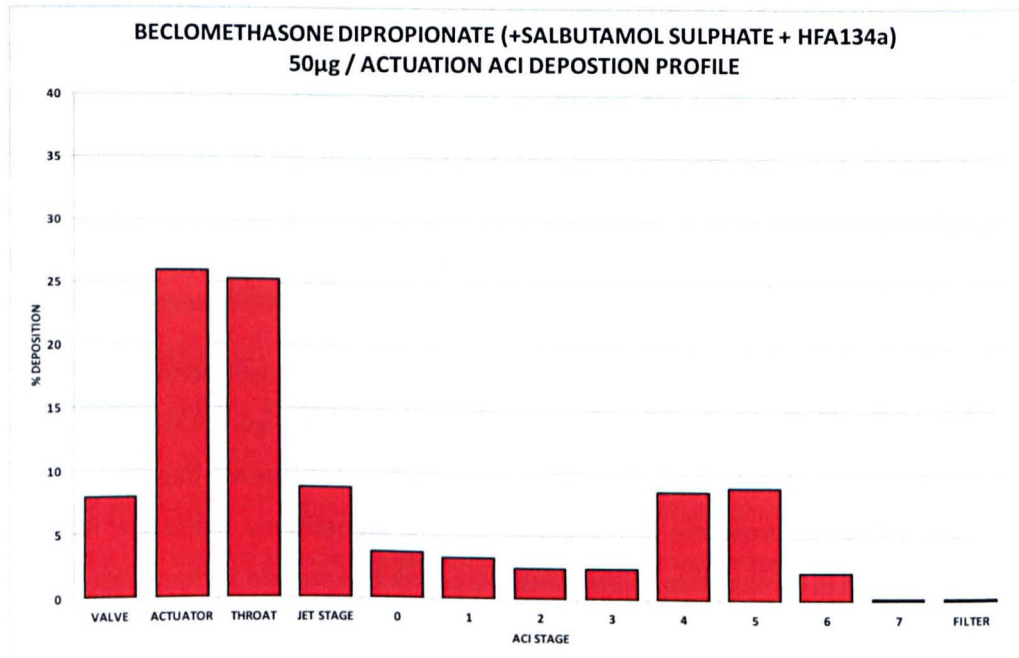


Figure 5.8: Percentage ACI deposition profile of total collected beclomethasone dipropionate from a salbutamol sulphate and beclomethasone 50µg / actuation pMDI formulation.

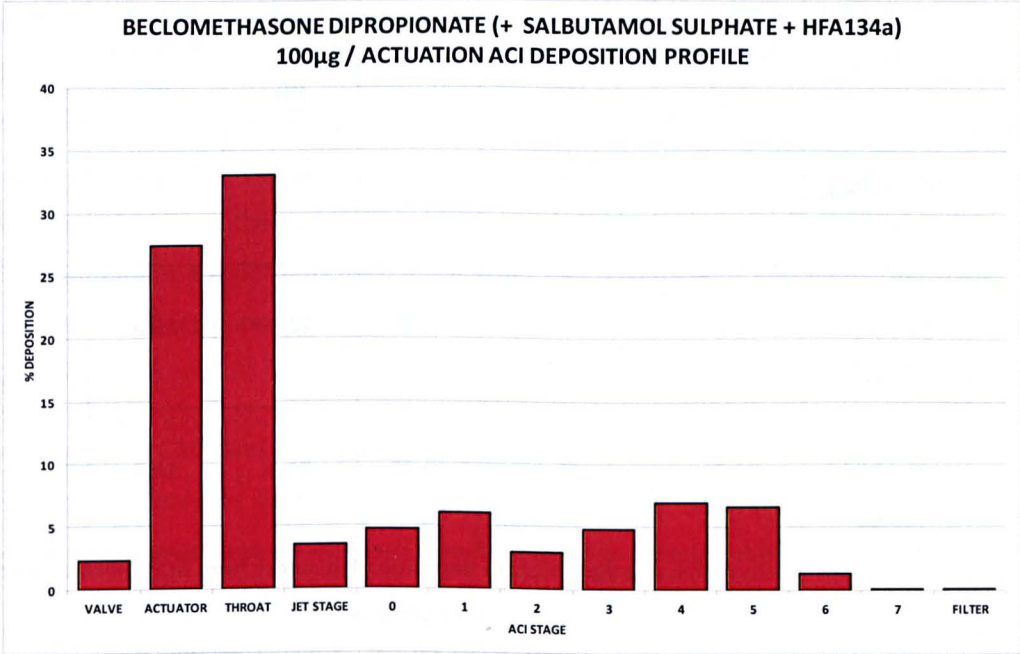


Figure 5.9: Percentage ACI deposition profile of total collected beclomethasone dipropionate from a salbutamol sulphate and beclomethasone 100µg / actuation pMDI formulation.

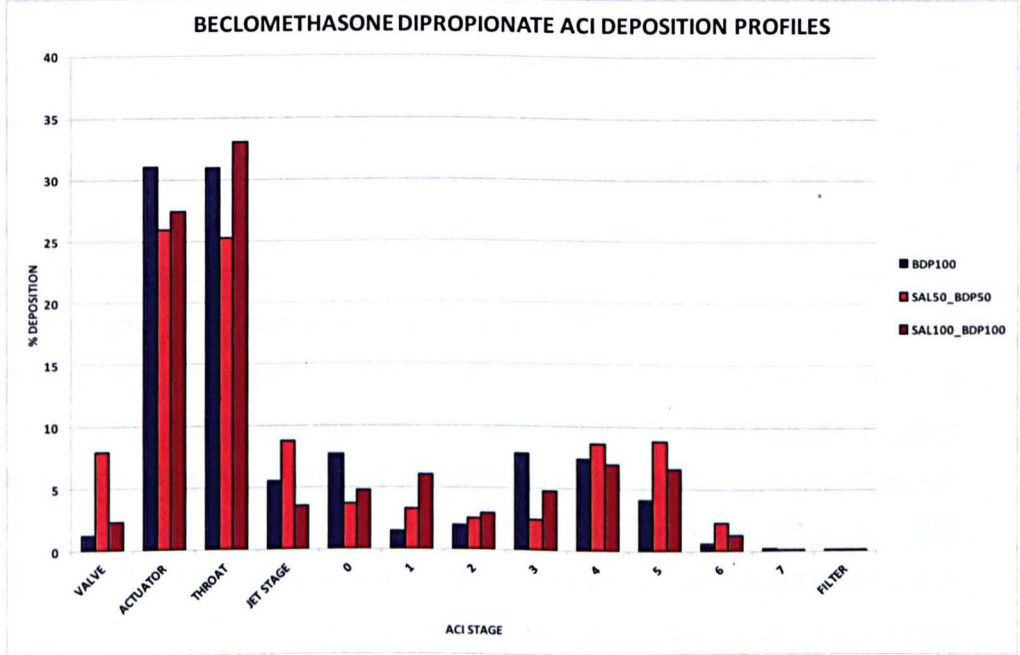


Figure 5.10: Percentage ACI deposition profiles of total collected dose of beclomethasone dipropionate from all formulations

Formulation (BDP Weight / Actuation)	Average Weight BDP / Actuation (µg)	Total Expelled Dose BDP Recovered (%)	FPD BDP (µg)	FPF Collected Dose BDP (%)	FPF Expected Dose BDP (%)	MMAD (µm)	GSD (µm)
BDP 100µg	65.29	65	13.17	20.2	13.2	3.82	1.75
SS + BDP 50µg	33.23	66	7.48	22.5	15.0	2.67	1.94
SS + BDP 100µg	52.01	52	10.35	20.0	10.4	3.76	2.68

Table 5.4: Beclomethasone dipropionate deposition indicators from ACI / HPLC data across all formulations

having the highest percentage deposition in the BDP 100 formulation, plate 5 (9%) in the SS BDP 50 formulation and plate 4 (7%) in the SS BDP 100 formulation.

More interestingly however, when table 5.4 is considered it is seen that the BDP 100 formulation shows only a 65% total recovery from the deposition profile, while the SS BDP 50 and the SS BDP 100 formulations show 66% and 52% total dose recovery respectively. These results are of significance as they imply that there is almost half the expected mass of BDP unaccounted for in the ACI HPLC samples. It also renders the deposition profiles less valid as they do not take account for the missing BDP. It is possible that the missing mass of BDP may be the result of device retention or instability in formulation but this requires further work to establish. Because of this consistent mass loss there were no further repeats performed of the BDP or SS assays, in lieu of further investigation (chapter 6). From the mass of BDP that was detected in the assay, we can infer little with confidence because of such significant unaccounted mass. However if we look at the FPF performance of the BDP recovered, we can see that all three formulations generated similar values. The BDP 100 formulation, the SS BDP 50 formulation and the SS BDP 100 formulation recording 20.2%, 22.5% and 20.0% FPFs respectively. This suggests that despite the inconsistency of the dominant fine particle plate there were similar percentage masses reaching the target respiratory zone. Notably, these

percentages are significantly lower than those of the SS (25%-35%) formulations. It could be suggested that the addition of SS has not had a significant impact on deposition performance, and by the fact that huge mass deficits were seen with the BDP only formulation too, it would imply the critical failing is not related to instability of the BDP due to SS. The fact that the greatest unaccounted mass of BDP comes from the SS BDP 100 formulation may suggest that the increased mass of the system has exaggerated the issue, but the fact that the FPF of the accounted mass is equivocal to that of the other two formulations also infers that there is no mass induced effect upon BDP aerodynamic particle performance, but rather a core stability issue.

The MMAD and GSD data for the BDP formulations is misleading in this instance. Because the calculation can only be based on particle mass within the calibrated ACI stack, the values reported ignore mass lost to pre-stack stages. Therefore although the BDP 100, SS BDP 50 and SS BDP 100 reported MMADs of 3.82, 2.67 and 3.76 μm respectively, the fact that the total recovered dose and FPD values are so small means that these have little quantitative or qualitative use. As such a significant mass appears to have been lost outside of the measureable system, much less the pre-stack stages (also not accounted for by the MMAD and GSD calculation), these reporters are largely irrelevant in this case.

5.4.1.3 The Deposition Performance of Salbutamol Sulphate and Beclomethasone Dipropionate

The data acquired from the salbutamol and beclomethasone assays is difficult to link to the CAB data acquired previously. Evidently from the loss of BDP mass from all of the BDP ACI assays there appears to be a performance issue aside from the impact of co-formulation on deposition. It is likely that there may be a stability issue of the BDP in HFA134a alone, or that the separate HPLC method utilised for BDP may have given rise to an operational failure that has excluded the BDP data from a useful comparison. In any case the necessity to use separate ACI runs, with separate solvent collections and HPLC runs was not ideal, as it means that for each co-formulation run it is impossible to directly compare the effect of one API to another. An indirect comparison is all that is capable in this fashion. But even this is compromised by the inexplicable BDP mass recovery. What can be seen from the data returned was that SS appeared to show a decrease in FPF performance when co-formulated with BDP. This might have suggested that the

cohesively dominated salbutamol suffered a reduced capacity to develop the same aerodynamic character in the presence of the adhesive dominated BDP. However it is difficult to do so in confidence without knowing if the co-formulated BDP was stable enough in the suspension to be actuated and played a part in the aerosolization process. From what BDP mass was recovered there was little suggestion of a change in overall FPF and certainly no confidence in the MMAD descriptors. Despite this, figure 5.10 did suggest that co-formulation may have shifted deposition further down the ACI stack; more deposition on plates 4 and 5, and less on plates 0 to 3. The FPF of the BDP formulations was around the 20% mark for all the formulations, comparing unfavourably with the SS FPFs ranging from 25%-35%. This shows that BDP suffers a worse aerodynamic deposition profile, however as it suffers a critical loss in overall mass, this is of little value, as the low percentage may be directly related to the critical formulation failure rather than the aerodynamic character of BDP.

5.4.2 Deposition of the Solo and Co-Formulated Salmeterol Xinafoate and Fluticasone Propionate

5.4.2.1 Deposition Performance of Salmeterol Xinafoate

Figures 5.11, 5.12 and 5.13 show the average (3 runs) individual stage by stage deposition of SX in a SX 100 formulation, SX with FP 50 formulation and SX with FP 100 pMDI formulation respectively. Figure 5.14 shows these deposition profiles in combination for comparison while table 5.5 shows the deposition indicators for the SX recovered from all the formulations. Considering the individual formulation runs and figure 5.14 for illustration, it can be seen that all the SX assays show similar characteristic fingerprinting to the SS and BDP deposition profiles. As seen with the SS and BDP assays all SX formulations show a large proportion of deposition across the pre-stack surfaces. Both the SX 100 μ g and SX FP 50 μ g formulations show the most deposition on the actuator (25.8% and 27.6%), while the SX FP 100 μ g formulation shows the most deposition on the throat (27.3%). In combination all the formulations show in the region of 45% total deposition across the valve, actuator and throat sections. However all the formulations also show significant deposition across the fine particle plates. More specifically plates 3 to plate 6 show high percentage SX depositions, with plate 4 consistently the best deposited (25.1% SX 100, 21.9% SX FP 50 and 14.5% SX FP 100). In both the SX 100 and SX FP 50

assays the deposition on plate 4 was actually the second most weighted behind the actuator, with plate 4 on the SX FP 100 assay falling to third behind the throat piece and actuator. This suggests a high proportionate level of the SX in formulations reaching the target respiratory zone. What figure 5.13 and the individual deposition profiles also suggest however is a decrease in the proportional mass of SX reaching the fine particle plates, with the addition of the FP to the formulation. The percentage of SX reaching plates 4 and 5 are the most obvious indicators. Plate 4 deposition decreasing by 3.2% between the SX only and SX FP 50 formulations, and showing a drop of 10.6% when additional mass is added to the system. Plate 5 shows a 5.2% drop in deposition between the SX 100 and SX FP 50 formulations, and a drop of 8.92% between the SX 100 and SX FP 100 formulations. Visually the ratio of the ‘second’ peak in the deposition pattern, in relation to that on the pre-stack stages, obviously decreases as the formulations are moved through. This seems to infer that the co-formulation of the two APIs has had a negative impact on the aerodynamic deposition of the beta₂-agonist. It can also be evidenced that the two formulations containing both APIs, showed the greatest variation about deposition performance across the three ACI runs. This decrease in reproducibility may suggest an increase in complexity of the interparticulate interactions occurring, and the additional variables that an extra component induces to aerodynamic particle definition. The variability within the SX FP 100 system may reflect the increase in total (both APIs) mass per actuation having a direct impact on dose reproducibility and aerodynamic character.

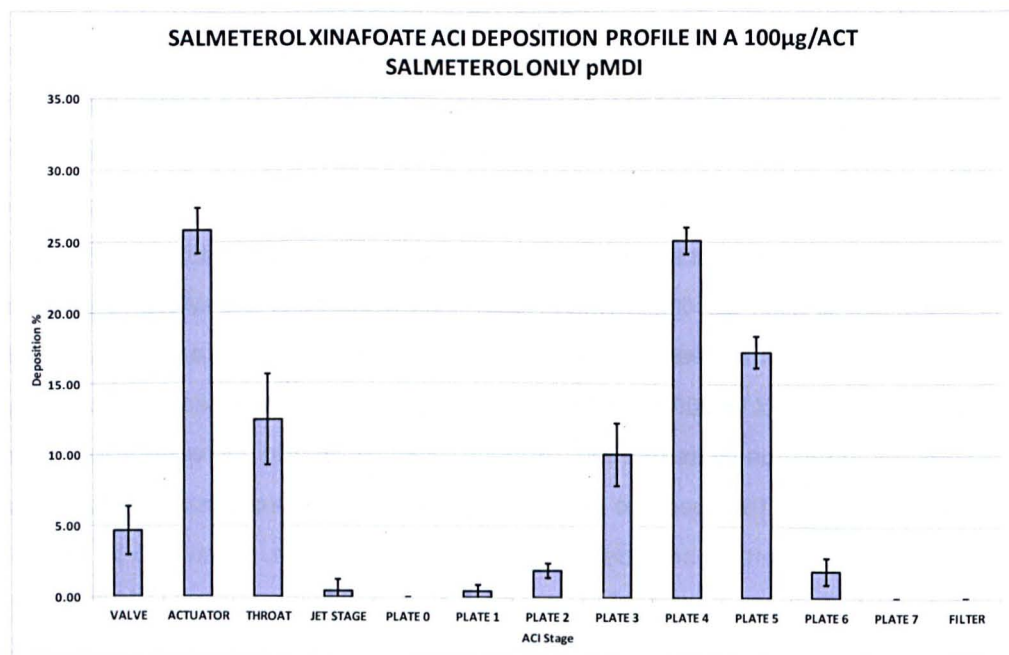


Figure 5.11: Percentage deposition profile across an Andersen Cascade Impactor of total collected salmeterol xinafoate from a salmeterol 100µg / actuation pMDI formulation.

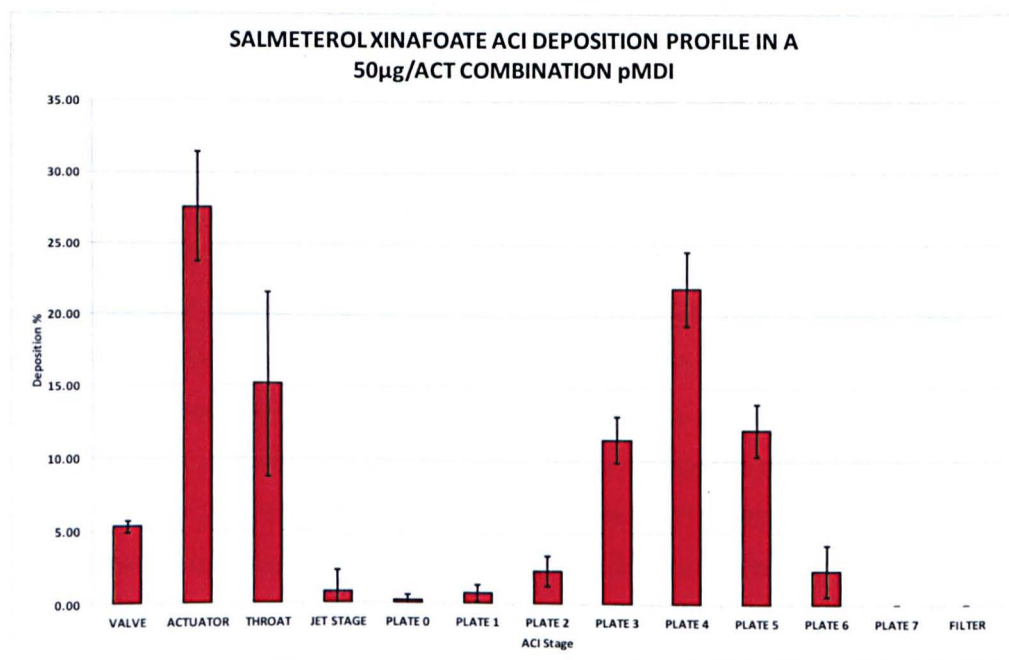


Figure 5.12: Percentage deposition profile across an Andersen Cascade Impactor of total collected salmeterol xinafoate from a salmeterol and fluticasone propionate 50µg / actuation pMDI formulation.

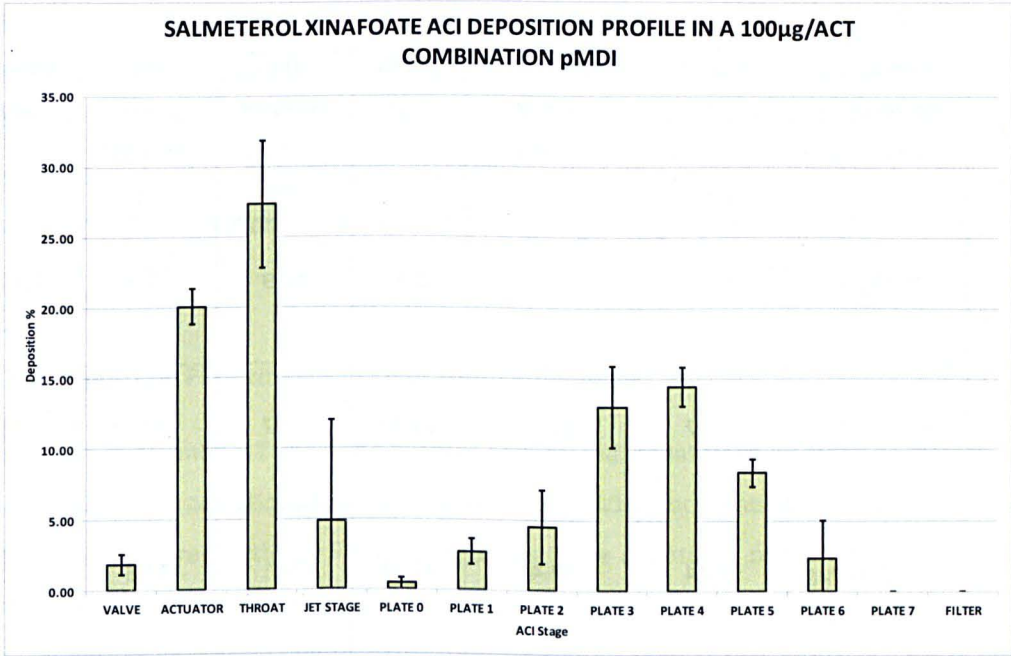


Figure 5.13: Percentage deposition profile across an Andersen Cascade Impactor of total collected salmeterol xinafoate from a salmeterol and fluticasone propionate 100µg / actuation pMDI formulation.

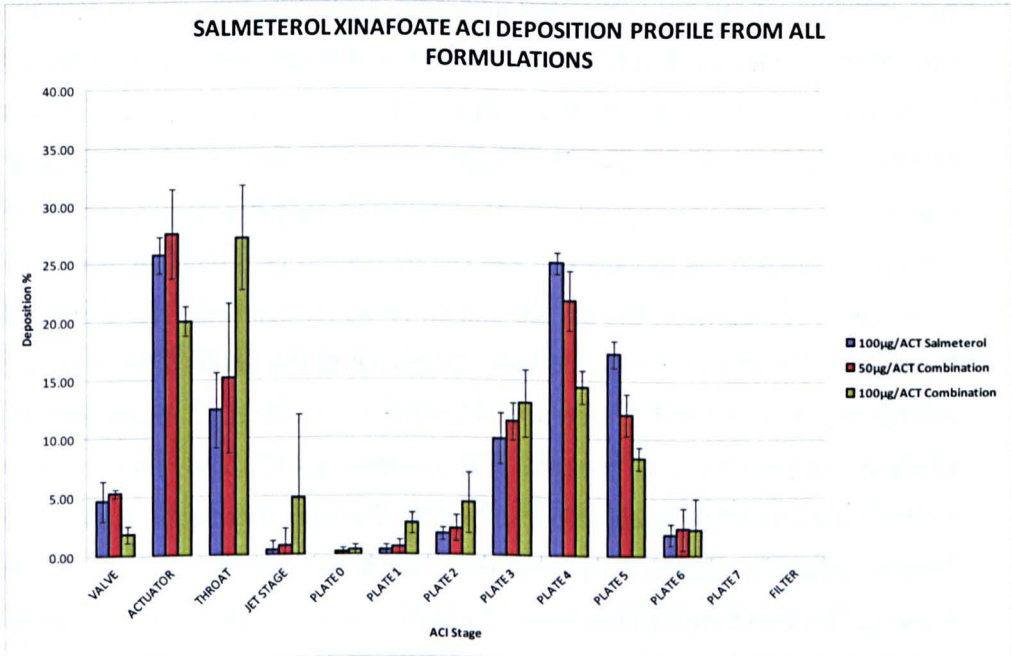


Figure 5.14: Percentage deposition profile across an Andersen Cascade Impactor of total collected salmeterol xinafoate from all pMDI formulations.

Formulation (SX Weight / Actuation)	Average Weight SX / Actuation (µg)	Total Expelled Dose SX Recovered (%)	FPD SX (µg)	FPF Collected Dose SX (%)	FPF Expected Dose SX (%)	MMAD (µm)	GSD (µm)
SS 100µg	80.45	80.5	32.77	48.9	32.8	2.46	1.46
SS + FP 50µg	41.97	83.9	15.29	43.7	30.6	2.63	1.49
SS + FP 100µg	94.44	94.4	31.82	37.1	31.8	3.09	1.69

Table 5.5: Salmeterol xinafoate deposition indicators from ACI / HPLC data across all formulations

Table 5.5 shows further that the total mass of the collected SX reaching plate 3 or below was consistently higher as a proportion than the masses of both the SS and BDP previously examined. This is reflected with FPFs of 48.9%, 43.7% and 37.1% for the SX 100, SX FP 50 and SX FP 100 formulations respectively. This suggests that between a third to a quarter of the SX in an actuation across the formulations is reaching the target fine particle plates. Evidently the difference between the formulations can still be seen to be prominent, with an average 5.2% reduction in FPF between the SX 100 and SX FP 50 formulations, and a difference of 11.8% between the SX 100 and SX FP 100 formulations. Of further interest is the gradual increase in MMAD from the SX 100 formulation (2.46µm) to the SX FP 50 (2.63µm) and then SX FP 100 (3.09µm), and the tentative increase in accompanying GSD (1.46, 1.49 and 1.69µm). This is further indicative that the aerodynamic particle diameter distribution is shifting in a negative fashion towards a larger bias by larger particulates, and that the spread of the distribution is growing. This would infer a proportional increase in larger particulates upon the co-formulation of SX with FP and then with additional mass in the system. This leads to less desirable aerodynamic deposition character and decreased consistency in particulate size ex-canister. In

combination these descriptors support the suggestion that the aerodynamic deposition performance of SX is adversely affected by co-formulation with FP. The significantly worse performance drop in terms of FPF and MMAD with the SX FP 100 formulation may again also infer that aerodynamic character is particularly affected with the additional particle mass present per actuation. This decrease in FPF is offset by a coincident increase in particle deposition in the throat and over the earlier stages (jet stage, plate 0 and plate 1) as seen in figure 5.13 and 5.14.

5.4.2.2 Deposition Performance of Fluticasone Propionate

Figures 5.15, 5.16 and 5.17 show the average (3 runs) individual stage by stage deposition of FP in a FP 100 μ g (per actuation) formulation, SX with FP 50 μ g formulation and SX with FP 100 μ g pMDI formulation respectively. Figure 5.18 shows these deposition profiles in combination for comparison while table 5.6 shows the deposition indicators for the FP recovered from all the formulations. Once more a similar general fingerprint of a deposition profile is seen across all three formulations. As the individual profiles show, there is a consistent 53-56% deposition of FP across the pMDI valve, actuator and throat piece. In all three formulations the deposition on the throat piece is the most significant 27%, 27% and 28% respectively, although the actuator follows closely (23%, 26% and 25%). The fine particle plates do see a second peak of deposition, but in this instance it is plate 3 that caps this fine particle deposition trend. Plate 3 consistently shows the most proportional deposition of FP with 12% on the FP 100 profile, 13% on the SX FP 50 profile and 15% on the SX FP 100 profile. Compared to the SX profiles there is obviously an increased proportion of the collected dose depositing on jet stage through to plate 2, especially from the solo API formulation. Figure 5.14 further suggests that the FP 100 formulation performs the worst of the three in terms of target deposition. Here is an obvious decrease in percentage deposition on the fine particle plates to go with the increase in deposition on the earlier plates. Further evident from all the deposition profiles is the large variability about each average, particularly exaggerated in the case of the FP 100 formulation. This variability is decreased in the SX FP 50 formulation, and decreases further again with the SX FP 100 formulation. The deposition profiles of each of the formulations therefore seem to suggest that the co-formulation of the SX with FP, improves the fine particle performance of FP. The doubling of the mass of both SX and FP in the SX FP 100 formulation further improves the deposition performance of FP and even seems to show greater consistency in deposition.

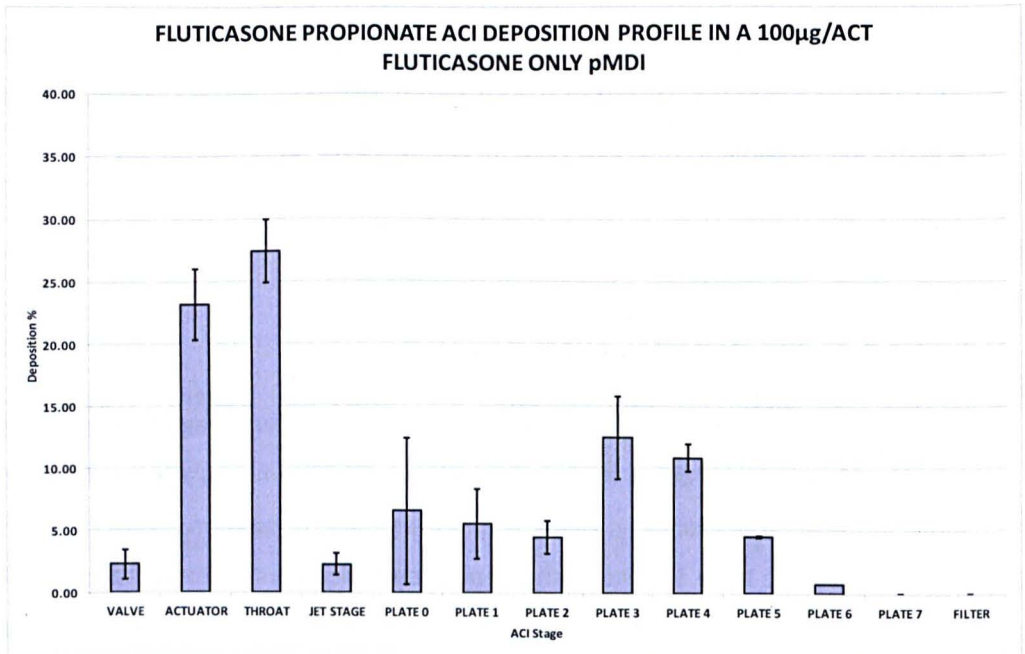


Figure 5.15: Percentage deposition profile across an Andersen Cascade Impactor of total collected fluticasone propionate from a fluticasone 100µg / actuation pMDI formulation.

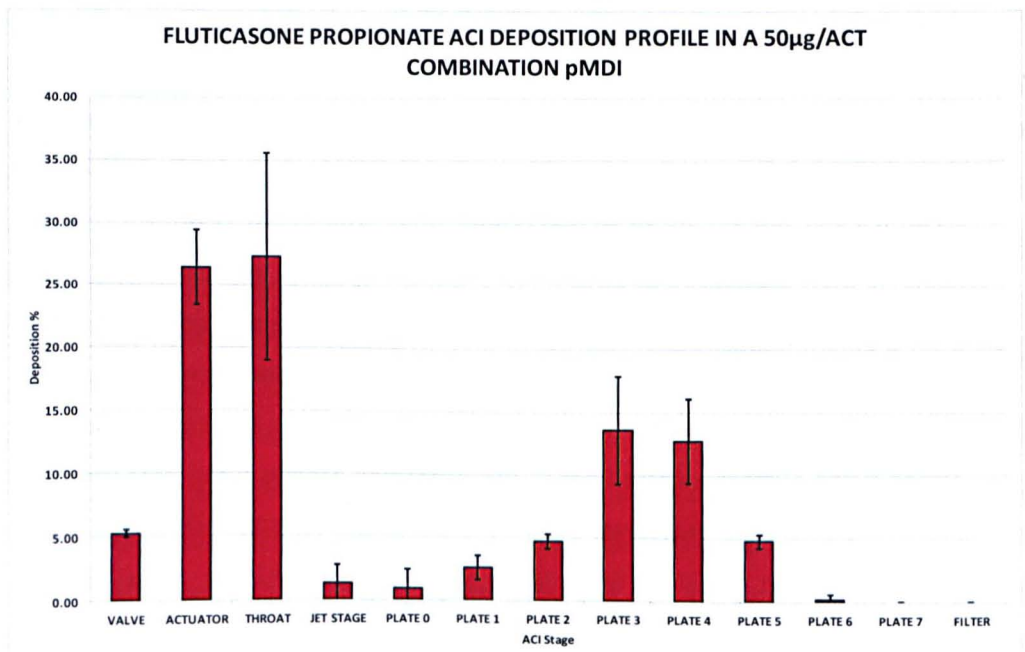


Figure 5.16: Percentage deposition profile across an Andersen Cascade Impactor of total collected fluticasone propionate from a fluticasone and salmeterol xinafoate 50µg / actuation pMDI formulation.

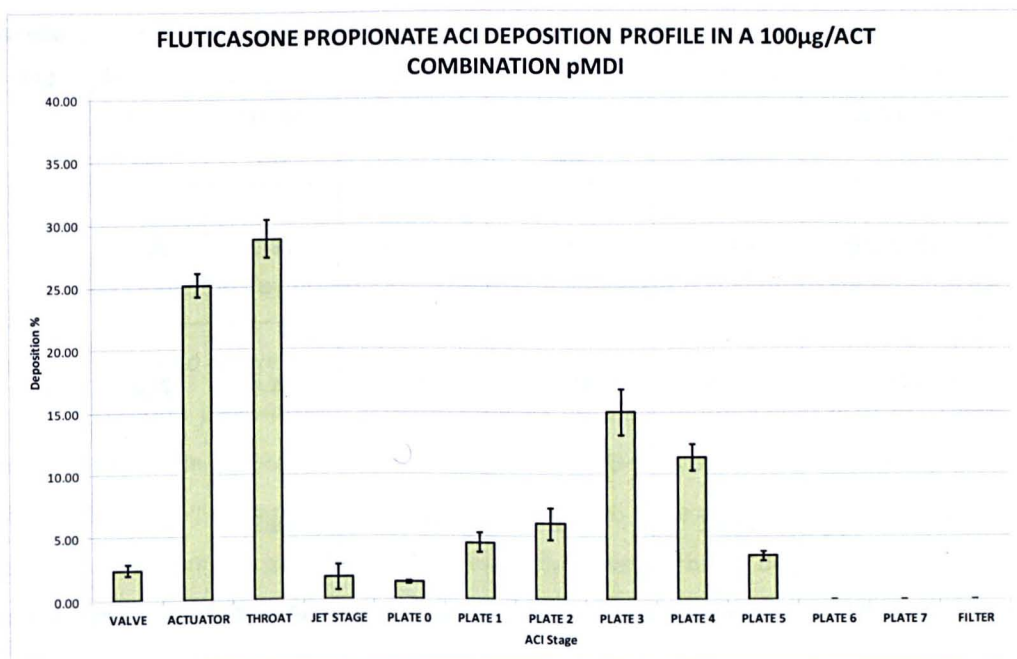


Figure 5.17: Percentage deposition profile across an Andersen Cascade Impactor of total collected fluticasone propionate from a fluticasone and salmeterol xinafoate 100µg / actuation pMDI formulation

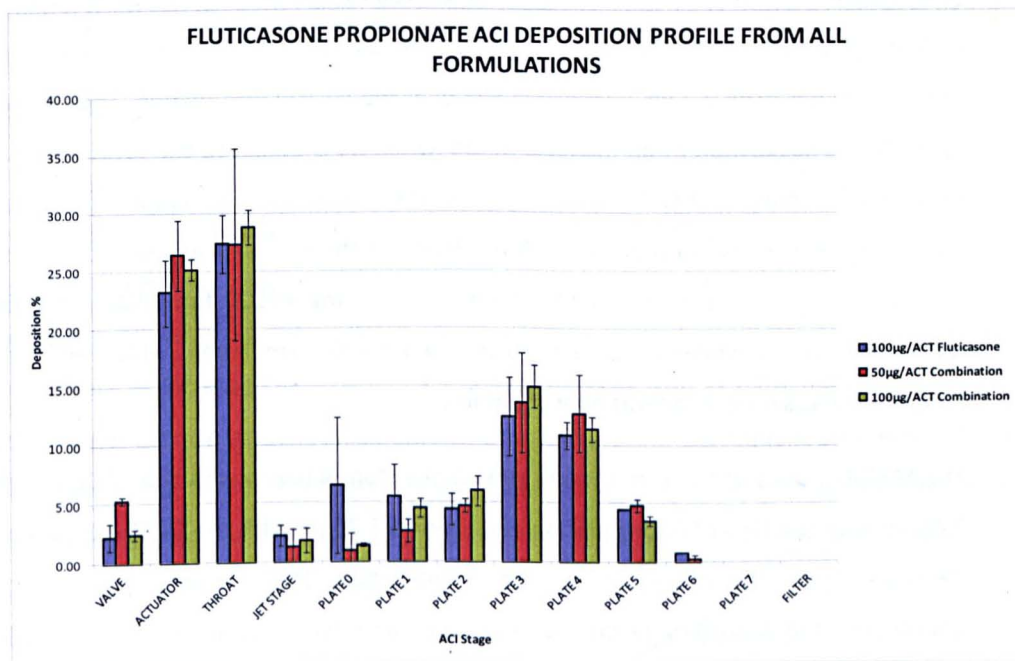


Figure 5.18: Percentage deposition profile across an Andersen Cascade Impactor of total collected fluticasone propionate from all pMDI formulations.

Formulation (FP Weight / Actuation)	Average Weight FP / Actuation (µg)	Total Expelled Dose FP Recovered (%)	FPD FP (µg)	FPF Collected Dose FP (%)	FPF Expected Dose FP (%)	MMAD (µm)	GSD (µm)
FP 100µg	93.86	93.9	26.65	28.5	26.7	4.08	2.09
SS + FP 50µg	42.84	85.7	13.40	31.4	26.8	3.48	1.48
SS + FP 100µg	89.81	89.8	30.26	33.7	30.3	3.79	1.46

Table 5.6: Salmeterol xinafoate deposition indicators from ACI / HPLC data across all formulations

This inference is further supported by table 5.6, which shows that the FPF performance of FP across the three formulations goes from 28.5% with the FP 100 formulation, to 31.4% with the SX FP 50 formulation and 31.8% with the SX FP 100 formulation. There can be seen an increase of 3.5% from the SX FP 50 formulation to the SX FP 100 formulation. And the SX FP 50 formulation has itself a 2.9% increase in FPF over the FP 100 formulation. These figures validate figure 5.18’s suggestion of an increase in FPF when SX is added to the formulation. Notably all the recovered masses of FP from all the formulations were of an acceptable quantity (85-115%). There is some suggestion that the co-formulation of the two APIs appears to have reduced the mass of FP recovered, however the decrease from the FP100 formulation to the SX FP 50 formulation is not worsened further to the SX FP 100 formulation, which may infer that the difference was simply in operational variability.

The MMAD values of the formulation runs move from 4.08µm with the FP 100 formulation, to 3.48µm with the FP SX 50 formulation and then to 3.79µm with the SX FP 100 formulation. This decrease from the mono-FP to the combination formulations, again emphasizes an improvement in deposition performance (smaller aerodynamic particle diameters). The increase in MMAD from the SX FP 50 formulation to the SX FP 100 formulation, may however evidence that despite the direct improvement in deposition performance on FP by co-formulation, that an

increase in total system mass remains detrimental as seen in the SX assay. The GSD values for the combination formulations are roughly equivocal, and both are smaller than that for the FP 100 formulation, which again suggests more consistent aerodynamic particle sizing on co-formulation.

5.4.2.3 The Deposition Performance of Salmeterol Xinafoate and Fluticasone Propionate

The data presented above highlights a very interesting trend. The suggestion is that the fine particle deposition performance of SX is reduced by the co-formulation with FX. There is an obvious decrease in FPF, and concurrent rise in MMAD and GSD. This would imply that the addition of the corticosteroid causes the SX particles to have reduced aerodynamic character upon actuation from the pMDI canister. Conversely however the FP data highlights that the co-formulation of FP with SX seems to have improved the deposition performance of the corticosteroid. This thereby infers an improvement in aerodynamic particle character, (seen by increasing FPFs and decreasing MMAD/GSD values) upon actuation in the presence of the beta₂-agonist. This data is particularly persuasive as the deposition profiles for both the APIs were extracted from the same ACI wash off samples and the same HPLC runs, as allowed by the joint HPLC method. This means that there is much less scope for bias induced by method inefficiencies, or operational anomalies.

As chapter 4 defined, the SX FP force balance is characterised by FP having an adhesively dominated relationship with SX, and SX having a slight cohesively dominated or neutral relationship with FX. One explanation of the results of the deposition study is that by co-formulating FP with SX, FP undergoes an increase in particle clustering aggregation as a consequence of increased interparticulate adhesive forces with SX particulates. This may in turn lead to larger particle agglomerates that on actuation, in the subsequent airstream, are subject to increased drag forces, causing improved particle dispersion and deagglomeration. Such a theory was discussed principally with respect to DPI formulations and the intrinsic autoadhesive forces of APIs (Begat et al, 2004, Jones et al, 2008). However it is feasible that such an effect may be seen with API mixtures from pMDI formulations. The force balance of a combination of two APIs may dictate subtle shifts in aggregation behaviour that alter aerodynamic particle character and therefore, aerodynamic drag forces and kinetic energy states. Smaller dispersed

particles as a result of larger agglomerates would then be capable of passing to lower levels of the ACI stack. Reversing this however, SX has a slightly cohesive favourability with respect to FP, and may see a slight decrease in agglomerate formation, as FP effectively dilutes the particulate content. This may reduce aerodynamic particle performance by reducing initial agglomerate genesis, resulting in smaller SX based particulates leaving the canister on actuation. These would be subject to smaller drag forces, and less likely to be disseminated. The persisting agglomerates would thereby be of larger aerodynamic diameter and impact further up the ACI stack with a concurrent reduction in FFP.

It is worth noting that despite the trend of improved performance with FP, and decreased performance with SX upon co-formulation, SX still maintains a better aerodynamic performance across all the formulations. The reported MMAD values indicate a persistent (although decreasing) larger median diameter of the FP particulates compared to the SX equivalents. From the mono-API formulations SX is reported with a MMAD of 2.46 μm and FPF of 48.9%, while FP has a MMAD of 4.08 μm and FPF of 28.5%. The SX FP 100 formulation gives a MMAD of 3.09 μm and FPF of 37.1%, for SX and a MMAD of 3.79 μm and of 33.7%. FPF for FP. Whilst the gap between the two has significantly reduced from the single API formulations, SX still retains better deposition at the fine particle plates than FP. This may suggest that the powder morphology has a significant role to play in determining deposition performance. Alternatively it may be that as SX had a higher surface free energy (as shown in AFM measurements in chapter 4) it forms stronger auto-adhesive agglomerates, which again lead to larger agglomerates on actuation favouring smaller friction induced particulate cast offs. It is also worth considering that in looking for a simple characterization technique, the relationship of each of the APIs to the HFA134a propellant has been ignored and it cannot be ruled out that the solvent forces involved between the propellant and the individual APIs may lead to an impact on deposition performance. Hence broad generalizations about the interaction between the APIs and their deposition performance must be tempered with caution. However, it is clear from the data above that there appears to be a significant impact on the deposition profiles of the two APIs when co-formulated that may be related to their CAB.

5.5 Conclusions

The deposition analysis by ACI and HPLC in this chapter has identified several points of note. Firstly the deposition profiles of salmeterol xinafoate and fluticasone propionate can be seen to change in an opposite manner from solo formulation in HFA134a to co-formulation. SX shows an increase in aerodynamic particle diameter with a reduction in fine particle performance when FP is co-formulated, while FP shows a decrease in aerodynamic particle diameter and an increase in fine particle performance when SX is co-formulated. This may reflect the CAB balance of the two APIs influencing aerodynamic particle character. That FP has an adhesively dominated relationship with SX, and that SX has a mildly cohesive relationship with FP may lead to subtle changes in the interparticulate forces in the formulation. This may in turn define the particle cluster sizing or constitution that upon actuation results in differing fluidization, and aerosol generation mechanics. One proposal is that the FP particles interact more strongly with co-formulated SX, generating tighter bound, larger agglomerates that are aerosolized and then subject to larger drag forces by virtue of their mass. This frictional force causes the originally larger agglomerates to break up into finer particulate bodies that can penetrate further into the ACI without inertial impaction. Conversely SX, will suffer a reduction in interparticulate or agglomerate strength and size by virtue of a less energetic contact with FP. This may lead to less coherent agglomerates that are aerosolized, therefore subject to reduced drag forces and ironically undergoing less particulate breakdown to fine particle bodies. The impact of additional mass in the system is unclear. It appears to have reduced the fine particle performance of SX, and slightly improved the fine particle performance of FP. This may reflect a forced increase in the extent of agglomerate formation of the two APIs if we persist with the theory above, that exacerbates the change in deposition trend seen with the mass equivalent formulations.

Unfortunately however the other combination of APIs in salbutamol sulphate and beclomethasone was not able to operate as a suitable comparator. The necessity to use separate HPLC methods was already a limitation, but the critical mass loss of BDP from the BDP assays suggests a stability issue in the formulations that has compromised the validity of assessing the impact of one API on the others deposition performance. From the data available it appeared SS suffered a small reduction in fine particle performance with the co-formulation of BDP. The comparison of the bespoke SS 100 pMDI and the commercial Ventolin® was largely equivocal, suggesting the stability of the SS in neat HFA134a was good. However the BDP data

available can be used to suggest little with confidence. There is some slight indication, in terms of plate to plate deposition shifts and fine particle performance, that there is a slight improvement with co-formulation with SS. Considering the SX and FP data these trends would be expected if we apply the same critical agglomerate philosophy. However given the significantly more polarised CAB ratios of the two APIs (1.69 and 0.35 for SS and BDP respectively compared to 1.05 and 0.63 for SX and FP) it would be assumed that this would exaggerate further the deposition impact seen between SX and FP. That is to say that we might expect SS deposition to suffer a much more severe drop off in performance on co-formulation with BDP, and that BDP would experience significantly improved deposition performance on co-formulation with SS. However if the BDP in formulation has been retained as a result of crystallization, polymorphism etc. this may explain the loss of recovered BDP, and the reduction in the deposition effect seen on the SX. This will be investigated further in chapter 6.

Consequentially while a successful deposition analysis has been performed using SX and FP formulations, and a link to the CAB of the two APIs has been put forward, there is no confident comparator to determine whether this deposition character can more broadly be linked to the fundamental force balances. However the identification of this trend defines this system as one of interest for further investigation and may infer a causative link between the APIs, as force modulators in an agglomerate driven dispersion mechanic.

5.6 References

P.Begat, D.A.V.Morton, J.N.Staniforth, R.Price. (2004) The Cohesive-Adhesive Balances in Dry Powder Inhaler Formulations II: Influence on Fine Particle Delivery Characteristics. *Pharmaceutical Research*; 21:10:1826-1833

European Pharmacopeia (2012) [viewed May 2012] European Directorate for the Quality of Medicines and Healthcare. Available from <http://www.edqm.eu>

M.D.Jones, H.Harris, J.C.Hooton, J.Shur, G.S.King, C.A.Mathoulin, K.Nichol, T.L.Smith, M.L.Dawson, A.R.Ferrie, R.Price. (2008) An investigation into the relationship between carrier-based dry powder inhalation performance and formulation cohesive-adhesive force balances. *European Journal of Pharmaceutics and Biopharmaceutics*; 69:496-507

MMADcalculator (2013) [accessed March 2013]; www.mmادcalculator.com/andersen-impactor-mmاد.html

6.0 Investigating the Co-Deposition of Active Pharmaceutical Ingredients from HFA134a pMDI systems

6.1 General Introduction

6.1.1 Combination Inhalers for the Treatment of Airways Disease

As described in chapter 1 the use of inhaled long acting beta₂-agonists (LABAs) and corticosteroids (ICS) is a pillar of respiratory medicine in treating the common airway disorders. Depending upon the particular condition, disease severity and presentation these APIs may be used independently or, as is becoming more frequent, in combination. Their concurrent use represents the third step of the British Thoracic Society and Scottish Intercollegiate Guidelines Network's asthma management ladder (BTS,SIGN,2011) and is the first line treatment for high risk COPD patients as per the Global Initiative for Chronic Lung Disease (GOLD, 2011). In asthmatics the addition of a long acting beta₂-agonist is considered if the use of short acting beta₂-agonists alone, and then in conjunction with regular inhaled corticosteroids, has failed to adequately control asthma symptoms. In COPD treatment, the combination of ICS and LABAs is deemed appropriate if the patient is assessed as having severe or greater airflow limitation (by spirometric classification, exacerbation risk, and scorings on the modified medical research council dyspnoea scale (MMRC) and COPD assessment test (CAT))(GOLD, 2011).

The common LABAs and ICS used clinically in COPD and asthma management, alongside their pharmacological impetus for use, were outlined in chapter 1, and it is widely accepted that concurrent use has a significant role to play in more refractory airways disease. In particular a significant collection of randomised trials has shown that the addition of LABA therapy to asthmatic adults not fully controlled using ICS alone, leads to a reduction in the rate of exacerbations requiring oral steroids; from 23% to 15-11% (RR 0.77, 95% CI 0.68 to 0.87 across 28 studies with 6808 participants), improves lung function and symptoms and modestly decreases use of rescue short-acting beta₂-agonists (Ducharme et al, 2010).

All of the common LABAs and ICS are available as individual DPI and or pMDI inhalers (e.g. *Serevent*[®] (salmeterol), *Atimos Modulite*[®] (formoterol), *Flixotide*[®] (fluticasone), *Oxis Turbohaler*[®] (budesonide) etc.) and are frequently prescribed in conjunction with each other.

There are also combination pMDI or DPI products available that provide both the LABA and ICS within the same formulation. The three most prevalent being **Symbicort**[®] (budesonide and formoterol), **Seretide**[®] (fluticasone and salmeterol) and **Fostair**[®] (beclomethasone and formoterol). In clinical practice, the combination products are advocated over the individual formulations. This is principally due to the fact that it has become clinically accepted that using just one inhaler to deliver two APIs increases patient compliance and guarantees that the LABA can't be taken without the ICS (BTS, SIGN, 2011). However to date it is also accepted that there is no significant body of evidence suggesting a difference in pharmacokinetic or pharmacodynamic efficacy between the individual inhalers or compound equivalents (BTS, SIGN, 2011).

6.1.2 The Co-Deposition of Salmeterol Xinafoate and Fluticasone Propionate

A collection of recent research offers evidence that this may not be the case across the board with all ICS and LABA combinations. Studies comparing the use of combination salmeterol xinafoate (SX) and fluticasone propionate (FP) DPI inhalers to their individual counterparts have been carried out. (Bateman et al, 1998. Chapman et al, 1999. Aubier et al, 1999. Van den Berg et al, 2000.). When meta-analyzed, these studies suggested that further to the pharmacological synergy of the two API classes, (seen with both individual and combination inhaler types), there was a significant improvement again in clinical efficacy with the combination delivery (as FEV₁ and morning PEF over 12 weeks) (Nelson et al, 2003).

It has been proposed that the improvement in clinical outcome seen with this combination formulation was as a consequence of an increase in local co-deposition of the two APIs (Nelson et al, 2003. Barnes, 2002, Theophilus et al, 2006). As described previously, the synergistic effects of LABAs and ICS are rooted in cellular signaling pathways, localized to individual locations within the respiratory tract. The rapid promotion of beta₂-receptor expression by ICS and the nuclear translocation of glucocorticoid receptors by LABAs in respiratory smooth muscle tissues (Black et al, 2009) would therefore suggest that the synergy of action is dependent upon having both LABAs and ICS working at the same cellular location. Therefore it is possible that the degree of co-localization of the APIs might correspond directly to a clinical response. As with all combination products co-deposition will occur more readily than from two separate inhalers as

the inherent natural variation in inspiratory maneuvers is negated, which will otherwise give different deposition patterns from breath to breath (Theophilus et al, 2006). Yet crucially as highlighted by other research into different combinations (including budesonide and formoterol) and the clinical guidance issued by the BTS and SIGN, this has not manifested as a marked improvement in clinical performance with other combination products (Zetterstrom et al, 2001. BTS, SIGN, 2011). Therefore the SX and FP combination may present unique formulation characteristics that lead to an advancement in clinical performance.

6.1.3 Assessing 'in-vitro' Co-Deposition

As discussed in chapter 4, the CAB of FP and SX shows that FP has an adhesively dominated relationship with SX, while SX has a slightly cohesively dominated relationship with FX. This led to distinct changes in deposition performance 'in-vitro' (chapter 5). The co-formulation of the two APIs gave rise to a reduction in fine particle performance of SX, but an improvement in that of FP. While a link between the CAB of the two APIs and the change to individual deposition character could be hypothesised, it remains of interest to see whether there is a link between the CAB of the APIs and the degree of co-deposition. It is therefore of particular interest whether with the application of a range of surface specific imaging techniques, both visual and chemical, the extent of co-deposition could be identified 'in-vitro' using an Andersen cascade impactor. Several analytical techniques allow the spatial mapping of surfaces, and it is of interest as to how well they can define the distribution of a multi-component system. Furthermore if it were possible to link the deposition association of two components (i.e. SX and FP) to a force balance as established by a semi-model CAB this would potentially offer significant insight into formulation design of prospective formulations. From chapter 5 we are also aware that in the attempt to characterize the influence of co-formulation of two other APIs, salbutamol sulphate (SS) and beclomethasone dipropionate (BDP) there was a critical loss of recovered BDP mass. This suggested instability in the BDP HFA134a system. It is of interest therefore to see whether supplementary imaging techniques support the data from the HPLC assay and show reduced BDP deposition post actuation in comparison to the SS delivered. Simultaneously if SS and BDP characterisation suggests any co-ordination between the API mass that has been delivered then this can be used as a rough comparator to the SX and FP system.

6.2 Aims and Objectives

6.2.1 Chapter Aim

The aim of this chapter was to investigate the use of several surface specific analytical imaging techniques in describing the extent and nature of the deposition of APIs from binary HFA134a pMDI systems. If possible to assess co-deposition behaviour '*in-vitro*' and link this to the force balances described by prior semi-model CAB experimentation.

6.2.2 Chapter Objectives

- To compare the surface specific characterisation of binary combinations of APIs from HFA134a pMDI suspensions by multiple analytical techniques including SEM, Raman Spectroscopy, ToF-SIMs and DESI.
- To describe the extent to which APIs from combination inhalers can be seen to co-deposit '*in-vitro*' on Andersen Cascade Impactor plates.
- To investigate the mass retention of BDP from BDP containing HFA134a pMDI formulations

6.3 Materials and Methods

6.3.1 Materials

Salmeterol xinafoate (SX), fluticasone propionate (FP), salbutamol sulphate (SS) and beclomethasone dipropionate (BDP) were chosen to follow up the work carried out in chapters 4 and 5. The SX and FP formulation was of specific interest due to documented research into the exaggerated synergy of the two APIs by co-deposition. SS and BDP were investigated further with interest in investigating the mass retention of BDP from the self-formulated HFA134a canisters. The micronized powders were all provided by 3M Healthcare (Loughborough, UK). All other reagents and accessories were sourced from Sigma Aldrich Company Ltd (Gillingham, UK) unless specified in the methods.

6.3.2 Methods

6.3.2.1 Formulation of pMDI canisters

The remaining combination formulations of SS with BDP and SX with FP produced in chapter 5 were used for the work described in this chapter. The formulations specifically chosen for this co-deposition investigation were the following:

- BDP 100:** **Beclomethasone Dipropionate 100µg**
SS BDP 100: **Beclomethasone Dipropionate 100µg, Salbutamol Sulphate 100µg**
- FP 100:** **Fluticasone Propionate 100µg**
SX 100: **Salmeterol Xinafoate 100µg**
SX FP 50: **Fluticasone Propionate 50µg, Salmeterol Xinafoate 50µg**
SX FP 100: **Fluticasone Propionate 100µg, Salmeterol Xinafoate 100µg**

The BDP 100 formulation was further investigated in an attempt to identify any physical or chemical instability of the API in neat HFA134a that may have led to the critically poor deposition performance seen in chapter 5. A high mass combination of SS and BDP was run

through the surface specific mapping techniques described below to identify if the observation of low BDP deposition was consistent and attempt to characterize any co-deposition of the API mass that was delivered.

The SX and FP low and high mass combinations were both investigated to examine the ACI based deposit structure by a variety of analytical techniques and help determine whether the extent of co-deposition could be established. Single API formulations were used as a means for proof of concept within some of the techniques. For a full description of the cold fill pMDI manufacture see chapter 5 (5.3.2.1).

6.3.2.2 Andersen Cascade Impaction

An eight stage Andersen Cascade Impactor (3M Healthcare Ltd, Loughborough, UK) was used for aerodynamic particle sizing and deposition profiling of the formulated aerosols. The same methodology as applied in chapter 5 was broadly utilized to generate ACI plates with the designated formulation particle impacts for analysis. For a complete description of the ACI stack operating parameters see chapter 5.3.2.2. The only alterations to this methodology were that for ToF-SIMS, Raman and DESI work each formulation was only actuated twice per run. As no quantification was required, the pMDI canister was not weighed for mass change, and did not have the valve cleaned down between waste firing and stack use. The ACI plates were not agitated into known volumes of sample diluent but extracted into petri dishes prior to use in the respective analytical methods outlined below.

The samples for SEM imaging were collected by inverting plate 5 of the ACI stack and securing several SPM specimen discs with double sided tape to the inverted plate surface below the stage nozzles. pMDI actuation was kept to two actuations for the sample production, and in this fashion, after the ACI run was complete the SPM discs could be extracted, mounted onto a SEM sample holder and gold coated for high vacuum work, without damaging or compromising the actual ACI plate.

6.3.2.3 SEM Imaging

SEM images of the morphology and topography of the deposited SX and FP particles on plate 5 of the ACI from the SX and FP 100 formulation were collected by a JEOL JSM-6060LV scanning electron microscope (JEOL Ltd, Tokyo, Japan) at various magnifications under vacuum. Samples were generated as described above on 13mm SPM specimen discs that were in turn mounted to SEM sample holders. The samples were then sputter coated in gold using a Balzers Benchtop Sputter Coater SCD 030 in an argon atmosphere (50Pa) at 30 mA for 4 minutes before SEM imaging took place in high vacuum mode. Samples were imaged at 90° from the electron gun before being tilted to 45° from incident, to allow an assessment of deposit height profile to be gained.

6.3.2.4 Raman Spectroscopy

All Raman spectroscopy was performed using a LabRAM HR confocal Raman microscope (Horiba Scientific, Kyoto, Japan) equipped with Olympus x10 or x50 optical lenses (Olympus Microscopy, Southend-On-Sea, UK) using a green (532nm) or near infra-red (785nm) laser with a 600 lines/mm grating and a thermoelectrically cooled Synapse CCD detector. Spectrum and hyperspectral imaging analysis was performed using LabSpec version 5 (Horiba Scientific, Kyoto, Japan).

The SS BDP formulation was analysed using a x50 objective lens at 532nm. Reference samples of the parent powders were first analysed for determination of reference spectra and to trial the choice of illumination source. It was determined that the green laser source used was adequate for the purpose of distinguishing the APIs as shown below. Subsequently the SS BDP formulation deposited on plate 4 of an ACI was mapped over a 250µm diameter spherical area using the 532nm source with 100% filter exposure, 300 µm confocal hole size, 1 second exposure time, a single spectrum per pixel point and one pixel per 2.5µm in X and Y (2.5µm resolution).

The SX and FP formulations were analysed using a x50 objective lens at 785nm. Attempts to use the 532nm laser to capture reference spectra from the API parent powders resulted in significant fluorescence from the SX samples that hid the Raman signal and would not suitably quench. As fluorescence generally occurs in the near UV to visible region, the use of a NIR laser

was trialled. This provided much more stable Raman spectra across both APIs with no interference from a fluorescent effect. Subsequently the individual API formulations SS 100, FP 100 and the SS FP 100 formulation were mapped across a 100 μm x 100 μm area, using the 785nm wavelength with a 75% filter exposure, 300 μm confocal hole size, 1 second exposure time, 1 spectrum per pixel point, and one pixel per 1 μm in X and Y (1 μm resolution). The combination formulations SX FP 50 and SX FP 100 were also mapped with the same parameters but across a larger 600 μm x 800 μm area, that encompassed an entire API spot for a macroscale appreciation of the API distribution. All Raman spectroscopy was performed on plate 4 of each formulation ACI run, as this plate was shown to consistently impact high masses of all APIs (except BDP) while showing a coherent on-plate deposit that would not be so concentrated as to hide individual particle layout.

With respect to the Raman methodology, the following procedures were followed for all work. After the selection and activation of the appropriate laser source, the requisite laser filters, electronic switches, grating and detector were also selected. The laser source was allowed to reach running temperature and stability. The instrument was then zero calibrated using white light, and Raman calibrated using a silicon calibration sample before each session of use or each mapping procedure. Powder samples were tapped onto a clean glass microscope slide before arrangement and light compaction using a clean glass coverslip. They were then loaded onto the microscope slide sample holder on the sample stage. ACI plates were secured directly onto the sample stage using double sided tape to avoid movement on sample stage rastering. All samples were located optically using a white light source and a x10 optical lens with manual adjustment of the microscope position. If a macroscale image was desired this objective was used to plot the mapping grid. For spectral mapping, increased magnification was required and the x50 objective lens would then be swapped into position. Optical focus was then maximised manually using the projected on screen image before a protective shield was placed around the microscope (to prevent laser exposure to the user and protect the sample from other light sources), and the optical alignment was readjusted to adjust for the slight loss of focus.

The white light source was then turned off and samples were exposed to the chosen laser source. A real time display of live spectra was used to maximise the Raman signal with fine movement of the microscope lateral position. Any samples that showed fluorescence (typically under the 532nm light source) were given 15 minutes of broad laser exposure across the

topographical area to be analysed. This was in an attempt to try and quench any fluorescence and improve the Raman signal. A rastering grid with desired geometry and operating parameters (as indicated below) was overlaid onto the optical image of the sample for mapping experiments to allow selection of an area of interest. In such experiments, an autofocus macro was utilised to automatically adjust the stage height with the raster position in maximising Raman signal to accommodate topographical variations.

6.3.2.5 Time of Flight Secondary Ion Mass Spectrometry and Multivariate Analysis

Time of Flight Secondary Ion Mass Spectrometry (ToF-SIMS) was carried out using a TOF-SIMS IV spectrometer with SurfaceLab 6 software (ION-TOF GmbH, Munster, Germany). All analysis was performed with a 25kV Bismuth liquid metal ion gun, utilising beam split and bunched incident Bi^{3+} ions for static SIMS analysis. Serial ACI plates were loaded directly into the TOF-SIMS instrument after pMDI ACI operation and secured to a sample stage. Individual deposits were located manually using the spectrometer chamber camera, and after the sample chamber was allowed to pump down to vacuum, the pre-designated spatial area was raster scanned. Positive and negative spectra were collected over an area of $500\mu\text{m} \times 500\mu\text{m}$ at 256×256 pixels to analyse individual API deposits. Sample surfaces were charge compensated with an electron gun at 20eV between primary ion bursts. Stage scan functionality was used to control sample raster, and all chemical imaging was performed at ambient temperatures.

Principal Component Analysis (PCA) was undertaken on the subsequent ToF-SIMS datasets using PLS_Toolbox version 5.2 (Eigenvector Research, Manson, WA, USA) for Matlab (Mathworks Inc., Natick, MA, USA). The PCA images were considered alongside the respective eigenvalues; the number of factors to model for using Multivariate Curve Resolution (MCR) was then manually determined. The same software was then utilised to carry out the MCR analysis. There was no data pre-processing carried out prior to MCR analysis in order that the non-negativity constraint (see chapter 2) be upheld. Spectral investigation was subsequently performed on MCR identified variates using SurfaceLab 6 software (as above) and in-house techniques using Microsoft Excel (Microsoft, Redmond, WA, USA).

6.3.2.6 Desorption Electrospray Ionization Mass Spectrometry

All Desorption Electrospray Ionization Mass Spectrometry (DESI) was carried out using a Prosolia Omnispray 2D Ion Source (Indianapolis, IN, USA), on a Thermo Scientific LTQ Velos ion trap mass spectrometer (Waltham, MA, USA). The DESI plume was generated from a 70% HPLC Grade Methanol: 30% HPLC grade Water mixture. This was run at 60 psi N₂ gas and a 2 μ l/min flow rate with a raster speed of 303 μ m/sec. The DESI spray was aligned 4mm away from the sample surface with a 50° spray to surface angle. The mass spectrometer (MS) inlet was at 10° from the sample surface, with an approximate 0mm distance (almost touching). The spray tip to MS inlet distance was 4mm. MS data was collected in positive mode at 4kV cone voltage, 250°C capillary temperature, m/z 150-2000 range, 2 microscans, 200ms maximum injection time and automatic gain control off. Multispectral image composition and analysis was carried out using Biomap 3x (Novartis Institutes for Biomedical Research, Basle Switzerland).

6.3.2.7 Differential Scanning Calorimetry

A TA Instruments DSC 2920 differential scanning calorimeter (TA Instruments, Delaware, US) was used to perform analysis of BDP extracted from the BDP 100 formulation. The BDP was extracted from formulation by first cooling the canister in an ice bath with acetone to below the boiling point of HFA134a. The canister lid was then punctured with a nail, and the canister was allowed to re-equilibrate slowly to room temperature in a fume hood. This led to the vaporization and escape of the propellant from the canister, leaving the API. Samples of the BDP were subsequently collected by cutting off the canister lid, and extracting the retained powder. Accurately weighed samples of about 6 mg were sealed in aluminum hermetic pans, equilibrated at 0°C, kept isothermal for 3 minutes and then heated at 10°C per minute under nitrogen to 250°C. Samples of the parent anhydrous BDP were also run as a comparator in the same fashion. Thermograms produced were analyzed using TA universal analysis –NT software (TA Instruments).

6.4. Results and Discussion

6.4.1 The Deposition of Salbutamol Sulphate and Beclomethasone Dipropionate

6.4.1.1 Desorption Electrospray Ionization Mass Spectrometry

Figure 6.1 shows DESI maps of the molecular ion of BDP (543 m/z) and SS (240 m/z) over 1cm x 1cm areas of plates 4, 5 and 6 of the ACI from the SS BDP 100 formulation. Figure 6.2 shows an example mass spectrum of both the API molecular ions from within a single drug spot on plate 4 of the same deposition profile. The chemical images for both APIs in figure 6.1 show very clear drug spot concentrations, and it is apparent that the DESI technique has succeeded in resolving multiple API deposits across a macroscale surface. These concentrated deposits are the result of particle impactions directly below the ACI stage nozzles above each plate. Notably the spread of the API deposition can be seen to decrease with increasing plate number, reflecting the decreasing nozzle size. However what is apparent from both figures is the differing predominance of BDP to SS. The images are scale matched for comparison, and it is subsequently evident that a very intense SS signal can be detected from each of the API spots, but that the comparative BDP spot is significantly weaker in intensity. This is true across all the plates that were imaged and most noticeable on plate 5. The apparent lack of BDP is further evidenced by comparing the mass spectrums in figure 6.2.

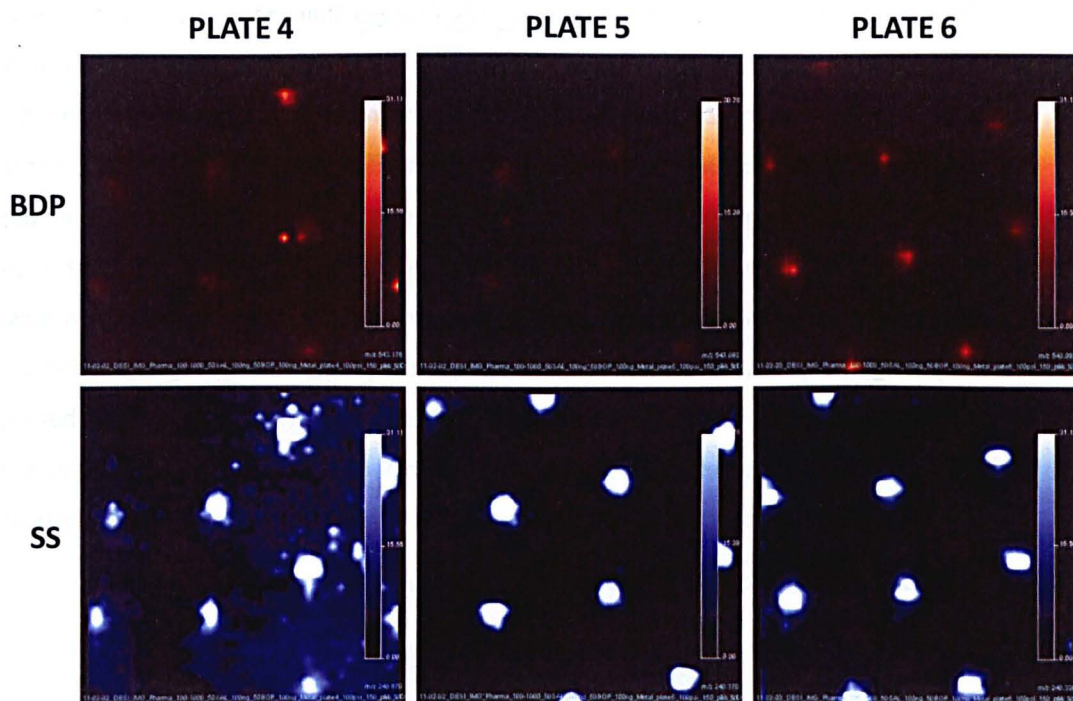


Figure 6.1: 1cm x 1cm DESI chemical maps of deposited beclomethasone dipropionate (543 m/z) and salbutamol sulphate (240 m/z) from an SS BDP 100 HFA134a pMDI formulation on plates 4, 5 and 6 of Andersen Cascade Impactor

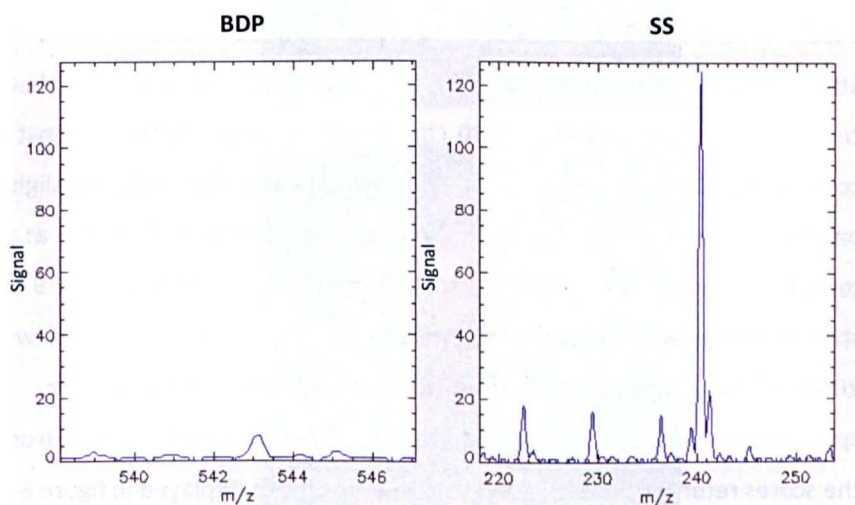


Figure 6.2: Representative DESI spectra of the parent BDP (543 m/z) and SS (240 m/z) molecular ions from within a single drug spot from a SS BDP 100 formulation on plate 4 of an Andersen Cascade Impactor

The signal detected for SS is approximately 12x stronger than that for BDP. What these chemical images and spectra infer is therefore that on these key fine particle plates, there is a significantly smaller proportion of BDP than SS. This observation must be tempered to some degree by the technical limitation of DESI in that the desorption efficiency of the two APIs is likely to differ. While the DESI plume was optimized with respect to the materials available, the differing chemistries of the two APIs may be reflected in the extent of desorption of each into the methanol : water mobile phase under raster. However further compensation was made by increasing the pressure of the system. As quantification was not desired this allowed the aerosolization of most of the powder impact of the spatial area under analysis, thereby reducing the bias of desorption efficacy. Significantly the lack of BDP observed was consistent with the ACI results from chapter 5, thereby adding further evidence that there exists a critical mass loss of BDP from the HFA134a system.

6.4.1.2 Raman Spectroscopy

Figure 6.3 shows the reference Raman spectra collected at 532nm for BDP and SS as analyzed from the parent API powders. The SS spectrum showed several key features including strong broad bands in the 2800-3200 cm^{-1} region. This is composed of an overlap of the $\nu(\text{NH})$ band at 3160 cm^{-1} , the $\nu(\text{CH}_2)$ and $\nu(\text{CH}_3)$ bands at 3062 cm^{-1} , the $\nu_{\text{as}}(\text{CH}_3)$ band at 2985 cm^{-1} , the $\nu(\text{CH})$ attached to an aliphatic (OH) at 2927 cm^{-1} , the $\nu(\text{CH}_2)$ attached to aliphatic (OH) band at 2899 cm^{-1} and the $\nu(\text{CH}_3)$ band at 2880 cm^{-1} (Ali et al, 2008). However most of these peaks were common to BDP with the exception of the $\nu(\text{NH})$ band, explaining the slightly less intense broad band in the same region. However a very strong aromatic C=C stretch at 1662 cm^{-1} was unique to BDP, and with the concurrent strong dominant $\nu_{\text{as}}(\text{C}-\text{OH})$ band at 978 cm^{-1} seen on the SS spectra (along with several other unique bands) the single spectral window of 500 cm^{-1} to 2000 cm^{-1} was subsequently chosen to map with and reference from. These single window spectra were then used to model for the hyperspectral mapping data from plates 3 and 4, and the scores returned according to these references are displayed in figure 6.4. The BDP signal was mapped as red and the BDP signal mapped as green. As figure 6.4 therefore demonstrates, there is a distinct predominance of SS compared to BDP across both the fine particle plates imaged.

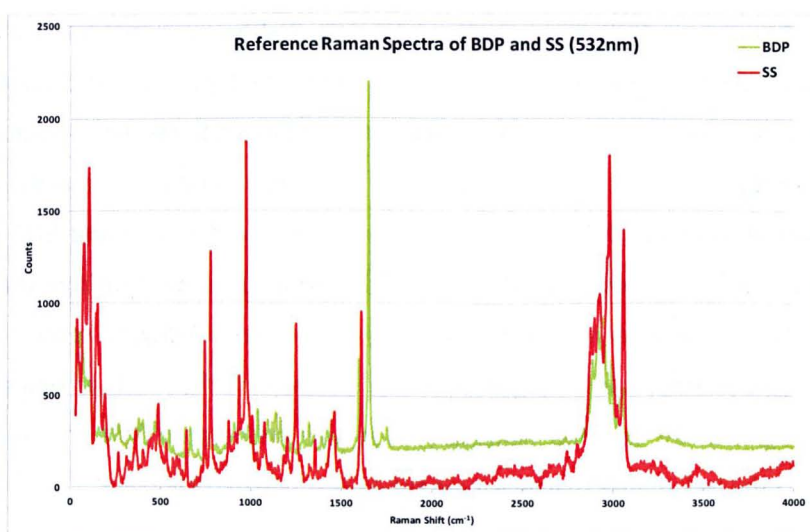


Figure 6.3: Reference Raman Spectra of BDP and SS at 532nm (Green Laser)

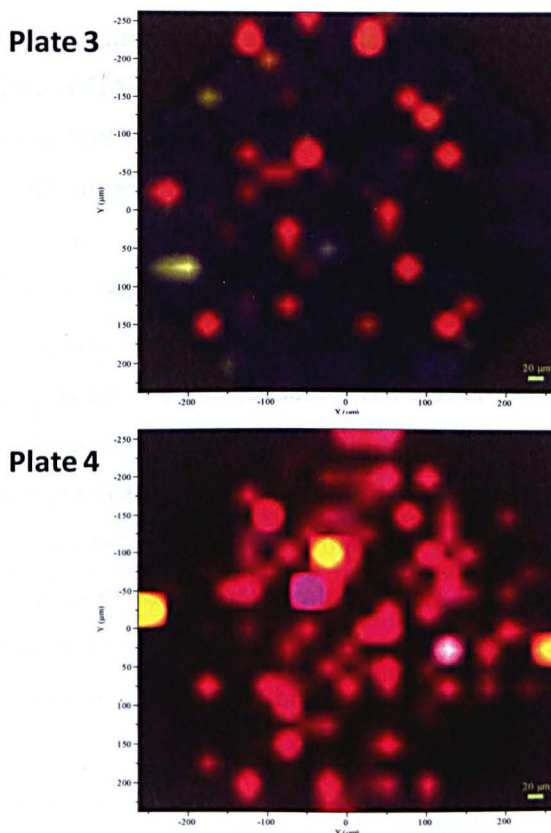


Figure 6.4: Raman Spectroscopy derived scores map of a 250µm diameter circular area of plate 3 and plate 4 deposition of SS and BDP from a SS BDP 100 formulation

Plate 4 shows no BDP score at all, while plate 3 shows minimal areas of BDP coverage. The Raman maps do show more concentrated particulate deposition on plate 4 with comparison to plate 3, but the spatial resolution of map was insufficient to resolve individual particle character. The scores maps therefore identify larger areas of strong API character, but because of the relative abundance of SS it is therefore possible that if the SS and BDP particles are closely associated that the increased mass of SS (that would be expected from the ACI and DESI work) leads to an overwhelming of the BDP signal, or the inability to resolve it. However for the purpose of further confirming the relative absence of BDP, further refinement of the Raman mapping was not deemed necessary as it was deliberated that the Raman maps collected support the lack of BDP reaching even the lowest fine particle plate.

6.4.1.3 Differential Scanning Calorimetry of Extracted BDP

Figure 6.5 shows the differential scanning thermograms of both the parent BDP and the BDP extracted from the BDP 100 formulation following HFA134a evaporation. While both traces can be seen to show the expected melting endotherm of BDP at around 211°C, the extracted BDP also shows a shallow but broad endotherm beginning at about 61°C, maximizing at 81°C, and ending at approximately 100°C. This endotherm is not seen on the thermogram for the parent API, but was consistent across all three extracted BDP samples. The transition suggests some form of rearrangement, which may represent one of several processes. It is possible that the BDP has undergone a solvate based reaction in the neat HFA134a. This may be hydration via the water load of the propellant to the mono-hydrate, where this transition represents the dehydration process. Or it is also possible that the BDP has clathrated with the HFA134a, and this endotherm represents a declathration process. Considering the temperature at which the endotherm occurs and the known infrequency of BDP HFA134a clathrate occurrence (Bouhroum et al, 2009), it is more likely representative of the former hypothesis. Unfortunately due to the lack of available BDP mass extracted and formulations available to re-extract, it was not possible to further analyze greater masses of the formulated BDP via techniques such as XRD or ATR-IR to better characterize the exact BDP product. Yet it is clear that there has been a change in the physicochemical state of the BDP that may reflect its exceptionally poor deposition performance. If hydration has occurred it is possible that this has led to changes in surface energy, particle size and agglomeration behavior that has instigated device retention.

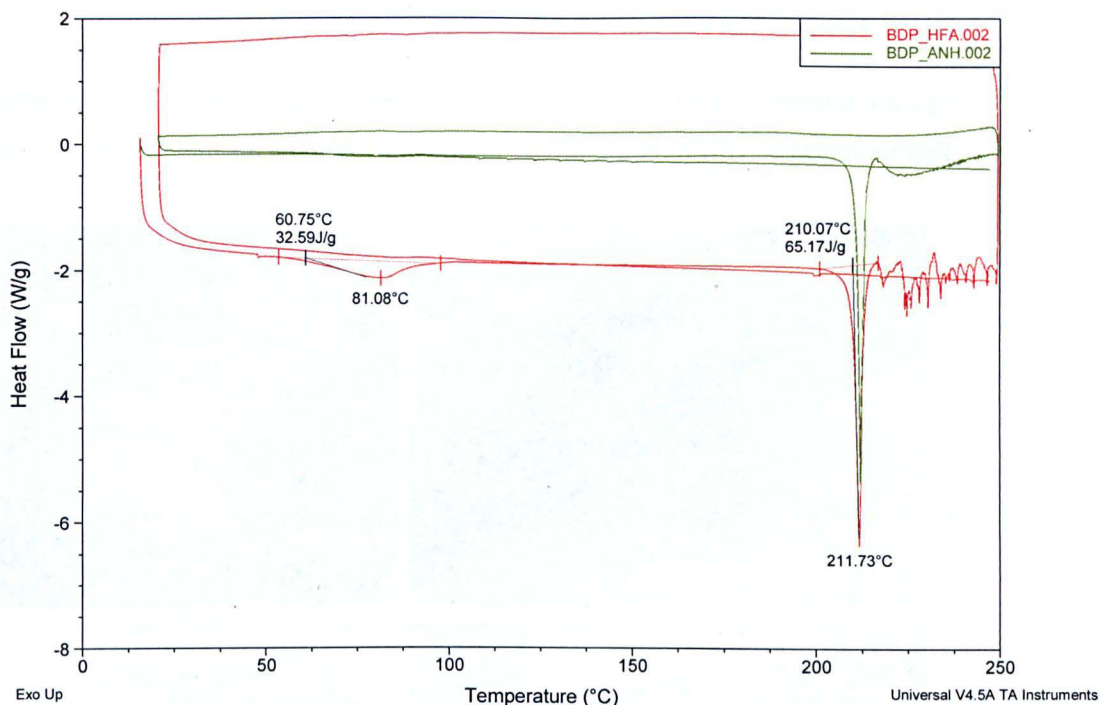


Figure 6.5: Representative differential scanning calorimetry thermograms of anhydrous BDP (green) and the BDP extracted from the BDP 100 formulation (red) after propellant evaporation.

All the formulations produced for analysis in chapter 5 were done so without any other excipients bar the propellant and the APIs. It is well known that stabilizing excipients are critical for the long term stability of many APIs in the new HFA formulations, due to the polarity of the solvent (as described in chapter 1). It is possible therefore that even on the short times scales between manufacture and use, that without the commonly employed co-solvents such as ethanol, the BDP has desolvated and crystallized out of suspension. This would explain why very little BDP is detectable on any analysis post actuation, as the remainder of the mass has been retained in the canister. Further analysis of this effect is necessary.

6.4.2 Investigating the Co-Deposition of Salmeterol Xinafoate and Fluticasone Propionate

6.4.2.1 Scanning Electron Microscopy

Figure 6.6 shows four SEM images of an API deposit from a SS FP 100 pMDI formulation on a SPM sample disc extracted from plate 5 of an ACI at differing magnifications and orientations.

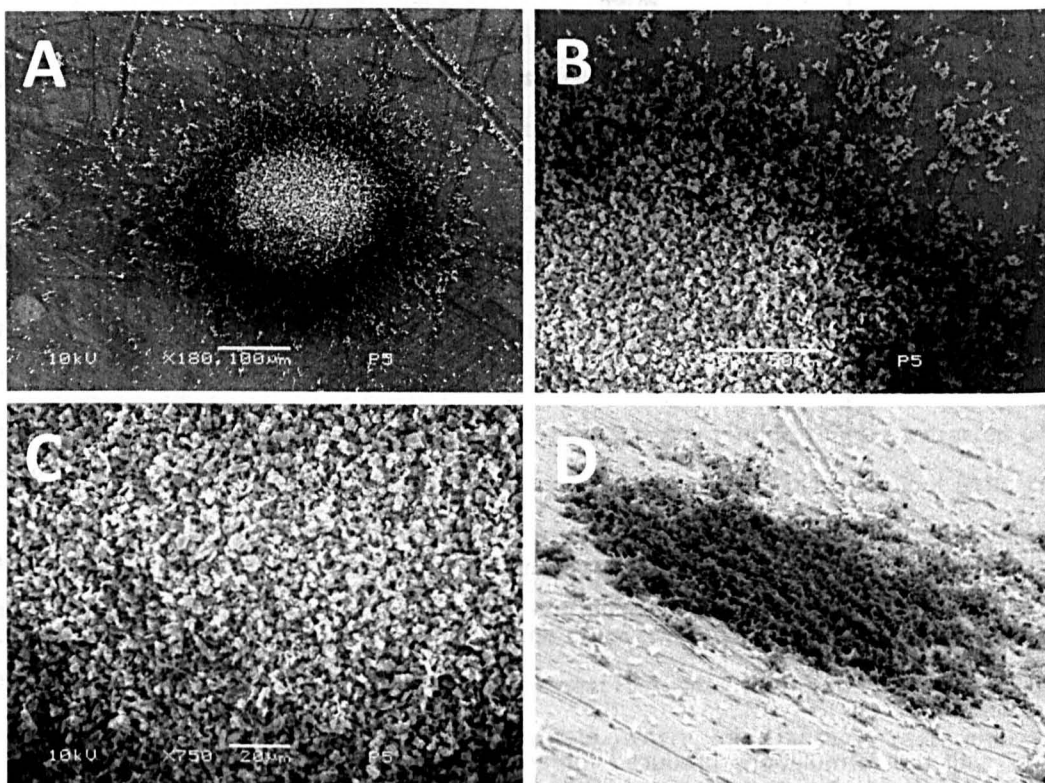


Figure 6.6: SEM images of an API deposit from a SS FP 100 formulation in an Andersen Cascade Impactor. A) x100 image of entire deposit and surrounding scatter, B) x500 image of deposit periphery, C) x750 image of deposit center and D) x500 image with 45° sample tilt of entire API deposit.

The individual particle character can easily be seen by SEM, as evidenced best in figure 6.6 C. Here we can see multiple irregularly shaped particles approximately 5 μ m in diameter. However while particle morphology can be determined there is no obvious distinction between SX and FP particles. What the images do show is that the center of these deposits become very

concentrated at this plate range. In all four images in figure 6.6 the center of the deposit shows significant particle overlay with no bare plate. This gradually trends towards smaller agglomerates and more diffuse scatter, before individual particles can be discerned on the plate surface several hundred microns away. With the nozzle size reducing with plate to plate progression, the particles that are deposited here were forced to do so in a smaller spatial area, thereby generating a smaller more concentrated deposit than would be the case further up the stack.

When looking directly onto the drug spot in figure 6.6 A, it appears as if the center of the deposit shows elevation and is proud of the peripheral particles. This impression is maintained by figure 6.6 B. However when we introduce tilt to the sample and image the deposit from a 45° angle (fig. 6.6 D) we can see that although the particles are more concentrated there is in fact not a significant increase in particle elevation in the center. It is likely in fact that the heavy concentrations of the particles at the center of the deposit insulate each other from the conductive metal substrate beneath. This means that despite the gold coating by sputtering, these insulated particles remain less able to conduct the incident electrons and are more likely to show charging behavior than those directly on the metal substrate. Perhaps more fundamentally, with particle overlay it is also possible that the sub layers are not well gold coated, therefore being very likely to charge. This charging effect is visualized as a whitening of the center of the spot. Regions nearer the metal surface are less likely to charge thanks to electron dissipation, and therefore remain visually darker. Collectively the effect is to artificially suggest more significant elevation than is the case.

However the technique is useful in generating a real appreciation of the particle to particle association in the impacted drug spot, and in visualizing the impacted particle morphologies. This information can then be used to help better understand the subsequent chemical characterizations.

6.4.2.2 Desorption Electrospray Ionization Mass Spectrometry

Figures 6.7 and 6.8 show the DESI maps of the molecular ions of SX (417 m/z) and FP (523 m/z) respectively. All the images within the individual figures are scale matched for comparison. What both figures show is that definitive drug deposits below the ACI stage nozzles can be broadly identified by both the signature ions for the two APIs on plate 2 and downwards. Figure 6.7 shows a signal for SX that builds from a weak but diffuse arrangement of six deposits on plate 2, to a very strong signal for SX on plate 4. Plates 2, 3 and especially 4 show significant SX scatter. This occurs almost to the point of overlap on the plate 4 map. This may simply reflect the cross over between the increasing mass of deposition according to aerodynamic character and the reducing nozzle size concentrating deposits. However it is also possible that with the increased mass on plate 4 there is some agitation of the deposits by the DESI plume as it rasters across nearby areas. Plates 5 and 6 continue to show strong spatial signals for SX in nine deposits, but the scatter is much reduced. Several of the drug deposits show slightly heterogeneous morphologies that may either reflect nozzle variability (blockages or imprecision) or knock on movement of the deposits due to the force of the DESI plume. Plate 7, shows a weaker and again slightly more diffuse signal for SX across three deposits. This compares very similarly with the spectral mapping of FP in figure 6.6. Here nothing but the uncoordinated dot of the signature ion can be identified on plates 0 and 1 before on plate 2 a diffuse spatial arrangement into nine deposits can be seen with a weak FP signal. Unexpectedly plate 3 shows very little coordinated FP signal and the differentiation of the deposits with scale matching is lost. Plate 4 however shows a strong FP spatial signal arrangement into six clear deposits with three poorly defined but still aligned peripheral spots. This plate again shows the most significant spot scatter, before plates 5 and 6 show more concentrated and consistent FP deposits. Plate 6 shows a stronger signal for FP in the nozzle deposits than plate 5, which may reflect either the signal boosting impact of a more heavily concentrated and smaller deposit, or simply be due to the variability of the DESI process.

It is worth clarifying that the signal strength of each plate deposits cannot be absolutely linked to quantification due to the variability of the desorption and ionization efficiency brought about by the chemistries of the APIs and also the physical nature of each deposit i.e. concentrated mounds, and diffuse scatter. Therefore it is not to be assumed that figure 6.6 shows more FP on plate 6 than plate 5, but it does suggest a significantly strong presence of the API that allows for

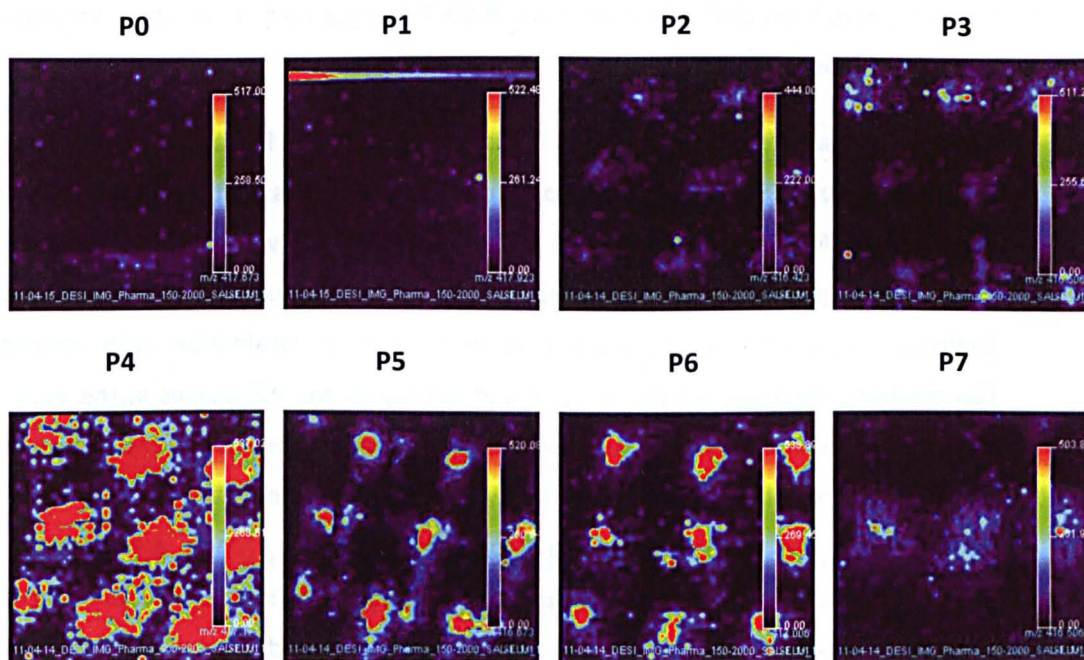


Figure 6.7: 1cm x 1cm DESI chemical maps of deposited salmeterol xinafoate (417 m/z) from an SX FP 100 HFA134a pMDI formulation on plates 1-7 of an Anderson Cascade Impactor

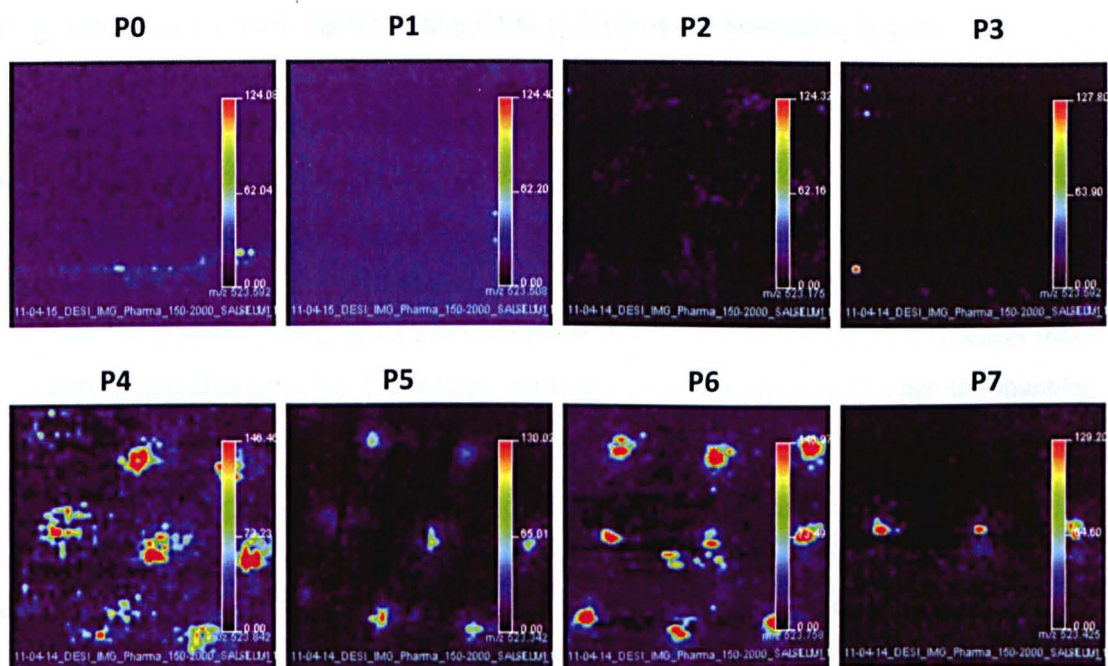


Figure 6.8: 1cm x 1cm DESI chemical maps of deposited fluticasone propionate (523 m/z) from an SX FP 100 HFA134a pMDI formulation on plates 1-7 of an Anderson Cascade Impactor

the characterization of the drug deposits. Plate 7 on figure 6.8 shows three very well defined and small deposits.

What we can see from figures 6.7 and 6.8 is that both SX and FP can be identified in the same drug deposits by DESI. This is not unexpected as each deposit is multi-particulate and the forced impaction by ACI use means that the impaction of any API will only ever occur under each nozzle. DESI currently lacks sufficient spatial resolution to be used to define individual particle chemical character, and therefore particle to particle localization with respect to API combinations. However we can see a broad overlap of the API signals in the each spot and indeed even for the deposits that show irregular morphologies such as the central deposit on plate 6, the irregular features consistently show signal from both APIs. Yet the detracting information is that the SX spatial signal consistently outlines broader areas around each API spot, where the FP signal is always more concentrated to the middle. This is most pronounced on plate 7 where the FP signal shows three very defined and concentrated spots but the SX image shows a much less concentrated and diffuse scatter around the same deposits. As previously explained this may not be explicitly linked to co-deposition character due to differences in DESI uptake efficiency that may mask true mass equivalence. Therefore if FP desorbs and ionizes less efficiently than SX the signal strength from areas of lower concentration such as the edges of each deposit would not show spectrally as well as the same areas of SX. It should also be further borne in mind that from the ACI work in chapter 5 we expect to see greater mass of SX reaching the fine particle plates, and the broader spatial signal may simply reflect the higher mass of SX at the peripheral regions of each deposit superseding a hypothetical signal minimum.

6.4.2.3 Raman Spectroscopy

Figure 6.9 shows the reference spectra from 1100cm^{-1} to 1800cm^{-1} for SX, FP and the ACI plate at 785nm. The distinct differences in Raman banding between the two APIs in this single window spectrum can be seen. The distinct and very strong aromatic C=C stretch at around 1662cm^{-1} is again unique to the corticosteroid, while the four bands between 1350cm^{-1} and 1475cm^{-1} representing the $\delta(\text{OCH}_2)$ deformation, $\delta(\text{C-H})$ deformations and ring stretches respectively, generate a very unique fingerprint for SX. Subsequently these reference spectra

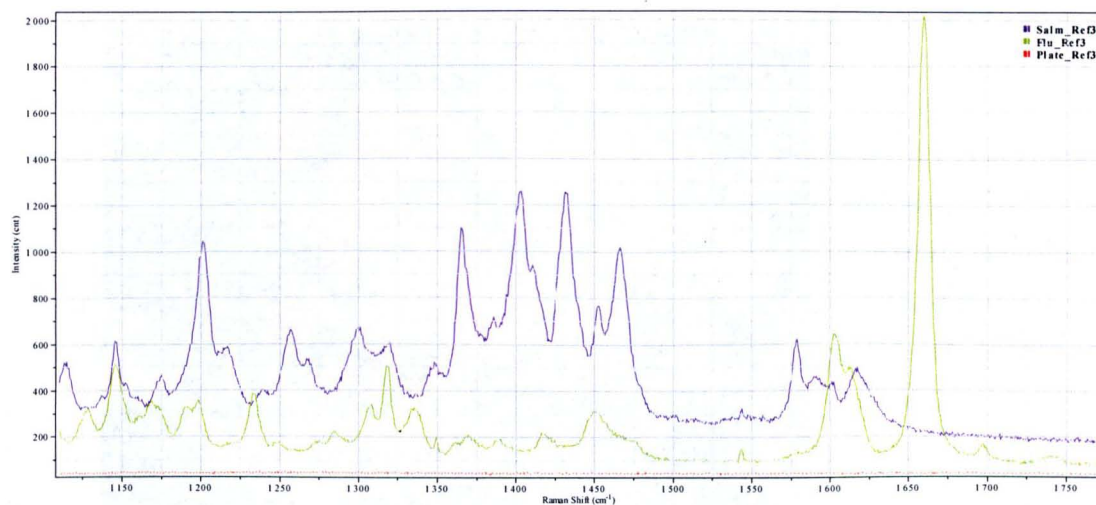


Figure 6.9: Reference NIR Raman spectra (785nm) of salmeterol xinafoate, fluticasone propionate and the stainless steel ACI plate.

were used to model the hyperspectral data sets acquired from the Raman mapping runs acquired on the ACI plates. Figures 6.10 and 6.11 show the overlay of a 100 μ m x 100 μ m modeled hyperspectral spatial dataset according to the above references, onto the microscope image of particles deposited on plate 4 of the ACI from a SX 100 and FP 100 formulation respectively. SX was modeled in red, FP green and the ACI plate blue. As is apparent from both figures, the individual API systems showed a strong correlation between particle deposition and the modeled Raman spectra obtained. Figure 6.10 shows a very good correlation of the red SX map to the particle surface distribution. Figure 6.11 does again shows a strong correlation between the green FP Raman score and the particle distribution. In this instance however there is a shift in spatial positioning. This can be attributed to drift of the lens through the mapping duration, but the areas of the Raman map modeled to fit the FP reference do appear to correspond well to the particle bodies captured in the bright field image. Notably both figures show some degree of artifact incidence. Both maps show areas mapped as strong blue (plate) and individual pixels modeled as the absent API. These artifacts are likely the consequence of only running a single spectrum per pixel. This was done to significantly reduce scan time, but renders the mapping process more susceptible to anomalous readings that may occur as a result of instrumental variation, loss of signal due to topographic differences or even contamination. In

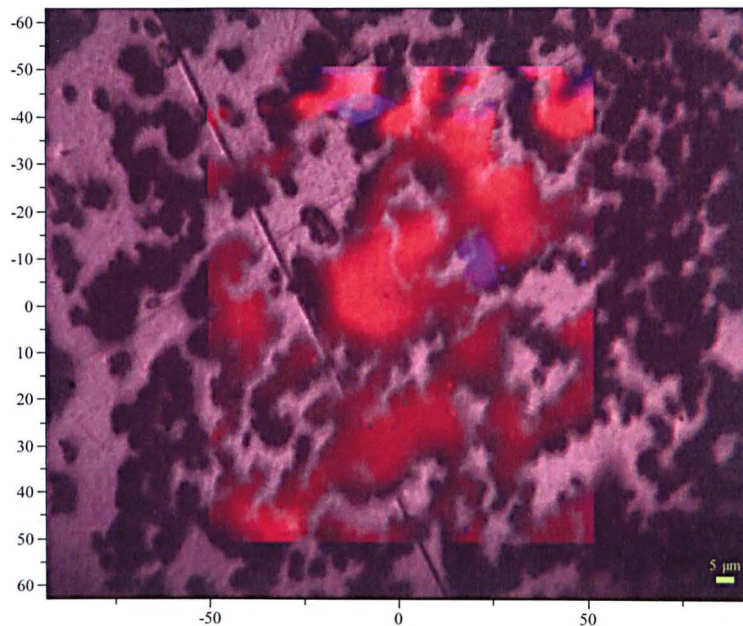


Figure 6.10: 100µm x 100µm hyperspectral Raman spectroscopy derived scores modeled overlay to salmeterol xinafoate deposition from a SX 100 formulation on plate 4 of an Andersen Cascade Impactor.

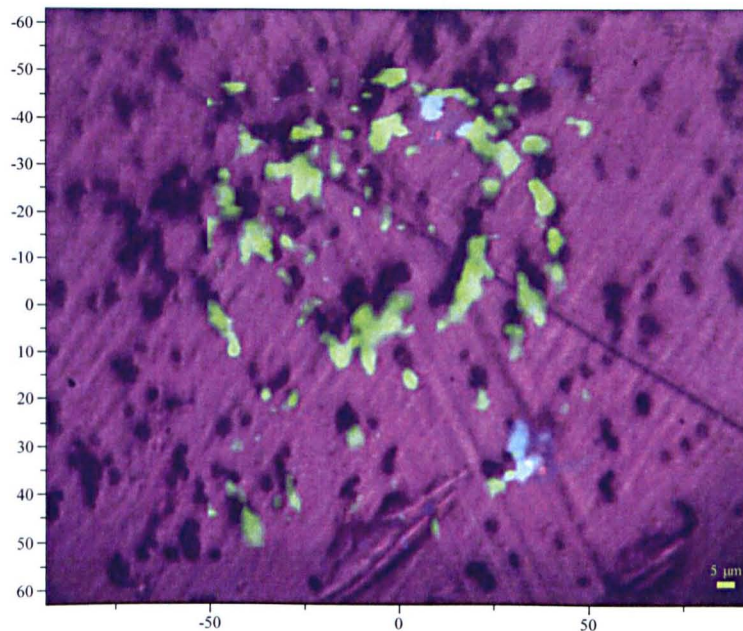


Figure 6.11: 100µm x 100µm hyperspectral Raman spectroscopy derived scores modeled overlay to fluticasone propionate deposition from a FP 100 formulation on plate 4 of an Andersen Cascade Impactor.

general these areas do not impede the generally positive correlation of the individual particulates to the Raman scores obtained.

Figure 6.12 shows two representative images of the overlay of the Raman derived scores model for SX and FP onto the particles deposited from a SX FP 100 formulation. Both images within the figure show similar characteristics. There is a strong correlation of the Raman scores obtained to the particle distribution on the ACI plate surface. Both SX and FP can be identified as strong red and green components of the entire particle masses. As would be expected considering the ACI results obtained in chapter 5, there is significantly more SX coverage of the mapping area than FP. However the distinction of the FP particulate areas can be made. This can be seen to suggest that the SX and FP particles are indeed often found as part of the same larger agglomerates. There are very few solely separate FP or SX agglomerates, with green particle masses seemingly often attached to the edges of larger SX agglomerates. This lends credence to the theory that the two APIs are co-associated on impaction. This may therefore reflect the co-association of the two APIs in the airstream upon aerosolization and a theory of critical agglomerate constitution being key to subsequent airstream kinetics and deposition performance. There are also several other features of interest in both these images that were seen repetitively across small areas of the Raman maps acquired. These include the appearance of several transparent particle features, several intense yellow or blue areas of mapping.

Figure 6.13 shows a 120 μm x 200 μm overlay of the Raman scores for SX and FP onto particles from a SS FP 50 formulation. It further shows the distinct association of the FP and SX particles even with a reduced particle mass. It also highlights the same anomalous features described above, and the figure includes example point spectra of both these anomalies and the strong SX and FP signals for comparison. Easily identifiable are the SX and FP spectra from the strong red and green areas overlapping particle bodies. In figure 6.10 A, figure 6.11 and most prominently in 6.12 B the transparent dispersed particle features can be seen on the bright field images. These only appear in the mapping area i.e. that exposed to the NIR laser. The fluid-like and crystalline appearance of these features would therefore suggest that these may be the product of a melting process. The lack of a definitive Raman signal from these features and the very low signal return can be seen in figure 6.13 C. This low, indistinct signal makes it unclear as to what has melted or undergone a transformation under the laser source. Because of the nature of the formulations, the only components present on the ACI plates should be the SX and the FP. FP

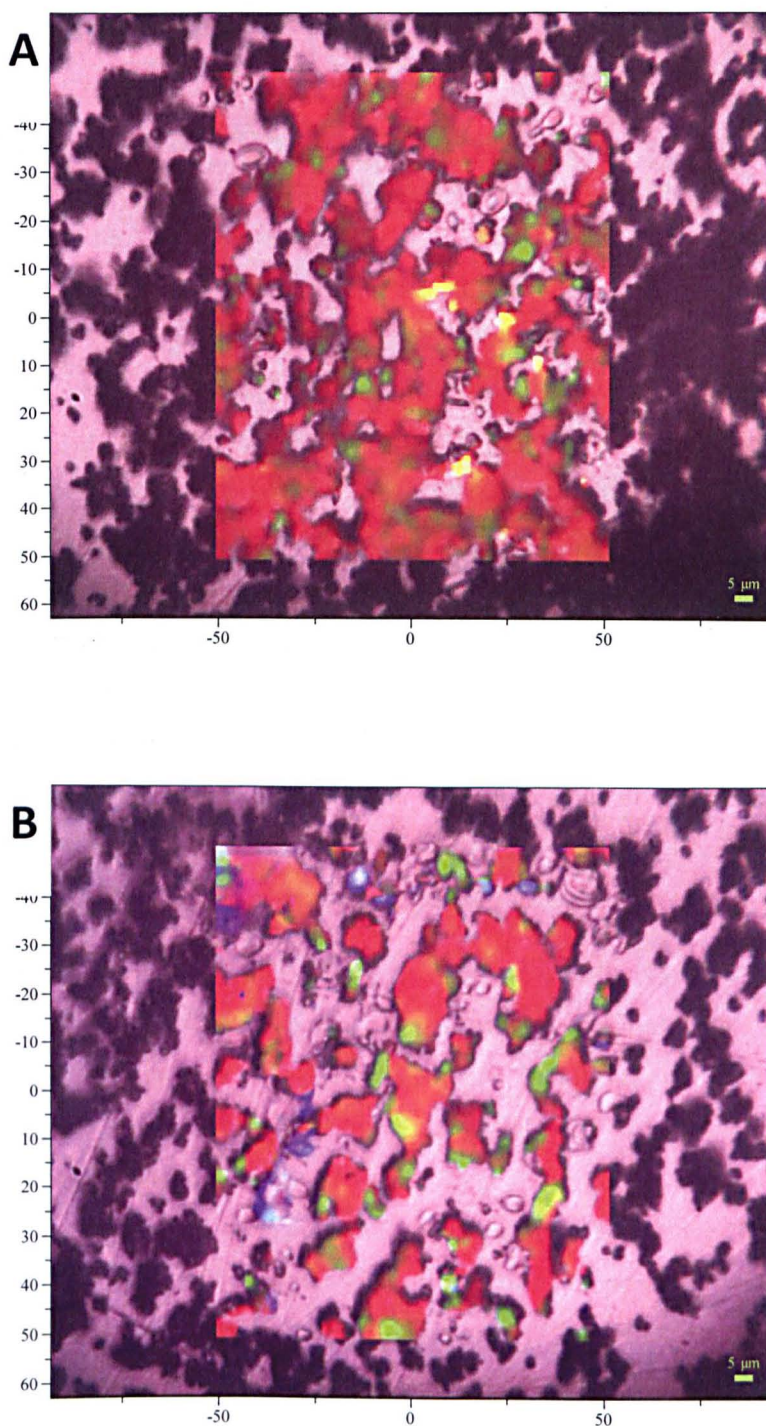


Figure 6.12: 100µm x 100µm hyperspectral Raman spectroscopy derived scores model of salmeterol xinafoate and fluticasone propionate deposition from a SS FP 100 formulation on plate 4 of an Andersen Cascade Impactor in two separate deposits A and B

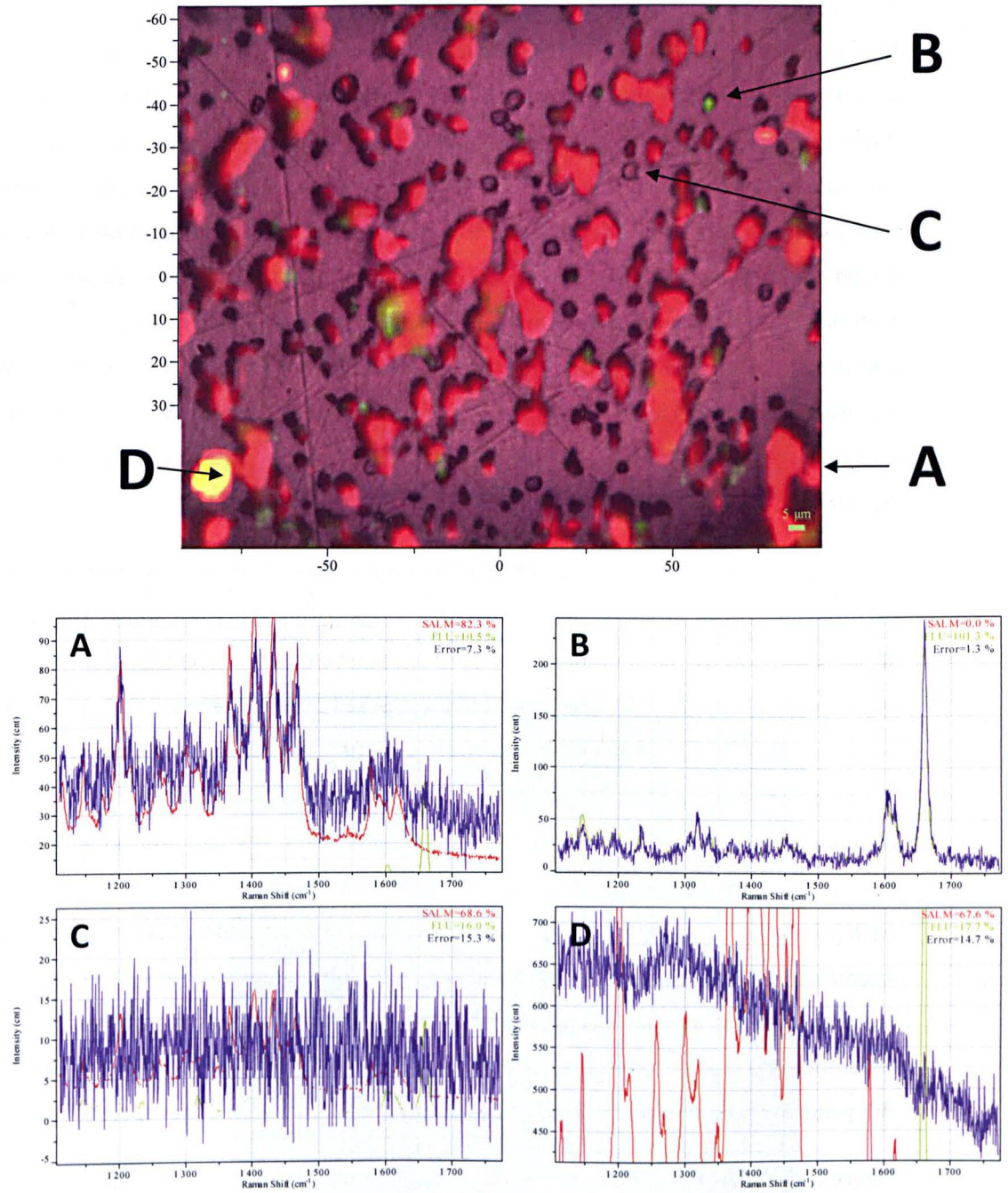


Figure 6.13: 120 μ m x 200 μ m Raman spectroscopy derived scores model of salmeterol xinafoate and fluticasone propionate deposition from a SS FP 50 formulation on plate 4 of an Andersen Cascade Impactor and associated point spectra of A) SX B) FP C) transparent anomaly and D) yellow anomaly

has a melting point of around 290°C while SX has a melting point of around 124°C, suggesting that if this is the melt of one of the APIs it would more likely be SX. The extent of these melts varied from image to image, with figure 6.12 B showing the most significant level and figure 6.12 A showing the least. What can be seen across the images collected was the nature of these melted particles to be near the periphery of larger particles and often near large exposed areas of the ACI plate. This may infer that this transition occurred as a process of heat radiation. This would occur as the ACI plate heated under continual exposure to the laser source as it was rastering. Therefore large particle masses shielding the plate surface reduce this phenomenon, and the occurrence of these features, but in areas of large expanses of bare plate, NIR laser exposure heats the plate gradually and this is conducted to proximal SX particulates that may eventually exceed their melting point. What is unclear is to why these subsequently give a very poor Raman signal.

Figure 6.13 D also shows the point spectrum from one of the intense yellow 'flares' that occurred in various areas of several mapping images. This spectrum shows that the Raman signal is very intense but unrefined and uncharacteristic of any of the principal components of the formulation. As such the reference model imposed assigns the most likely character based on percentage match to the references given, and the intensity of the spectrum is reflected in the colour intensity shown. It is therefore likely that these areas reflect either some degree of contamination, or more likely are the effect of some photo reactive process with an impurity such as fluorescence. This is given support by the nonlinear baseline of the spectrum. Because each pixel point was only analyzed by one spectrum, with no repeats, that means that any such anomalous regions will not be averaged out with subsequent exposure. The intense yellow features and the intense blue features showed very similar spectra profiles. The principal difference was that the yellow regions were modeled more towards SX while the blue more the ACI plate. In real terms neither really showed any consistency with either spectral reference.

Figure 6.14 shows the optical microscope image through the 10x objective lens of an entire API spot from a SX FP 50 formulation as deposited on plate 4 of an ACI run. Figure 6.15 shows the corresponding Raman derived scores model for SX and FP (via mapping using the x50 lens) for the same surface area. These figures in conjunction show a very good correlation between the visual particles and the SX and FP modeling of the Raman spectra. All major particulate features can be corresponded from figure to figure and both SX and FP character can be discerned. Once

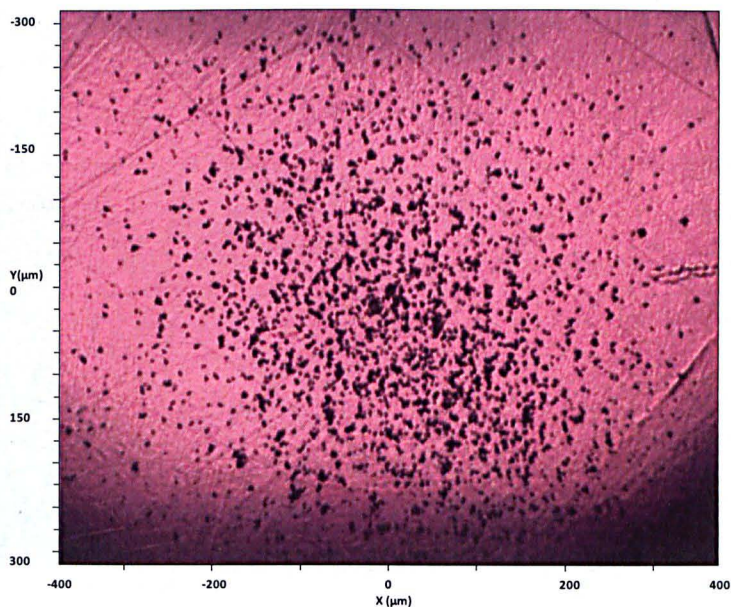


Figure 6.14: 600μm x 800μm optical microscope image of a deposited API spot from a SX FP 50 HFA134a formulation on plate 4 of an Anderson Cascade Impactor

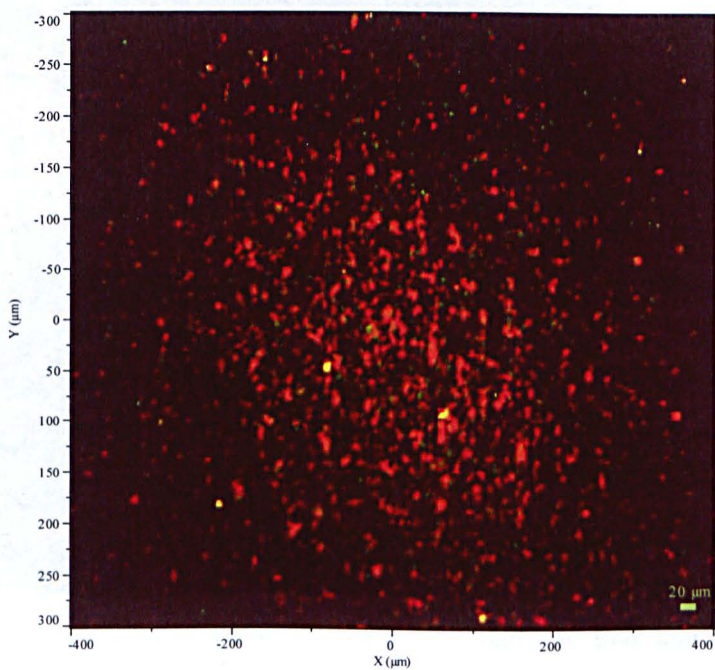


Figure 6.15: 600μm x 800μm Raman spectroscopy derived scores model of salmeterol xinafoate and fluticasone propionate deposition from a SX FP 50 formulation on plate 4 of an Andersen Cascade Impactor

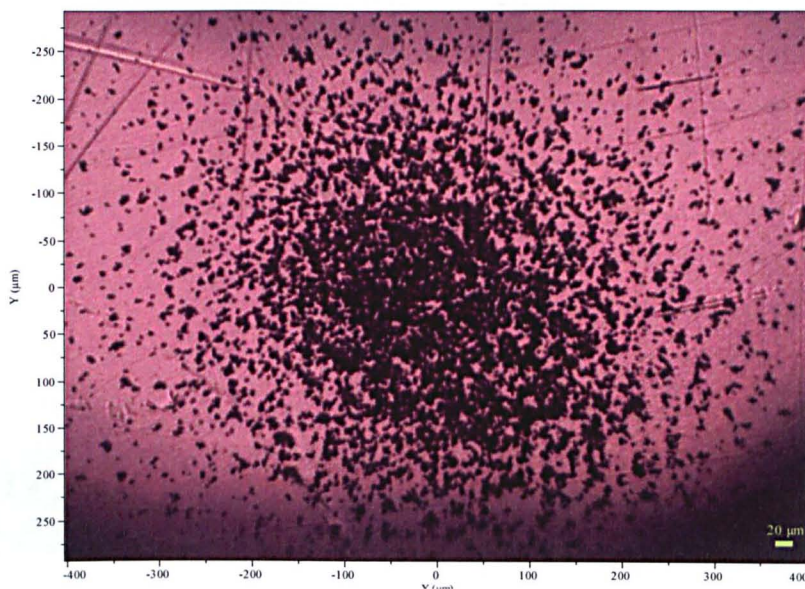


Figure 6.16: 600μm x 800μm optical microscope image of a deposited API spot from a SX FP 100 HFA134a formulation on plate 4 of an Anderson Cascade Impactor

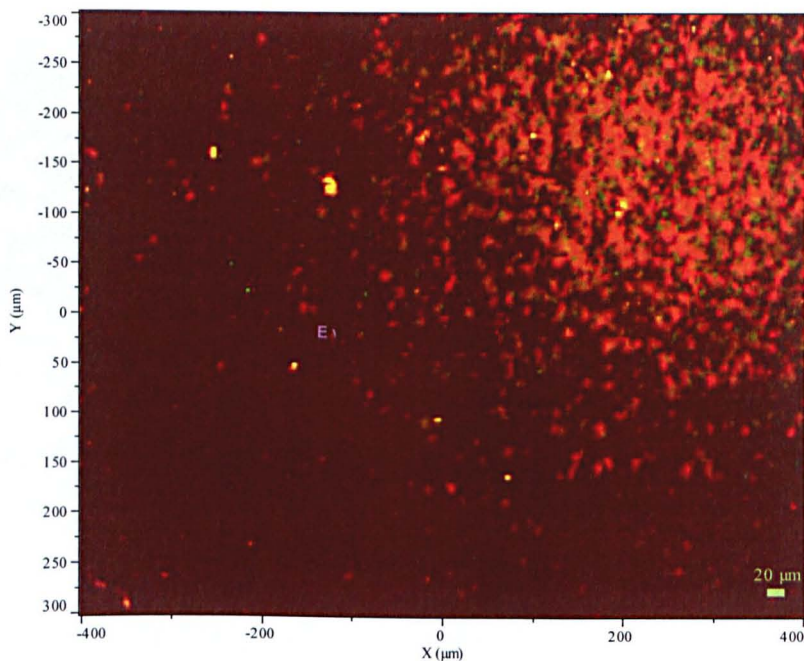


Figure 6.17: 600μm x 800μm Raman spectroscopy derived scores model of salmeterol xinafoate and fluticasone propionate deposition from a SX FP 100 formulation on plate 4 of an Andersen Cascade Impactor

more the proportionally greater abundance of SX across the entire spot can be seen, and therefore the existence of several SX only particle bodies is unsurprising. However while the localization of FP particles can again be seen to be co-existent with many SX particle bodies, there is also evidence over this scale of separate FP particulates. This is especially true at the periphery of the API spots. Figure 6.16 shows the optical microscope image of an entire API spot on plate 4 of an ACI from a SX FP 100 formulation. This mass doubling from the SX FP 50 spot can be visualized clearly by comparing the images. The center of the spot is now much more concentrated and particle scatter to the periphery has increased.

Figure 6.17 shows the Raman derived hyperspectral data modeling for SX and FP across part of this same API spot in figure 6.16 with bias on the x and y axis to focus on the peripheral particle scattering. The figure shows the concentrated particle mass at the center of the spot, and the decreasing gradient of distribution as we move outwards. Notably particle scatter can still be characterized up by the Raman as far away as 350 μ m - 400 μ m from the spot center. In the center of the concentrated API deposit, there is again a large degree of co-localization of the two APIs, with the predominant SX particles inter-dispersed with associated FP particles. Small and infrequent individual particle bodies can be distinguished. However as with the SX FP 50 formulation, as we move from the center of the spot to the periphery, we start to see more and more separate particles corresponding to each API. Approximately 250 μ m away from the deposit center, there is more separate character than combined. This directly opposes the trend at the center of the spots and may suggest that the co-deposition of the two APIs in the ACI is actually the result of interaction at the plate, rather than in the formulation and in the airstream leading to deposition. In this circumstance the FP and SX particles have agglomerated at the point of impaction according to particle-particle contact as particles exit the airstream and impact into the surface and each other. Particles that are only just unable to remain in the airstream, deposit to the outside of the API spots and do not subsequently contact further API particles and deposit alone. However it is also equally possible that the particles at the edge of each API spot are moved there by collisions from the center mass. The subsequent actuations of the pMDI formulation provide more and more API particles that inertially impact onto previously deposited particles. This may forcibly displace the previous material, leading to destructive relocation of these particles. As such the breakup of SX and FP agglomerates could occur, resulting in peripherally dispersed API particles.

6.4.2.4 Principal Component Image Analysis of Hyperspectral Time of Flight Secondary Ion Mass Spectrometry Data

The first step in the ToF-SIMS analysis of the SX and FP ACI plates was to analyze the acquired hyperspectral data by PCA to determine the number of factors to model for by subsequent MCR analysis. Figures 6.16 to 6.19 show the PCA image analysis of ACI plates 4 to 7 (in the negative or positive spectrum as indicated). The analysis was done for all plates from 0 to 7 in both positive and negative spectrums. From these figures it can be seen that the PCA analysis alone does not consistently model for the visual definition of the impacted drug spots. Figure 6.21 shows that the 1st principal component (PC) intensely highlights coordinated variants within the small impact spot on plate 7 and on figure 6.19 PC2 models the drug spot on plate 5. This was also the case with some additional spectral datasets but figures 6.18 and 6.20 show the more common peripheral spot definition by the primary principal components. This is not unexpected because while the technique identifies combinations of chemical spectra that reflect the correlations and anti-correlations of the variant ions across the image, certain chemical components may be projected onto multiple factors and therefore become difficult to categorise in a co-ordinated fashion.

The Eigenvalue plots show that the majority of the variance in the datasets is projected onto the first 1 to 4 PCs. There is a slight exception in figure 6.20, where a larger spread onto further PCs can be seen, but this is highlighted as a general anomaly, with only three more spectral datasets (positive and negative spectral datasets for plate 6 and plate 2) showing similar Eigenvalue plots among the total 14. Even for these datasets however, when we look at the visual projection of the scores onto the first 12 PCs we can see little discrimination in structural differences after PC4. Beyond this component there appears to be little variability besides minimal alteration to the background composition. This is the same in figure 6.16 and the majority of the other plate datasets. Figures 6.17 and 6.19 appear to show some coherent variability on later PCs (PC 11 in figure 6.19 and PC 6 in figure 6.21), yet in these instances the variability projected as Eigenvalues onto these components is minimal. From the PCA images generated it is possible to infer that there is a large degree of background variability across the ACI plates. A significant number of components seemingly represent variance in the distribution of plate components, with respect to the spatial positioning of deposited API. A 'halo' effect can be seen across many of the primary principal components around the drug spots themselves, which may suggest the

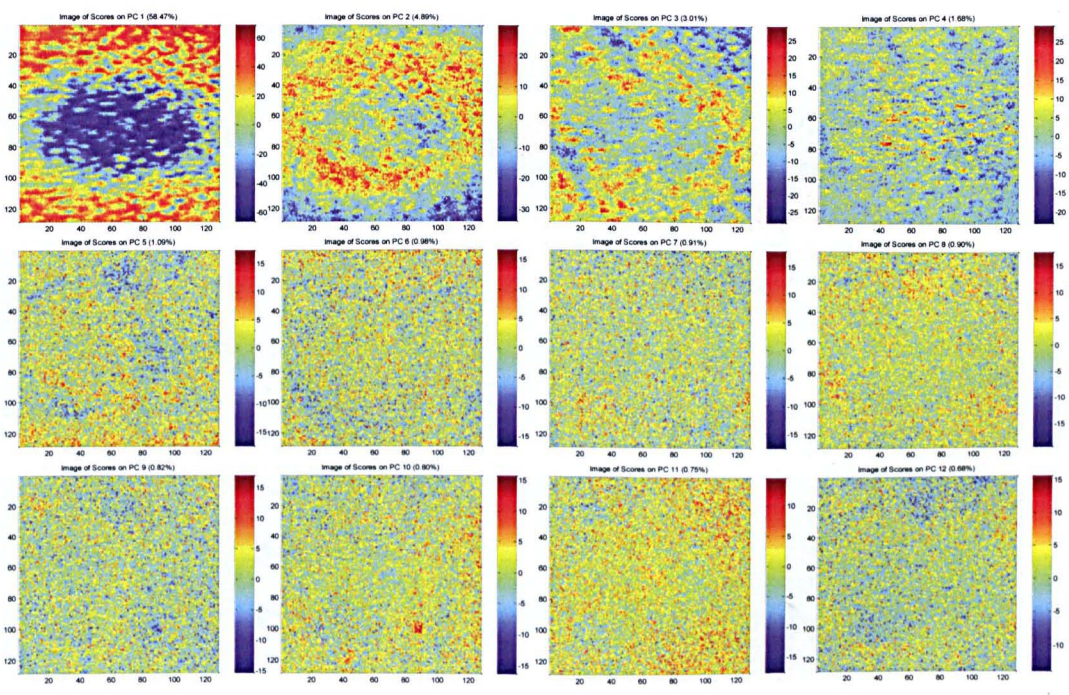
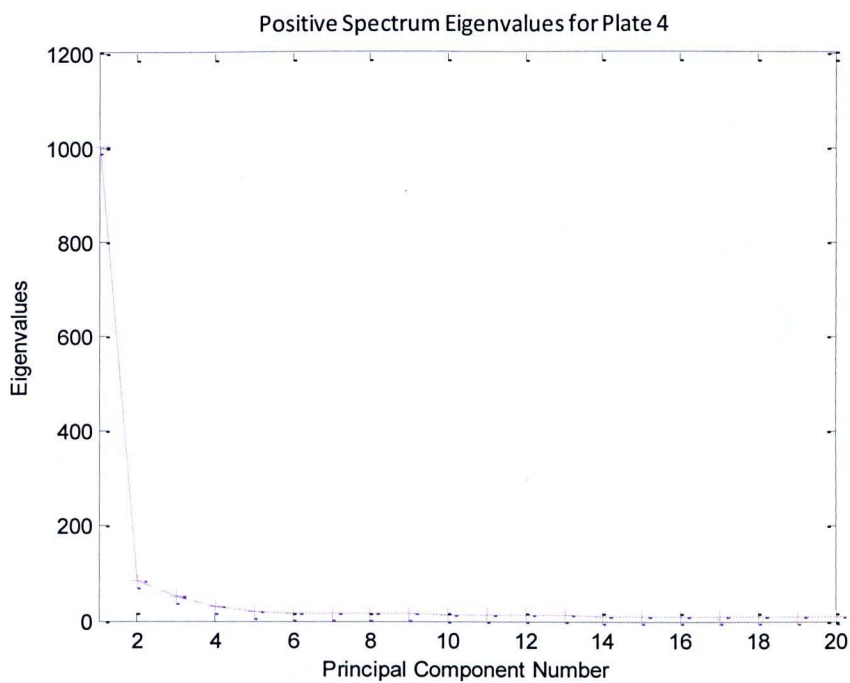


Figure 6.18: Positive Spectrum Eigenvalue plot and PCA score images on principal components 1 – 12 from a 500 μ m x 500 μ m area around a single API spot from a SX FP 100 formulation on plate 4 of an Andersen Cascade Impactor

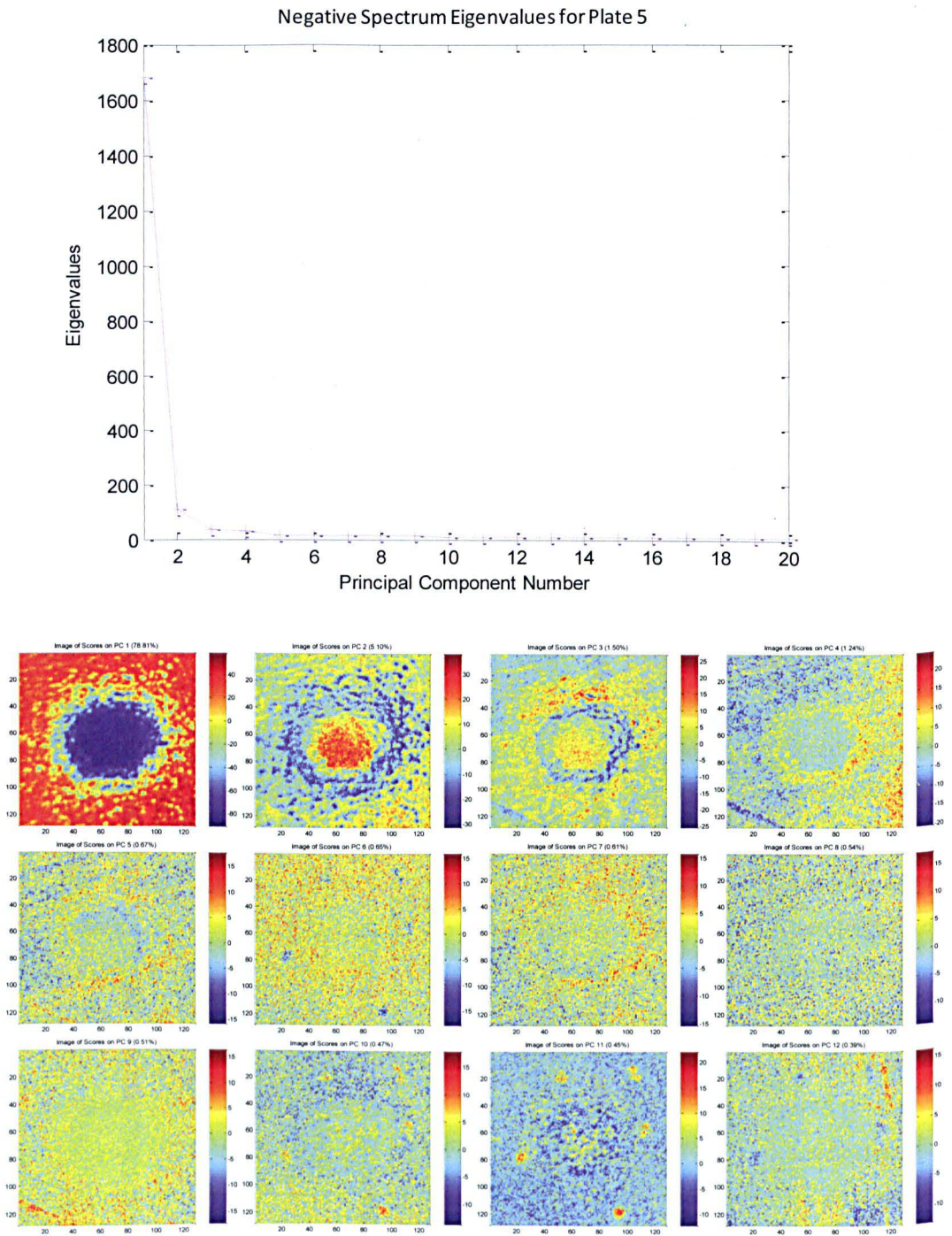


Figure 6.19: Negative Spectrum Eigenvalue plot and PCA score images on principal components 1 – 12 from a 500 μ m x 500 μ m area around a single API spot from a SX FP 100 formulation on plate 5 of an Andersen Cascade Impactor

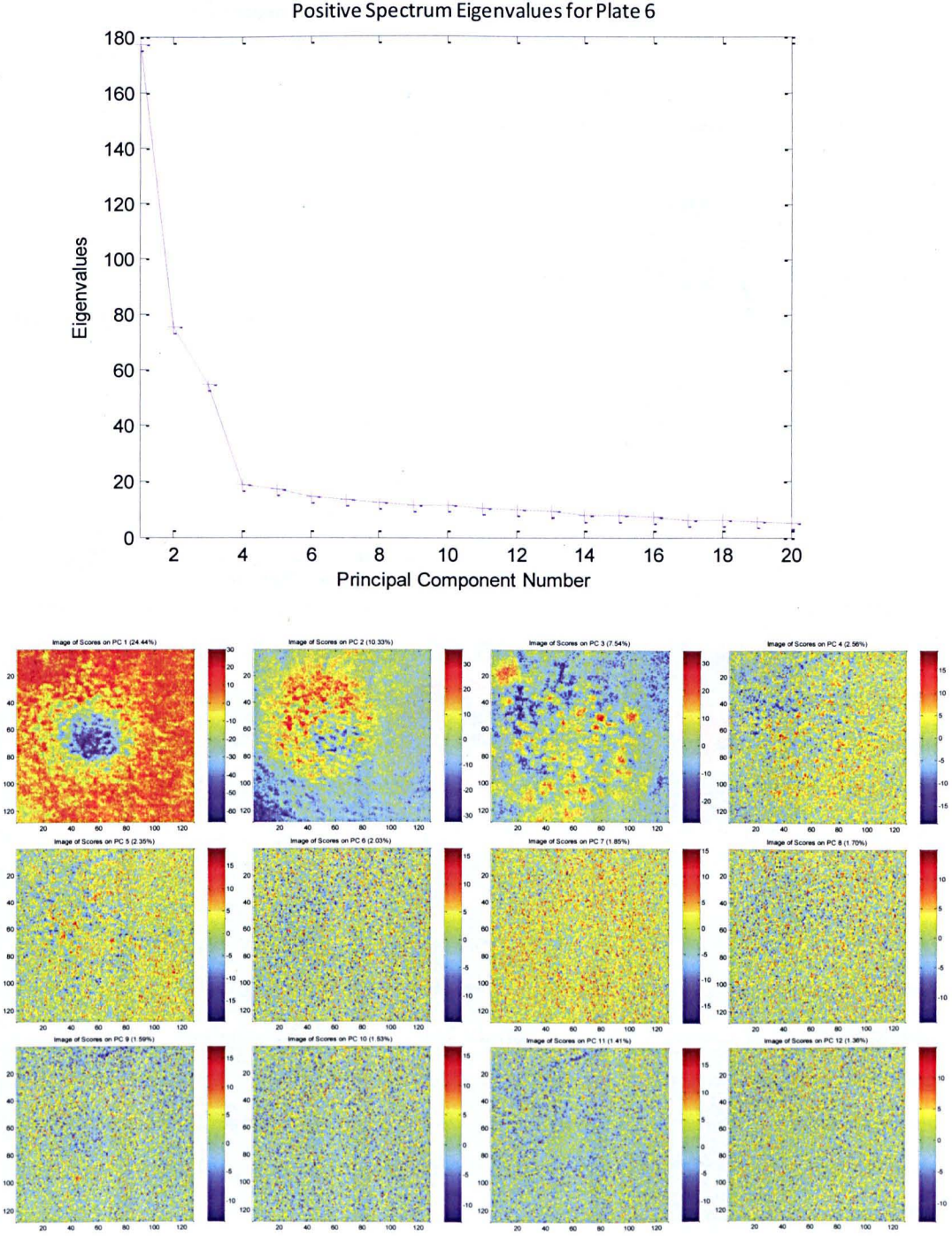


Figure 6.20: Positive Spectrum Eigenvalue plot and PCA score images on principal components 1 – 12 from a 500µm x 500µm area around a single API spot from a SX FP 100 formulation on plate 6 of an Andersen Cascade Impactor

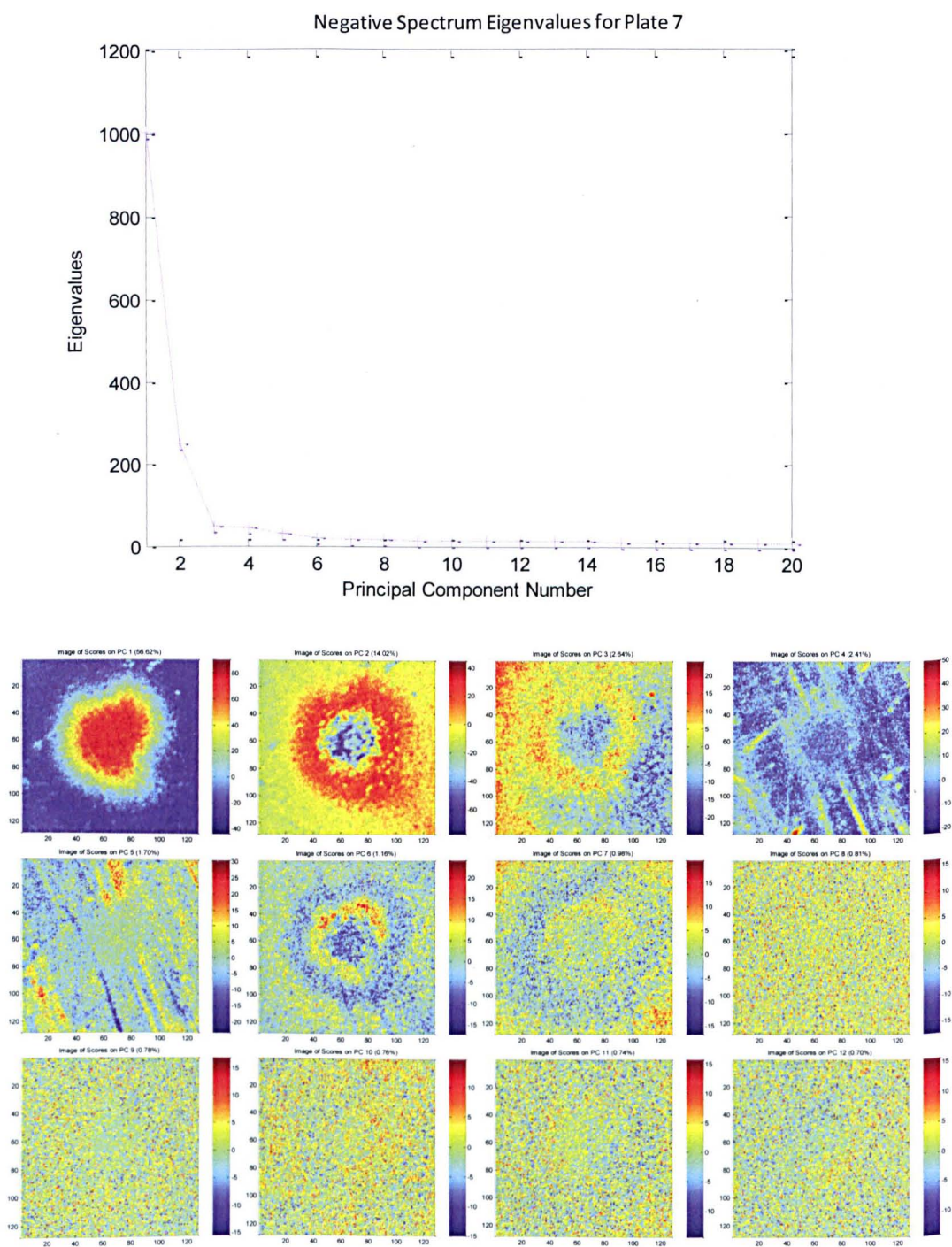


Figure 6.21: Negative Spectrum Eigenvalue plot and PCA score images on principal components 1 – 12 from a 500 μ m x 500 μ m area around a single API spot from a SX FP 100 formulation on plate 7 of an Andersen Cascade Impactor

segregation of chemical constituents. This in turn may reflect API separation. However as already stated, PCA alone is not always the most suitable analysis of hyperspectral images. Hence the PCA data was used to determine that subsequent MCR analysis should be based around a 4 component model.

6.4.2.5 Multivariate Curve Resolution Image Analysis of Hyperspectral Time of Flight Secondary Ion Mass Spectrometry Data

The ToF SIMS datasets were subject to MCR analysis with modeling for 4 components. Figure 6.22 shows the resulting MCR images for all the ACI plates analyzed from the positive spectrum, while figure 6.23 shows the same but from the negative spectrum. In these figures it can be seen visually that in nearly all instances the API deposits appear to have been identified by a positive correlation of MCR scores within one of the four MCR components modeled. The only exception is from the data in the negative spectrum on plate 0 of the ACI, where no positive chemical arrangement matches the particles deposited. However the distinct negative correlation from the components assembled does provide an outline of what appears to be the particle matter. In general however as we move down the plates from plate 0 we see single sparsely arranged positively identified particulate arrangements, begin to increase in frequency across plates 1, 2 and 3 before on plate 4 there is a distinct overlap into a central mass. Plates 4, 5, 6 and 7 show more and more coherent and smaller central chemical structures by MCR identification.

For the early plates (P0 – P3) the remaining components of each plate seem to represent various indistinct chemical arrangements that surround the API deposits. However in the later plates, (P4 – P7) with the exception of plate 5, there is the distinct appearance of a 'corona' or strong outline of the central particulate mass. In order to identify this and the other features designated by the MCR component images it was necessary to look at the loadings on each component. Figures 6.24, 6.25, 6.26 and 6.27 show the positive spectrum loadings on the MCR components 1 to 4 for the plate 5 data respectively. This is included along with the assignments of the evident key ion mass contributors and the parent chemical surface they are most likely to have come from. Figures 6.28, 6.29, 6.30 and 6.31 show the negative spectrum equivalents of

the same information. These figures are representative of the work done on all the components across all the plates.

From figure 6.24 we can see that the central region identified by MCR component 1 has a few key ions with significant loadings. The most prominent ion contributor, with a loading of $7.10E^{-01}$ was $C_7H_7^+$. This ion, as identified by looking at the reference samples, and by chemical deconstruction can be attributed to a fragment of SX inclusive of the tail aromatic ring. While a couple of the other more prominent ions can be found universally in the FP SX and plate references, the rest of the other key ions can again all be matched as shown to one of the APIs or the other. As such it is evident that this central chemically distinct feature is a combination of FP and SX, and most definitively the API deposit structure. By looking at figure 6.28 and MCR component 1 in the negative spectrum the same conclusion can be drawn. Here where a similar central chemically defined feature is evident, the most important ion mass contributors can be assigned as $C_{11}H_7O_3^-$ and $C_{10}H_7O^-$, both natural fragments of the beta₂-agonist. While both these component images have the most contribution from SX derived fragments, and this was generally true of most of the API containing component images, it is important to note that they also do show significant contributions from ion fragments derived from FP. Ions such as $C_3H_5O^+$, $C_3H_5O_2^-$, CH_2SF^- and F^- can all be seen to be significant contributors to the MCR component. The later plates show more of bias towards the contribution of the SX ions, but this expected as the from the ACI work carried out previously, it is known that mass of SX relative to FP increases at the fine particle plates are reached. At higher (lower plate number) plates such as plate 0 and 1 the most dominant API ion in the API components were derived from FP. More importantly however is that in figures 6.24 and 6.28, aside from some universally derived (both APIs and background) ion fragments there are no ions that can be directly attributed to the background plate. What this tells us is that these components describe the principal mass of the API deposition. For the remainder of the plates, this observation was consistent. In all instances (with the exception of the negative spectrum plate 0 MCR images), an API specific component can be identified visually and then with chemical confirmation. The first plates, 0 – 2 do show some slight overlap with background derived ions, but this is not unexpected given the much less concentrated covering of the API particles from the larger nozzles and reduced mass at that plate level giving rise to more surface exposure.

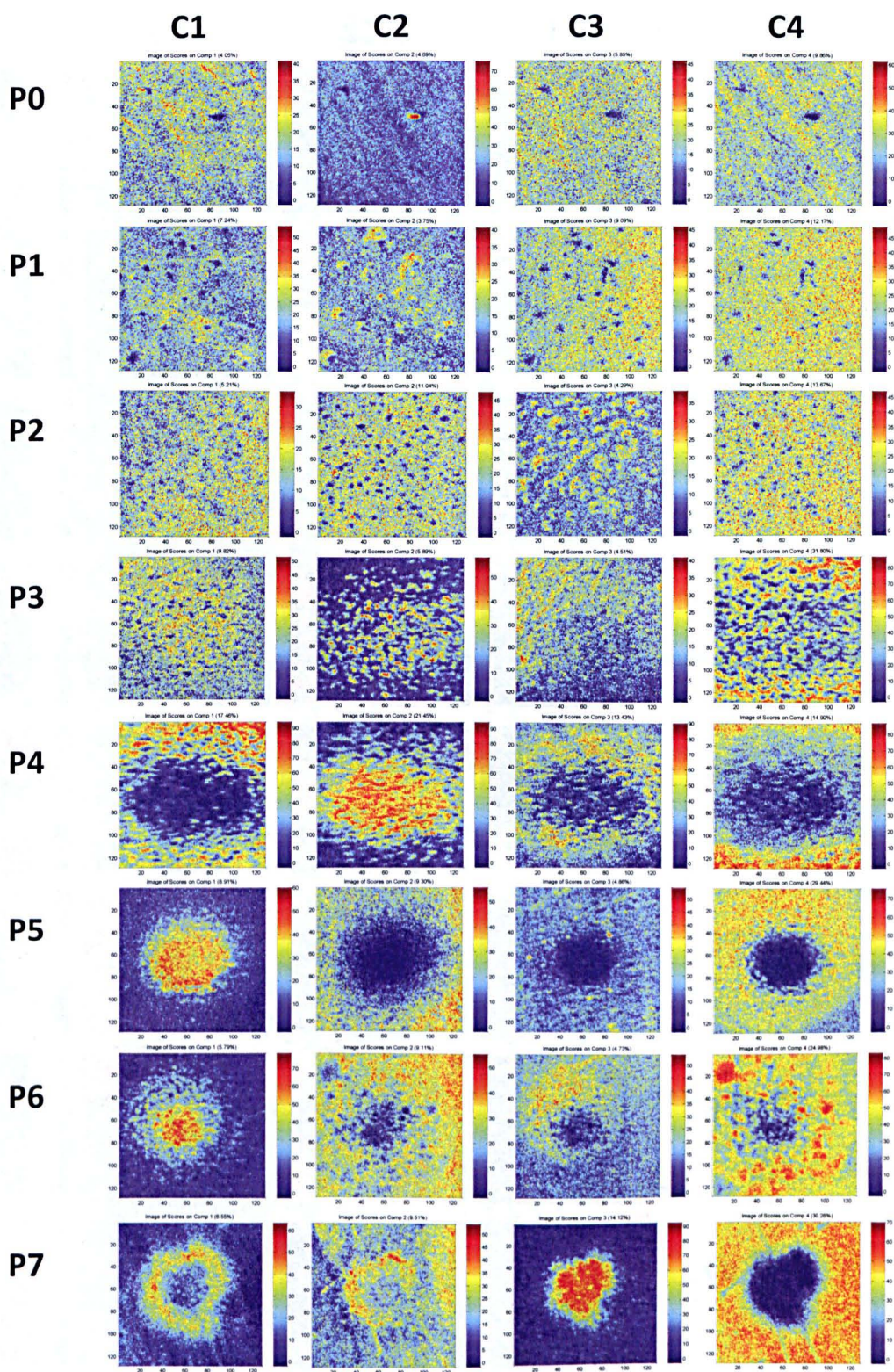


Figure 6.22: 500 μ m x 500 μ m images of the positive spectrum MCR scores on four components for plates 0 – 7 of a SX FP 100 pMDI deposit

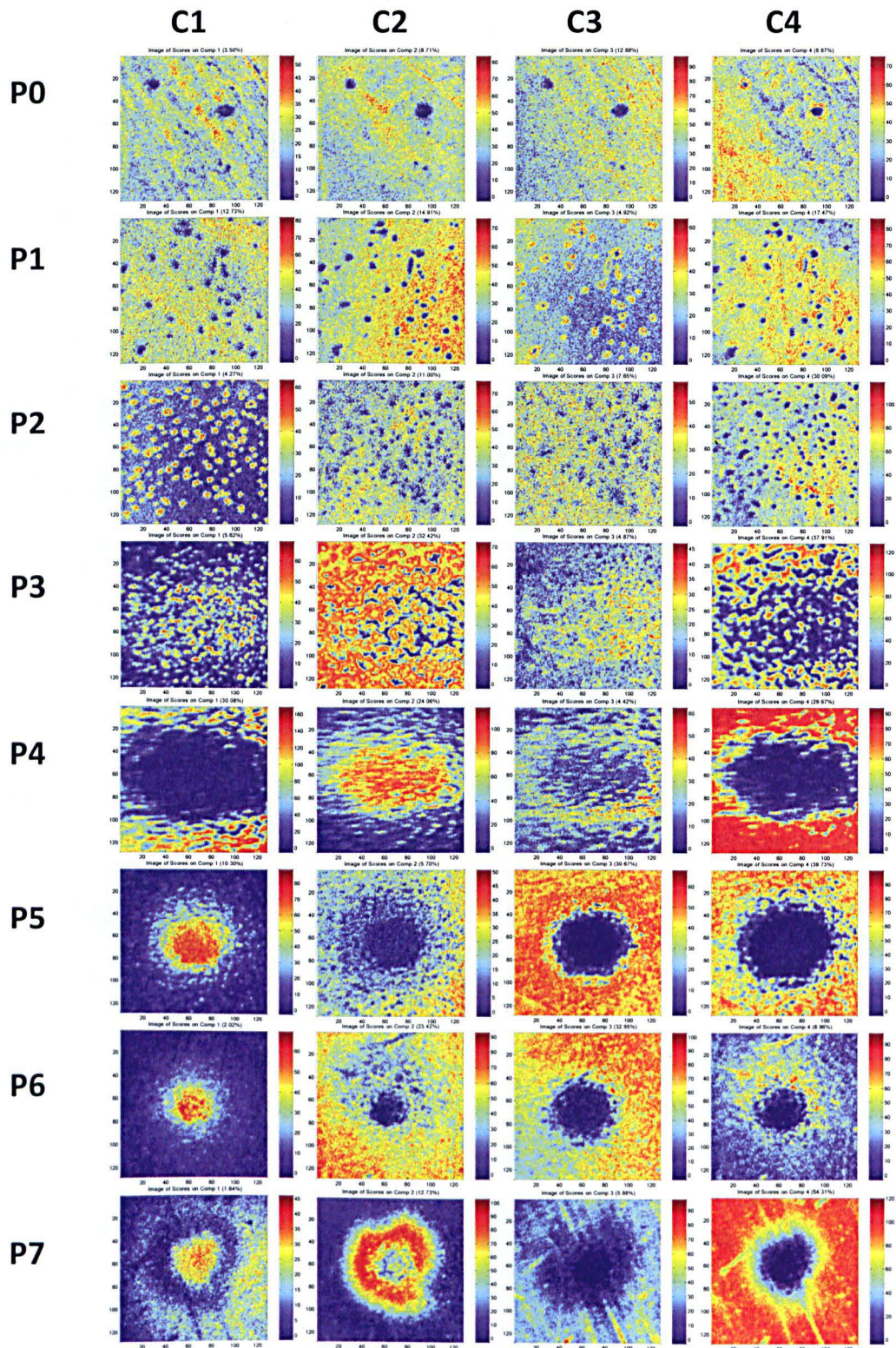


Figure 6.23: 500µm x 500µm images of the negative spectrum MCR scores on four components for plates 0 – 7 of a SX FP 100 pMDI deposit

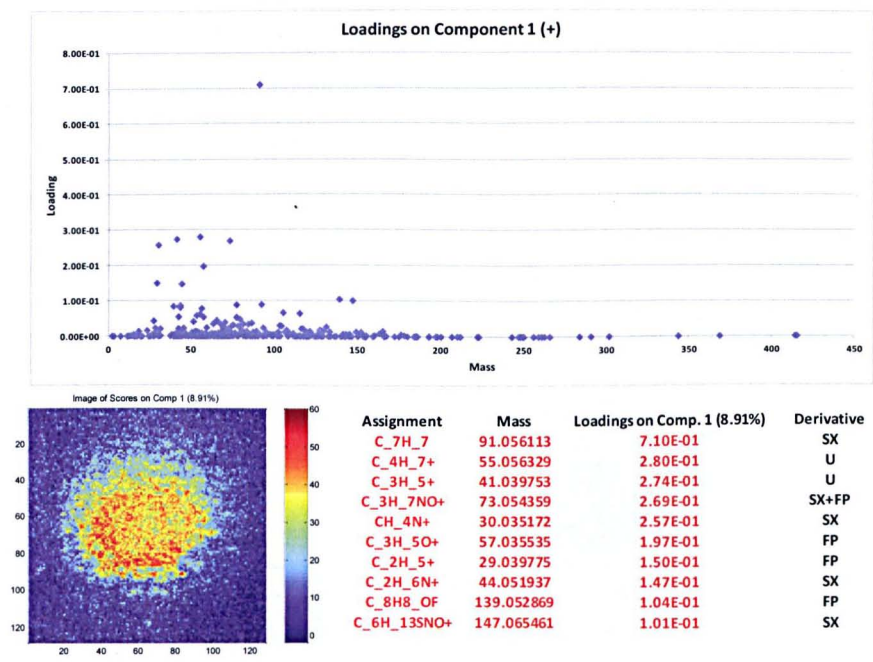


Figure 6.24: Positive Spectrum loadings and ion mass assignments on MCR component 1 of plate 5 of a SX FP 100 formulation deposit

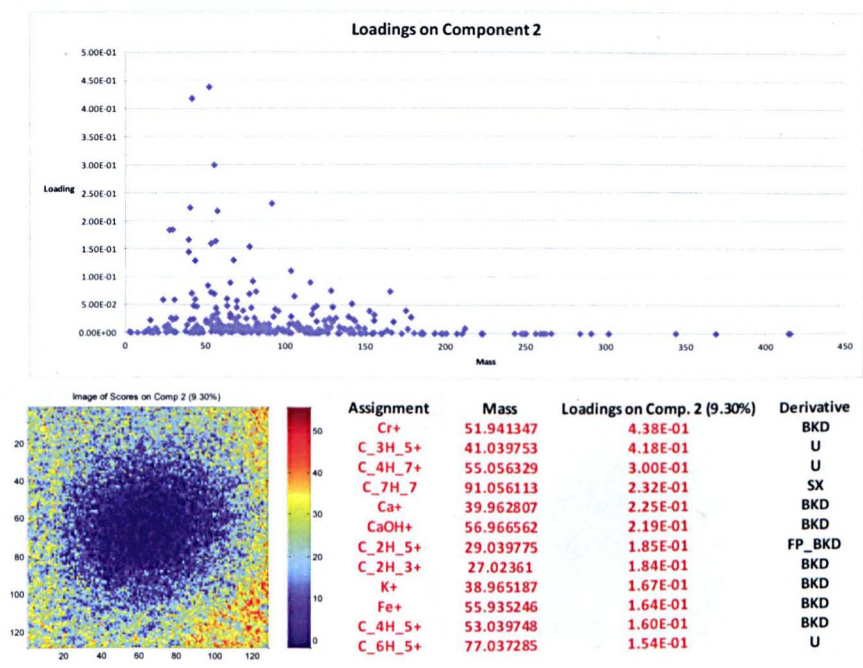


Figure 6.25: Positive Spectrum loadings and ion mass assignments on MCR component 2 of plate 5 of a SX FP 100 formulation deposit

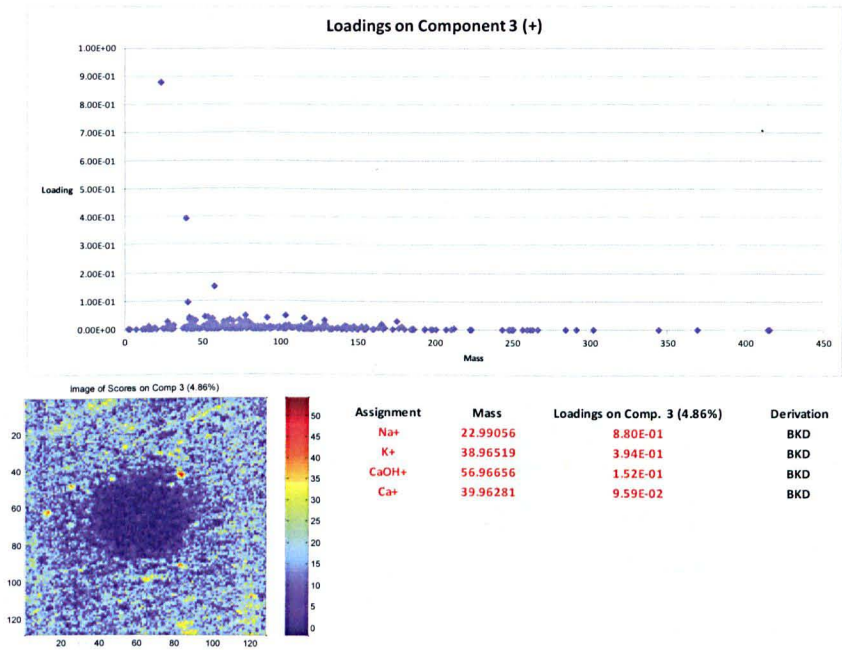


Figure 6.26: Positive Spectrum loadings and ion mass assignments on MCR component 3 of plate 5 of a SX FP 100 formulation deposit

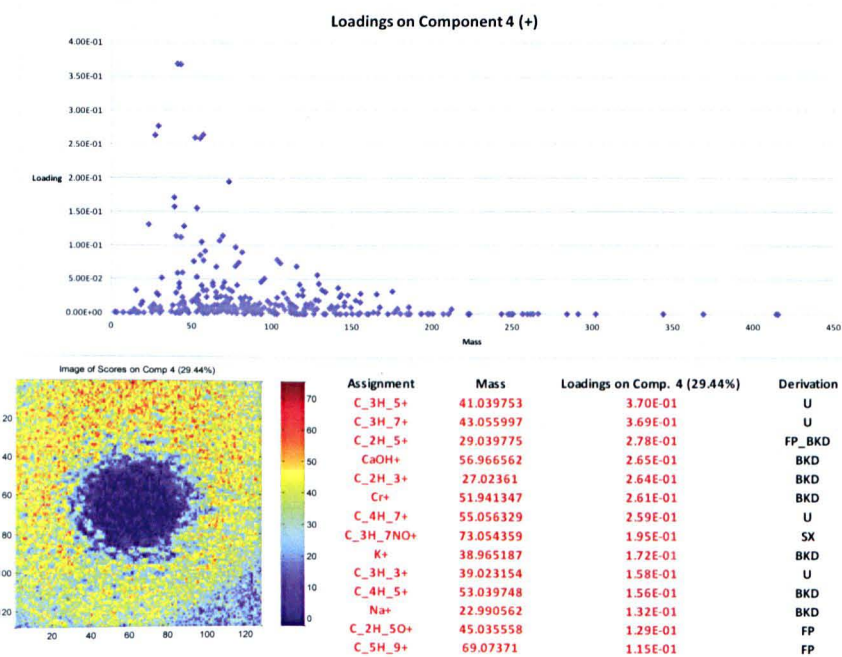


Figure 6.27: Positive Spectrum loadings and ion mass assignments on MCR component 4 of plate 5 of a SX FP 100 formulation deposit

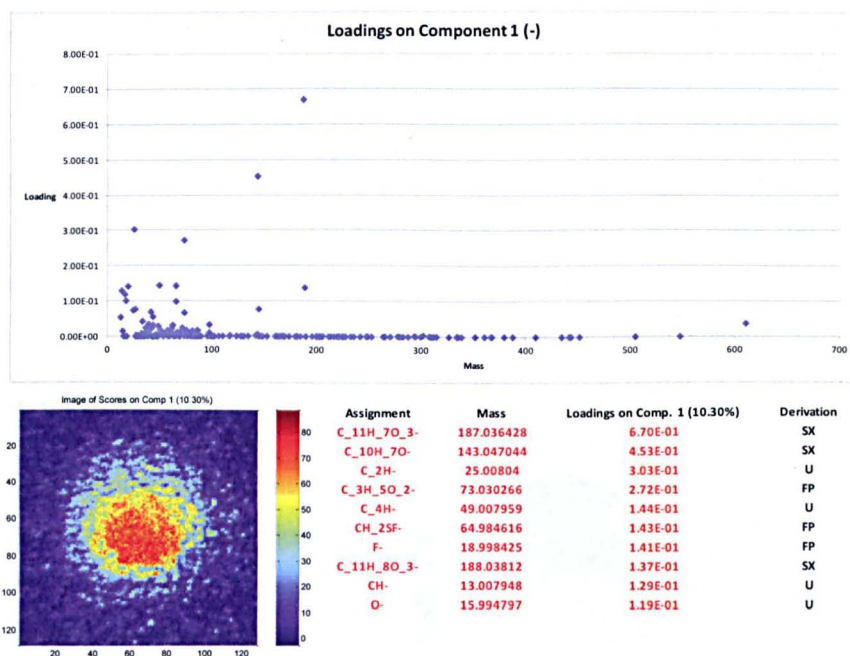


Figure 6.28: Negative Spectrum loadings and ion mass assignments on MCR component 1 of plate 5 of a SX FP 100 formulation deposit

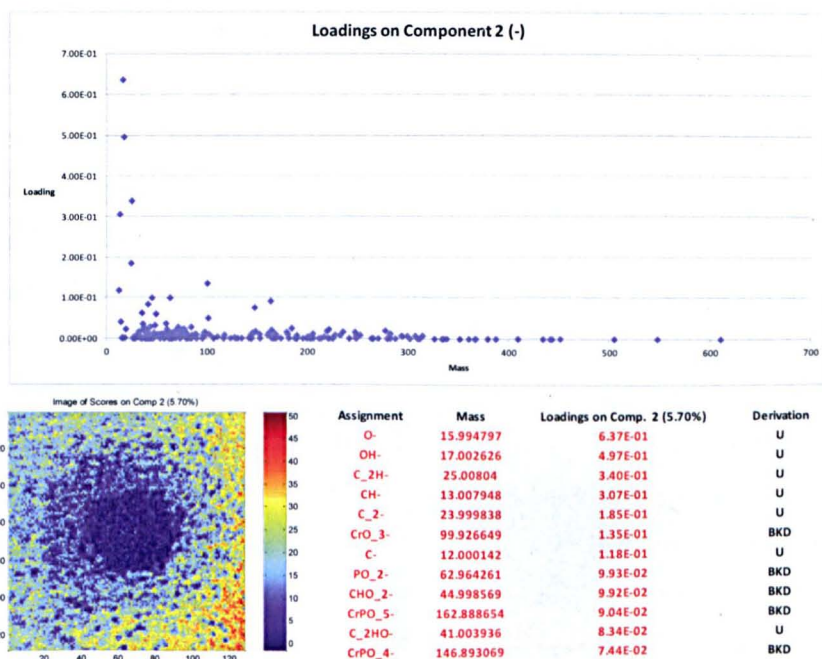


Figure 6.29: Negative Spectrum loadings and ion mass assignments on MCR component 2 of plate 5 of a SX FP 100 formulation deposit

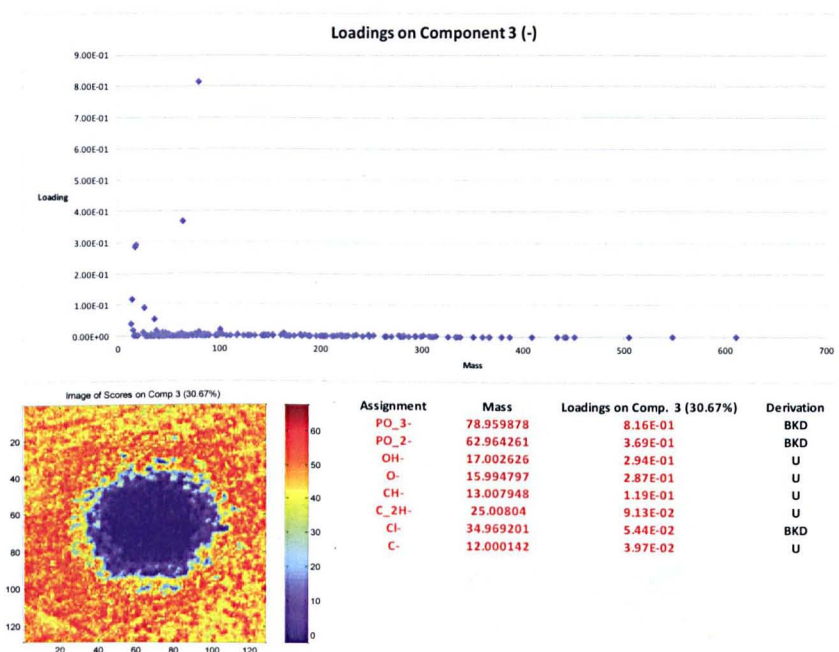


Figure 6.30: Negative Spectrum loadings and ion mass assignments on MCR component 3 of plate 5 of a SX FP 100 formulation deposit

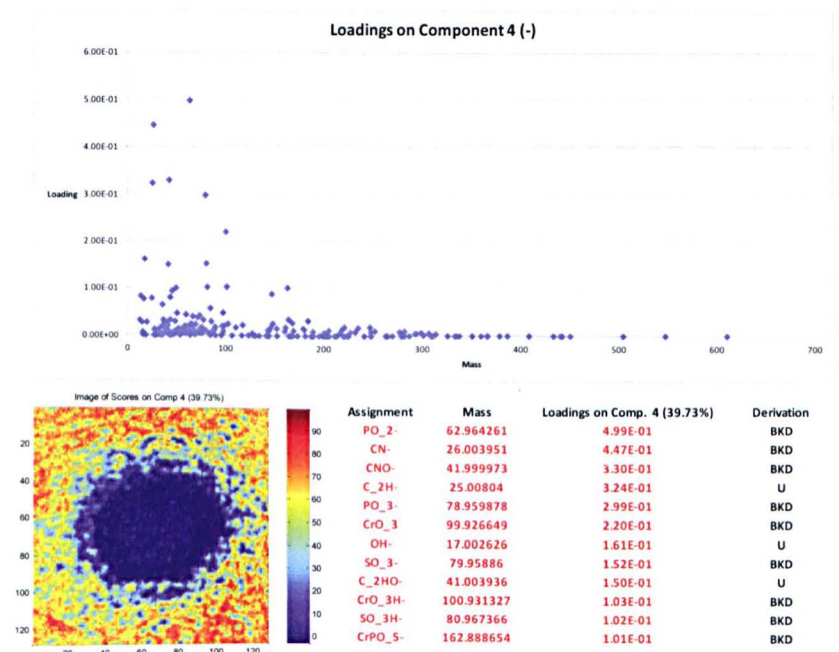


Figure 6.31: Negative Spectrum loadings and ion mass assignments on MCR component 4 of plate 5 of a SX FP 100 formulation deposit

As figures 6.25, 6.26, 6.27 and their negative spectrum equivalents, figures 6.29, 6.30 and 6.31 subsequently show, the remaining components are described by ion masses that are typically attributable to the background plate. The stainless steel ACI plate showed consistent and repetitive metal ion contributions (Cr^+ , K^+ , Na^+ , CaOH^+) in the positive spectrum, sulfur and phosphate group ions (PO_3^- , PO_2^- , SO_3^-) in the negative spectrum. These were abundant in the plate reference and distinguish the remaining MCR components from the API containing component. In plate 5 as an example there was no significant contribution to any of the remaining three MCR components from ion masses deriving from either SX or FP. With respect to the other plates this was also generally the case. In some instances there was the occasional low ion mass loading on a component that was associated with either of the two APIs. Examples include the presence of fluorinated ions in the negative spectrum of the 3rd MCR component of the negative spectrum analysis of plate 3. While FP should be the only fluorine containing entity present, there is the capacity for fluorinated contamination to have left small traces on the plate surfaces. Regardless it is worth noting that these loadings were not the most significant contributors to the MCR component.

However as mentioned already, in agreement with the PCA images in figures 6.18, 6.19, 6.20 and 6.21 the MCR component images in figures 6.22 and 6.23 do show some component images that present what appears to be a corona effect around the API component. This halo effect is distinct on plates 4, 6 and 7, but despite some suggestion of it by PCA not on plate 5 or the other plates. To identify whether these apparent surface features are related to any particular chemical moieties figures 6.32 and 6.33 show these extracted MCR components and their primary ion contributors from the positive and negative spectrum respectively, alongside the requisite assignment and suggested material source. What is apparent from both figures is that the principal contributions to all these MCR component images appear to be background (ACI plate) derived ions. There are a lot of small hydrocarbon ions e.g. C_3H_5^+ , C_3H_7^+ , C_2H_5^+ and metal ions e.g. Na^+ , Ca^+ and Cr^+ in the positive spectrum, as well as small oxygenated species such as O^- , OH^- , SO_3^- and PO_3^- in the negative spectrum that were particularly prevalent in the ACI plate reference. Some of these ions were however found universally across all the reference samples, and this makes it more difficult to identify the source. However there are also some ions that contribute to all these component images that are particularly associated with the APIs. Whilst their loadings on the component are much reduced from the top contributing ions, they are still

listed as within the top ten or so ions that define the MCR chemical map. Such examples include the $C_3H_7NO^+$, $C_2H_6N^+$, $C_{10}H_7O_3^-$ and $C_{10}H_7O^-$ ions from SX, the $C_2H_5O^+$, $C_5H_9^+$ and F^- ions from FP.

This data may suggest that this apparent corona is actually a region of the plate where the scatter of some API particles supplements the already high levels of small hydrocarbons, or oxygenated species which in turn is then modeled as a separate MCR component by variance. Certainly there is no evidence that there is segregation of the APIs into separate regions of the API spot. That we can see strong contributions from both APIs in the components reflecting the API deposit, as well as weaker contributions from both APIs again to these 'artificial' corona components, suggests that both APIs are distributed throughout the API spot. That this halo effect does not appear on the MCR components for plates above plate 4, and grows in intensity with the concentrating of the spot material as we move to smaller nozzle sizes (down to plate 7) might further infer that a matrix effect is being observed. This is to say that the intensity of the detected secondary ion signal is directly affected by the chemical constitution of the surrounding material 'matrix' (Belu et al 2003). As we have seen with the SEM images, the overlay of the API particles in the center of the deposit leads to alterations in electron conductivity because of insulation from the metal surface. In a similar fashion, as we concentrate the API powder into a smaller area and generate particle stacked deposits, the material at the peak of the resultant mound is unlikely to possess the same secondary ion yielding characteristics as those that lie on the metal plate. It is therefore possible that the secondary ion yield from the center of the insulating particle stack is less than that of the peripheral material which on a conductive surface generates high secondary ion yields. This artificial alteration to secondary ion yield coupled with the surface specific ions localized to this area may therefore lead to what appears to be such a 'halo' or 'corona' effect. With larger nozzles and less concentrated API particle mass, this effect is significantly reduced and hence not visible on plates 0 to 3.

To reinforce the hypothesis that the APIs are co-combined within one component by MCR analysis, and that the apparent 'halo' effect is artificial, figure 6.34 shows single ion ToF-SIMS images of the plate 7 drug spot using three ions that represent SX, FP and the plate background. The ion intensities presented next to the images reflect the intensity from the reference samples so as to infer the ion genesis. What the figure illustrates is that both the SX and FP derived ions ($C_{11}H_7O_3^-$ and $C_3H_5O_2^-$) originate from the center of the deposit. While the SO_3^- ion

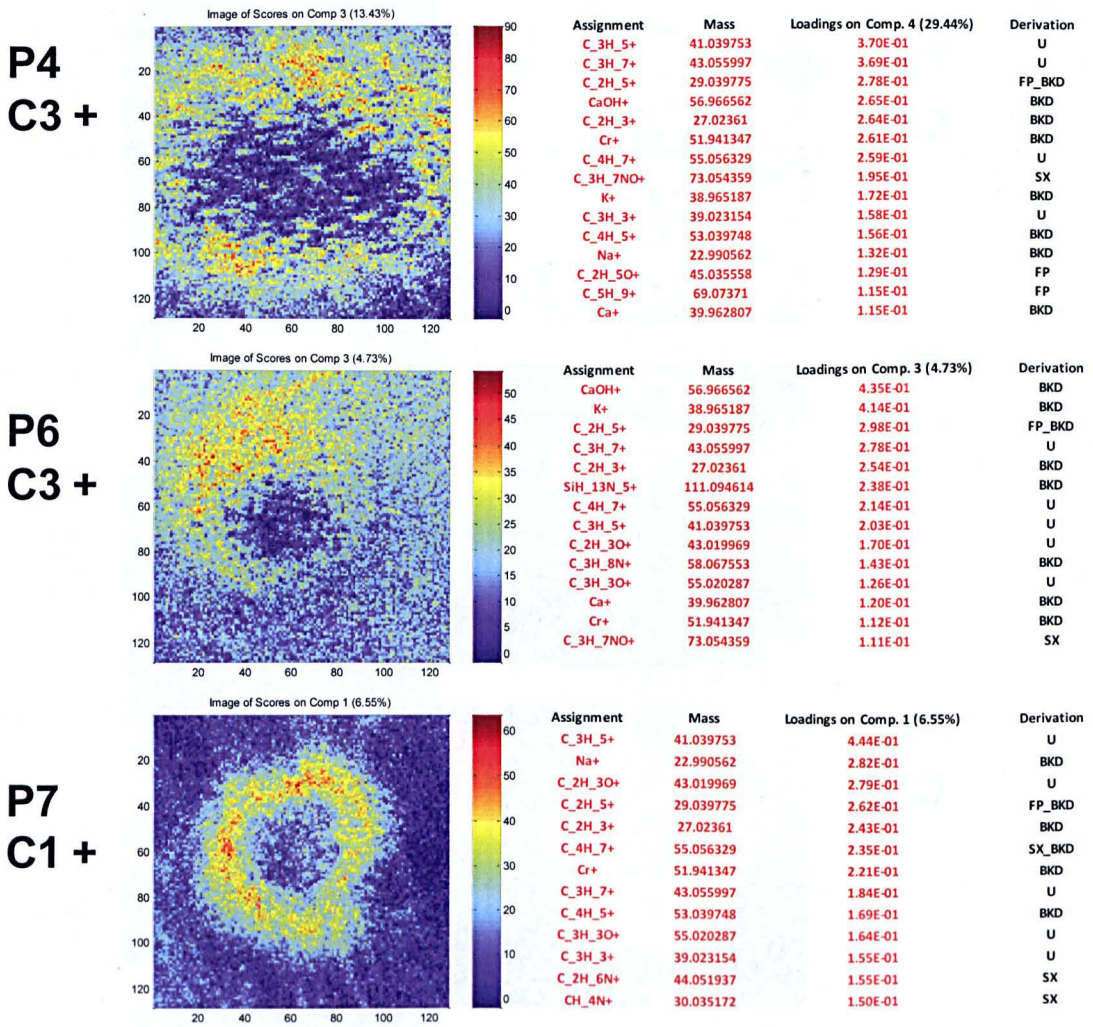


Figure 6.32: Positive Spectrum loadings and ion mass assignments on MCR components showing halo effect.

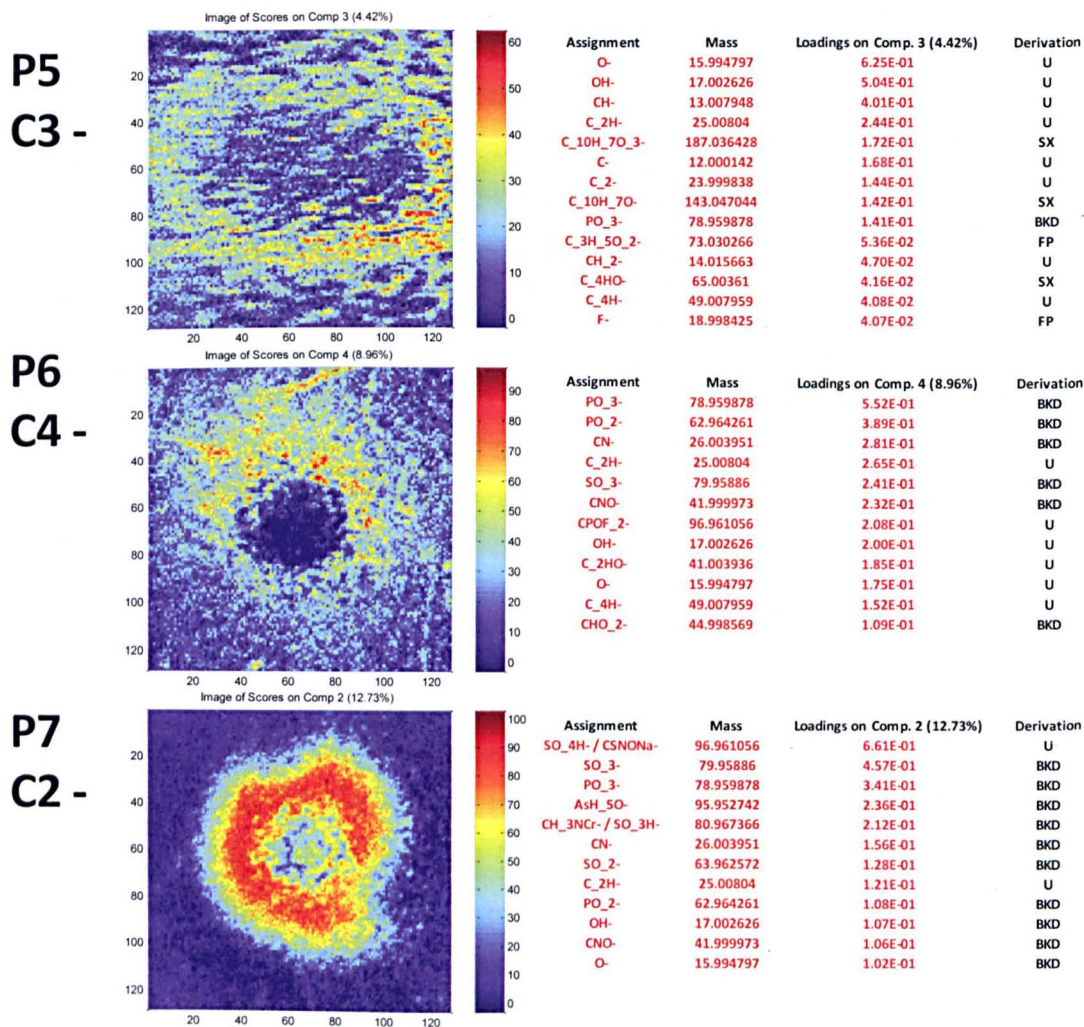


Figure 6.33: Negative Spectrum loadings and ion mass assignments on MCR components showing halo effect.

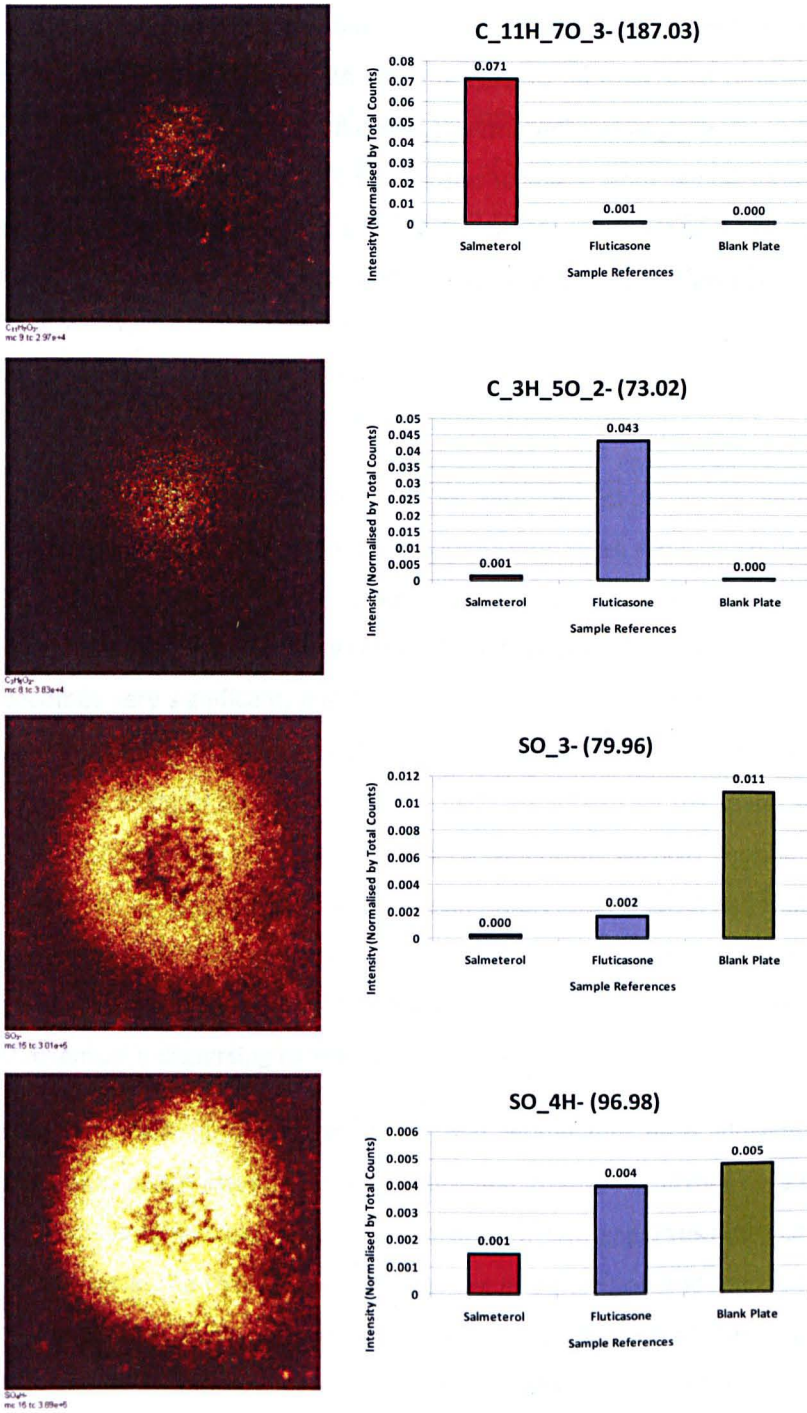


Figure 6.34: Negative spectrum single ion images of an Andersen Cascade Impactor plate 7 SS FX 100 deposit with the relative intensities of each ion found in the sample references.

associated heavily with the background shows an intense band around this spot that corresponds to the halo seen via MCR modeling. However when we look at the SO_4^- ion which shows low intensity counts but is relatively much closer across all the three surfaces, there is an exaggerated halo, with an overlap into the API spot. This seems to confirm that the halo is a function of exaggerated low intensity ion character by matrix effect. The MCR components presented above show a similar pattern for all the plates where this effect can be observed. Furthermore, all the strong API signals show a very good coherence on an ion by ion basis to the MCR described API components across all the plates.

6.5 Conclusions

From the complementary data presented on API co-localization several conclusions can be drawn. Firstly, the complementary use of multiple surface specific analytical mapping techniques provides a wealth of physicochemical information describing the broad deposition character of individual drug spots produced '*in-vitro*' of a binary pMDI system. The combination of SX and FP, which has previously been suggested to be more effective '*in-vivo*' thanks to increased levels of co-deposition of the two API particles appears to show significant co-deposited character by SEM, DESI, ToF-SIMS and Raman spectroscopy. All these techniques used evidenced particular strengths and weaknesses in making an assessment of co-deposition character and the physical make-up of the API deposits themselves.

SEM was unable to define the localization of SX with respect to FP by virtue of particle morphology alone. However it did highlight the composition of an API deposit and in particular the particle concentrating effect of the lower plates. Here where nozzle size decreases the impacted particles become more spatially confined. Particle overlay in the center of these lower plate spots becomes very significant, and this in turn leads to an influence on the SEM images returned. As the centrally deposited particulates insulate each other from the surface they are less able to dissipate electron charge than those particles spread on the metal substrate. This leads to a false intensity impression that suggests a significant particle 'mound'. However by rotating the sample to 45° it was seen that this height impression is false, and that although the central regions were highly concentrated with particle agglomerates, they did not stack to exaggerated heights. As we move from the center of each API spot we see smaller and smaller agglomerates, eventually dispersing to individual particles.

DESI suffered from a lack of spatial resolution that would not allow individual particulate definition or the appropriate assessment of an individual drug spot. Furthermore there remains a question of the bias introduced by the relationship of two separate and distinct chemical entities to the solvent in the DESI plume. Differences in desorption and ionization efficiencies mean that, it is difficult to assess accurately the broad quantification of mass equivalence in a given location. However the technique is relatively very rapid, and requires no special preparation of the samples. It is easily applied to large surface areas, and is still able to allow the broad localization of the two APIs within single drug spots. This therefore suggests that it offers

the opportunity for macroscale high throughput analysis. The DESI data collected in this chapter seemed to suggest that SX and FP could both be found within the same drug spots, spreading from the center out. However the stronger SX signal suggested this API was more broadly scattered from each spot, with FP more centrally contained. It is likely however that this reflects the better desorption character and greater mass of SX deposited on the fine particle plates.

Raman spectroscopy showed the best facility to assign chemical character to individual particles with confidence and thereby assess the individual particle co-ordination. By operating with a spatial resolution of 1 μ m it was possible to see that the vast majority of the FP particles mapped, were co-associated with SX particles. This was especially true in the center of each deposit. However as we move further away from the center of each spot, the frequency of independent API particles increases. Therefore the question of whether the particles co-deposit straight from the airstream or actually upon the impaction surface was raised. While the Raman maps were particularly useful in relating chemical identity to individual particles, at both small scales and across entire spots, they were very time consuming to run with the larger scan sizes taking several days to complete. In an attempt to reduce the run time, repeat spectra were not performed at each pixel point which meant the Raman maps were liable to anomalous spectra collection. In some instances photo reactive processes, such as fluorescence, interfered with the Raman signal and generated false modeling data. Furthermore the process proved to be partially destructive, with some API particles showing melting behavior under the NIR laser (785nm) as a result of the ACI plate radiating heat. This was already with a longer wavelength laser than would have been desired, due to unworkable fluorescence of SX under a green laser (532nm), which further reduced the Raman intensity of the samples, and prolonged run times. This suggests that Raman spectroscopy should be used for more detailed small spatial scale analysis of particle co-ordination experimentation.

ToF-SIMS combined with a multivariate approach to analysis generates image analysis data that again highlights the co-localization of the two APIs. Individual particle character was generally lost due to the overlap of variants analyzed (fragment ion masses), but following PCA analysis in order to define an MCR image analysis, the SIMS data yielded MCR components that show consistently strong API drug spots across all the ACI plates. These components were defined by ion mass loadings from ions that were confidently derived from both SX and FP, suggesting these areas were a blend of the two APIs. Both PCA and MCR analysis of the lower fine particle

plates seemed to suggest some form of peripheral surface feature surrounding the primary API spot, but this was attributed to a matrix effect borne of the concentrating effect of the smaller nozzle sizes on the API particles. Similarly to the SEM data, the insulation of the particles from the plate surface led to separate secondary ion yields depending on spatial location.

In collusion the techniques utilized suggest that there is high level co-deposition of SX and FP from a combination pMDI formulation on ACI plates. While the co-localization of the two APIs can be seen broadly in all the techniques (except SEM) the Raman data specifically shows FP and SX particles in co-association. While the degree of this co-association diminishes with distance from the center of the deposits, there is sufficient evidence to suggest that the two APIs either undergo a particular association in the airstream that leads to co-deposition or, co-deposit with adhesive contact on the impacted surface. This data therefore further supports the research carried out previously evidencing that these two APIs have a strong tendency to co-associate post-actuation. It is therefore viable to hypothesize that this observation may be intrinsically linked to the force balance of the system. Unfortunately it has not been possible to compare this formulation with another force balance characterized combination, so as to assess the relationship of a force balance to co-deposition further. The apparent instability of BDP in a HFA134a suspension without additional excipients has been highlighted, and the retention of this API made further deposition characterization alongside SS difficult and significantly less viable. In this instance the inability of Raman spectroscopy to identify more than the faintest BDP deposit, and the very low BDP mass spectra intensities returned with DESI meant little more could be followed up with respect to deposition analysis. With further BDP material and formulation, it would be of great interest to identify the exact changes that had occurred in the HFA134a propellant by XRPD or FT-IR spectroscopy so as to define the instability fully.

6.6 References

- H.R.H.Ali, H.G.M.Edwards, M.D.Hargreaves, T,Munshi, I.J.Scowen, R.J.Telford. (2008) Vibrational spectroscopic characterization of salmeterol xinafoate polymorphs and a preliminary investigation of their transformation using a simultaneous in-situ portable Raman spectroscopy and differential scanning calorimetry. *Analytica Chemica Acta*;620:103-120
- M.Aubier, W.Pieters, N.Schlosser, K-O Steinmetz. (1999) Salmeterol/fluticasone propionate (50/500 mcg) in combination on a Diskus inhaler (Seretide) is effective and safe in the treatment of steroid dependent asthma. *Respiratory Medicine*; 93:876-84
- P.J.Barnes. (2002) Scientific rationale for inhaled combination therapy with long acting beta₂-agonists and corticosteroids. *European Respiratory Journal*; 19:182-191
- E.D.Bateman, M.Britton, J.Carrillo, J.Ameida, C.Wixon. (1998) Salmeterol/fluticasone (50/100 mcg) combination inhaler. A new, effective and well-tolerated treatment for asthma. *Clinical Drug Investigation*; 16:193-201
- A.M.Belu, D.J.Graham, D.G.Castner. (2003) Time-of-flight secondary ion mass spectrometry:techniques and applications for the characterization of biomedical surfaces. *Biomaterials*; 21:3635-3653
- J.L.Black, B.G.G.Oliver, M.Roth. (2009) Molecular Mechanisms of Combination Therapy with Inhaled Corticosteroids and Long-Acting β -Agonists. *Chest*; 136:1095-1100
- A.Bouhroum, J.C.Burley, N.R.Champness. R.C.Toon, P.A.Jinks, P.M.Williams, C.J.Roberts. (2009) An Assessment of in situ Beclomethasone Dipropionate Clathrate Formation in Suspension Metered Dose Inhalers. *LBSA, School of Pharmacy, University of Nottingham*
- British Thoracic Society, Scottish Intercollegiate Guidelines Network. (2011) British Guideline on the Management of Asthma Quick Reference Guide. www.brit-thoracic.org.uk; accessed November 2011
- K.R.Chapman, N.Ringdal, V.Backer, M.Palmqvist, S.Saarelainen, M.Briggs. (1999) Salmeterol and fluticasone propionate (50/250 mcg) administered via combined Diskus inhaler: as effective as when given via separate Diskus inhalers. *Canadian Respiratory Journal*; 6:45-51

F.M.Ducharme, M.Chroinin Ni, I.Greenstone, T.J.Lasserson. (2010) Addition of long-acting beta2-agonists to inhaled corticosteroids versus same dose inhaled corticosteroids for chronic asthma in adults and children (Review) *John Wiley & Sons Ltd, The Cochrane Collaboration, www.thecochranelibrary.com; accessed November 2011*

Global Initiative for Chronic Obstructive Lung Disease Inc. (2011) Pocket Guide to COPD Diagnosis, Management and Prevention 2011. *www.goldcopd.org; accessed November 2011.*

M.P.Nelson, P.J.Treado. (2010) Raman Imaging Instrumentation. In: S.Sasic, Y.Ozaki. Raman, Infrared and Near-Infrared Chemical Imaging. *John Wiley & Sons, Hoboken, NJ, USA*

A.Theophilus, A.Moore, D.Prime, S.Rossomanno, B.Whitcher, H,Chrystyn. (2006) Co-deposition of salmeterol and fluticasone propionate by a combination inhaler. *International Journal of Pharmaceutics; 313:14-22*

N.J.Van den Berg, M.Ossip, C.A Hederos, H.Anttila, B.L.Riberio, P.I.Davies. (2000) Salmeterol/fluticasone propionate (50/100 mcg) in combination in a Diskus inhaler (Seretide) is effective and safe in children with asthma. *Pediatric Pulmonology; 30:97-105*

O.Zetterstrom, R.Buhl, H.Mellem, M.Perpina, J.Hedman, S.O'Neill, T.Ekstrom. (2001) Improved asthma control with budesonide/formoterol in a single inhaler compared with budesonide alone. *European Respiratory Journal; 18:262-268*

7.0 Final Conclusions

7.1 General Introduction

This thesis has examined the application of the AFM based CAB approach to the force quantification of real (as formulated) and semi-model active pharmaceutical ingredients for inhalation. It has further gone on to link measured force balances of binary combinations of APIs, to the '*in-vitro*' deposition performance of the co-formulated drugs, as examined by aerodynamic particle sizing and chemical mapping. Work has focused on the constraints and adaptability of using surface specific analytical techniques to qualify and quantify the force relationship between combination APIs, screen their deposition performance, and establish any casual links as appropriate. Below follows a concise summary of the chapters of the thesis in sequence.

7.2 Application of the CAB Approach to Inhalation Materials with 'Non-Ideal' Surfaces

Chapter 3 attempted to use CAB methodology to describe the force balance between combinations of API particles and pMDI component surfaces. Micronized particles of BDP and two BDP clathrate polymorphs (with relatively smooth and large particle surfaces) were attached to AFM tips as functional probes and challenged to the surfaces of a stainless steel metering chamber, uncoated aluminium canister wall and fluorinated ethylene propylene coated canister. Prior characterisation of the component materials using SEM and AFM showed surfaces that were in the region of 20-40 times rougher than typical recrystallized CAB substrates. Combined with API cohesive surfaces that ranged from 12-100 times rougher than normal CAB substrates the attempted CAB balances failed. Tip series from all the APIs showed little linear correlation, and the plotting of several tip values on opposing sides of the adhesive/cohesive divide within a CAB plot, was indicative that the contact regimes between the adhesive and cohesive surfaces were not showing sufficient parity. This reflected a loss of normalisation capability for the adhesion forces, making them incomparable. This failure was attributed to the relatively large surface rugosity of the 'raw' materials in combination with the

use of very large functional particle tips (some in the region of 60 μm) that exacerbated such topographical variability. While the model as a whole was seen to have failed, the constant rank affinity of all the APIs did seem to suggest that the FEP coated canister underwent the least forceful interaction with all three BDP polymorphic forms, which supported its use as a force modulator.

7.3 Application of the CAB approach to, and Characterization of Semi-Model Inhalation Substrates

Chapter 4 used the information from chapter 3 to direct the selective functionalization of AFM tips with small and well defined API particles, for use with compressed (reduced rugosity) powder substrates of API. The compressed substrates were characterised by AFM, SEM and DSC. The improved facility to perform surface energy measurements indicated more consistent surface topographies, and allowed a rank assessment of the API surface interactivities from which to choose combinations for further investigation. The AFM and SEM images of SS and BDP showed surface roughness reductions of the magnitude of 14-20 times from unprocessed. This rendered powder compacts with surface roughness values equivocal to 10-15 times rougher than usual CAB substrates. These surfaces were successfully utilised to produce a broad force balance by adapted CAB methodology. SS showed a cohesively dominated relationship with BDP (CAB ratio 1.69, R^2 0.57), while BDP showed an adhesively dominated relationship with SS (CAB ratio 0.35, R^2 0.57). The coefficient of determination with respect to the linear fitting of the tip series gave confidence to the force balance as a rough descriptor of the relationship of the two APIs. A second CAB balance using salmeterol xinafoate (SX) and fluticasone propionate (FP) was then performed and generated a force balance with a stronger linear regression. SX had a mildly cohesive relationship with FP (CAB ratio 1.05, R^2 0.97) while FP had an adhesively dominated relationship with SX (CAB ratio 0.63, R^2 0.63). These results together suggested that the use of semi-model substrates and tightly controlled functional technique had brought the topographical variability within a tolerance of an adapted CAB approach. However, the visualisation of the AFM and SEM images coupled with DSC analysis suggested that the compression process might have induced physicochemical changes that would compromise the viability of these semi-model replacements. This requires further investigation

7.4 The Cohesive Adhesive Balance of Inhalation Formulations and their 'in-vitro' Deposition Performance

Chapter 5 used combinations of SS with BDP, and SX with FP in HFA134a pMDI systems to evaluate the link between the force balance of the materials and their 'in-vitro' deposition performance in an Andersen cascade impactor. The SX and FP pMDI systems showed that the co-formulation of the two APIs improved the fine particle performance of FP, but worsened the fine particle performance of SX. This effect was exacerbated with increased formulation mass. It was concluded that the effect might be linked to the force balance of the system and the impact on aerodynamic particle behaviours. As FP interacts with more force with SX than itself, it would form stronger bound and bigger particle agglomerates when co-formulated. These agglomerates would then be subject to greater drag forces in the airstream upon aerosolization, aiding the deagglomeration process and dispersion to smaller depositing particle matter. FP only agglomerates would be smaller initially, being subject to lesser drag forces and dispersing less well. The reverse is hypothesised for SX, where co-formulation effectively dilutes agglomerate strength and size, and perversely may increase effective aerodynamic particle size. This effect could not be duplicated or compared with the SS and BDP combination. While there was some evidence of a declining fine particle performance of SS and of improving fine particle performance of BDP on co-formulation, there was a consistent critical loss of BDP mass across all BDP formulations. The lack of recovered BDP mass suggested instability in the manufactured pMDI systems leading to device retention. This requires further analysis.

7.5 Investigating the Co-Deposition of Salmeterol Xinafoate and Fluticasone Propionate from a HFA134a Pressurized Metered Dose Inhaler System

Chapter 6 went on to provide an extensive array of physical and chemical data characterization of the 'in-vitro' deposition of the combined SX and FP pMDI system. Complementary techniques such as SEM, DESI, Raman spectrometry and ToF-SIMS (with multivariate curve resolution analysis) combined to show that the two APIs could be identified as having co-localised within deposits on an ACI plate. Only Raman spectroscopy was able to resolve particle by particle

chemical identity using a NIR mapping process, but its long run times, and anomalous point propensity alongside the physical damage (melting) of the APIs makes it less suitable for rapid throughput investigations over large spatial scales. Techniques like DESI were much faster and could quickly confirm the presence of both APIs, but concerns about differences in ionization and desorption efficiencies coupled with poor spatial resolution limit its use to broad and macroscale mapping procedures. SEM imaging was able to identify particle morphologies, but not distinguish the two APIs apart.

Multivariate analysis of the ToF-SIMS data provided confirmation of the blend of two APIs within deposits with no discernible segregation. Although some component images suggested a 'halo' effect, with a combination of API and predominant background character, this was unique to highly concentrated drug spots on the lower plates. Here a particle 'mound' was likely to induce a matrix effect where differences in ionisation efficiency and topographical differences arise as the incident beam moves from plate to concentrated (insulated) drug spot. While the techniques were able to identify and characterise both APIs from an '*in-vitro*' deposit, it was unclear whether the ACI material was at all representative of the complex deposition mechanisms '*in-vivo*' and therefore whether any observed co-deposition was pre-determined by aerodynamic interaction, or by forced mixing on the plate. It is possible that the force balance of the two APIs improves the co-deposition frequency of this particular formulation with respect to other combinations of API, but this requires further research for comparison with other quantified systems.

7.6 Future Research Suggestions

The work in this thesis has generated several points of interest, and also lays the basis for further investigation into broader aspects of the field. Of particular note, better characterisation of the impact of the compression of APIs into powder compacts is needed. DSC suggested that the compression process may have changed the polymorphic balance of SX, with more form II as a consequence. Further investigation, using such techniques as FT-IR or confocal Raman would be appropriate to ascertain the extent, type and location of any polymorphic change with respect to both SX, and the others APIs. This is important because the use of a semi-model substrate has been suggested as more facile and potentially representative model of an API than

the traditional CAB substrates (molecularly smooth crystals). Yet this is detracted from if in the process of producing a powder compact the physical form has been altered.

Another area where follow up would be recommended is into the instability of BDP within a pure HFA134a system. The commonplace use of co-solvents and surfactants was deliberately avoided in these studies so as to avoid compromising the force balance between composite materials. It was assumed that the short lifespan between manufacturing and using the pMDI canisters would therefore negate stability issues, which are normally mid- to late- lifetime issues. However the obvious device retention of BDP from all BDP formulations as seen by deposition analysis, was compounded by evidence in the DSC traces of additional endothermic processes in the extracted API. It would be of great benefit to identify this transition, and with the availability of more extractable product run more analytical techniques such as XRD or FT-IR to identify what changes have been brought about and understand the process.

Moving forward generally, two areas of further research would be particularly beneficial. Firstly, this body of work was based on the principle of using a simple AFM based methodology to identify a force trend with demonstrable impact on pMDI formulation behaviour. However the array of solvent forces experienced by API particles within a propellant such as HFA134a, contribute significantly to API character, and specifically can determine adhesive behaviour. Therefore while it is a success to link a basic force balance between two APIs to performance from a HFA pMDI system, the natural progression of the work is to perform a balance in a model propellant (e.g. decafluoropentane) to compare the results and evaluate the impact of solvent forces on a given force balance. Working with AFM to perform colloidal probe microscopy based experimentation in liquid media (especially that which is volatile) suffers from technical difficulties and detracts from the goal of a rapid and uncomplicated screening tool. However a force balance in such conditions would better describe the actual force balance of a pMDI combination in a given solvent, and would then allow the impact of subsequent force modulators, such as surfactants, to be evaluated alongside the API combinations.

Secondly, the characterization work achieved in chapter 6 generated a large array of chemical and physical information surrounding the SX and FP deposits. However while some of this was novel, and could be used to better understand the '*in-vitro*' mechanics of the system, it would be made more significant if the process was repeated with further combinations of APIs, especially those with differing force balances. If alterations to fine particle performance, particle

co-ordination in deposits and morphological characteristics could be qualified or and quantified for comparison, a better understanding of the influence of a range of force balances would be obtained. This would potentially allow the whole CAB process to function as a quick and simple formulation screen, in prospective formulations, and between suggested combinations of drugs, thereby validating the methodology.

It is my hope that some of these issues and questions can be addressed by further research to expand upon the information and insight I have been able to gain throughout the last 3 years.

Matthew Piggott